

University of Warwick institutional repository: <http://go.warwick.ac.uk/wrap>

A Thesis Submitted for the Degree of PhD at the University of Warwick

<http://go.warwick.ac.uk/wrap/47055>

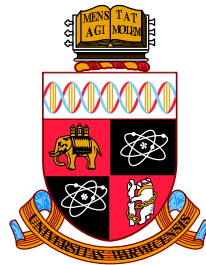
This thesis is made available online and is protected by original copyright.

Please scroll down to view the document itself.

Please refer to the repository record for this item for information to help you to cite it. Our policy information is available from the repository home page.

THE UNIVERSITY OF WARWICK

School of Engineering



A Numerical Investigation of Three-dimensional
Unsteady Turbulent Channel Flow Subjected to
Temporal Acceleration.

PhD. Thesis

TARIQ TALHA

March 1, 2012

THE UNIVERSITY OF WARWICK

SCHOOL OF ENGINEERING

Centre for Scientific Computing(CSC)

A Numerical Investigation of Three-dimensional
Unsteady Turbulent Channel Flow Subjected to
Temporal Acceleration.

by

TARIQ TALHA

Supervisor

Dr. Yongmann M Chung

This thesis is submitted in partial fulfilment of the requirements for
the degree of
Doctor of Philosophy in Engineering

MARCH 1, 2012

©Warwick University

To my family.

Declaration

This thesis, and the material in it, is my own work. It has not been submitted for a degree at any other university.

As part of the work carried out, the following paper was published:

Y.M Chung and T.Talha. Effectiveness of active flow control for turbulent skin friction drag reduction. *Physics of Fluids*, 23(2):025102, 2011.

Abstract

Investigation of turbulence response during constant temporal acceleration and deceleration can assist in improving the understanding of turbulence evolution and flow physics. Such flows have potential importance in engineering applications for example the air flow through the main trachea during the breathing cycle experience temporal acceleration and deceleration. The previous experimental and theoretical investigations based on conventional computational fluid dynamics (CFD) modelling could not provide the detailed information about turbulence response in the near-wall region in such types of flows. In particular, the response of near-wall structures has not been studied for turbulent flow with temporal acceleration and deceleration. In the present study, turbulent flows involving temporal acceleration and deceleration has been investigated using DNS and LES.

A fully implicit fractional step method is implemented in the present study. The Navier-Stokes equations are discretised using finite volume method. Second-order-implicit Crank-Nicolson method is used for temporal discretisation for the convective and viscous terms. Second-order accuracy of spatial discretisation is achieved using four neighbouring points to calculate velocity gradients. A uniform grid is used in the streamwise and spanwise directions while a non-uniform grid is employed in the wall-normal direction. The numerical implementation has been validated for three test cases. The dynamic subgrid-scale model has been implemented for LES calculations. The LES model implementation has been validated through comparison with benchmark data available in literature.

As one of the first DNS of accelerating turbulent flow, this study has produced a comprehensive database of turbulent statistics which can be used for unsteady turbulence modelling and validation. The detailed investigation has substantially enhanced the understanding of turbulence response for such flows. The flow physics has been studied in detail using turbulent kinetic energy budget analysis, vorticity analysis, anisotropy invariant maps and energy spectra. The evolution of new turbulent structures during the acceleration has been investigated using low-speed streaks and λ_2 plots and many interesting flow characteristics have been found. The effect of different acceleration rates has been studied using LES. The turbulence propagation in the core region has been studied for different acceleration rates. Turbulent flow subjected to constant temporal deceleration has also been investigated using LES. The effect of different deceleration rates has been also studied. The turbulent flow response to temporal deceleration has been analysed using the rms velocity and vorticity, kinetic energy budget and Reynolds stress anisotropy tensor analysis.

Acknowledgments

I would like to thank the Pakistan Government and School of Engineering for providing me with the necessary financial support, without which this work could not have been achieved. Special thanks to my supervisor Dr. Yongmann M. Chung to keep me motivated and to supervise me throughout the PhD. I am grateful to him for the invaluable feedback, he has provided in proof-reading this thesis. Many thanks to my parents who brought me to life and have always encouraged me to aim higher. Lots of thanks to my beloved wife Musfirah who gave the necessary moral support to finish this work.

Contents

List of Figures	xv
List of Tables	xvii
Nomenclature	xviii
1 Introduction	1
1.1 Project overview	2
1.2 Thesis road map	4
2 Literature Review	9
2.1 Non-periodic transient flows	10
2.1.1 Accelerating/decelerating flows	10
2.1.2 Three-dimensional strained transient flows	17
2.2 Spatially evolving transient flows	18
2.3 Periodic transient flows	21
3 Numerical Methods.	23
3.1 Direct numerical simulation (DNS)	23
3.1.1 Projection FSM	27
3.1.2 Splitting FSM	29
3.2 Solution procedure	33
3.2.1 Momentum equations	33
3.2.2 Spatial discretisation	36

3.2.3	Poisson equation solution	38
3.3	Validation	41
3.3.1	Decaying vortex test case	41
3.3.2	Turbulent channel flow	44
3.3.3	Boundary condition implementation validation	46
3.4	Large eddy simulation (LES)	47
3.4.1	LES equations	49
3.4.2	Subgrid-scale (SGS) models	50
3.4.3	LES validation	56
4	Preliminary Simulations.	61
4.1	Simulations details	61
4.1.1	Acceleration parameter	62
4.1.2	Simulation parameters	65
4.2	Domain size test	68
4.3	Time step size test	73
4.4	Turbulent statistics	77
5	DNS of Temporal Acceleration.	86
5.1	Simulation parameters	87
5.2	Wall shear stress	88
5.3	Mean velocity	93
5.4	RMS velocity fluctuations	99
5.5	Reynolds stresses	108
5.6	RMS vorticity fluctuations	112
5.7	Turbulent kinetic energy (TKE) budgets	116
5.8	Probability density function (pdf) analysis	120
5.9	Conclusions	130

6	Effect of acceleration on turbulent structures.	133
6.1	Low-speed streaks	134
6.2	Structures visualisation	138
6.3	Active area quantification procedure	144
6.4	Conditional average statistics	150
6.5	Reynolds stress anisotropy tensor analysis	156
6.5.1	Energy spectra analysis	163
6.6	Conclusion	165
7	Effect of Different Acceleration Rates.	167
7.1	Simulation parameters	168
7.2	Wall shear stress	171
7.3	Mean velocity	175
7.4	RMS velocity fluctuations	179
7.5	RMS vorticity fluctuations	188
7.6	PDF analysis	192
7.7	Turbulent structures	196
7.8	Conclusions	206
8	LES of Temporal Deceleration.	208
8.1	Simulation parameters	209
8.2	Wall shear stress	213
8.3	Mean velocity	216
8.4	Turbulence intensities	219
8.5	RMS vorticity fluctuations	226
8.6	TKE budgets	230
8.7	Reynolds stress anisotropy tensor analysis	234
8.8	Conclusions	237
9	Conclusions.	239

List of Figures

3.1	Flow chart of the main DNS/LES code.	34
3.2	Staggered grid for spatial discretisation for primitive variables.	36
3.3	Maximum error for decaying vortex test case.	42
3.4	Velocity and pressure contours for decaying vortex test case.	43
3.5	Comparison of turbulent statistics for fully-developed turbulent channel DNS.	45
3.6	Comparison of turbulent statistics for active flow control simulation.	46
3.7	Log-law profiles for fully-developed turbulent channel LES at several Reynolds numbers.	58
3.8	RMS velocity profiles for fully-developed turbulent channel LES at several Reynolds numbers.	59
3.9	Limiting behaviour of the SGS viscosity.	59
3.10	Relationship of C_w with Re_τ	60
4.1	Time histories of the bulk-mean velocity and mean pressure gradient during the constant acceleration	64
4.2	Comparison of Re_τ histories during temporal acceleration for several domain sizes.	69
4.3	RMS velocity profiles for $f = 0.2$ acceleration case for several domain sizes.	71
4.4	RMS velocity profiles for $f = 0.5$ acceleration case for several domain sizes.	72
4.5	Time histories of the turbulent kinetic energy and shear stress for time step size parametric study.	76
4.6	The Reynold stress budget profiles for fully-developed turbulent channel.	79

4.7	A description of anisotropy invariant map (AIM) taken from Simon- sen and Krogstad (2005).	82
4.8	AIM for fully-developed turbulent channel flow at several Reynolds numbers.	83
4.9	λ_2 plots for fully-developed turbulent channel flow at several Reynolds numbers.	85
4.10	Profiles of rms λ_2 fluctuations at several Reynolds numbers.	85
5.1	Time history of Re_τ during temporal acceleration.	90
5.2	Variations of U_m^+ and C_f during the acceleration.	92
5.3	Time histories of boundary layer parameters during the acceleration.	92
5.4	Mean velocity profiles at several Re numbers during the acceleration.	94
5.5	Log-law profiles during the stage III.	94
5.6	Variation of the defect law profiles during the acceleration.	95
5.7	Time histories of the mean velocity at several wall-normal locations.	96
5.8	2D variations of U , dU/dy , and $dU/d\xi$	97
5.9	The rms velocity fluctuation profiles at several Re numbers during the acceleration.	100
5.10	Variations of rms velocities at several y locations.	102
5.11	2D Variations of rms velocities in wall units.	104
5.12	Variations of maximum values of u_{rms} and v_{rms} during the acceleration.	105
5.13	Time histories of y locations for maximum rms velocity fluctuations.	106
5.14	Propagation of u_{rms} in the channel core region during the acceleration.	107
5.15	Time histories of the turbulent shear stress during the acceleration.	108
5.16	2D variation of $-\overline{uv}/U_m^2$	109
5.17	Time histories of $-\overline{uv}/k$ at several y locations.	110
5.18	2D variations of a_1 and ν_t/ν during the acceleration.	111
5.19	Vorticity fluctuation profiles at several Re numbers during the accel- eration.	113
5.20	Time histories of $\omega'_{x,wall}$, $\omega'_{x,min}$, $\omega'_{x,max}$, $\omega'_{y,max}$, and $\omega'_{z,wall}$ during the acceleration.	114

5.21	Time histories of y locations of $\omega'_{x,min}$, $\omega'_{x,max}$ and $\omega'_{y,max}$ during the acceleration.	115
5.22	Time histories of maximum values of several budget terms	116
5.23	2D variations of budget terms of \overline{uu} transport equation during the acceleration.	118
5.24	Wall-normal profiles of various budget terms during the acceleration.	119
5.25	PDF of u' and v' at several y locations for a fully-developed turbulent channel flow.	122
5.26	Frequency of quadratic events during the acceleration.	124
5.27	Magnitude of quadratic events during acceleration.	125
5.28	Magnitude of quadratic events at several y locations (in absolute percentage).	126
5.29	Weighted pdf of u' and v' at $y^+ = 3$ at several Reynolds numbers during the acceleration.	127
5.30	Weighted pdf of u' and v' at $y^+ = 10$ at several Reynolds numbers during the acceleration.	128
5.31	Weighted pdf of u' and v' at $y^+ = 50$ at several Reynolds numbers during the acceleration.	129
6.1	Mean streak spacing variation in the wall-normal direction for fully-developed turbulent channel flow.	135
6.2	Low-speed streaks at several Reynolds numbers during the acceleration.	137
6.3	Time history of $\lambda'_{2,max}$ during the acceleration.	139
6.4	λ_2 iso-surfaces at several Reynolds numbers during the stage II.	140
6.5	λ_2 iso-surfaces at several Reynolds numbers during the stage III.	141
6.6	2D xz contours of the instantaneous streamwise vorticity at several Reynolds numbers during the acceleration.	142
6.7	λ_2 iso-surfaces at $Re = 11000$	143
6.8	PDF of λ_2 fluctuations at several Re numbers during the acceleration.	145
6.9	PDF of λ'_2 for fully-developed turbulent channel flow at several Reynolds numbers.	146
6.10	Active area quantification procedure.	147
6.11	Time history of new turbulent area during acceleration.	149

6.12	Conditionally-averaged λ'_2 profiles.	150
6.13	Time histories of conditionally-averaged maximum λ'_2 and u_τ	151
6.14	Conditionally-averaged mean velocity and rms velocity fluctuations profiles.	152
6.15	Conditionally-averaged rms vorticity fluctuations profiles.	154
6.16	ω'_x profiles for the non-active area at several Reynolds numbers during the acceleration.	155
6.17	Time histories of conditionally-averaged $\omega'_{x,min}$ and $\omega'_{x,max}$	155
6.18	Time histories of anisotropy stress tensor terms at several y locations.	157
6.19	Wall-normal profiles of anisotropy stress tensor terms at several Reynolds numbers.	158
6.20	2D variations of II and III during the acceleration.	159
6.21	Wall-normal profiles of F and G invariant functions.	159
6.22	Anisotropy invariant maps at several Reynolds numbers during the acceleration.	161
6.23	Time histories of maximum values of $-II$ and III	162
6.24	Turbulent kinetic energy spectra in the near-wall region during the acceleration.	163
6.25	Turbulent kinetic energy spectra at the channel centreline during the acceleration.	164
7.1	Re_τ time history comparison between DNS and LES.	169
7.2	Comparison of the mean velocity and the rms velocity fluctuations between DNS and LES.	170
7.3	Time histories of the wall shear stress for the three acceleration rates.	171
7.4	Time histories of $du_\tau/d\xi$ for different f values during temporal acceleration.	173
7.5	Variations of boundary layer parameters for the three acceleration rates.	174
7.6	Mean velocity profiles for different acceleration rates.	175
7.7	Variations of the log-law for different acceleration rates.	176
7.8	Time histories of the mean velocity at several y locations.	177
7.9	2D contour plot of (dU/dt) for the three acceleration rates.	178

7.10	RMS velocity profiles for the $f = 0.2$ and $f = 0.5$ cases.	180
7.11	2D contours of u'^+ and v'^+ for the three acceleration rates.	181
7.12	Variations of maximum values of u_{rms} and v_{rms} for the three f values.	182
7.13	Time history of maximum value of turbulent production term in \overline{uu} budget equation	182
7.14	Turbulent kinetic energy profiles at two Re_τ and time instances. . . .	183
7.15	Time variations of k/U^2 at several y locations during the acceleration.	184
7.16	2D contours of $du_{rms}/d\xi$, $dv_{rms}/d\xi$ and $dw_{rms}/d\xi$ for $f = 0.2$ case. . .	185
7.17	Propagation of u_{rms} and v_{rms} in the core region for several a_ϕ values.	186
7.18	Turbulence propagation of different flow properties in the core region.	187
7.19	Variations of maximum values of ω'_x , ω'_y and ω'_z for the three f values.	189
7.20	Variations of y locations of $\omega'_{x,min}$, $\omega'_{x,max}$ and $\omega'_{y,max}$ during the stage IV.	190
7.21	2D contours of ω'^+_x and ω'^+_y for the three f values.	191
7.22	Time histories of quadratic contributions in the near-wall region for the three f values.	193
7.23	Joint pdf of u' and v' at $y^+ = 3$ at several Reynolds numbers.	194
7.24	Joint pdf of u' and v' at $y^+ = 20$ at several Reynolds numbers.	195
7.25	Two-point correlation variation of $\langle u, u \rangle$ in the streamwise direction.	197
7.26	Two-point correlation variation of $\langle v, v \rangle$ in the streamwise direction.	198
7.27	Two-point correlation variation of $\langle u, u \rangle$ in the spanwise direction.	198
7.28	Low-speed streaks at several Reynolds numbers for $f = 0.2$ case. . . .	200
7.29	Low-speed streaks at several Reynolds numbers for $f = 0.5$ case. . . .	201
7.30	λ_2 iso-surfaces at several Reynolds numbers for $f = 0.2$ case.	202
7.31	λ_2 iso-surfaces at several Reynolds numbers for $f = 0.5$ case.	203
7.32	New turbulence generation for the three acceleration rates during the acceleration.	204
7.33	Conditionally averaged ω'_x profile in non-active area at different stages of the acceleration.	205
8.1	Re_τ comparison for the domain size test for temporal deceleration. . .	211

8.2	The rms velocity fluctuations profiles for the domain size test for temporal deceleration.	212
8.3	Re_τ time history during deceleration.	214
8.4	C_f and the mean pressure gradient variations during deceleration. . .	214
8.5	Boundary layer parameters variations during deceleration.	215
8.6	Mean velocity profiles during deceleration at several Reynolds numbers.	216
8.7	dU/dy profiles during deceleration at several Reynolds numbers. . . .	217
8.8	The log-law variations during deceleration.	217
8.9	Mean velocity variations in the near-wall region during the final stages of deceleration.	218
8.10	The rms velocity fluctuations profiles during the deceleration.	220
8.11	Time histories of rms velocity fluctuations at several y locations during the deceleration.	221
8.12	Variations of the turbulent shear stress and structure parameter during the deceleration.	222
8.13	Time histories of maximum u_{rms} and v_{rms} during the deceleration. . .	224
8.14	Turbulence relaxation in the core region during the deceleration. . . .	225
8.15	RMS vorticity profiles during the deceleration.	227
8.16	Time histories of maximum rms vorticity during the deceleration. . .	228
8.17	Variations of y locations of $\omega'_{x,min}$, $\omega'_{x,max}$ and $\omega'_{y,max}$ during the deceleration.	228
8.18	Flow visualisation using λ_2 plots during the deceleration.	229
8.19	Time histories of maximum values of various budget terms during the deceleration.	230
8.20	y profiles of turbulent kinetic energy budget terms during the deceleration.	233
8.21	Variations of different invariants of anisotropy tensor during the deceleration.	235
8.22	Anisotropy invariant maps at several Reynolds numbers during the deceleration.	236

List of Tables

3.1	Simulation parameters for fully-developed turbulent channel DNS. . .	44
3.2	Comparison of Re_τ values with data available in literature.	44
3.3	Simulation parameters for active flow control simulation.	46
3.4	Simulation parameters for fully-developed turbulent channel LES. . .	57
3.5	Re_τ variations for different values of WALE constant (C_w).	60
4.1	Simulation parameters used in DNS for temporal acceleration.	65
4.2	Grid resolutions used for temporal acceleration DNS.	65
4.3	Simulation parameters used in LES for temporal acceleration.	66
4.4	Grid resolutions used for temporal acceleration LES.	66
4.5	Simulation parameters for steady turbulent DNS/LES.	67
4.6	A literature review of computational domain sizes used for turbulent channel flow simulations.	68
4.7	Details of simulations performed for the domain size test for temporal acceleration.	69
4.8	Details of simulations for time step size parametric study.	76
5.1	Simulation parameters used in DNS based on $Re_\tau = 800$	87
5.2	Initial mean flow variables of the simulation.	88
5.3	Response times for maximum values of rms velocity fluctuations during the acceleration.	105
5.4	Response times for maximum values of Reynolds stresses during the acceleration.	109
5.5	Quadratic contributions at several y locations for a fully-developed turbulent channel.	121

6.1	Ratio of cut-off λ'_2 to the $\lambda'_{2, plane}$	146
7.1	Simulation parameters for LES of temporal acceleration.	168
7.2	Comparison of various flow properties for the three acceleration rates.	172
7.3	Variations of Reynolds number and time ranges for different stages of temporal acceleration for the three acceleration rates.	172
7.4	Response times for maximum values of Reynolds stresses for the three acceleration rates.	183
8.1	Simulation parameters for LES of temporal deceleration.	209
8.2	Grid resolutions for LES of temporal deceleration	210
8.3	Details of simulations performed for the domain size test for temporal deceleration.	211
8.4	Response times for maximum values of Reynolds stresses during the deceleration.	223
8.5	Response times for maximum values of \overline{uu} budget terms during the deceleration.	231
8.6	Response times for maximum values of \overline{vv} budget terms during the deceleration.	231
8.7	Response times for maximum values of \overline{vv} budget terms during the deceleration.	231

Nomenclature

δ^*	displacement thickness
γ	acceleration parameter used in experiments
λ'_2	λ_2 rms fluctuations
$\lambda'_{2,max}$	λ_2 maximum rms fluctuations.
λ_2	Second eigenvalue of $S^2 + \Omega^2$
μ	dynamic viscosity
ν	kinematic viscosity
Re_τ	Reynolds number based on friction velocity, $u_\tau h/\nu$
ρ	fluid density
τ_{sgs}	subgrid-scale stress
τ_w	wall shear stress
θ	momentum thickness
u'_{max}	maximum value of u_{rms}
$u_{rms}, v_{rms}, w_{rms}$	streamwise, wall-normal and spanwise rms velocity fluctuations
u'^+, v'^+, w'^+	streamwise, wall-normal and spanwise rms velocity normalised by u_τ
u_τ	friction velocity, $\sqrt{\tau_w/\rho}$
u_{τ_0}	initial wall friction velocity
\overline{uu}	streamwise normal Reynolds stress
$-\overline{uv}$	Reynolds shear stress
v'_{max}	maximum value of v_{rms}
\overline{vv}	wall-normal Reynolds stress
w'_{max}	maximum value of w_{rms}

\overline{ww}	spanwise Reynolds stress
$\omega'_x, \omega'_y, \omega'_z$	streamwise, wall-normal and spanwise rms vorticity
$\omega'_{x,max}$	maximum value of ω'_x
$\omega'_{x,min}$	local minimum value of ω'_x
$\omega'^+_x, \omega'^+_y, \omega'^+_z$	streamwise, wall-normal and spanwise rms vorticity normalised by u_τ^2/ν
$\omega'_{x,wall}$	wall value of ω'_x
$\omega'_{y,max}$	maximum value of ω'_y
$\omega'_{z,wall}$	wall value of ω'_z
ξ	non-dimensional time used in transient simulations, tU_{m0}/h
x^+, y^+, z^+	x, y and z coordinates normalised by ν/u_τ
y_0^+	wall-normal coordinate normalised by ν/u_{τ_0}
a_1	turbulent structures parameter, $-\overline{uv}/2k$
b_{ij}	Reynolds stress anisotropy tensor, $\overline{u'_i u'_j}/2k - \delta_{ij}/3$
C_f	coefficient of friction
C_s	Smagorinsky constant
C_w	WALE constant
F	invariant function, $1 + 9II + 27III$
f	acceleration parameter used in present study
G	invariant function, $-(III/2)^2/(II/3)^3$
H	shape factor, $= \frac{\delta^*}{\theta}$
h	half-channel height
II	second invariants of b_{ij} , $-b_{ij}b_{ji}/2$
III	third invariants of b_{ij} , $b_{ij}b_{jk}b_{ki}/3$
k	turbulent kinetic energy, $(u'^2 + v'^2 + w'^2)/2$
L_x, L_y, L_z	domain size in x, y and z directions
L^+_x, L^+_y, L^+_z	domain size in x, y and z directions normalised by ν/u_τ
N_x, N_y, N_z	number of points in x, y and z directions

p	pressure
P_x	mean pressure gradient
Re	Reynolds number
Re_0	initial Reynolds number
Re_f	final Reynolds number
Re_m	Reynolds number based on mean velocity and channel height, $2U_m h/\nu$
Re_s	Reynolds number for fully-developed turbulent flow
t	time
T_e	total acceleration/deceleration time
U	mean streamwise velocity
u, v, w	streamwise, wall-normal and spanwise instantaneous velocities
U^+	streamwise mean velocity normalised by u_τ
U_m	bulk-mean velocity
U_{m0}	initial bulk mean velocity
x, y, z	streamwise, wall-normal and spanwise coordinates

1

Introduction

Unsteady turbulent flows are encountered in many engineering applications as well as in natural systems such as nuclear and conventional power plants, blood flow in large arteries, combustion engines, civil engineering, etc. For instance, the accurate predication of the wall shear stress in the case of transient turbulent pipe flows is a very critical parameter in the design of pipeline systems. There are many engineering applications involving rapid changes in flow where understanding of the flowfield and correct prediction of unsteady wall shear stress are very important. Another example is the flow through the main trachea where temporal acceleration and deceleration occur during the breathing cycle. Determination of flow physics

is crucial in understanding the development and propagation of turbulence in such flows. Accurate prediction/modelling of flows undergoing transience requires a thorough understanding of flow physics for the particular case. As it is shown later in the literature review section of the thesis (Chapter 2), although many experimental investigations and numerical modelling effort have been made in order to understand underlying physics of turbulence in transient temporal flows, the information does not provide complete insight into the flow physics due to lack of experimental data in the very near-wall region and due to scarcity of discussion about the response of near-wall turbulent structures.

The motivation of this study arises from the need for detailed investigation of transient turbulent flows by using direct numerical simulations (DNS) and large eddy simulations (LES) in order to enhance understanding of flow physics in the very near-wall region and as well as to study the response of near-wall coherent structures during temporal acceleration and deceleration.

1.1 Project overview

Understanding the transient turbulent flows subjected to unsteady acceleration and deceleration is of primary importance in many engineering applications. From the literature review presented in Chapter 2, it is clear that transient turbulent flows can be categorised in the following types:

The first is periodic transient flows: These flows have two types namely oscillating flow (having zero temporal mean) and pulsating flow (non-zero temporal mean). The flow through a combustion engine, for instance, can be characterised as a pulsating flow. The second type is non-periodic transient flows: These kind of flows involve flows undergoing temporal changes as a result of the mass flow rate or the mean pressure gradient. The temporal acceleration and deceleration can be due

1.1. PROJECT OVERVIEW

to either a step change or constant change. Examples of flows with constant transience include blood flows through main arteries while a step change in pressure gradient is encountered in a flow situation involving sudden opening and closing of a hydraulic valve. Boundary layer flows subjected to favourable pressure gradient (FPG) and adverse pressure gradient (APG) are non-equilibrium flows undergoing spatial acceleration/deceleration. Previous studies have attempted to make comparisons between the boundary layer flows subjected to FPG/APG with the temporal transient flows and several similarities between temporal and spatial non-equilibrium flows have been found.

The present study focuses on the numerical investigation of transient turbulent flow of non-periodic temporal acceleration and deceleration which has received, so far, relatively little attention as compared to the periodic flows. DNS and LES methods are employed for the numerical investigation for flows subjected to temporal acceleration and deceleration, especially in the very near-wall region.

Aims and objectives

The aim of the present study is to investigate transient flows with temporal acceleration and deceleration in order to enhance the understanding of turbulence dynamics, flow physics and the wall shear stress response for these particular cases. Turbulent channel flow is considered for the present numerical investigation. Unsteady turbulent flow subjected to constant acceleration and deceleration has been investigated by using DNS/LES calculations. The present study involves the study of turbulence response subjected to constant acceleration and deceleration applied suddenly to a fully-developed turbulent channel flow. The main focus of the study is the transient response of turbulence and near-wall turbulent structures due to the imposed acceleration and deceleration. The effect of different acceleration and deceleration rates has been studied in comparison with the corresponding steady state

counterparts. Detailed turbulence statistics has been generated which provides a clear understanding of the turbulence dynamics of such flows, and can be used as a benchmark for the development of turbulence modelling. The following work has been done in this study in order to complete the above mentioned

1. Implementation and validation of fully implicit fractional step method (FSM).
2. Detailed investigation of flow physics and turbulence response of unsteady turbulent flow subjected to constant acceleration.
3. Characterisation of response of near-wall turbulence structures during constant acceleration.
4. Investigation of different acceleration rates on turbulence response and propagation during constant acceleration.
5. Investigation of flow physics and turbulence response during constant deceleration.

1.2 Thesis road map

Chapter 1 : Introduction

A brief description of the objectives of the present study with the thesis outline is presented.

Chapter 2: Literature review

This chapter presents a comprehensive literature review of experimental and numerical studies of transient turbulent flows and discusses the major findings related to

this study. A detailed literature review of non-periodic transient turbulent flows subjected to constant/sudden acceleration and deceleration has been presented. This is followed by a brief overview of research efforts made for turbulent boundary layers subjected to FPG and APG. Finally, a literature review regarding periodic transient turbulent flow studies is presented.

Chapter 3: Numerical methods

An overview of different numerical schemes developed for the solution of three-dimensional incompressible Navier-Stokes equations has been presented with emphasis on fractional step method (FSM). The advantages and disadvantages of two different types of FSM are discussed with brief numerical implementation. It is followed by a description of different steps in the unsteady solution method with spatial discretisation used. The validation is presented afterwards with a decaying vortex test case. Turbulent statistics for fully-developed turbulent channel flow at several Reynolds numbers are compared with the available DNS data found in literature. Then, a brief overview of research conducted in the field of LES modelling is presented with the main focus on subgrid-scale (SGS) models. Mathematical foundations and governing equations of LES are presented, which is followed by the detailed mathematical description and numerical implementation of the dynamic SGS model and the wall-adapting local eddy viscosity (WALE) SGS model. Finally, the validation of LES models, implemented in the present study, is ascertained by the comparison of turbulent statistics from LES of fully-developed turbulent channel flow with the DNS results.

Chapter 4: Preliminary simulations

This chapter provides a detail description of simulation parameters for the DNS/LES of temporal acceleration. A domain size test is presented in order to determine the suitable computational domain length for the present study. A time step size test is also presented in order to ascertain the time accuracy of the present simulations. Finally, a brief description of turbulent statistics later to be used for the analysis of transient turbulent flows has been presented. These statistics include turbulent kinetic energy budgets, anisotropy invariant map (AIM) analysis and vortex identification method.

Chapter 5: DNS of temporal acceleration

This chapter presents the results of DNS of constant temporal acceleration. Response of the wall shear stress, mean velocity and turbulent Reynolds stresses is discussed in detail, and the response times for each property are evaluated. Response of rms velocity and vorticity fluctuations is discussed, and the time histories of wall-normal locations of the maximum rms vorticity is also shown. Flow physics for such a flow is investigated in terms of the kinetic energy budget analysis. Finally, probability density function (pdf) analysis is presented to investigate the Reynolds stress producing events.

Chapter 6: Effect of acceleration on turbulent structures

This chapter discusses the effect of temporal acceleration on the near-wall turbulent structures during different phases of acceleration. Response of turbulent structures has been studied using low-speed streaks and the λ_2 vortex identification method (which is discussed in Chapter 4). Two different types of flow structures have been

found in the present study. Old turbulent structures are associated with the initial flow field, while new turbulent structures are generated during acceleration. A novel procedure to identify regions of new turbulence has been developed, and the conditionally-averaged statistics from both distinct regions have been presented afterwards. Finally, anisotropy invariant analysis and turbulent kinetic energy spectra have been presented to investigate the modification to the turbulence structures with temporal acceleration.

Chapter 7: Effect of different acceleration rates

The effect of different acceleration rates on turbulence development and propagation is studied using LES. Moreover, the final Reynolds number is increased from $Re = 15000$ used in DNS to $Re = 22600$ because only early response of turbulence during temporal acceleration is studied in Chapter 5. Three different acceleration rates are employed in the present LES study. First of all, validation of LES is presented by comparing the flow statistics with the DNS results in Chapter 5. The effect of different acceleration rates on the wall shear stress, mean velocity and rms fluctuations is discussed in detail. LES results clearly show the presence of pseudo-steady state after $Re = 15000$. The turbulence propagation in the core region has been investigated for three acceleration cases. The response of the near-wall structures is studied using the two-point correlations in the streamwise and spanwise directions. New turbulence identification procedure developed in DNS (Chapter 6) has been used to study the effect of acceleration rates on turbulence generation.

Chapter 8: LES of linear temporal deceleration

This chapter presents the results of LES of constant temporal deceleration. Two deceleration rates are employed to investigate the effect of different deceleration

rates on turbulence response. First of all, a domain size test is presented in order to determine the suitable computational domain length. The response of the wall shear stress and mean velocity is discussed in detail for different deceleration rates. The rms velocity and vorticity fluctuations response is studied in detail. Turbulent kinetic energy budgets are analysed to examine flow physics. The turbulent structure variations are studied using anisotropy invariants maps (AIM).

Chapter 9: Conclusions

This chapter presents a brief summary of major conclusions drawn from all the results presented in the previous chapters.

2

Literature Review

Transient turbulent flows have been an area of interest for the last few decades due to their frequent occurrence in various engineering applications. Extensive research has been carried out in different types of transient flows. Owing to its complex turbulent nature, however, the underlying physics is not completely understood. Flow transience can be of several types which include constant acceleration/deceleration, impulsive (step change) acceleration/deceleration, pressure-driven and shear-driven transient flows, laminar to turbulent transition. The temporal transient flows can be divided into periodic (oscillating and pulsating) flows and non-periodic (accelerating/decelerating) flows.

This chapter is organised as follows: First of all, a literature review of non-periodic transient flows is presented, focusing on accelerating/decelerating flows, which is the main area of interest in the present study. Afterwards, spatially evolving flows have been discussed. Although, these flows are not transient flows, however they share certain similarities with the accelerating/decelerating flows. Examples of spatially evolving flows are boundary layer flows subjected to a favourable pressure gradient (FPG) and an adverse pressure gradient (APG). Finally, the relevant studies in the field of periodic transient flows are discussed.

2.1 Non-periodic transient flows

Non-periodic transient flows are encountered frequently in real life situations, for instance, flow thorough turbo machines, swept-wings, blood flow through main arteries, flows involving rapid changes in mass flow or pressure gradient due to the opening/closing of a valve and flow over hulls of marine vehicles are a few to mention. A brief overview of the relevant studies performed for these flows is presented in two sections: Accelerating/decelerating flows and three-dimensional strained flows.

2.1.1 Accelerating/decelerating flows

These types of flows have received comparatively less attention as compared to the other types of transient flows. In these flow situations acceleration/deceleration is caused by either step change or constant change in pressure gradient or mass flow rate. Flow through the main trachea is an example of where constant acceleration/deceleration occurs during the breathing cycle, while a sudden opening/closing of a hydraulic valve causes a step acceleration/deceleration.

Step acceleration/deceleration flows has been investigated experimentally by several

2.1. NON-PERIODIC TRANSIENT FLOWS

authors in the past. The main emphasis of research in these studies was the effect of temporal acceleration/deceleration on the laminar to turbulent transition in case of acceleration and subsequent turbulence development. Start-up response to a step change in flow rate for a laminar to turbulent transient pipe flow was studied by Kataoka et al. (1975), where the step increase in flow rate is achieved by sudden opening of a solenoid valve. It was found that the time taken to achieve laminar to turbulence transition decreases with increase in Reynolds number. Maruyama et al. (1976) studied the behaviour of transient pipe flow subjected to step increase and step decrease in flow rate by using electrochemical technique. They observed that the turbulence response starts near the wall for the step increase experiments and it subsequently moves outwards as the newly generated turbulence is propagated in the core region. Step decrease experiments exhibited the decay of turbulence first in the near-wall region and showed a similar behaviour of lack of response of core region turbulence as found for step increase experiments. It was shown that the near-wall turbulence change propagates approximately in the similar fashion for both types of transient flows.

Kurokawa and Morikawa (1986) performed a theoretical as well as an experimental study, for a transient pipe flow with gradually increasing and decreasing flow rates. Various flow rates were used during the study. They reported different patterns of velocity profiles development during the laminar to turbulent transition for slow and fast acceleration cases, and the critical Reynolds number for flow transition was found to increase with the increase in the imposed acceleration. Wall shear stress was found to be smaller than the steady corresponding value after the turbulent transition for the accelerated flow case while it was found to be higher in decelerated case. Experimental investigation of laminar to turbulent transition for linearly accelerated pipe flow was performed by Lefebvre and White (1989) and Lefebvre and White (1991). They found that the critical Reynolds number for transition increased with the increase in acceleration rate.

Greenblatt and Moss (2003) studied the rapid transition to turbulence for a pipe flow initially at rest. The flow was subjected to rapid acceleration followed by sharp deceleration towards the final Reynolds number. The transition was reported in the deceleration phase and the time taken to achieve transition was significantly reduced in comparison to the time, taken by a monotonically accelerated pipe flow. The transition time required for laminar to turbulent transition was found to decrease with the increase in acceleration rate, in the more recent experimental investigations for a start-up response of a laminar pipe flow subject to constant acceleration (Nakahata et al., 2007; Annus and Koppel, 2011).

Fully-developed turbulent flow subjected to constant acceleration/deceleration has been investigated experimentally by several authors in the past. Greenblatt and Moss (1999) performed an experimental and numerical investigation of turbulent pipe flow subjected to rapid temporal acceleration. The main objective of the study was to investigate the complex behaviour of flow relaminarisation process. It was found that the relaminarisation resulted in a significant reduction of turbulent Reynolds stresses in the near-wall region ($y^+ \leq 50$). On the other hand, the core region remained in a “frozen” state and was largely unaffected by the imposed acceleration.

He and Jackson (2000) conducted a comprehensive experimental study of turbulent pipe flow subjected to constant temporal acceleration and a few results from constant deceleration were also presented. They employed two-component Laser Doppler Anemometer (LDA) measurement system in their study. A new dimensionless parameter for temporal acceleration/deceleration was defined as following

$$\gamma = \frac{D}{U_{\tau 0}} \left(\frac{1}{U_{b0}} \frac{dU_b}{dt} \right), \quad (2.1)$$

where D is the diameter of the cylinder, U_{b0} is the bulk-mean velocity at the initial Reynolds number, $U_{\tau 0}$ is the friction velocity at initial Reynolds number and $\frac{dU_b}{dt}$ is

2.1. NON-PERIODIC TRANSIENT FLOWS

the rate of bulk-mean velocity change. The Reynolds number based on initial bulk-mean velocity was increased from $Re = 7000$ to 45200 in most of the experiments while some experiments used higher initial Reynolds numbers to investigate the initial Reynolds number effect. The same Reynolds number range was used for the constant deceleration experiments

Mean velocity profiles during the initial stages of the acceleration showed significant deviations from the steady corresponding mean velocity profiles, before reaching the pseudo-steady equilibrium stage. Near-wall Reynolds stress terms exhibited a certain delay in responding to the imposed acceleration with streamwise component increasing first. The delay in response increased with increase in the distance from the wall. Three distinct delays were reported namely: delay in turbulent production, delay in radial diffusion and delay in energy redistribution among the three components. The deviation of turbulence intensities from the pseudo-steady corresponding values was found to reduce with decrease in acceleration rate. On the other hand, the time taken by the newly generated near-wall turbulence to propagate at the center line of the pipe, was found to be independent of the acceleration rate. The delay in turbulence response was found to decrease with increase in the initial Reynolds number.

Post transient analysis for the fastest acceleration case showed a considerable increase in turbulent intensities because the flow was not adjusted to the imposed acceleration completely at the final stage of the acceleration. Inertia was found to be dominant in the initial stages of the acceleration. Turbulent intensities in the pipe flow experiments, subjected to constant deceleration, was found to be greater than the steady corresponding values.

Greenblatt and Moss (2004) conducted experiments for a turbulent pipe subjected to rapid temporal acceleration at relatively higher initial Reynolds number and higher acceleration rates, as compared to those used by He and Jackson (2000). The ini-

tial and final Reynolds numbers for their study were $Re = 31000$ and $Re = 82000$ respectively and LDV technique was used for flow field measurements at 25 radial locations. Three acceleration rates were considered to produce flow acceleration of three types which include the acceleration involving maintenance of equilibrium, breakdown of equilibrium and flow relaminarisation. One of the most significant findings of their work, for the slowest acceleration case, was the simultaneous turbulence generation in two distinct regions namely: the near-wall region and the outer-layer region at $y_0^+ \approx 300$, where ‘0’ denotes the wall normalisation by using initial u_τ value. Moreover, there was a distinct kink in the mean velocity profile at $y_0^+ \approx 600$ which was referred to as *inflection* region. This unusual behaviour of turbulence generation in the outer region is not reported in any of the the previous studies of transient turbulent flows and the authors attributed this phenomenon to the higher acceleration rates and initial higher Reynolds number used. The propagation of the outer-layer new turbulence towards the wall, as observed for the slowest acceleration case, was not found in the fastest acceleration case. Mean velocity profiles exhibited a shift towards the wall with increase in acceleration rate. The initial delay in turbulence response was also reported and the propagation of turbulence was found to be largely independent of the acceleration rate.

He et al. (2008) employed unsteady turbulence modelling to investigate the turbulent pipe flow subjected to constant acceleration. The simulation parameters in this study were selected to replicate the experimental conditions used by He and Jackson (2000). The main objective of this study was to study the near-wall turbulence behaviour during the constant acceleration which is difficult to study through experiments. It was found that the wall shear stress overshoots in the initial stages of the acceleration due to inertial effects, followed by a subsequent reduction of wall shear stress below its steady value. Wall shear stress achieved the pseudo-steady corresponding value after exhibiting a rapid increase during the later stages of the acceleration. Similar wall shear stress response for constant acceleration is also

2.1. NON-PERIODIC TRANSIENT FLOWS

reported in the LES study of Jung and Chung (2009).

Recently, Mehdi et al. (2011) performed a DNS study of a fully-developed turbulent channel subjected to step acceleration/deceleration. It was found that the turbulence intensities are more sensitive to step acceleration as compared to the step deceleration of similar magnitude. The wall shear stress response for step acceleration was found to be similar with the constant acceleration, with wall shear stress exhibiting earlier response in terms of time. Turbulent intensities exhibited a two-phase response in the decelerated case with an initial negligible reduction followed by a faster reduction, however the intensities remain higher than the steady corresponding values throughout the deceleration.

Coleman et al. (2003) performed a DNS of decelerating turbulent channel flow by applying a mean streamwise negative strain. Slip boundary conditions were used on channel walls to reproduce the effects of the inner and outer layers of turbulent boundary layer subjected to APG. Flow separation at the wall was reported towards the end of the deceleration. A reduction in turbulent intensities near the wall, accompanied by a corresponding increase in turbulent intensities in the outer-layer was found.

Chung (2005) performed a DNS of a fully-developed turbulent channel flow subjected to step deceleration through sudden decrease in the mean pressure gradient. Reynolds number ranges employed for flow deceleration were relatively low. The Reynolds number based on wall friction velocity u_τ and half channel height, Re_τ , was decreased from $Re_\tau = 180$ to $Re_\tau = 150$ in one experiment and to $Re_\tau = 120$ in the other experiment. Two different turbulence relaxations were found: a fast relaxation in the beginning of the deceleration, followed by a secondary relatively slow relaxation phase towards the steady state. The near-wall turbulence exhibited an anisotropic response during the deceleration with the streamwise intensity first to relax.

Recently, Ariyaratne et al. (2010) studied the wall shear stress and turbulence response for turbulent pipe flow subjected to constant deceleration. The unsteady turbulence modelling approach of He et al. (2008) was employed in this study. The experimental conditions of He and Jackson (2000) were replicated in this study. The initial and final Reynolds numbers were chosen as $Re = 45200$ and $Re = 7000$ respectively, based on the initial bulk-mean velocity and the pipe diameter. Four distinct regions of wall shear stress response were reported in this study namely: a sudden reduction of wall shear stress below steady value due to inertial effect at the beginning of the deceleration, followed by an increase of wall shear stress above the steady value due to delay in turbulence response. This is followed by an increased response of the wall shear stress in the third phase and finally the fourth phase is characterised by a large reduction of wall shear stress below the steady corresponding value. Flow separation towards the final stages of the deceleration was reported for cases with relatively higher deceleration rates. Turbulence intensities in the near-wall region exhibited certain delay in response to the deceleration while the core region remained approximately in a frozen state.

In hydraulic systems involving flow acceleration/deceleration, the response of the wall shear stress is a critical parameter for pipe design purpose due to its occurrence in situations involving sudden opening or closing of hydraulic valve and flow passing through contraction or expansion. The wall shear stress is normally divided into two parts for one-dimensional modelling purpose as following

$$\tau_{w,u} = \tau_w - \tau_{w,s},$$

where τ_w , $\tau_{w,s}$ and $\tau_{w,u}$ are the total wall shear stress, steady and unsteady wall shear stress respectively.

Extensive efforts have been put in order to model the unsteady part of the wall shear stress ($\tau_{w,u}$). Wall shear stress modelling efforts can be segregated in terms

2.1. NON-PERIODIC TRANSIENT FLOWS

of modelling based on flow histories and/or the usage of instantaneous flow field conditions. Zielke (1968) proposed first model for unsteady wall shear stress calculation based on the weighted sum of quasi steady value and a flow dependent term, and this flow dependent term is calculated from the previous velocity history. This model has been extensively used in the past due to its solid theoretical foundations. Following the idea of Zielke (1968), Vardy and Brown (2003) and Vardy and Brown (2007) developed the 2D weighing function models for unsteady pipe friction based on instantaneous and past velocity profiles. One important assumption in construction of these models is ‘frozen eddy viscosity’ assumption which can lead to incorrect prediction of the unsteady pipe friction due to lack of consideration of turbulence dynamics during the flow transient (He et al., 2008). Vardy and Brown (2010a) analytically investigated the influence of the the transient behaviour of kinematic viscosity on the unsteady wall shear stress in a pipe. The unsteady component of the total wall shear stress was found to be strongly influenced by the mean acceleration. The same authors have recently proposed an improvement to the Zielke’s theoretical model (Vardy and Brown, 2010b).

2.1.2 Three-dimensional strained transient flows

These types of flows are encountered in situations where the flow is being strained from its original two-dimensional characteristics to become three-dimensional, either by the change of pressure gradient or by the application of mean shear via boundary conditions. Turbulence characteristics of three-dimensional strained boundary layer have been studied extensively by many researchers in the past. The important characteristics of these types of flow include a reduction of drag and shear stress of the resultant flow field (Moin et al., 1990; Coleman et al., 1996), a reduction in the ratio of shear stress to turbulent kinetic energy (Schwarz and Bradshaw, 1994) and a significant lag of turbulent shear stresses behind mean shear (Bradshaw and Pontikos,

1985). Le et al. (2000) investigated the behaviour of near-wall turbulent structures in three-dimensional strained transient flows. The mean three-dimensionality resulted in the breakup of the symmetry and alignment of the near-wall structures. This symmetry breakup results in a reduction of turbulent kinetic energy. Coleman et al. (2000) presented the results from several cases of flow configurations subjected to mean three-dimensionality (pressure driven and shear-driven and with as well as without adverse pressure gradient). The velocity-pressure gradient correlation term Π_{ij} was found responsible for the energy redistribution and propagation in the core region. Since the near-wall turbulence attenuates with the application of mean shear in spanwise direction, extensive efforts have been made lately in investigation and optimization of turbulent drag reduction by spanwise oscillations (Jung et al., 1992; Quadrio and Ricco, 2004) and streamwise travelling waves in spanwise direction (Quadrio et al., 2009).

2.2 Spatially evolving transient flows

Although spatially-evolving boundary layers flows are steady flows, however as mentioned earlier, boundary layers subjected to FPG and APG share several similarities with the transient turbulent flows. Spatially-evolving boundary layers have been investigated for more than five decades due to their rich occurrence in several engineering applications. Flow past through an object having convex curvature is equivalent to having a boundary layer subjected to FPG while objects having concave curvature resembles to that of a boundary layer subjected to APG.

One of the most striking characteristics of boundary layers subjected FPG is the reversion of turbulence to relaminarisation which was first reported by Launder (1964). Flow relaminarisation has been studied extensively in the past. The boundary layer flow tends to revert back to laminar flow in case if the acceleration parameter (K)

2.2. SPATIALLY EVOLVING TRANSIENT FLOWS

is higher than critical value. This critical value is found to be in the range of $2.8 \times 10^{-6} \leq K \leq 3.4 \times 10^{-6}$. The acceleration parameter K is given as

$$K = \frac{\nu}{U(x)^2} \frac{dU(x)}{dx},$$

where $U(x)$ is the streamwise velocity and ν is the kinematic viscosity. Kline et al. (1967) found out that turbulent bursting events reduces in FPG boundary layers while Narayanan and Ramjee (1969) observed the decrease in turbulent intensities at the time of relaminarisation. Sreenivasan (1982) proposed a two-layer model to explain the relaminarisation and argued that the relaminarisation is the result of the “domination of pressure forces over the slowly responding Reynolds stresses in the outer-layer, accompanied by the generation of a new laminar sub-boundary layer, which itself is maintained stable by the acceleration”. It was also proposed that high acceleration results in the decay of the inner-layer turbulence while the outer-layer turbulent stresses remain largely unchanged.

Recent advancement in computer power and sophisticated experimental apparatus has made it possible to perform in depth numerical and experimental studies in the past two decades. Piomelli et al. (2000) numerically investigated the turbulent boundary layer flow subjected to FPG using LES. They found that the low-speed streaks became elongated, accompanied with a reduction in number of quasi-streamwise vortices. The mean spanwise spacing of low-speed streaks was also found to reduce due to FPG. In the relaminarisation zone for strong acceleration case, the streaks were reported to be even longer with a tendency of alignment in the streamwise direction. The contributions from second quadrant, *i.e.*, ejections was reduced and the structure parameter (a_1) was also decreased implying a reduction in turbulence intensity in the near-wall region.

Some of the recent studies for boundary layers subjected to FPG includes Ichimiya et al. (1998), Fernholz and Warnack (1998), Warnack and Fernholz (1998), and

Mukund et al. (2006). Boundary layers subjected to FPG exhibit distinct characteristics (Bourassa and Thomas, 2009) which includes: a) thinning of boundary layer, b) departure of mean velocity profile from the log-law and law of wake, c) an initial decrease followed by a sharp increase in shape factor, d) an initial increase in the wall shear stress followed by a significant decrease, e) a reduction in relative turbulent intensity, f) a rapid decline of bursting events in the near-wall region, g) spreading of turbulent intermittency from the outer-layer to the inner-layer and h) the decay of turbulent Reynolds stress.

Turbulent boundary layers (TBL) subjected to adverse pressure gradient (APG) are found in many engineering applications of interest which include a flow through a diffuser, flow past the trailing edge of an aerofoil, flow past an object having concave curvature like ramp. Earlier studies for the TBL subjected to APG reported a tendency of flow separation near the wall, an enhancement in turbulent shear stress and kinetic energy, and non universality of the log-law during deceleration. Krogstad and Skare (1995) found in their experimental study of TBL subjected to APG that the near-wall anisotropy reduces during the transient and APG results in a reversal of direction of turbulent transport due to development of secondary peak in turbulent kinetic energy approximately at half way through boundary layer. Alving and Fernholz (1996) investigated the TBL subjected to APG having mild separation with downstream reattachment. The location of maximum Reynolds stresses was found to shift away from the wall significantly and the recovery process in the near-wall region after the mild separation exhibited a considerable delay. The authors attributed this phenomenon to the survival of outer-layer vortices during separation.

Computational studies regarding the characteristics of separation bubble are conducted by Na and Moin (1998), Manhart and Friedrich (2002), and Skote and Henningson (2002). Extensive efforts have been made to determine the appropriate

2.3. PERIODIC TRANSIENT FLOWS

scaling for the mean velocity and turbulent Reynolds stresses for TBL subjected to APG. A very comprehensive literature review for the scaling efforts is given in Aubertine and Eaton (2005). Lee and Sung (2009) investigated the coherent structures response for TBL subjected to APG. It was found that the strength of the low-speed streaks decreased and the spacing between two adjacent streaks increased four times of the normal spacing. Dominance of low momentum regions in the buffer layer and the inner log-layer was found, moreover the enhancement of turbulent kinetic energy in the outer-layer was attributed to the presence of large-scale outer-layer hair-pin vortices.

2.3 Periodic transient flows

Pulsating flow is found in many practical applications, for example, the flow driven by piston inside internal combustion engines. Mizushima et al. (1973) performed experiments for pulsating flow in a tube. It was found from the instantaneous velocity profiles and turbulent intensities that turbulence characteristics strongly depend upon the pulsating period. Turbulence generation and propagation in the core region was studied by Mizushima et al. (1975). The turbulence propagation time, scaled using wall parameters, was found to be independent of the pulsating frequency. Tu and Ramaprian (1983) and Ramaprian and Tu (1983) carried out a detailed experimental investigation of fully-developed turbulent pipe. It was found in these studies that the mean flow field and turbulence are largely dependent on the pulsating frequency and mean flow-rate, while the effects of amplitude of oscillation are relatively small.

Several non-dimensional similarity parameters have been proposed to characterise the pulsating pipe flows *i.e.*, Ramaprian and Tu (1983) used $\omega D/u_\tau$ to classify five distinct regimes of turbulent pipe flow, where ω is pulsating frequency in radians, D

is the pipe diameter, and u_τ is the wall friction velocity. Mao and Hanratty (1986) used $\omega^+ = \omega\nu/u_\tau^2$ in their experimental study of the wall shear stress in pulsating pipe while Tardu et al. (1994) used Stokes-Reynolds number, $l_s^+ = l_s u_\tau / \nu$, where $l_s = \sqrt{2\nu/\omega}$, in their experiments of turbulent channel flow. Tardu et al. (1994) found that the time averaged velocity and wall shear stress is largely independent of the imposed pulsating frequency for same pulsation amplitudes.

Scotti and Piomelli (2001) performed the first DNS and LES study of the pulsating channel flow driven by oscillating mean pressure gradient and reported detailed turbulence statistics and typology of the near-wall coherent structures. Manna and Vacca (2008) performed Reynolds stress tensor analysis and velocity spectrum analysis in their LES study to investigate the response of the near-wall coherent structures to the periodic pulsation. The reduction in turbulence structure parameter was reported in the near-wall region due to the imposed unsteadiness. The energy transfer from larger to smaller scales remained unaffected for the smaller oscillation amplitudes while larger amplitude oscillations significantly reduced energy transfer from large scale to smaller scales. The two-point correlation factor in the streamwise direction exhibited an increase, indicating an increased coherence of the near-wall vortical structures.

More recently, He and Jackson (2009) performed an experimental investigation of the pulsatile turbulent pipe flow. They reported the measurements for streamwise and wall normal velocity components using two-component Laser Doppler Anemometer (LDA) system. Flow in the core region exhibited frozen slug like behaviour for high pulsating frequencies. The response of turbulence to the imposed pulsation started from the wall which then propagated into the core region. Considerable efforts have been made in the development of near-wall models for pulsating turbulent flows which includes Mankbadi and Liu (1992), Scotti and Piomelli (2002) and Cotton (2007).

3

Numerical Methods.

3.1 Direct numerical simulation (DNS)

Direct numerical simulation (DNS) is the most accurate method of all turbulent treatments. In DNS every scale of flow is resolved in both time and space. DNS can be considered as a close realisation of flow field in a laboratory experiment. The Navier-Stokes equations are directly computed in DNS calculations and the smallest scales of motion in time and space are resolved. Solution methods for the three-dimensional incompressible Navier-Stokes equations have been addressed extensively in the past three decades (Chorin, 1967; Kim and Moin, 1985; Perot,

1993; Kim et al., 2002). The major problem lies in the fact that the pressure is coupled with velocity variables in the momentum equations and there is no time dependent term in the continuity equation (Kim and Moin, 1985).

$$\frac{\partial u_i}{\partial t} + \frac{\partial}{\partial x_j} u_i u_j = -\frac{\partial p}{\partial x_i} + \frac{1}{Re} \frac{\partial^2 u_i}{\partial x_j^2}, \quad (3.1)$$

$$\frac{\partial u_i}{\partial x_i} = 0. \quad (3.2)$$

Harlow and Welch (1965) proposed an operator splitting method in which the pressure is taken out of the momentum equations by taking the divergence of Equation 3.1, and the mass conservation constraint is satisfied in the sense that the pressure at the current time step is calculated such that the continuity equation is satisfied at the next time step. This method is fully explicit, which puts severe restrictions on the time step size for flows with strong velocity gradients. Chorin (1967) proposed a solution procedure by introducing an artificial compressibility in the continuity equation to introduce time dependence in it so that semi-implicit and fully implicit time advancement schemes such as alternating-direction-implicit (ADI) can be used. The artificial compressibility effect must be minimised in this method making this method highly stiff in certain cases.

Kim and Moin (1985) proposed a solution procedure for unsteady problems based on a fractional step method (FSM), in which the pressure is taken out of the momentum equations, and the momentum equations are solved for intermediate velocities. The Poisson equation for the pressure is formulated by using the incompressibility constraint, and the pressure calculated in the Poisson equation is used to update the velocity field at the end of time advancement. In Kim and Moin (1985), decoupling of the Navier-Stokes equations was performed in semi-discrete form which introduces two problems: the momentum equations require intermediate velocity boundary conditions which are not physical and the splitting error, arising from the

3.1. DIRECT NUMERICAL SIMULATION (DNS)

semi-discrete decoupling, makes it impossible to satisfy tangential and normal velocity boundary conditions simultaneously for the Poisson equation (Gresho, 1990). On the other hand, the semi-discrete decoupling has the advantage of being independent of any particular spatial discretisation scheme. There have been several studies to restore the second-order time accuracy of such semi-discrete decoupling procedure either by modifying intermediate velocity boundary conditions, or the boundary conditions for the Poisson equation or by both. These intermediate velocity boundary conditions lack physical justification, and they are generally regarded as a source of error.

To avoid the use of intermediate velocity boundary conditions, Dukowicz and Dvinsky (1992) proposed a splitting approach based on approximate factorisation which employs the splitting in matrix form after temporal and spatial discretisation. The main advantage of this scheme lies in the fact that, since the time splitting is performed after the temporal and spatial discretisation of the Navier-Stokes equations, it eliminates the need to specify the artificial intermediate boundary conditions for the momentum equations and pressure boundary conditions for the Poisson equation. Perot (1993) proposed a fully discrete form of FSM based on the Block LU decomposition and clearly showed that the problem of first-order time accuracy for its continuous counterpart arises from the method itself rather than the intermediate boundary conditions. Moreover, the issues of time accuracy and intermediate velocity boundary conditions were fully resolved and a trapezoidal pressure advancement scheme was introduced. He found that the discrete pressure solution is always first-order in time irrespective of the time splitting scheme used, and it does not affect the order of accuracy of velocity field.

When explicit or semi-implicit scheme is used, the time advancement of the unsteady compressible Navier-Stokes equations is restricted by Courant-Freidrichs-Lewy (CFL) condition to ensure numerical stability. This time step size restric-

tion makes the solution significantly more expensive in the regions with refined meshes. Fully implicit treatment of the Navier-Stokes equations requires either iterative solvers such as Newton-iterative method (Choi and Moin, 1994) due to the coupling of primitive velocity variables, or the linearisation scheme for velocity variables decoupling. A three time-level linearisation scheme was proposed by Rosenfeld (1996) which is expensive in terms of memory because the velocity field at the previous and current time steps is employed to determine the velocity at the next time step. Kim et al. (2002) extended the block LU decomposition method, and used Crank-Nicolson temporal discretisation for both convective and diffusive terms. A second-order accurate linearisation scheme (Beam and Warming, 1978) was employed to linearise the nonlinear convective term, and the momentum equations are decoupled by a second block LU decomposition.

In summary, FSM can be categorised into two: In continuous or projection type FSM, spatial discretisation is performed after the time splitting, which makes this type of method independent of spatial discretisation. However, there are two major problems with this type of methods regarding the intermediate velocity boundary conditions and the degradation of the temporal accuracy. In discrete or splitting type FSM, spatial and temporal discretisation is performed before the time splitting. Therefore, there is no need to specify intermediate velocity boundary conditions while temporal accuracy is also maintained during splitting. The DNS code based on sem-implicit formulation (written in Fortran 77) was provided. In the present study, Splitting FSM is implemented and WALE sub-grid scale model is implemented. Moreover, FFTW subroutines were implemented for the Poisson equation solution. A brief numerical detail of the projection FSM (Le and Moin, 1991) and the Splitting FSM (Kim et al., 2002) is presented in Subsections 3.1.1 and 3.1.2, respectively.

3.1.1 Projection FSM

Kim and Moin (1985) proposed a fractional step method to solve the three-dimensional incompressible unsteady Navier-Stokes equations. They employed the second-order explicit Adams-Bashforth scheme for the convective terms and the second-order implicit Crank-Nicolson for the viscous terms. Le and Moin (1991) made a modification to Kim and Moin (1985) scheme to reduce the restrictions on the time step size. They incorporated a low storage third-order Runge-Kutta scheme for time splitting. The incompressible Navier-Stokes equations in Le and Moin (1991) can be written as:

$$\begin{aligned} \frac{u_i^k - u_i^{k-1}}{\Delta t} = & \alpha_k L(u_i^{k-1}) + \beta_k L(u_i^k) - \gamma_k N(u_i^{k-1}) \\ & - \zeta_k N(u_i^{k-2}) - (\alpha_k + \beta_k) \frac{\partial P^k}{\partial x_i}, \quad i = 1, 2, 3 \end{aligned} \quad (3.3)$$

$$\frac{\partial u_i^k}{\partial x_i} = 0, \quad (3.4)$$

where $k = 1, 2, 3$ denotes the sub-step number. The coefficients $\alpha_k, \beta_k, \gamma_k$ and ζ_k are constants selected such that the total time advancements between t^n and t^{n+1} is third-order accurate for the convective terms and second-order accurate for the viscous terms.

$$\begin{aligned} \gamma_1 &= 8/15, & \gamma_2 &= 2/12, & \gamma_3 &= 3/4, \\ \zeta_1 &= 0, & \zeta_2 &= -17/60, & \zeta_3 &= -5/12, \\ \alpha_1 &= \beta_1 = 4/15, \\ \alpha_2 &= \beta_2 = 1/15, \\ \alpha_3 &= \beta_3 = 1/6. \end{aligned}$$

$L(u)$ and $N(u)$ in Equation 3.3 represent second-order finite difference operators for the viscous and convective terms, respectively. The numerical stability is restricted by the explicit treatment of the convective terms. The stability limit, CFL, de-

fined as $\max(|u_i/\Delta_i|) \Delta t$, is $\sqrt{3}$ based on the total time step (Δt). This allows a larger time step than Kim and Moin (1985). After the application of fractional step method, Equations 3.3 and 3.4 can be written as:

$$\begin{aligned}
 \frac{\hat{u}_i^k - u_i^{k-1}}{\Delta t} &= (\alpha_k + \beta_k) (u_i^{k-1}) + \beta_k L (\hat{u}_i^k - u_i^{k-1}) \\
 &\quad - \gamma_k N (u_i^{k-1}) - \zeta_k N (u_i^{k-2}) - (\alpha_k + \beta_k) \frac{\partial P^{k-1}}{\partial x_i}, \quad (3.5)
 \end{aligned}$$

$$\frac{u_i^k - \hat{u}_i^k}{\Delta t} = - \frac{\partial \phi^k}{\partial x_i}, \quad (k = 1, 2, 3). \quad (3.6)$$

It is worth noting that in this FSM, the Poisson equation (Equation 3.6) is solved for the *pseudo-pressure* (ϕ) rather than actual pressure, and the actual pressure can be calculated from Equation 3.7:

$$\frac{\partial \phi^k}{\partial x_i} = (\alpha_k + \beta_k) \left(\frac{\partial P^k}{\partial x_i} - \frac{\partial P^{k-1}}{\partial x_i} \right) - \beta_k L (u_i^k - \hat{u}_i^k). \quad (3.7)$$

The overall temporal accuracy of the fractional step method remains to be second-order when it is used in conjunction with the Runge-Kutta method. The modified momentum equations are solved after the application of a second-order accurate matrix splitting to reduce the size of a large sparse matrix into smaller matrices, which in turn, can be solved using efficient direct solvers such as TDMA or penta-diagonal matrix solver depending upon the spatial discretisation used. This scheme suffers from two drawbacks; firstly, it requires artificial intermediate boundary conditions which can potentially require second-order or fourth-order accurate spatial derivatives while solving them for unsteady boundary conditions. Secondly, the time step size is limited owing to its semi-implicit temporal discretisation.

3.1.2 Splitting FSM

The splitting FSM (Kim et al., 2002) is implemented and used in the present study and its numerical implementation is discussed briefly here. Kim et al. (2002) proposed the fully implicit version of the FSM in which both convective and viscous terms are discretised using second-order-implicit Crank-Nicolson method. This method uses a linearisation scheme to decouple the primitive variables in the momentum equations to avoid iterative solvers for the intermediate velocities solution. After temporal and spatial discretisation, Equations 3.1 and 3.2 can be written as

$$\begin{aligned} \frac{u_i^k - u_i^{k-1}}{\Delta t} = & \frac{1}{Re} (\alpha_k \mathbf{L} u_i^{k-1} + \beta_k \mathbf{L} u_i^k) - \gamma_k \mathbf{N} u_i^k \\ & - \zeta_k \mathbf{N} u_i^{k-1} - (\alpha_k + \beta_k) \mathbf{G} p^k + \mathbf{mbc}, \end{aligned} \quad (3.8)$$

$$\mathbf{D} u_i^k = 0 + \mathbf{cbc}, \quad (3.9)$$

where \mathbf{L} , \mathbf{N} , \mathbf{G} and \mathbf{D} are the discrete Laplacian viscous, convective, gradient and divergence operators respectively. It is very important to note that these operators contain information only from interior points while the boundary points information is stored in \mathbf{mbc} and \mathbf{cbc} matrices before the application of fractional step method, which eliminates the intermediate velocity boundary condition application as required in the case of projection FSM. The coefficients $\alpha_k, \beta_k, \gamma_k$ and ζ_k are all equal to 0.5 in Crank-Nicolson temporal discretisation and time advancement is single-step, which makes this method more efficient than those with three-step time advancement due to the Runge-Kutta time discretisation for the convective term. Equation 3.8 is nonlinear because of the implicit treatment of the convective terms. The nonlinear terms are linearised using a second-order accurate linearisation scheme (Beam and Warming, 1978),

$$u_i^k u_j^k = u_i^k u_j^{k-1} + u_i^{k-1} u_j^k - u_i^{k-1} u_j^{k-1} + O(\Delta t^2). \quad (3.10)$$

Writing Equations 3.8 and 3.9 after linearisation in matrix form

$$\begin{pmatrix} A & \mathbf{G} \\ \mathbf{D} & 0 \end{pmatrix} \begin{pmatrix} u_i^k \\ \delta p \end{pmatrix} = \begin{pmatrix} r \\ 0 \end{pmatrix} \begin{pmatrix} \mathbf{mbc} \\ \mathbf{cbc} \end{pmatrix}, \quad (3.11)$$

where

$$r = u_i^{k-1} + \frac{\Delta t \alpha_k}{Re} \mathbf{L} u_i^{k-1} - \Delta t \mathbf{G} p^{k-1}, \quad (3.12)$$

$$A = I - \frac{\Delta t \beta_k}{Re} \mathbf{L} + \Delta t \gamma_k \mathbf{N}, \quad (3.13)$$

$$\delta p = p^k - p^{k-1}. \quad (3.14)$$

The linearisation of the nonlinear term $\mathbf{N}u_i^k$ results in the cancellation of $\mathbf{N}u_i^{k-1}$ term and therefore there is no convective terms on the right hand side of the momentum equation. Moreover, the momentum equation is written in δp formulation to make block LU decomposition second-order accurate as explained later. By applying block LU factorisation to Equation 3.11,

$$\begin{pmatrix} A & 0 \\ \mathbf{D} & -\Delta t \mathbf{D} \mathbf{G} \end{pmatrix} \begin{pmatrix} I & \Delta t \mathbf{G} \\ 0 & I \end{pmatrix} \begin{pmatrix} u_i^k \\ \delta p \end{pmatrix} = \begin{pmatrix} r \\ 0 \end{pmatrix} \begin{pmatrix} \mathbf{mbc} \\ \mathbf{cbc} \end{pmatrix}. \quad (3.15)$$

The error term arising from the above LU decomposition is $\Delta t \mathbf{G} \delta p$ which is second-order in time because of $\delta p = p^k - p^{k-1}$. Equation 3.15 can be written as

$$\begin{pmatrix} A & 0 \\ \mathbf{D} & -\Delta t \mathbf{D} \mathbf{G} \end{pmatrix} \begin{pmatrix} \hat{u}_i^k \\ \delta p \end{pmatrix} = \begin{pmatrix} r \\ 0 \end{pmatrix} \begin{pmatrix} \mathbf{mbc} \\ \mathbf{cbc} \end{pmatrix}, \quad (3.16)$$

$$\begin{pmatrix} I & \Delta t \mathbf{G} \\ 0 & I \end{pmatrix} \begin{pmatrix} u_i^k \\ \delta p \end{pmatrix} = \begin{pmatrix} \hat{u}_i^k \\ \delta p \end{pmatrix}. \quad (3.17)$$

3.1. DIRECT NUMERICAL SIMULATION (DNS)

Writing Equations 3.16 and 3.17 into equation form

$$\begin{aligned} \left(I - \frac{\Delta t \beta_k}{Re} \mathbf{L} + \Delta t \gamma_k \mathbf{N}\right) \widehat{u}_i^k &= u_i^{k-1} + \frac{\Delta t \alpha_k}{Re} \mathbf{L}(u_i^{k-1}) \\ &\quad - \Delta t (\alpha_k + \beta_k) \mathbf{G} p^{k-1} + \mathbf{m} \mathbf{b} \mathbf{c}, \end{aligned} \quad (3.18)$$

$$\Delta t \mathbf{D} \mathbf{G} \delta p = D \widehat{u}_i^k - \mathbf{c} \mathbf{b} \mathbf{c}, \quad (3.19)$$

$$u_i^k = \widehat{u}_i^k - \Delta t \mathbf{G} \delta p. \quad (3.20)$$

Equation 3.18 requires the inversion of matrix A , which is very expensive by considering the sparse nature of matrix A . Therefore, it is approximately factorised into smaller matrices in each direction, which can then be solved by tri- or penta-diagonal matrix solvers. In order to make this approximate factorisation second-order, Equation 3.18 can be rewritten in $\delta \widehat{u}_i$ as

$$\begin{aligned} \left(I - \frac{\Delta t \beta_k}{Re} \mathbf{L} + \Delta t \gamma_k \mathbf{N}\right) \delta \widehat{u}_i &= \frac{1}{Re} \Delta t (\alpha_k + \beta_k) \mathbf{L} u_i^{k-1} \\ &\quad - \Delta t \gamma_k \mathbf{N} u_i^{k-1} - \Delta t \mathbf{G} p^{k-1} + \mathbf{m} \mathbf{b} \mathbf{c}, \end{aligned} \quad (3.21)$$

$$A \delta \widehat{u}_i = A u_i^{k-1} + r + \mathbf{m} \mathbf{b} \mathbf{c} = R,$$

where

$$\delta \widehat{u}_i = \widehat{u}_i^k - u_i^{k-1}.$$

Rewriting Equation 3.21 in matrix form gives

$$\begin{pmatrix} I + \Delta t M_{11} & \Delta t M_{12} & \Delta t M_{13} \\ \Delta t M_{21} & I + \Delta t M_{22} & \Delta t M_{23} \\ \Delta t M_{31} & \Delta t M_{32} & I + \Delta t M_{33} \end{pmatrix} \begin{pmatrix} \delta \widehat{u}_1 \\ \delta \widehat{u}_2 \\ \delta \widehat{u}_3 \end{pmatrix} = \begin{pmatrix} R_1 \\ R_2 \\ R_3 \end{pmatrix}, \quad (3.22)$$

where

$$M = \mathbf{N} - \frac{\alpha_k}{Re} \mathbf{L}.$$

As three velocity components are coupled in Equation 3.22, Kim et al. (2002) ap-

plied another second-order accurate approximate factorisation based on block LU decomposition in order to decouple velocity variables. It is important to note that this second approximate factorisation is another error in addition to the linearisation error in Equation 3.10. After the secondary decoupling, the momentum equations can be finally written as

$$(I + \Delta t M_{11})\delta\hat{u}_1^* = R_1, \quad (3.23)$$

$$(I + \Delta t M_{22})\delta\hat{u}_2^* = R_2 - M_{21}\delta\hat{u}_1^*, \quad (3.24)$$

$$(I + \Delta t M_{33})\delta\hat{u}_3 = R_3 - M_{31}\delta\hat{u}_1^* - M_{32}\delta\hat{u}_2^*, \quad (3.25)$$

$$\delta\hat{u}_2 = \delta\hat{u}_2^* - \Delta t M_{23}\delta\hat{u}_3, \quad (3.26)$$

$$\delta\hat{u}_1 = \delta\hat{u}_1^* - \Delta t M_{23}\delta\hat{u}_2 - \Delta t M_{13}\delta\hat{u}_3, \quad (3.27)$$

where the variables with “*” superscript are the variables resulting from second block LU decomposition, and Equations 3.23-3.27 are the resulting momentum equations to be solved for the intermediate velocity variables. The advantage of this scheme is that boundary conditions are separated from the main solver before the application of FSM. This makes the numerical implementation easier. Furthermore, the Poisson equation is solved for the actual pressure rather than the pseudo-pressure, as in projection FSM, and this eliminates the need to solve another equation for the pressure to update the actual pressure using Equation 3.7.

3.2 Solution procedure

Figure 3.1 shows the flow chart of the main DNS/LES code. The code consists of an initial setup module which contains the reading of input parameters, grid generation, initial flow field generation and the determination of grid coefficients to be used later in the computation of flow field gradients. The main unsteady calculations start with the calculation of boundary conditions for the next time step, followed by SGS viscosity calculation in case of LES. This is followed by the intermediate velocities computations for the three velocity components. The divergence of the intermediate velocity is fed into the Poisson equation to determine the pressure gradient which would ensure mass conservation. Finally, the velocities are updated using the pressure gradient calculated from the Poisson equation.

In Subsections 3.1.1 and 3.1.2, the numerical implementation of projection and splitting FSM is explained, however, it is important to note that the fully implicit code based on splitting FSM is used for all the main simulations in the current work. In Subsections 3.2.1-3.2.3, a brief introduction to the solution procedure is presented.

3.2.1 Momentum equations

Rewriting the modified momentum equations resulting from splitting FSM (Equations 3.23-3.25) in a generalised form as following

$$(I - \Delta t M_{ii}) \delta \hat{u}_i^* = R_i, \quad (3.28)$$

$$(1 - A_1 - A_2 - A_3) \delta \hat{u}_i^* = R_i, \quad (3.29)$$

where A_1 , A_2 , A_3 contain the viscous and convective contributions in case of the fully implicit formulation, while only the viscous contributions in case of the semi-implicit formulation in the streamwise, wall-normal and spanwise directions respec-

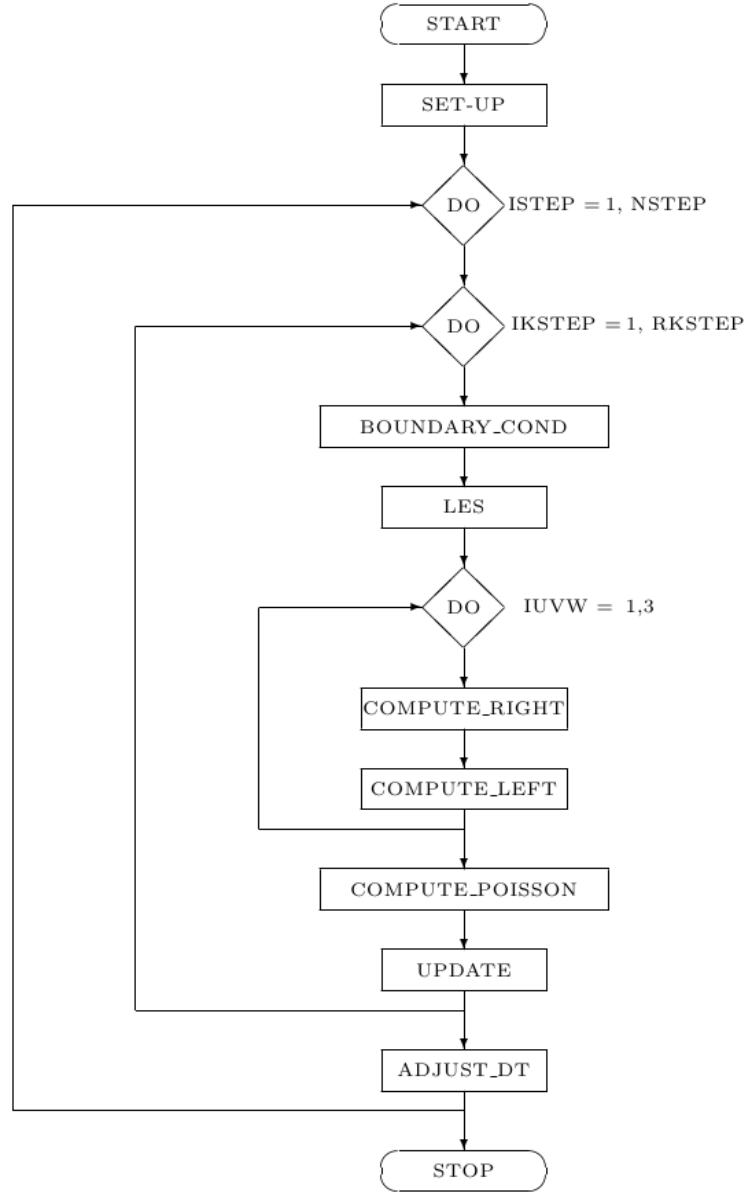


Figure 3.1: Flow chart of the main DNS/LES code.

tively. The solution of Equation 3.29 is significantly expensive because it needs the inversion of a large matrix. Kim and Moin (1985) introduced a third-order accurate approximation to split the above matrix into three one-dimensional matrices

$$(1 - A_1 - A_2 - A_3)\delta\hat{u}_i^* = (1 - A_3)(1 - A_2)(1 - A_1)\delta\hat{u}_i^*. \quad (3.30)$$

3.2. SOLUTION PROCEDURE

The momentum equations after the splitting become

$$(1 - A_3)(1 - A_2)(1 - A_1)\delta\hat{u}_i^* = R_i. \quad (3.31)$$

Now, Equation 3.31 can be inverted directly by inverting three relatively small matrices in each direction. The sparsity of matrices allows the use of efficient direct solvers *i.e.* TDMA and penta-diagonal matrix algorithm depending upon the number of points employed to compute the velocity gradients. Let

$$\delta\hat{u}_i^{**} = (1 - A_2)(1 - A_1)\delta\hat{u}_i^*, \quad (3.32)$$

then Equation 3.31 can be written as

$$(1 - A_3)\delta\hat{u}_i^{**} = R_i. \quad (3.33)$$

Equation 3.33 is solved in the spanwise direction for $\delta\hat{u}_i^{**}$. Now rewriting Equation 3.32

$$(1 - A_2)\delta\hat{u}_i^{***} = \delta\hat{u}_i^{**}, \quad (3.34)$$

where

$$\delta\hat{u}_i^{***} = (1 - A_1)\delta\hat{u}_i^*. \quad (3.35)$$

Equation 3.34 is solved in the wall-normal direction for $\delta\hat{u}_i^{***}$, and finally Equation 3.35 is solved in the streamwise direction for $\delta\hat{u}_i^*$ as following

$$(1 - A_1)\delta\hat{u}_i^* = \delta\hat{u}_i^{***}. \quad (3.36)$$

3.2.2 Spatial discretisation

Cartesian coordinate system is used in the present study. It uses staggered grid formulation (Harlow and Welch, 1965) for spatial discretisation to prevent artificial pressure oscillations associated with pressure checker board problem. In staggered grid formulation, the vectors (velocity components) are defined at the cell face while the scalars (pressure) are defined at the cell center. The staggered grid does not require any pressure boundary conditions, and conservation of mass, kinetic energy and circulation are ensured (Kim and Moin, 1985). In a staggered grid, the control volumes for u , v and w velocities are displaced by half control volume in each direction as compared to the normal cell. Therefore, the standard control volume can be called pressure control volume, and in the same context u control volume, v control volume and w control volume can be generated by shifting the grid by half cell in respective directions. Figure 3.2 shows the staggered grid formulation, representing the pressure, u and v control volumes.

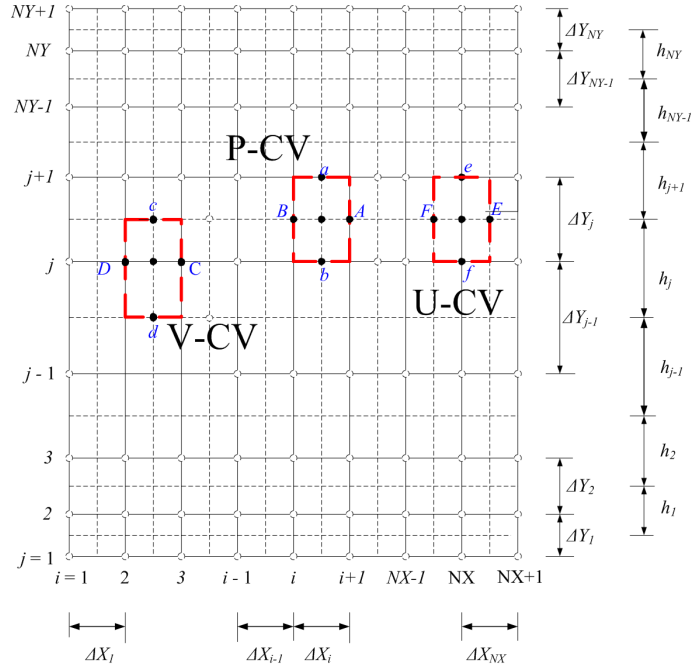


Figure 3.2: Staggered grid for spatial discretisation for primitive variables.

3.2. SOLUTION PROCEDURE

Each momentum equation is discretised on the corresponding staggered grid resulting in a set of partial differential equations which need to be solved in time to obtain flow field solution. Finite volume discretisation is employed and each momentum equation is integrated on the corresponding staggered mesh. Spatial discretisation procedure for u momentum equation, using four neighbouring points for the calculation of velocity gradients, is explained as following. Equation 3.34 is rewritten for u momentum equation

$$(1 - A_2)\delta\hat{u}^{***} = \delta\hat{u}^{**}, \quad (3.37)$$

where $\delta\hat{u}^{***} = (1 - A_1)\delta\hat{u}^*$. After integrating over the u -control volume and dividing by the staggered u control volume ($\Delta x^s \Delta y \Delta z$) :

$$\int_{\Delta x^s \Delta y \Delta z} (1 - A_2)\delta\hat{u}^{***} dx dy dz / \Delta x^s \Delta y \Delta z = \int_{\Delta x^s \Delta y \Delta z} \delta\hat{u}^{**} dx dy dz / \Delta x^s \Delta y \Delta z,$$

where Δx^s is the length of the u control volume in x direction. Thus

$$(1 - \overline{A}_2^y / \Delta y)\delta\hat{u}^{***} = \delta\hat{u}^{**}. \quad (3.38)$$

Here an overline indicates the integrated variable,

$$\overline{A}_2^y = \int_{\Delta y} A_2 dy = \overline{B}_2^y + \delta_c \overline{C}_2^y, \quad (3.39)$$

where \overline{B}_2^y and \overline{C}_2^y are the viscous and convective contributions, and δ_c is a constant which is equal to 1 for Crank-Nicolson treatment of convective term while 0 for Runge-Kutta discretisation.

$$\overline{B}_2^y = \beta_k \Delta t \left(\left[\frac{\partial}{\partial y} \right]_{j+1} - \left[\frac{\partial}{\partial y} \right]_j \right) \delta\hat{u}^{***}, \quad (3.40)$$

$$\overline{C}_2^y = \gamma_k \Delta t \left([v^{k-1} \delta\hat{u}^{***}]_{j+1} - [v^{k-1} \delta\hat{u}^{***}]_j \right). \quad (3.41)$$

The terms in Equations 3.40 and 3.41 are calculated by using finite difference second-

order accurate discretisation. For viscous terms, the gradient is calculated by using four neighbouring points to ensure second-order accuracy on a non-uniform mesh,

$$\left[\frac{\partial \widehat{u}^{***}}{\partial y} \right]_j = b_j^1 \widehat{u}_{j+1}^{***} + b_j^2 \widehat{u}_j^{***} + b_j^3 \widehat{u}_{j-1}^{***} + b_j^4 \widehat{u}_{j-2}^{***}.$$

Therefore, the total viscous contribution can be written as

$$\begin{aligned} \overline{B}_2^y &= \beta_k \Delta t \left[b_{j+1}^1 \widehat{u}_{j+2}^{***} + b_{j+1}^2 \widehat{u}_{j+1}^{***} + b_{j+1}^3 \widehat{u}_j^{***} + b_{j+1}^4 \widehat{u}_{j-1}^{***} \right] \\ &\quad - \beta_k \Delta t \left[b_j^1 \widehat{u}_{j+1}^{***} + b_j^2 \widehat{u}_j^{***} + b_j^3 \widehat{u}_{j-1}^{***} + b_j^4 \widehat{u}_{j-2}^{***} \right]. \end{aligned}$$

Similarly, the convective contribution is calculated as following

$$\overline{C}_2^y = \gamma_k \Delta t \left[c_j^1 \widehat{u}_{j+1}^{***} + c_j^2 \widehat{u}_j^{***} + c_j^3 \widehat{u}_{j-1}^{***} \right],$$

where b^1, b^2, b^3, b^4 , c^1, c^2 and c^3 are the finite difference diffusive and convective coefficients calculated from grid information. Substituting the values of viscous and convective terms into Equation 3.38, and writing the equation in matrix form gives

$$\frac{\Delta t}{\Delta y_j} \begin{pmatrix} -\beta_k b_{j+1}^1 \\ \beta_k b_j^1 - \beta_k b_{j+1}^2 - \delta_c c_j^1 \\ 1 + \beta_k b_j^2 - \beta_k b_{j+1}^3 - \delta_c c_j^2 \\ \beta_k b_j^3 - \beta_k b_{j+1}^4 - \delta_c c_j^3 \\ \beta_k b_j^4 \end{pmatrix} \begin{pmatrix} \widehat{u}_{j+2}^{***} \\ \widehat{u}_{j+1}^{***} \\ \widehat{u}_j^{***} \\ \widehat{u}_{j-1}^{***} \\ \widehat{u}_{j-2}^{***} \end{pmatrix} = \widehat{u}^{**}. \quad (3.42)$$

Now Equation 3.42 can be solved by using penta-diagonal solver.

3.2.3 Poisson equation solution

The Poission equation is solved to determine the pressure for the next time step which would ensure the divergence free velocity field at next time step. The Poisson

3.2. SOLUTION PROCEDURE

equation is derived from the velocity update equation of FSM using the incompressibility condition. The velocity update equation is given by

$$\frac{u_i^k - \widehat{u}_i^k}{\Delta t} = \frac{\partial \delta p}{\partial x_i}, \quad (3.43)$$

Taking the divergence of Equation 3.43 and using the continuity equation,

$$\frac{1}{\Delta t} \frac{\partial \widehat{u}_i^k}{\partial x_i} = \frac{\partial^2 \delta p}{\partial x_i^2}, \quad (3.44)$$

$$\frac{\partial^2 \delta p}{\partial x^2} + \frac{\partial^2 \delta p}{\partial y^2} + \frac{\partial^2 \delta p}{\partial z^2} = \frac{1}{\Delta t} \frac{\partial \widehat{u}_i^k}{\partial x_i} = f(x, y, z). \quad (3.45)$$

It is worth noting that no additional pressure correction is required at the end of each time step for the implicit method. The Poisson equation can be solved by iterative solvers like the multigrid method but this can be expensive in terms of computing cost. Direct solvers such as Fast Fourier Transforms (FFT) can be used for the Poisson equation solution in the homogeneous directions. In the present case, a uniform mesh is used in the streamwise and spanwise directions which makes it possible to apply FFT in the xz plane with TDMA used in the wall-normal direction. Application of Fourier transform to Equation 3.45 in the x and z directions gives

$$-k_x^2 \widehat{\delta p} + \frac{\partial^2 \widehat{\delta p}}{\partial y^2} - k_z^2 \widehat{\delta p} = \widehat{f}(k_x, y, k_z), \quad (3.46)$$

where $k_x = 2\pi f_x$ and $k_z = 2\pi f_z$ are the modified wave numbers in the x and z directions respectively, and $\widehat{f}(k_x, y, k_z)$ is the transformation counterpart of $f(x, y, z)$. The modified wave numbers are defined as

$$k_x(l) = 2[1 - \cos(2\pi l/N_x)]/\Delta x^2, \quad (3.47)$$

$$k_z(m) = 2[1 - \cos(2\pi m/N_z)]/\Delta z^2. \quad (3.48)$$

Integration Equation 3.46 in the wall-normal direction results in

$$\int_{\Delta y_j} -k_x^2 \hat{\delta p} + \frac{\partial^2 \hat{\delta p}}{\partial y^2} - k_z^2 \hat{\delta p} dy = \int_{\Delta y_j} \hat{f}(k_x, y, k_z) dy, \quad (3.49)$$

$$\frac{1}{\Delta y_{j-\frac{1}{2}}} \hat{\delta p}_{j-1} - \left(k_x^2 + k_z^2 + \frac{1}{\Delta y_{j-\frac{1}{2}}} + \frac{1}{\Delta y_{j+\frac{1}{2}}} \right) \hat{\delta p}_j + \frac{1}{\Delta y_{j+\frac{1}{2}}} \hat{\delta p}_{j+1} = \hat{f} \Delta y_j, \quad (3.50)$$

where $\Delta y_{j\pm\frac{1}{2}}$ are the staggered wall-normal gradients and are given as

$$\Delta y_{j-\frac{1}{2}} = (\Delta y_{j-1} + \Delta y_j)/2, \quad (3.51)$$

$$\Delta y_{j+\frac{1}{2}} = (\Delta y_j + \Delta y_{j+1})/2. \quad (3.52)$$

Equation 3.50 is solved by using a direct solver (TDMA) in the wall-normal direction and FFT is applied in the streamwise and spanwise directions to obtain the pressure which guaranties the divergence free flow field at the next time step. FFTW library is used for fast Fourier transformation in forward and backward directions. This pressure field is then used to update the velocity field by using Equation 3.43.

3.3 Validation

Three test cases are considered to validate the the fully implicit method implementation.

3.3.1 Decaying vortex test case

A two-dimensional decaying vortex flow has been chosen to validate the numerical accuracy of the implicit method. This flow has an analytic solution (Brachet et al., 1983).

$$u(x, y, t) = -\cos(\pi x) \sin(\pi y) \exp^{-2\pi^2 t/Re}, \quad (3.53)$$

$$v(x, y, t) = \sin(\pi x) \cos(\pi y) \exp^{-2\pi^2 t/Re}, \quad (3.54)$$

$$p(x, y, t) = -\frac{1}{4}(\cos(2\pi x) + \sin(2\pi y)) \exp^{-4\pi^2 t/Re}. \quad (3.55)$$

The flow is periodic in the horizontal (x, z) directions and periodic boundary conditions are used in the simulation. The domain size used is 2×2 . The Reynolds number based on the initial maximum velocity and the vortex diameter is $Re = 10$. Simulations were performed on a uniform mesh by keeping the CFL number constant. Figure 3.3 verifies that the implementation is second-order accurate, and the error in the fully implicit schemes is comparable with the error from semi-implicit scheme. This is remarkable considering that additional approximate factorisation was required in the fully implicit method to decouple velocities in the momentum equations. The effect of convective boundary condition was also tested in Figure 3.3. Velocity and pressure contours are shown in Figure 3.4.

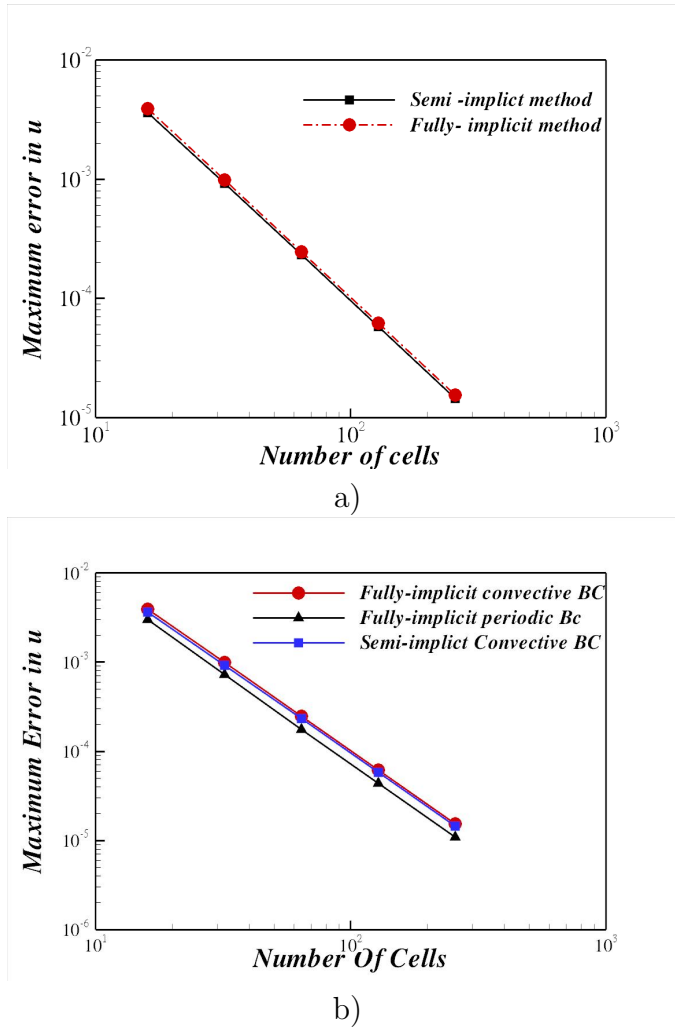


Figure 3.3: Maximum error in u for the two numerical schemes at $t = 0.3$ using a) periodic, and b) convective boundary conditions.

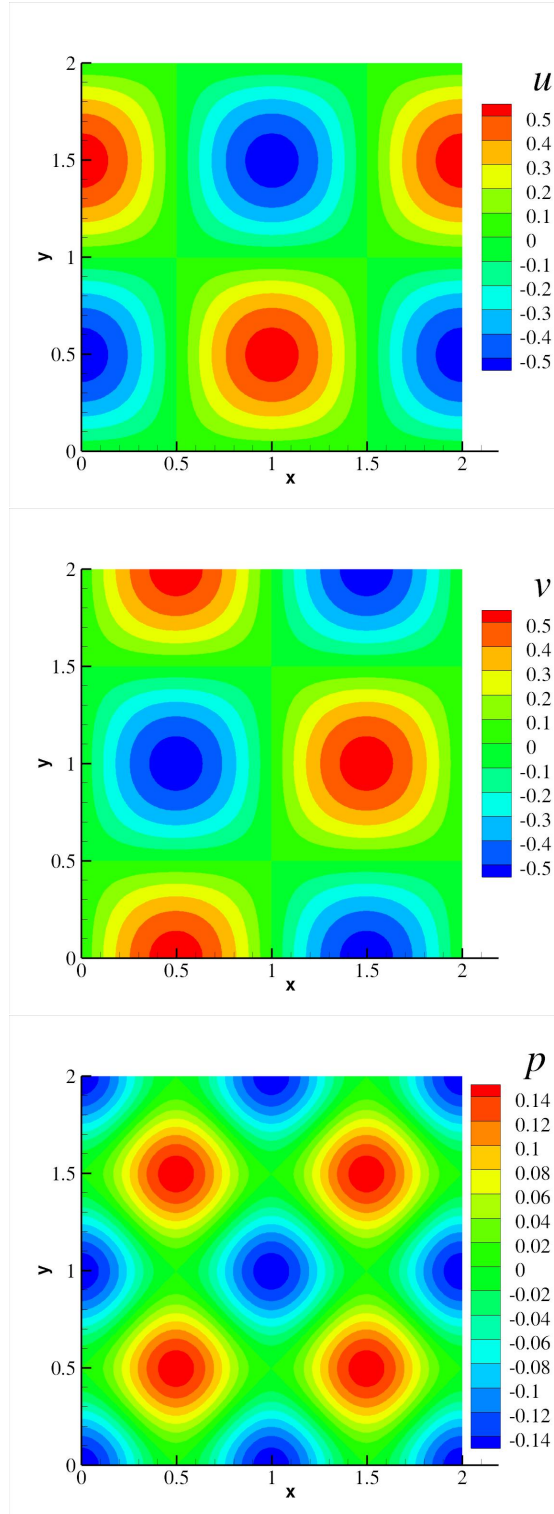


Figure 3.4: Decaying vortices test case. Velocities and pressure contours at $t = 0.3$.

3.3.2 Turbulent channel flow

The fully-developed turbulent channel flow was considered at $Re = 2800$ and $Re = 6900$ where the Reynolds number is based on the half-channel height and the bulk-mean velocity. The mass flow rate is kept constant during the simulations allowing slight variation of the mean pressure gradient. Simulation parameters used in this study are shown in Table 3.1. DNS data of Moser et al. (1999) are also included in the table for comparison. The Reynolds numbers based on the friction velocity Re_τ , are summarised in Table 3.2.

Simulation	Re	$L_x \times L_z$	$N_x \times N_y \times N_z$	Δx^+	Δz^+	Δy_{min}^+	Δy_{max}^+
Present	2800	12×4	$128 \times 129 \times 128$	16.8	5.6	0.4	5.8
Moser et al. (1999)	2800	$4\pi \times \frac{4}{3}\pi$	$128 \times 129 \times 128$	17.7	5.9	-	4.4
Present	6900	6×4	$256 \times 192 \times 288$	9.2	5.4	0.4	9.6
Moser et al. (1999)	6900	$2\pi \times \pi$	$256 \times 192 \times 192$	10	6.5	-	6.5

Table 3.1: Simulation parameters used in the present simulations.

Re	Dean's formulae	Moser et al. (1999)	semi-implicit	fully implicit
2800	182	178	179	180
6900	400	392	391	392

Table 3.2: Comparison of Re_τ from both numerical schemes with values available in literature.

The Re_τ values from the fully implicit method exhibit very good agreement with the values from semi-implicit method and available literature. It is important to note that the simulations from the fully implicit code are approximately three time faster than the semi-implicit method as the fully implicit method solves the momentum equations once per time step as compared to three sub-steps solution in case of the semi-implicit method. Figure 3.5 shows the comparison of the mean velocity and the rms velocity fluctuation for the two Reynolds numbers. All the profiles from fully implicit method are in excellent agreement with the semi-implicit method.

3.3. VALIDATION

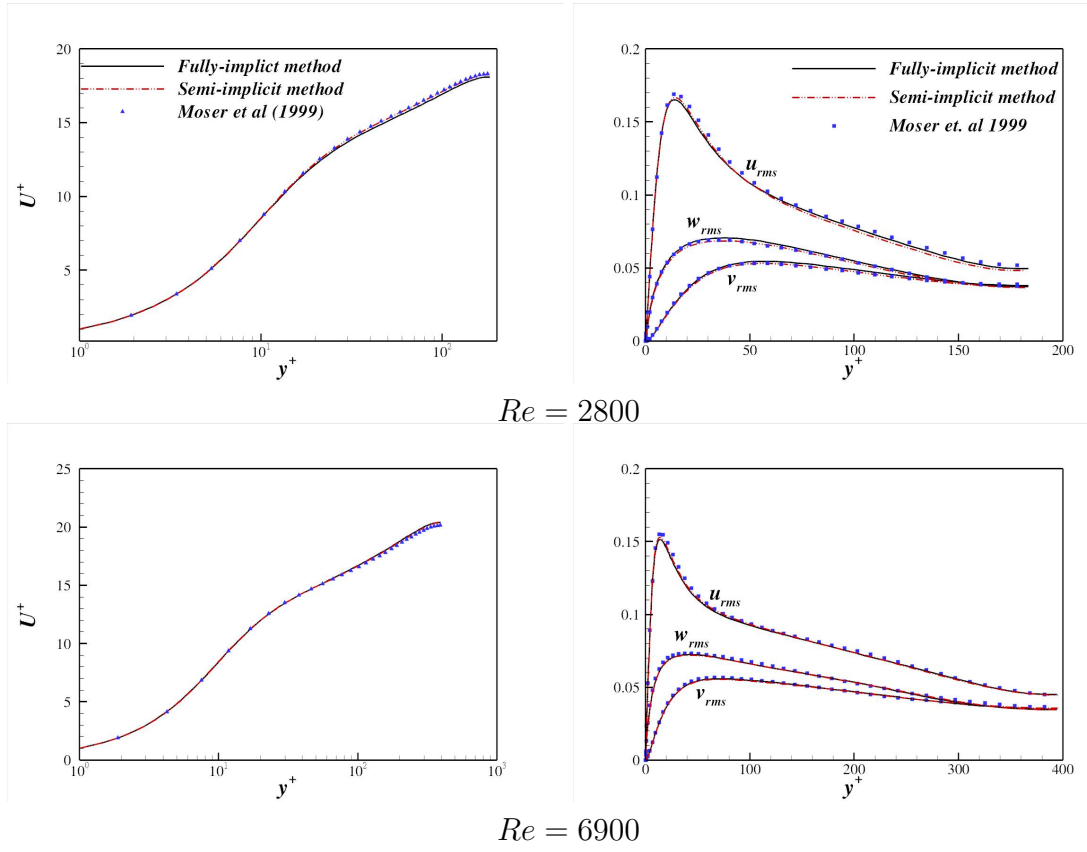


Figure 3.5: The mean velocity and rms velocity fluctuations. The DNS data of Moser et al. (1999) are included for comparison.

3.3.3 Boundary condition implementation validation

Boundary conditions implementation of fully implicit scheme with *mbc* and *cbc* formulations are tested for active blowing and suction flow control proposed by Choi and Moin (1994). Simulation parameters are shown in Table 3.3. v velocity is imposed on the walls exactly opposite to the v velocity on the detection plane. Detection plane is chosen as $y_d^+ = 15$ which is found to be the optimal case of drag reduction. Percentage drag reduction from the semi-implicit and the fully implicit methods are 22.2 % and 22.5 % respectively. Results from the semi-implicit method are published in Chung and Talha (2011). Time history of drag reduction after the application of flow control and the rms velocity fluctuations are shown for the two methods for the optimal case in Figure 3.6. The results from fully implicit method are in very good agreement with the semi-implicit method. This test case verifies the correct implementation of boundary condition matrices *mbc* and *cbc* for the fully implicit method.

Re	$L_x \times L_z$	$N_x \times N_y \times N_z$	Δx^+	Δz^+	Δy_{min}^+	Δy_{max}^+
2800	12×4	$128 \times 129 \times 144$	16.9	5.6	0.2	6.9

Table 3.3: Simulation parameters for active flow control simulation.

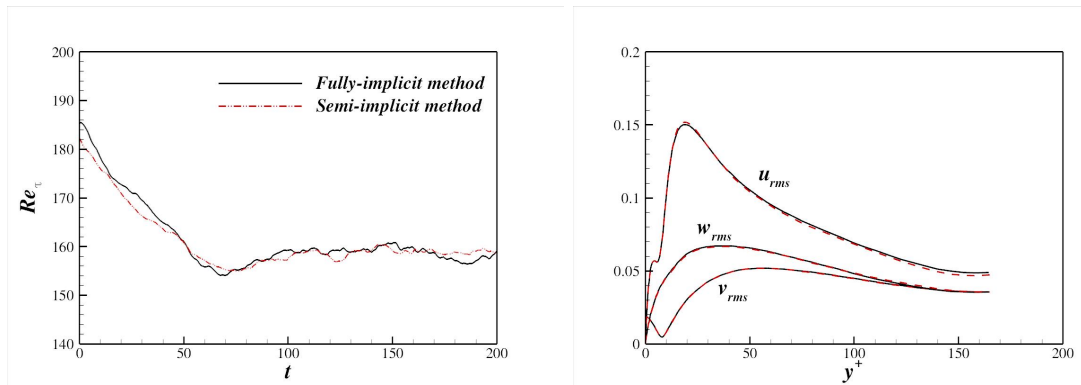


Figure 3.6: Re_τ time history, and rms velocity fluctuations for active flow control simulation.

3.4 Large eddy simulation (LES)

DNS has made a significant contribution to our understanding of the underlying physics in many turbulent flows. However, its applicability has been restricted to relatively low and moderate Reynolds number flows due to the computational cost. DNS resolves the smallest scales of motion in time and space and the near-wall turbulent structures become smaller as the Reynolds number increases. Therefore, the spatial grid resolution becomes increasingly fine and the computational cost becomes prohibitively high for high Reynolds number flows of practical interest. The number of grid points required to resolve all scales of turbulence is proportional to the ratio between the largest and smallest eddies in the flow. This ratio is proportional to $Re_L^{3/4}$ (Reynolds, 1990), where L is the integral length scale of the flow. This restriction necessitates the grid points required in three dimension to $Re_L^{9/4}$ for DNS calculations.

In large eddy simulation (LES), the spatial scales are divided into two categories: the large scales which are computed directly by solving the Navier-Stokes equations and the small scales which should be modelled by a subgrid-scale (SGS) model. LES is an intermediate approach between DNS and RANS modelling as it can represent instantaneous flow characteristics and can compute the large scales directly as DNS while RANS modelling involves the computation of the averaged flow properties. On the other hand, LES is not as accurate as DNS because the small scales are not computed directly which, in turn, relaxes the grid resolution restrictions, and this makes LES more feasible for relatively high Reynolds number flows. LES is based on the assumption that most of turbulent energy is contained in the large energy containing structures, while only a fraction of energy is contained in the small unresolved scales. These small scales can be considered as universal and isotropic, making it possible to model them by simpler models. In essence, LES has mostly dissipative contribution to the Navier-Stokes equations accounting for the energy

left over by overlooking the contribution from unresolved scales. However, in some flow situations, energy is transferred back from the small scales to large scales, and this phenomenon is called backscatter. A good LES model also needs to cater for the possibility of backscatter.

The large scales are separated from the small scales by applying a filtering operation to the Navier-Stokes equations. This filtering procedure can be thought of as a low-pass filtering in which only the large energy carrying scales are considered, while the effect of the small scales is included by SGS modelling term in the Navier-Stokes equations. In mathematical terms, this decomposition of the two scales can be written as

$$u_i = \bar{u}_i + u'_i, \quad (3.56)$$

where an overbar denotes the filtered variable and u'_i is the fluctuating component which is filtered out during filtering operation. The low-pass filtering can be defined by a filter function G (Leonard, 1974),

$$\bar{f}(x) = \int_D G(x - x') f(x') dx', \quad (3.57)$$

where D is the integration domain. Most commonly used filters in LES are box or top-hat filters, spectral or sharp cut-off filters and Gaussian filters. The sharp cut-off filter (spectral) clearly separates the larger scales from the smaller scales and therefore represents the effect of smaller scales on larger scales. The smooth filter (Gaussian or top-hat) does not make a sharp distinction between the two separated scales which also allows the small scales to affect the larger scales. Detailed comparison of effects of using sharp cut-off filters versus the smooth filters, and the selection of appropriate SGS models and filters, can be found in Stefano and Vasilyev (2002).

3.4. LARGE EDDY SIMULATION (LES)

The top-hat filter is given by

$$G(x - x') = \begin{cases} (1/\Delta_i), & |x_i - x'_i| < \Delta/2 \\ 0, & |x_i - x'_i| > \Delta/2 \end{cases}, \quad (3.58)$$

where $i = 1, 2, 3$ and Δ is the filter width.

The Gaussian filter in physical space is given by

$$G(x - x') = \left(\frac{6}{\pi \Delta_i^2} \right)^{1/2} \exp \left(-\frac{6(x_i - x'_i)^2}{\Delta_i^2} \right). \quad (3.59)$$

In the present study, the top-hat filter is used for the filtering operation as suggested by Germano et al. (1991).

3.4.1 LES equations

Applying low-pass filtering to the incompressible Navier-Stokes equations and assuming that differentiation and filtering operations are commutable

$$\frac{\partial \bar{u}_i}{\partial t} + \frac{\partial}{\partial x_j} (\bar{u}_i \bar{u}_j) = -\frac{\partial \bar{p}}{\partial x_i} + \frac{1}{Re} \frac{\partial^2 \bar{u}_i}{\partial x_j^2}, \quad (3.60)$$

$$\frac{\partial \bar{u}_i}{\partial x_i} = 0. \quad (3.61)$$

The nonlinear convective term on the left hand side of Equation 3.60 can not be computed directly. Therefore, Equation 3.60 is modified as

$$\frac{\partial \bar{u}_i}{\partial t} + \frac{\partial}{\partial x_j} (\bar{u}_i \bar{u}_j) = -\frac{\partial \bar{p}}{\partial x_i} + \frac{1}{Re} \frac{\partial^2 \bar{u}_i}{\partial x_j^2} - \frac{\partial}{\partial x_j} \tau_{ij}, \quad (3.62)$$

where τ_{ij} is the SGS stress term which includes the effect from unresolved smaller scales and is given as

$$\tau_{ij} - \frac{1}{3} \delta_{ij} \tau_{kk} = \bar{u}_i \bar{u}_j - \overline{u_i u_j} = -2\nu_{sgs} S_{ij}, \quad (3.63)$$

where ν_{sgs} is the SGS viscosity and S_{ij} is the large-scale strain-rate tensor which is given as

$$S_{ij} = \frac{1}{2} \left(\frac{\partial \bar{u}_i}{\partial x_j} + \frac{\partial \bar{u}_j}{\partial x_i} \right). \quad (3.64)$$

Substituting τ_{ij} from Equation 3.63 and S_{ij} from Equation 3.64 into Equation 3.62 results in the modified momentum equations for LES.

$$\frac{\partial \bar{u}_i}{\partial t} + \frac{\partial}{\partial x_j} (\bar{u}_i \bar{u}_j) = -\frac{\partial \bar{p}}{\partial x_i} + \frac{1}{Re} \frac{\partial^2 \bar{u}_i}{\partial x_j^2} + \frac{\partial}{\partial x_j} \left(\nu_{sgs} \frac{\partial \bar{u}_i}{\partial x_j} + \nu_{sgs} \frac{\partial \bar{u}_j}{\partial x_i} \right). \quad (3.65)$$

3.4.2 Subgrid-scale (SGS) models

The SGS viscosity, ν_{sgs} , in Equation 3.65 is calculated using SGS modelling. SGS modelling is the subject of interest for last four decades and extensive research has already been performed in this area. A brief overview of SGS modelling efforts is presented in Moin (2002). The effectiveness of SGS modelling involves the correct asymptotic *i.e.* y^3 near-wall behaviour of the SGS viscosity and the correct prediction of the SGS dissipation *i.e.* $\varepsilon_{SGS} = \tau_{ij} S_{ij}$. A good SGS model should also be able to cater for backscatter. Piomelli et al. (1990) reported some inaccuracies in LES calculations for transitional flow because of the inability of their SGS model to account for backscatter. A brief overview of the SGS models, implemented in the present study, is given in the following subsections

Smagorinsky model

Smagorinsky (1963) proposed a linear relationship between the SGS viscosity and the large-scale strain-rate magnitude ($|\bar{S}|$). This model is based on the eddy viscosity assumption which assumes that the energy production is in balance with the energy

3.4. LARGE EDDY SIMULATION (LES)

dissipation. This yields the expression for ν_{sgs} as following

$$\nu_{sgs} = (C_s \Delta)^2 |\bar{S}|, \quad (3.66)$$

where C_s is the Smagorinsky constant, Δ is the filter width (which is proportional to the grid spacing) and $|\bar{S}| = \sqrt{2\bar{S}_{ij}\bar{S}_{ij}}$. This model has been successfully applied to various simple turbulent flows. However, it had encountered several issues. First major debatable issue is the choice of C_s and the filter width Δ . Lilly (1966) proposed the value of $C_s = 0.23$ based upon the isotropic homogeneous turbulence theory but this value is found to be excessively high (Deardorff, 1971; Piomelli et al., 1988). The higher value of C_s results in excessive SGS dissipation in mean shear flows and it was concluded that this value should be reduced to 0.1 for turbulent channel flow. The value of C_s is found to be flow dependent. This model does not produce the correct asymptotic near-wall behaviour of SGS viscosity and it does not vanish at solid boundaries. These limitations necessitate the use of damping function such as Van Driest damping to obtain the correct SGS viscosity near the solid walls (Moin and Kim, 1982). In addition, this model is only dissipative and can not account for backscatter.

Dynamic SGS model

Germano et al. (1991) proposed a dynamic procedure to calculate the Smagorinsky constant. This procedure uses the Leonard identity (Germano, 1990) to calculate the Smagorinsky constant. This model incorporates two levels of filtering: first is the grid filtering and second is the test filtering. The test filtering is normally applied at comparatively large scale (usually twice) as compared to the grid filtering. Rewriting the grid-filtered Navier-Stokes equations.

$$\frac{\partial \bar{u}_i}{\partial t} + \frac{\partial}{\partial x_j} (\bar{u}_i \bar{u}_j) = -\frac{\partial \bar{p}}{\partial x_i} + \frac{1}{Re} \frac{\partial^2 \bar{u}_i}{\partial x_j^2} - \frac{\partial}{\partial x_j} \tau_{ij}, \quad (3.67)$$

where

$$\tau_{ij} = \overline{u_i u_j} - \overline{u_i} \overline{u_j} = -2 C \overline{\Delta}^2 |\overline{S}| \overline{S}_{ij}. \quad (3.68)$$

Please note that here C is the square of Smagorinsky constant *i.e.*, $C = C_s^2$. Now applying test filtering to the Equation 3.67

$$\frac{\partial \widetilde{u}_i}{\partial t} + \frac{\partial}{\partial x_j} (\widetilde{u}_i \widetilde{u}_j) = -\frac{\partial \widetilde{p}}{\partial x_i} + \frac{1}{Re} \frac{\partial^2 \widetilde{u}_i}{\partial x_j^2} - \frac{\partial T_{ij}}{\partial x_j}, \quad (3.69)$$

where

$$T_{ij} = \widetilde{\overline{u_i u_j}} - \widetilde{u_i} \widetilde{u_j} = -2 C \widetilde{\Delta}^2 |\widetilde{S}| \widetilde{S}_{ij}. \quad (3.70)$$

τ_{ij} in Equation 3.68 and T_{ij} in Equation 3.70 can be linked through Leonard identity which is given by

$$L_{ij} = T_{ij} - \widetilde{\tau}_{ij} = \widetilde{\overline{u_i u_j}} - \widetilde{u_i} \widetilde{u_j}. \quad (3.71)$$

L_{ij} is representative of contribution of smaller resolved scales to the turbulent shear stress *i.e.* the scales in between the test and grid filters. This contribution is used to calculate C by exploiting the algebraic relationship between L_{ij} , T_{ij} and $\widetilde{\tau}_{ij}$. Now contracting this identity with \overline{S}_{ij} results in

$$(\widetilde{\overline{u_i u_j}} - \widetilde{u_i} \widetilde{u_j}) \overline{S}_{ij} = -2 C (\widetilde{\Delta}^2 |\widetilde{S}| \widetilde{S}_{ij} \overline{S}_{ij} - \overline{\Delta}^2 |\overline{S}| \overline{S}_{ij} \overline{S}_{ij}). \quad (3.72)$$

Contraction with \overline{S}_{ij} has been performed in order to avoid ill-conditioned value of C (Germano et al., 1991). Moreover this model requires spatial averaging to avoid nonphysical local large C values. Therefore, spatial averaging is normally performed in homogeneous directions and the resulting value of C is a function of time and

3.4. LARGE EDDY SIMULATION (LES)

inhomogeneous directions only. Constant C can be determined as

$$C = -\frac{1}{2} \frac{\langle \widetilde{\widetilde{u_i u_j}} - \widetilde{\widetilde{u_i}} \widetilde{\widetilde{u_j}} \rangle \overline{S_{ij}}}{\langle \widetilde{\widetilde{\Delta^2}} |\widetilde{\widetilde{S}}| \widetilde{\widetilde{S_{ij}}} - \widetilde{\widetilde{\Delta^2}} |\widetilde{\widetilde{S}}| \widetilde{\widetilde{S_{ij}}} \rangle} = -\frac{1}{2} \frac{\langle L_{ij} \overline{S_{ij}} \rangle}{\langle M_{ij} \overline{S_{ij}} \rangle}, \quad (3.73)$$

Where “ $\langle \rangle$ ” denote the averaging in homogeneous directions and M_{ij} is given as

$$M_{ij} = \widetilde{\widetilde{\Delta^2}} |\widetilde{\widetilde{S}}| \widetilde{\widetilde{S_{ij}}} - \widetilde{\widetilde{\Delta^2}} |\widetilde{\widetilde{S}}| \widetilde{\widetilde{S_{ij}}} \quad (3.74)$$

This procedure produces the correct asymptotic behaviour (y^3) of SGS viscosity. Another advantage of the dynamic SGS model is the ability to model backscatter phenomenon. The only adjustable parameter in this model is the ratio of the test filter to the grid filter *i.e.* $\widetilde{\widetilde{\Delta}}/\overline{\Delta}$. The optimum value of this ratio is found to be equal to 2 (Germano et al., 1991). Explicit test filtering is recommended in only the homogeneous directions because differentiation and filtering operations are found to be incommutable in the inhomogeneous directions (Ghosal and Moin, 1995). Lilly (1992) proposed an improvement to the calculation of C by contracting the Leonard identity by M_{ij} instead of original contraction by $\overline{S_{ij}}$ which removes a source of singularity from solution procedure and the new formulation for C can be written as

$$C = -\frac{1}{2} \frac{\langle L_{ij} M_{ij} \rangle}{\langle M_{ij} M_{ij} \rangle}. \quad (3.75)$$

The numerical implementation of dynamic SGS model involves following steps:

1. Calculate the grid-filtered velocity at the center location of the pressure control volume.
2. Calculate the test-filtered velocity at the test grid level using second-order accurate interpolation.

3. Calculate strain-rate magnitude tensors at the grid filter and the test filter level.
4. Calculate $\langle L_{ij} M_{ij} \rangle$ and $\langle M_{ij} M_{ij} \rangle$ on the test grid level.
5. Apply the spatial averaging in the homogeneous directions for the terms calculated in Step 4 and calculate C .
6. Interpolate C value from the test filter level back to the grid filter level.
7. Calculate SGS viscosity (ν_{sgs}) by using Equation 3.66.

This model has been successfully applied to various flow configurations. However, it needs spatial averaging or *ad hoc* viscosity clipping procedure to avoid nonphysical values of constant C . This constraint restricts its application to comparatively simple flow geometries and it has been used extensively in the past for turbulent boundary layer and turbulent channel flow simulations.

Many researchers have proposed various improvements and new model approaches to make it suitable for complex geometries. Two early proposed models are the dynamic localization model (Ghosal et al., 1995) and the Lagrangian dynamic model (Meneveau et al., 1996). These models have been used successfully in turbulent flow simulations for complex geometries. However, the implementation effort required for these models is significantly higher as compared to the original dynamic SGS model. Vreman (2004) proposed a new SGS model with fixed coefficient in space which ensures the correct SGS dissipation for laminar and transitional flows. Park et al. (2006) reported that the model coefficient of Vreman (2004) model is flow dependent, and they proposed a new dynamic procedure to calculate the model coefficient based on the assumption of global equilibrium between SGS dissipation and viscous dissipation. You and Moin (2007) proposed a single-level filter dynamic procedure for the model coefficient calculation as compared to the two-level filtering procedure used by Park et al. (2006). This model removes the constraint of averaging

3.4. LARGE EDDY SIMULATION (LES)

or ad hoc viscosity clipping, and moreover it is suitable for low order discretisation schemes and unstructured grid formulations.

Wall-adapting local eddy-viscosity (WALE) model

Nicoud and Ducros (1999) proposed a new SGS model for complex geometries with single-level filtering. They proposed that the SGS viscosity is proportional to the square of velocity gradient tensor.

$$\nu_{sgs} = (C_w \Delta^2) \frac{(\mathfrak{D}_{ij}^d \mathfrak{D}_{ij}^d)^{3/2}}{(\overline{S}_{ij} \overline{S}_{ij})^{5/2} + (\mathfrak{D}_{ij}^d \mathfrak{D}_{ij}^d)^{5/4}}, \quad (3.76)$$

where C_w is a constant and \mathfrak{D}_{ij}^d is the traceless symmetric part of the square of velocity gradient tensor which is given by

$$\mathfrak{D}_{ij}^d = \frac{1}{2}(\overline{g}_{ij}^2 + \overline{g}_{ji}^2) - \frac{1}{3}\delta_{ij}\overline{g}_{kk}^2, \quad (3.77)$$

where $\overline{g}_{ij}^2 = \overline{g}_{ik}\overline{g}_{kj}$ and \overline{g}_{ij} represents the velocity gradient of large resolved scales. WALE model includes the effects of strain rate and rotation rate. Equation 3.77 can be written in symmetric part of tensor \overline{g} *i.e.* \overline{S} , and anti-symmetric part (rotation) *i.e.* $\overline{\Omega}$ as following

$$\mathfrak{D}_{ij}^d = \overline{S}_{ik} + \overline{S}_{kj} + \overline{\Omega}_{ik} + \overline{\Omega}_{kj} - \frac{1}{3}\delta_{ij}[\overline{S}_{mn}\overline{S}_{mn} - \overline{\Omega}_{mn}\overline{\Omega}_{mn}], \quad (3.78)$$

where $\overline{\Omega}$ is given as

$$\overline{\Omega}_{ij} = \frac{1}{2} \left(\frac{\partial \overline{u}_i}{\partial x_j} - \frac{\partial \overline{u}_j}{\partial x_i} \right). \quad (3.79)$$

By using Cayley-Hamilton theorem of linear algebra, $\mathfrak{D}_{ij}^d \mathfrak{D}_{ij}^d$ can be written as

$$\mathfrak{D}_{ij}^d \mathfrak{D}_{ij}^d = \frac{1}{6}(S^2 S^2 + \Omega^2 \Omega^2) + \frac{2}{3}S^2 \Omega^2 + 2IV_{S\Omega}, \quad (3.80)$$

where

$$S^2 = \overline{S}_{ij}\overline{S}_{ij}, \quad \Omega^2 = \overline{\Omega}_{ij}\overline{\Omega}_{ij}, \quad IV_{S\Omega} = \overline{S}_{ik}\overline{S}_{kj}\overline{\Omega}_{jl}\overline{\Omega}_{li}.$$

Nicoud and Ducros (1999) calculated the value of C_w by using the isotropic homogeneous theory and suggested the the model coefficient C_w should be in the range of $0.50 \sim 0.60$. This model have shown promising features including the correct asymptotic near-wall behaviour (y^3) of ν_{sgs} , the correct prediction of SGS dissipation and relatively a straight forward implementation for unstructured grids.

Recently, Huang and Li (2010) combined WALE model with the one-equation model proposed by Kajishima and Nomachi (2006). The one-equation model (Kajishima and Nomachi, 2006) is based on the treatment of production of SGS kinetic energy and energy loss in grid-scale portion with different mechanisms. This treatment is claimed to be more reasonable as compared to the assumption of the local equilibrium between the SGS production and the SGS dissipation, as employed by all algebraic SGS models. The algebraic SGS model relates the SGS stress to the strain-rate of large scales through a scaler quantity i.e. SGS viscosity ν_{sgs} .

3.4.3 LES validation

The fully-developed turbulent channel flow is simulated with two SGS models: the dynamic Smagorinsky and WALE models. Run time memory requirement for the WALE model is found to be 25% more than the dynamic model while computational cost for both models is approximately the same. For the dynamic model, the explicit test filtering is applied only in the homogeneous directions (the streamwise and spanwise directions) in order to avoid any errors arising from lack of commutativity of differentiation and filtering in the inhomogeneous (wall-normal) direction. LES simulations were performed at four different Reynolds num-

3.4. LARGE EDDY SIMULATION (LES)

bers: $Re = 2800, 6900, 11000$ and 20720 . These Reynolds numbers correspond to $Re_\tau = 180, 395, 590$, and 1020 respectively. Simulation parameters detail is shown in Table 3.4. Results from LES simulations were compared with the available DNS data. The LES results give good agreement with the DNS data.

Simulation	Re	$L_x \times L_z$	$N_x \times N_y \times N_z$	Δx^+	Δz^+	Δy_{min}^+	Δy_{max}^+
Present	2800	20×4	$128 \times 64 \times 64$	28.2	11.3	1.0	11.1
Moser et al. (1999)	2800	12×4	$128 \times 129 \times 128$	16.8	5.6	0.4	5.8
Present	6900	7×4	$128 \times 128 \times 144$	21.6	10.9	1.0	12.5
Moser et al. (1999)	6900	$2\pi \times \pi$	$256 \times 192 \times 192$	10	6.5	-	6.5
Present	11000	6×4	$128 \times 128 \times 256$	27.7	9.2	1.0	20.9
Moser et al. (1999)	11000	$2\pi \times \pi$	$384 \times 257 \times 384$	9.7	4.8	-	7.2
Present	20720	6×4	$256 \times 192 \times 384$	23.9	10.6	0.9	25.6
Abe et al. (2004)	20720	12.8×6.0	$2048 \times 384 \times 1536$	6.38	4.25	0.15	7.3

Table 3.4: Simulation parameters for LES calculations

It is well known that the shear stress has a limiting behaviour of y^3 , and a good SGS model should have the correct limiting behaviour of the SGS viscosity. The limiting behaviour for the dynamic model and the WALE model is plotted in Figure 3.9. Both models show approximately the correct behaviour of SGS viscosity. Nicoud and Ducros (1999) suggested that the value of C_w should be constant for isotropic turbulence. In the present study, different values for C_w were chosen to determine its effect on correct wall shear stress prediction. It is found that at relatively high Reynolds number ($Re_\tau = 1020$), the value of constant needs to be increased from 0.60 to 0.75 to produce correct wall shear stress prediction. For the turbulent channel flow, a linear relation of C_w with Re_τ can be calculated from the least square method and is given as

$$C_w = c_1 Re_\tau + c_2, \quad (3.81)$$

where $c_1 = 2.4 \times 10^{-4}$, $c_2 = 0.5$.

Test simulations were performed from both dynamic and WALE model for temporal acceleration. Linear relationship in Equation 3.81 is used to increase C_w during the

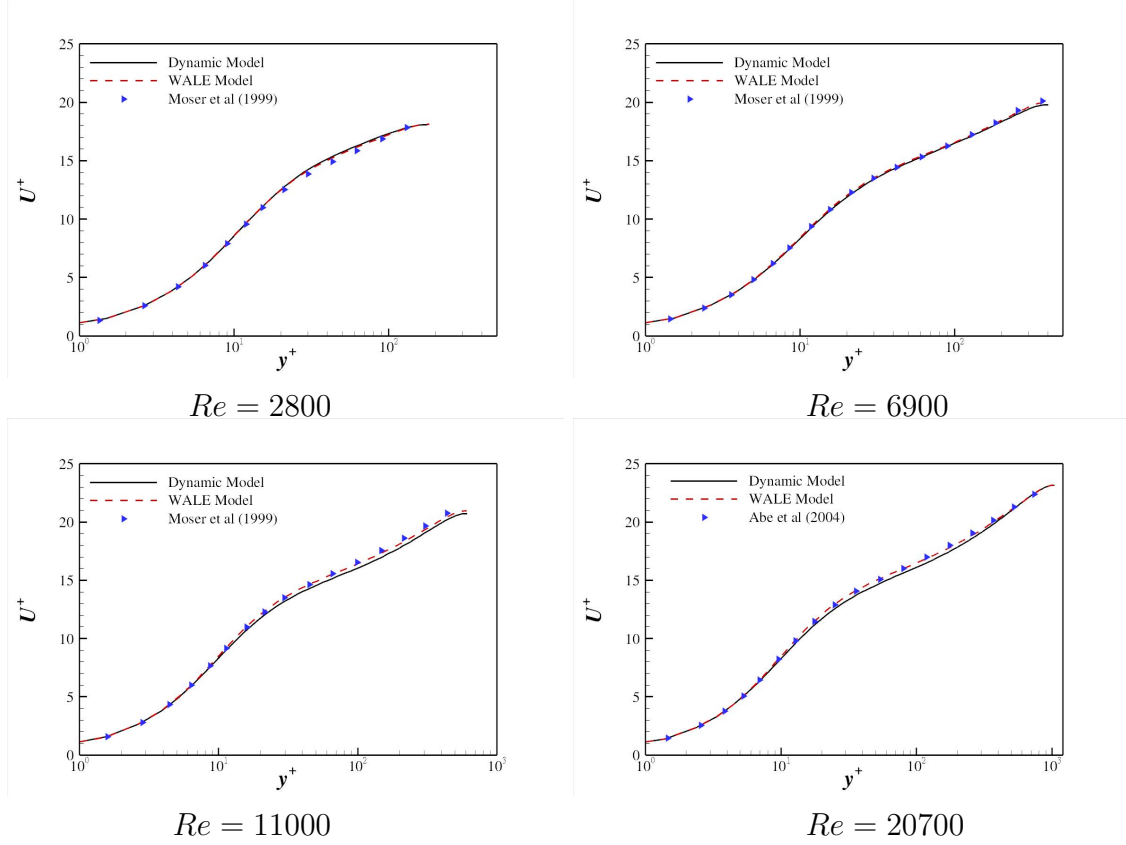


Figure 3.7: Comparison of log-law profiles for the dynamics and WALE models at several Reynolds numbers for fully-developed turbulent channel. Data from Moser et al. (1999) and Abe et al. (2004) are included for comparison.

acceleration. WALE model required approximately 8 Gigabytes of run time memory as compared to 6 Gigabytes for dynamic model. The results from both models were compared with the DNS data and are shown in Appendix A. Dynamic SGS model exhibits a better agreement with the DNS data moreover the run time memory requirement for dynamic model is less as compared to the WALE model. Therefore, dynamic SGS model is selected for LES in the present study.

3.4. LARGE EDDY SIMULATION (LES)

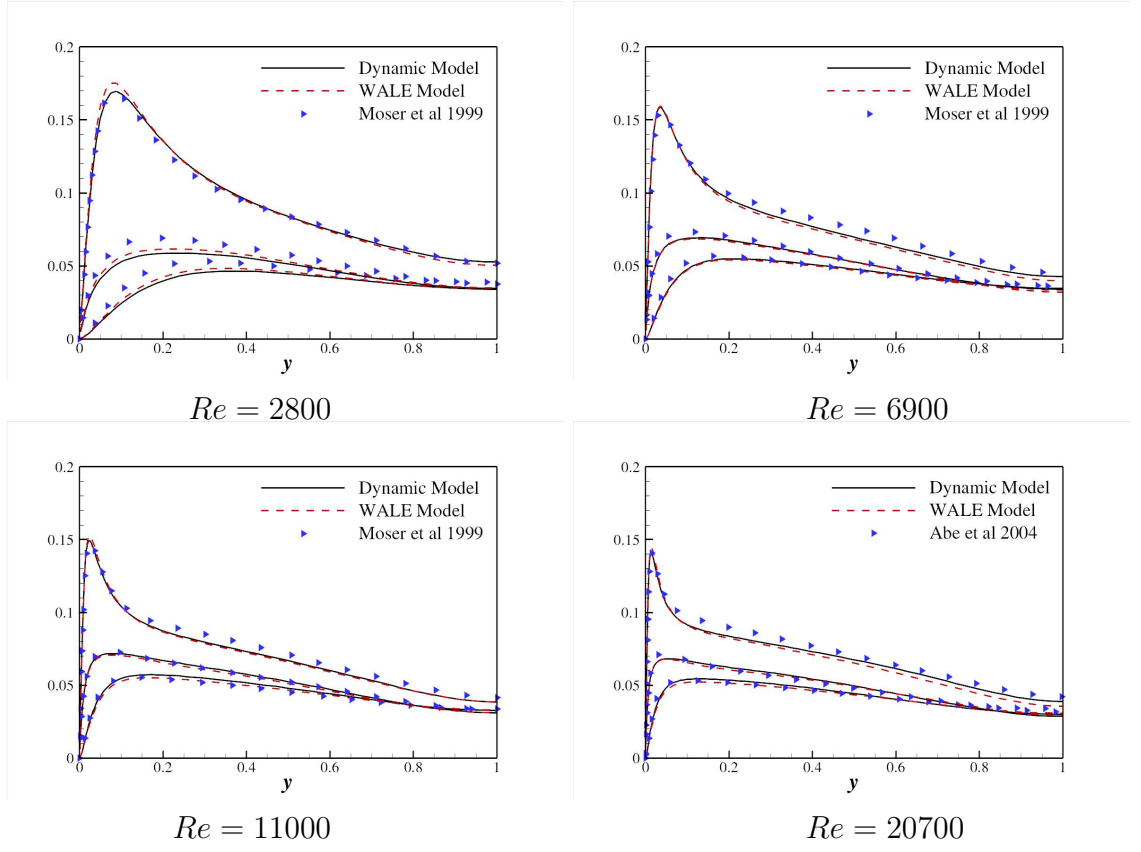


Figure 3.8: Comparison of rms velocity fluctuations for dynamics and WALE models at several Reynolds numbers for fully-developed turbulent channel. Data from Moser et al. (1999) and Abe et al. (2004) are included for comparison.

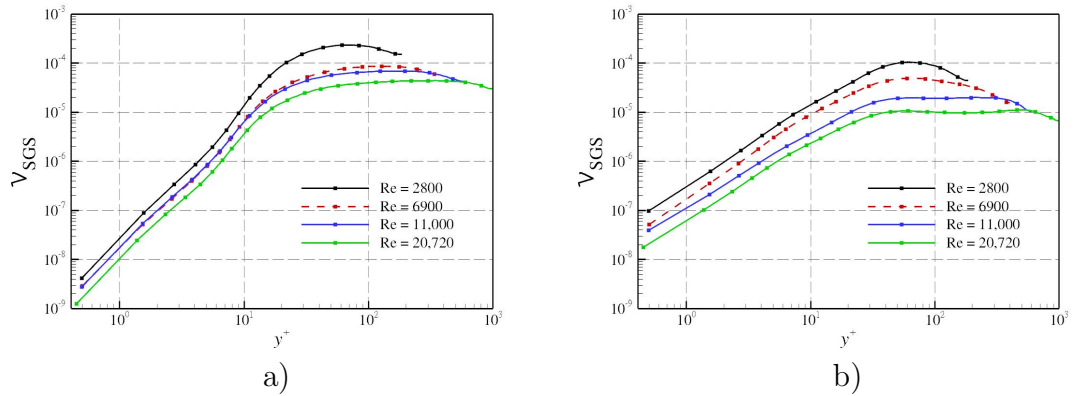


Figure 3.9: Limiting behaviour of the SGS viscosity at several Reynolds numbers from a) the dynamic model, and b) the WALE model.

Re_τ	Case-1		Case-2		Case-3		Re
	C_w	Re_τ	C_w	Re_τ	C_w	Re_τ	
180	0.50	180	0.55	178	0.6	175	2800
395	0.55	394	0.60	392	0.65	389	6900
590	0.60	600	0.65	596	0.70	592	11000
1020	0.60	1042	0.75	1022	0.85	1006	20700

Table 3.5: Re_τ variations for different values of WALE constant (C_w) for fully-developed turbulent channel flow at several Reynolds number.

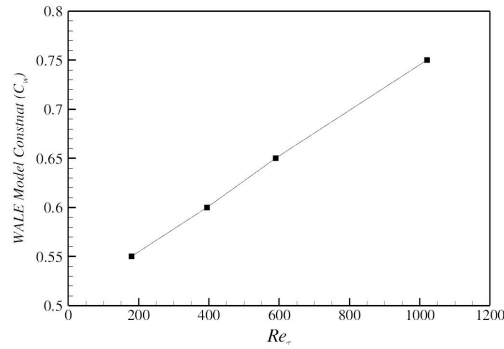


Figure 3.10: Relationship of C_w with Re_τ .

4

Preliminary Simulations.

4.1 Simulations details

Transient turbulent flow has been investigated in the past mainly by experiments. There have been some CFD with turbulence modelling, but there is no DNS study for temporal acceleration until now to study the near-wall turbulent structures response. The present study uses DNS and LES to simulate turbulent channel flows subjected to constant acceleration/deceleration. In the present chapter the details of preliminary simulations performed for constant acceleration case is presented, while the details of simulations for constant deceleration are presented in Chapter 8.

4.1.1 Acceleration parameter

The non-dimensional acceleration parameter for the present study is given as:

$$f = \frac{dU_m^*}{dt^*}, \quad (4.1)$$

where U_m^* and t^* are the non-dimensional bulk-mean velocity and time respectively, and f is the acceleration parameter. The experimental parameters of pipe experiments conducted by He and Jackson (2000) are used in the present numerical calculations. The acceleration parameter used by He and Jackson (2000) was defined as:

$$\gamma = \frac{D}{u_{\tau 0}} \left(\frac{1}{U_{m0}} \frac{dU_m}{dt} \right), \quad (4.2)$$

where, U_m and D is the bulk-mean velocity and the pipe diameter respectively, and the subscript 0 indicates the initial value. In this study, all the variables are non-dimensionalised by the initial bulk-mean velocity (U_{m0}) and the channel half-height (h). With this non-dimensionalisation, Equation 4.2 can be rewritten as:

$$\begin{aligned} \gamma &= \frac{U_{m0}}{u_{\tau 0}} \frac{2h}{U_{m0}} \left(\frac{1}{U_{m0}} \frac{dU_m}{dt} \right), \\ &= 2 \frac{U_{m0}}{u_{\tau 0}} \left(\frac{d(U_m/U_{m0})}{d(tU_{m0}/h)} \right), \\ &= 2 \frac{Re_{m0}}{Re_{\tau 0}} \left(\frac{dU_m^*}{dt^*} \right). \end{aligned}$$

Finally, γ can be written as follows

$$\gamma = 2 \frac{Re_{m0}}{Re_{\tau 0}} f. \quad (4.3)$$

It can be easily shown that for $\gamma = 6.1$ used in experiments, the corresponding f value is equal to 0.2 ($Re_{m0} = 3500$ corresponding to $Re_{m0} = 7000$ in the pipe exper-

4.1. SIMULATIONS DETAILS

iments and $Re_{\tau 0} \approx 215$). The corresponding reference time used in the simulations is h/U_{m0} and this corresponds to 0.184 sec in the pipe experiment. The total time taken for the acceleration in the experiment for $\gamma = 6.1$ was 5 sec, which corresponds to the acceleration time of $\xi = 27.2$ in the present study, where $\xi = t^*$.

The Navier-Stokes equations for the temporal acceleration are given as:

$$\frac{\partial u_i}{\partial x_i} = 0, \quad (4.4)$$

$$\frac{\partial u_i}{\partial t} + \frac{\partial}{\partial x_j} (u_i u_j) = -\frac{\partial p}{\partial x_i} + \frac{1}{Re} \frac{\partial^2 u_i}{\partial x_j \partial x_j} - \frac{\partial}{\partial x_j} \tau_{ij} + P_x \delta_{i1}, \quad (4.5)$$

where P_x is the mean-pressure gradient (note that p contains only the fluctuating component). Equations 4.4 and 4.5 are solved using a second-order accurate, fully implicit method. Details of the numerical method are given in Chapter 3. The mean pressure gradient was carefully updated at each time step so that the mass flow rate changes according to the prescribed rate (determined by f). The acceleration parameter is set to be $f = 0$ for a steady turbulent flow, and f has a positive value when the flow is accelerated.

In fully-developed turbulent channel flow, either the mass flow rate or the mean pressure gradient is kept constant. In case of constant mass flow rate calculations, the mass flow rate is kept constant by allowing small variations in the mean pressure gradient, P_x , such that the instantaneous mean pressure gradient value fluctuates around the time averaged mean pressure gradient value. The mean pressure gradient P_x , is calculated at each time step by the force balance between wall shear stress and the total pressure gradient (ΔP). In case of temporal acceleration, the mean pressure gradient is increased by adding f term. The inclusion of f term increases the bulk-mean velocity linearly in time, resulting in a subsequent increase in u_τ and mean pressure gradient values.

Figure 4.1a shows the variation of the bulk-mean velocity during the temporal acceleration for the three cases shown in Table 4.3. Constant linear acceleration was

achieved for all the cases considered in the present study, whereas He and Jackson (2000) reported some difficulties to achieve linear acceleration for the fastest acceleration case ($\gamma = 15.3$ or $f = 0.5$ case) due to mechanical limitations of the hydraulic valve. The time histories of the mean pressure gradient, during the temporal acceleration in Figure 4.1b, show that the mean pressure gradient increases all the time during the acceleration, however the rate of change of the mean pressure gradient is rather complex due to nonlinear response of u_τ .

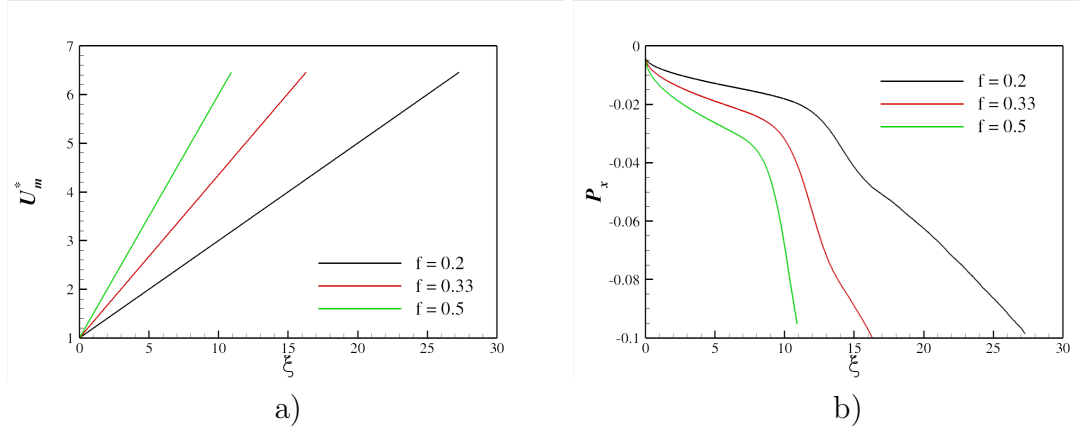


Figure 4.1: Time histories of a) the bulk-mean velocity, and b) the mean pressure gradient, during the constant acceleration for three f values tabulated in Table 4.3.

4.1. SIMULATIONS DETAILS

4.1.2 Simulation parameters

DNS is performed by using approximately 190 million grid cells. The initial and final Reynolds numbers of the simulation are $Re_0 = 3500$ and $Re_f = 15000$, respectively. The final Reynolds number was chosen from the preliminary grid independence test. Tables 4.1 and 4.2 show the simulation parameters and grid resolutions used for the present DNS study. $f = 0.2$ was used in the present DNS and this value corresponds to $\gamma = 6.1$ case used in the experiments by He and Jackson (2000).

$L_x \times L_y \times L_z$	Re_0	Re_f	f	T_e	$dRe/d\xi$	γ
$12h \times 2h \times 4h$	3500	15000	0.20	16.4	700	6.1

Table 4.1: Simulation parameters used in DNS for temporal acceleration. T_e , Re_0 and Re_f correspond the total time, the initial and final Reynolds numbers respectively.

$L_x \times L_y \times L_z$	$N_x \times N_y \times N_z$	Δx^+	Δy_{min}^+	Δy_{max}^+	Δz^+
$12h \times 2h \times 4h$	$768 \times 384 \times 640$	12.5	0.4	9.7	5.0

Table 4.2: DNS grid resolutions used in the present study. Please note that the grid resolution is calculated on the basis of the final u_τ value for steady turbulent case *i.e.*, $Re_\tau = 800$ for $Re_f = 15000$.

Simulation was started with the fully-developed turbulent channel flowfield at $Re = 3500$. The initial data are in very good agreement with the DNS of Kim et al. (1987). Five temporally independent realisations were performed in order to take ensemble averaging at each time instance. An increase in number of realisations also increases the solution independence from the initial conditions. Total sampling of data at each time location in the wall-normal direction comprises of information from approximately 5 million grid cells. The spatial averaging is performed in the streamwise and spanwise directions due to flow homogeneity, and as well as over top and bottom halves of channel due to flow symmetry.

The effect of various acceleration parameter values was studied using LES. Tables 4.3 and 4.4 show the simulation parameters for the present LES. The final Reynolds number was increased to $Re_f = 22600$ in LES, same as in He and Jackson (2000), as compared to $Re_f = 15000$ used in DNS. LES calculations were performed at three f values in order to determine the effect of different acceleration rates. Approximately 40 million grid points were used in the present LES.

$L_x \times L_y \times L_z$	Re_0	Re_f	f	T_e	$dRe/d\xi$	γ	Maximum K
$12h \times 2h \times 4h$	3500	22600	0.20	27.3	700	6.1	1.42×10^{-6}
$12h \times 2h \times 4h$	3500	22600	0.33	16.3	1170	10.3	1.57×10^{-6}
$12h \times 2h \times 4h$	3500	22600	0.50	10.9	1750	15.3	1.73×10^{-6}

Table 4.3: Simulation parameters used in LES for temporal acceleration. Captions same as of Table 4.1.

The LES grid resolution in the homogeneous directions were about twice the DNS grid spacing. Please note that the grid resolution was calculated at the final Re number and the grid resolution during acceleration would be always finer than this final resolution. Dynamic subgrid-scale model (Germano et al., 1991; Lilly, 1992) was used to account for unresolved SGS stresses. The test filtering was applied in the homogeneous directions (the streamwise and spanwise directions) only.

$L_x \times L_y \times L_z$	$N_x \times N_y \times N_z$	Δx^+	Δy_{min}^+	Δy_{max}^+	Δz^+
$12h \times 2h \times 4h$	$512 \times 192 \times 384$	25.7	1.0	27.5	11.4

Table 4.4: LES grid resolutions used in the present study. Please note that the grid resolution is calculated on the basis of the final u_τ value for steady turbulent case *i.e.*, $Re_\tau = 1100$ for $Re = 22600$.

In order to study the differences between steady and unsteady flows, steady turbulent channel DNS/LES calculations were performed at several Reynolds numbers. Table 4.5 shows the grid resolutions for steady simulations. For LES calculations, the same grid is used for all the steady simulations.

4.1. SIMULATIONS DETAILS

DNS/LES	Re	Re_τ	$N_x \times N_y \times N_z$	Δx^+	Δy_{min}^+	Δy_{max}^+	Δz^+
DNS	6900	390	$256 \times 192 \times 288$	9.2	0.4	9.6	5.4
DNS	11000	590	$384 \times 256 \times 480$	9.2	0.4	11	4.9
DNS	15000	780	$384 \times 384 \times 640$	12.5	0.4	9.7	5.0
LES	7000	400	$256 \times 192 \times 384$	9.5	0.26	7.6	4.2
LES	9000	500	$256 \times 192 \times 384$	11.7	0.33	9.4	5.2
LES	12000	650	$256 \times 192 \times 384$	15.2	0.42	12.2	6.8
LES	15000	780	$256 \times 192 \times 384$	18.3	0.52	14.7	8.1
LES	17000	880	$256 \times 192 \times 384$	20.6	0.58	16.6	9.2
LES	20000	1015	$256 \times 192 \times 384$	23.8	0.67	19.1	10.6
LES	22600	1100	$256 \times 192 \times 384$	25.7	1.0	27.5	11.4

Table 4.5: Simulation parameters for steady turbulent DNS/LES. Domain size of $6h \times 2h \times 4h$ is used for all the simulations.

4.2 Domain size test

The size of the computational domain is an important parameter in the turbulent channel flow simulation. The size should be large enough in case of periodic boundary conditions that there is no effect of periodicity of the domain on the flow solutions. Jimenez and Moin (1991) studied the turbulent channel flow to determine the size of minimal flow unit in the streamwise and spanwise directions, which would sustain acceptable turbulence level in the near-wall region ($y^+ \leq 40$). It was found that the minimum size of the computational box should be in the range of $L_x^+ \approx 250 \sim 350$ in the streamwise direction and $L_z^+ \approx 100$ in the spanwise direction. Flow relaminarisation and decay of turbulence intensity was observed for sizes below the critical sizes.

Table 4.6 shows the domain sizes used for the numerical investigations of turbulent channel flow at several Reynolds numbers in the previous studies. It is clear from the table that domain size of approximately 12 is used in streamwise direction for $Re = 2800$, while relatively smaller domain size is employed at higher Reynolds numbers calculations. This is partly due to the decrease in size of the near-wall structures at higher Reynolds numbers.

Reference	$L_x \times L_z$	Re_τ	$L_x^+ \times L_z^+$
Kim et al. (1987)	$4\pi \times 4\pi/3$	180	2260×750
Abe et al. (2001)	12.8×6.4	180	2304×1152
Rai et al. (1991)	$4\pi \times 4\pi/3$	180	2260×750
Chung (2005)	$4\pi \times 4\pi/3$	180	2260×750
Moser et al. (1999)	$2\pi \times \pi$	395	2480×1240
Abe et al. (2001)	6.4×3.2	395	2528×1264
Moser et al. (1999)	$2\pi \times \pi$	590	3700×1850
Abe et al. (2001)	6.4×3.2	640	4096×1280
Abe et al. (2004)	12.8×6.4	1020	13056×6528

Table 4.6: Computational domain sizes used for turbulent channel flow simulations.

A parametric study was conducted using LES to study the effect of length of com-

4.2. DOMAIN SIZE TEST

putational domain for turbulent channel flow subjected to temporal acceleration. Three lengths of the domain were selected as shown in Table 4.7. Computations were performed for the three acceleration cases (cf. Table 4.3) to determine the sensitivity of domain size with respect to acceleration rate.

Case	$L_x \times L_y \times L_z$	$N_x \times N_y \times N_z$	Δx^+	Δy_{min}^+	Δy_{max}^+	Δz^+
Case-1	$6h \times 2h \times 4h$	$256 \times 192 \times 384$	25.7	1.0	27.5	11.4
Case-2	$12h \times 2h \times 4h$	$512 \times 192 \times 384$	25.7	1.0	27.5	11.4
Case-3	$18h \times 2h \times 4h$	$768 \times 192 \times 384$	25.7	1.0	27.5	11.4

Table 4.7: Domain sizes used in the domain size test.

Figure 4.2 shows the time histories of Re_τ during the acceleration for the three domains. It is clear that the sudden increase in Re_τ value towards the middle stage of the acceleration ($Re \approx 12000$) for $f = 0.20$ is delayed for case-1 (the shortest domain considered), while negligible difference is observed between case-2 and case-3 domains. It is interesting to note that the difference between case-1 and case-2 domains increases with increase in acceleration rate, as clearly seen in Re_τ history graphs for $f = 0.33$ and $f = 0.50$.

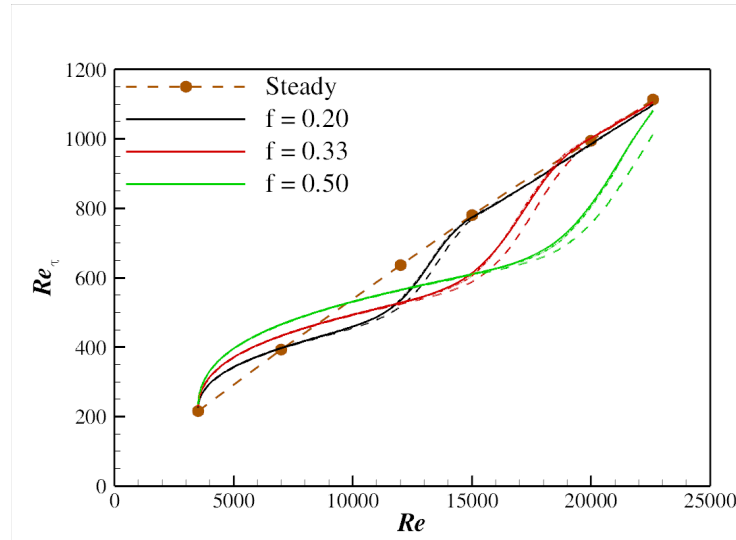


Figure 4.2: Comparison of Re_τ histories for the domain sizes. Dashed lines denote length case-1 results while solid lines denote case-2 and dashed-dot-dot lines denote case-3 results.

Figures 4.3 and 4.4 show comparison of the rms velocity fluctuations for the three domains for $f = 0.20$ and $f = 0.50$ respectively. u_{rms} profiles show negligible difference between the three domains for $f = 0.20$, while v_{rms} and w_{rms} are significantly smaller in the near-wall region for case-1 at $Re = 12000$. The suppression of v_{rms} and w_{rms} is even more significant in the near-wall region for the fastest acceleration ($f = 0.5$) case considered in the present study, as shown in Figure 4.4. It is clear from this test that the small domain length ($L = 6h$) results in a significant suppression of turbulent intensities in the near-wall region. This turbulence suppression increases with increase in acceleration rate. Jimenez and Moin (1991) also reported the turbulence decay for small domain size. Based on the results shown, domain length of $L = 12h$ is used in the present study.

4.2. DOMAIN SIZE TEST

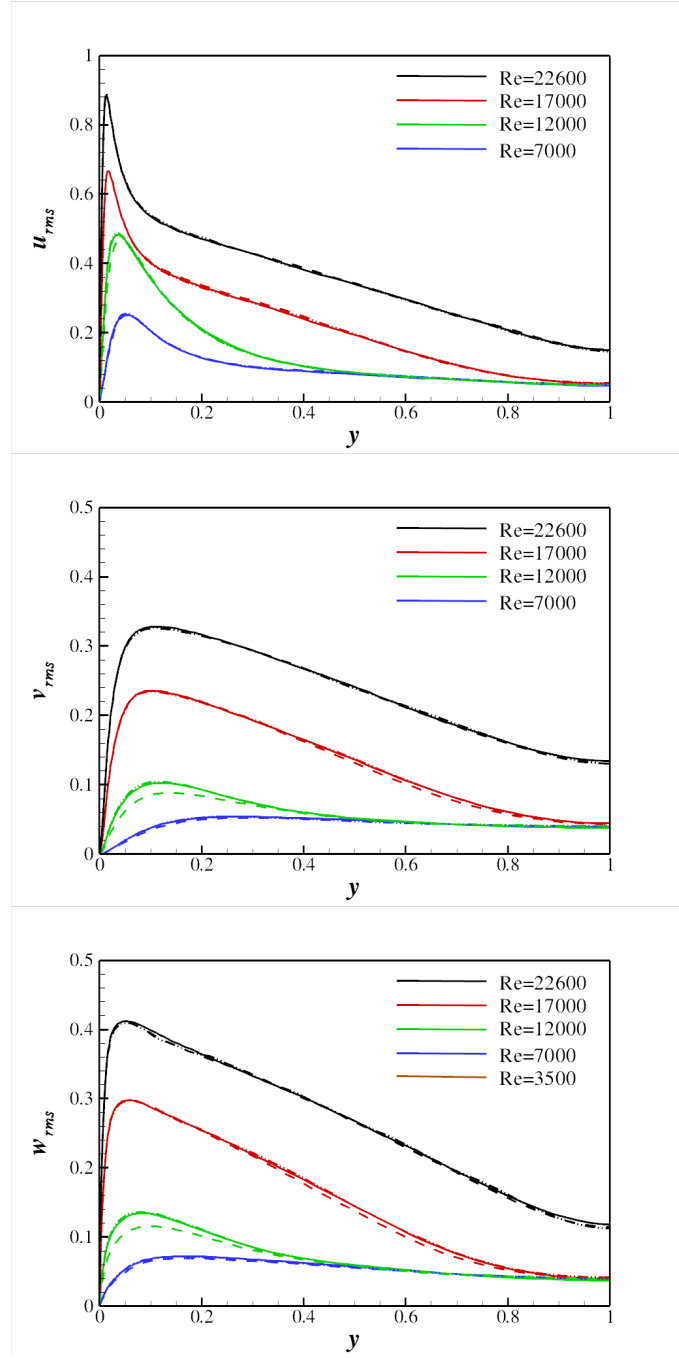


Figure 4.3: Comparison of the rms velocity fluctuations at several Reynold numbers for $f = 0.2$. Dashed lines denote length case-1 results while solid lines denote case-2 and dashed-dot-dot lines denote case-3 results.

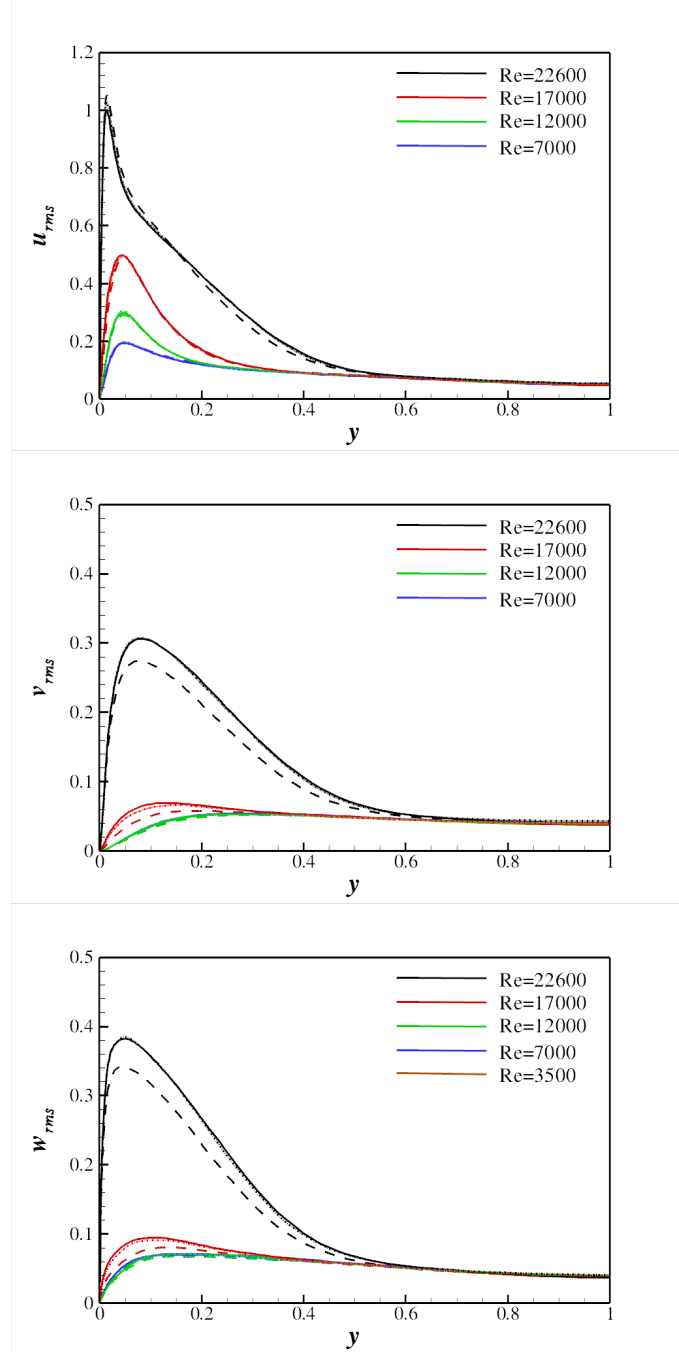


Figure 4.4: Comparison of the rms velocity fluctuations at several Reynold numbers for $f = 0.5$ case. For figure captions, see Figure 4.3.

4.3 Time step size test

The time step size is an important parameter for the numerical simulation of unsteady turbulent flows. The time step size has a dual effect namely; numerical stability and numerical accuracy. Time step size restriction in terms of numerical stability comes from the temporal discretisation scheme as well as the grid used in the simulation. Flow configurations involving sharp velocity field gradients require a very fine grid to capture flow physics accurately. This, in turn, restricts the time step size considerably, if an explicit time advancement scheme is used. The numerical stability is associated with the viscous and convective terms in the Navier-Stokes equations. The stability criterion associated with the non-linear term is known as Courant, Friedrich and Lewy (CFL) condition, which is given as

$$\Delta t \leq \left[\frac{|U|}{\Delta x} + \frac{|V|}{\Delta y} + \frac{|W|}{\Delta z} \right]^{-1}.$$

This condition should be satisfied for numerical methods using explicit time advancement for the convective terms. The stability criterion associated with the diffusion term is known as viscous stability and is given as

$$\Delta t \propto \left[\frac{1}{\Delta x^2} + \frac{1}{\Delta y^2} + \frac{1}{\Delta z^2} \right]^{-1}.$$

Most numerical methods commonly employ implicit treatment such as Crank-Nicolson for the viscous terms due to its linearity while explicit treatment like Runge-Kutta or Adams-Bashforth for the convective terms. Moin and Mahesh (1998) illustrated the effects of time advancement on the error at different scales by the von Neumann analysis and concluded that smaller scales are more sensitive to the time step size. Fully implicit schemes are more useful in those situations where the discrete equations represent frequencies significantly larger than those required by the flow

physics. One example of such flow is the DNS study of flow over riblets (Choi and Moin, 1993), where approximately 5 fold CPU savings were achieved using a fully implicit solver.

The time step size for any turbulent flow is also restricted in terms of numerical accuracy by the size of turbulent eddies. The time step size should be small enough to capture the motion of the smallest turbulent scales. The smallest eddy scales require a time step size to be of the order of Kolmogorov time scale (t_k) which is the ratio of the kinematic viscosity and the viscous dissipation and is given by:

$$t_k = \left[\frac{\nu}{\varepsilon} \right]^{\frac{1}{2}},$$

where the viscous dissipation can be approximated as

$$\varepsilon \approx \frac{u_\tau^2 U_m}{\delta}.$$

Therefore, Kolmogorov time scale can be approximated as

$$t_k \approx \frac{\delta}{u_\tau} Re_m^{-1/2}.$$

The time step size can also be determined by the flow physics. As the smallest scales are usually present in the near wall region of the turbulent flow, this time scale is defined in terms of wall units *i.e.*, ν/u_τ^2 . A larger time step can result in incorrect solutions as demonstrated by Choi and Moin (1994). They used the fully implicit time integration scheme with Newton-Raphson iteration method to decouple velocity variables and simulated unsteady turbulent channel with $\Delta t^+ = \Delta t u_\tau^2 / \nu = 0.2, 0.4, 0.8, 1.2, 1.6$ and 2. The flow relaminarisation was observed for larger time step sizes. It was found that $\Delta t^+ \leq 0.4$ gives accurate prediction of velocity fluctuations. Δt^+ criteria provides the limit of time step in

4.3. TIME STEP SIZE TEST

terms of numerical accuracy.

A few numerical studies of transient turbulent flows has mentioned about the time step size used in their simulations. Howard and Sandham (2000) used a time step size of 0.001 in global units *i.e.*, $\Delta t = 0.001h/U_m$ for their DNS of skewed turbulent channel flow calculations. Coleman et al. (2009) used a time step size of 0.001 in initial wall units for their RANS calculations for laterally strained turbulent channel flow. Holstad et al. (2010) used a time step size $\Delta t^+ = \Delta t u_\tau^2/\nu = 0.013$. It is important to note that in all these numerical studies the bulk-mean Reynolds number is constant and lies in relatively low range *i.e.*, from $Re = 2800$ to $Re = 7000$ based on the half-channel height and the bulk-mean velocity.

In the present study, a parametric study of a time step size is performed to make sure that the solution accuracy is not affected by the time step size. Table 4.8 shows the details of the simulations performed. Test simulations were performed with LES calculations for the slowest acceleration ($f = 0.20$) case considered in the present study. As the near-wall structures become smaller at higher Reynolds numbers, the time step size in global units should be reduced during the acceleration. In the present study, three ranges of the time step size variations were identified in terms of Reynolds number. Figure 4.5 shows the time histories for the turbulent kinetic energy (k) and the turbulent shear stress ($-\overline{uv}$). Please note that the time history is shown for the maximum value and the centreline value. It can be seen that the centreline time histories are largely insensitive to the different time step sizes used. Based on the above test simulations, $\Delta t = 0.003$ (or $\Delta t^+ \leq 0.1$) was chosen for Range-1 ($3500 < Re < 11000$), $\Delta t = 0.002$ (or $\Delta t^+ \leq 0.1$) for Range-2 ($11000 < Re < 17000$) and $\Delta t = 0.001$ (or $\Delta t^+ \leq 0.06$) for Range-3 ($17000 < Re < 22600$).

Range	Re_0	Re_f	Case-1	Case-2	Case-3
Range-1	3500	11000	0.001	0.003	0.005
Range-2	11000	17000	0.001	0.002	0.003
Range-3	17000	22600	0.0005	0.001	0.002

Table 4.8: Details of simulations for time step size parametric study.

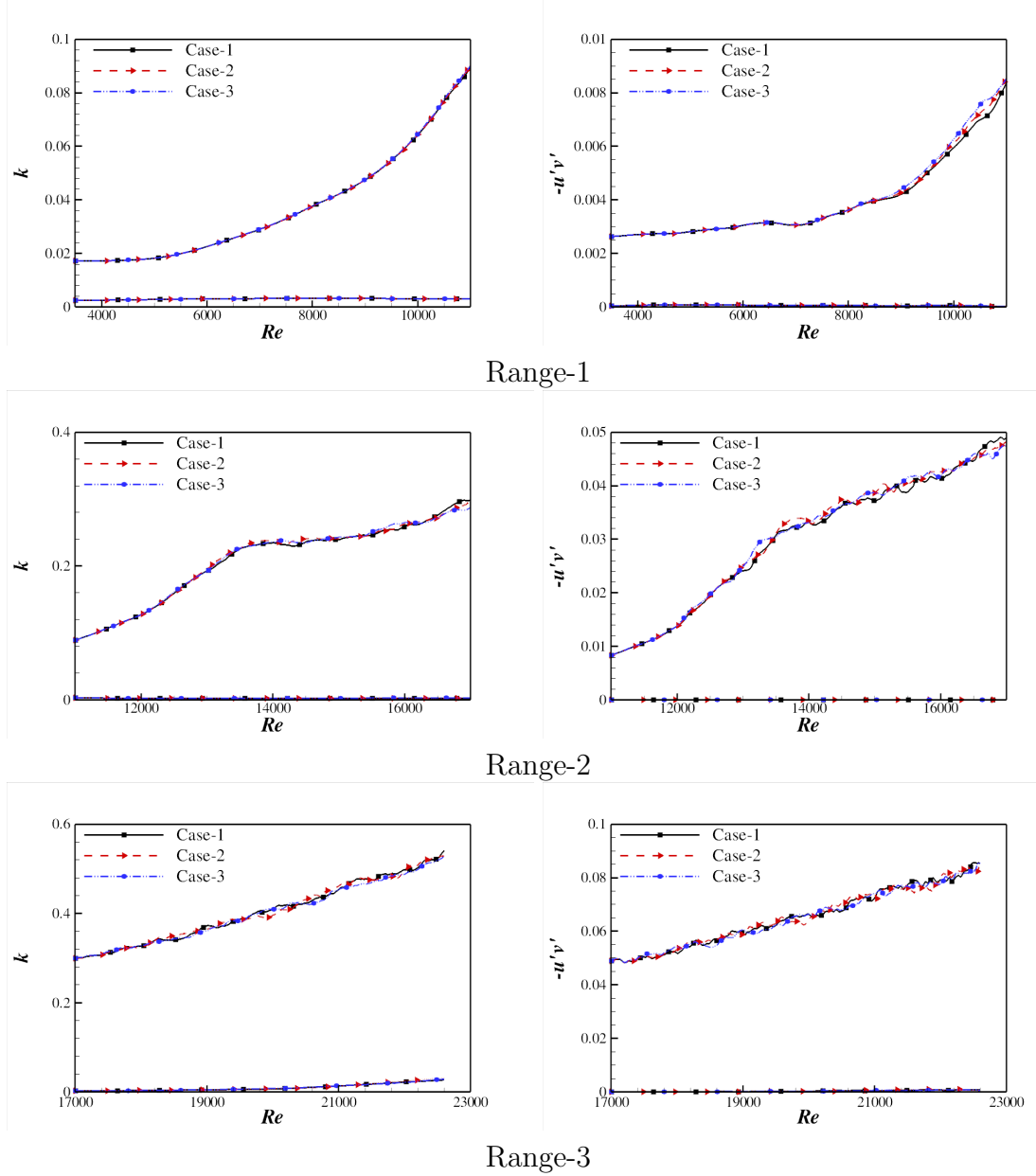


Figure 4.5: Time histories of the turbulent kinetic energy and turbulent shear stress for different cases. Time histories of maximum and centreline values are plotted.

4.4 Turbulent statistics

In case of turbulent channel flow, the turbulent statistics are averaged over the homogeneous directions (the streamwise and spanwise directions) as well as across the centreline due to flow symmetry. Turbulent statistics are averaged over time for fully-developed turbulent statistics calculation to achieve statistical convergence such that the averaged values does not change with the inclusion of new data. In the case of the channel flow subjected to temporal acceleration, time averaging can not be performed. Therefore, to improve the statistics and reduce the effect of initial conditions, ensemble averaging is performed over 5 realisations for DNS and 10 realisations for LES. In the coming subsection, turbulent kinetic energy budget analysis, Reynolds stress anisotropy tensor analysis and vortex identification method used in this study are briefly discussed.

Turbulent kinetic energy (TKE) budgets

The transport equations for Reynolds stress can provide a thorough insight into the turbulence behaviour for each stress component. The transport equations for the incompressible turbulent flow are given as

$$\frac{\partial \overline{u_i u_j}}{\partial t} + C_{ij} = P_{ij} + T_{ij} + \Pi_{ij} + \Phi_{ij} + D_{ij} + \varepsilon_{ij}. \quad (4.6)$$

Here

$$\begin{aligned} C_{ij} &= U_k \frac{\partial}{\partial x_k} \overline{u_i u_j}, \\ P_{ij} &= - \left(\overline{u_i u_k} \frac{\partial U_j}{\partial x_k} + \overline{u_j u_k} \frac{\partial U_i}{\partial x_k} \right), \\ T_{ij} &= - \frac{\partial}{\partial x_k} \overline{u_i u_j u_k}, \\ \Pi_{ij} &= - \frac{1}{\rho} \left(\frac{\partial}{\partial x_i} \overline{p u_j} + \frac{\partial}{\partial x_j} \overline{p u_i} \right), \end{aligned}$$

$$\Phi_{ij} = \frac{1}{\rho} \overline{p \left(\frac{\partial u_i}{\partial x_j} + \frac{\partial u_j}{\partial x_i} \right)},$$

$$D_{ij} = \nu \frac{\partial^2}{\partial x_k^2} \overline{u_i u_j},$$

$$\varepsilon_{ij} = -2\nu \overline{\frac{\partial u_i}{\partial x_k} \frac{\partial u_j}{\partial x_k}},$$

where C_{ij} , P_{ij} , T_{ij} , Π_{ij} , Φ_{ij} , D_{ij} and ε_{ij} denote the turbulent convection, production, turbulent transport, pressure-transport, pressure-strain correlation, viscous diffusion and viscous dissipation terms. Mansour et al. (1988) referred the sum of pressure-transport and pressure-strain as the velocity-pressure gradient term.

Figure 4.6 shows the turbulent kinetic energy budgets for \overline{uu} , \overline{vv} , \overline{ww} and $-\overline{uv}$. The DNS results are in good agreement with Moser et al. (1999). The area of interest in the case of turbulent budget terms is the near-wall region where most of turbulent activities occur. For \overline{uu} transport equation, the viscous dissipation at wall is balanced by the pressure-strain term. The production term increases sharply near the wall with maximum at $y^+ \approx 15$. The pressure-strain term decreases sharply from the wall to become negative and increases after reaching a local minimum. The turbulent transport term increases similarly as that of production initially before following the trend of the pressure-strain term. The pressure transport term is zero for \overline{uu} and the viscous dissipation is balanced by the the production term in the outer layer region.

The production term is zero in case of \overline{vv} and \overline{ww} transport equation as the energy is transferred from the mean flow to the near-wall turbulent structures through the \overline{uu} production term. In \overline{vv} budgets, the pressure transport and the pressure-strain terms balance each other in the very near-wall region while the pressure-strain term has positive contribution in the outer layer region and is balanced by the viscous dissipation term. The pressure-strain term is largely responsible for energy transfer from the streamwise component to the other two normal stress components. In \overline{ww}

4.4. TURBULENT STATISTICS

transport equation, the pressure-strain term and the viscous dissipation term are dominant terms making positive and negative contributions respectively. For off-diagonal component $-\overline{uv}$, the production term has negative contribution, which is balanced by the pressure-strain term.

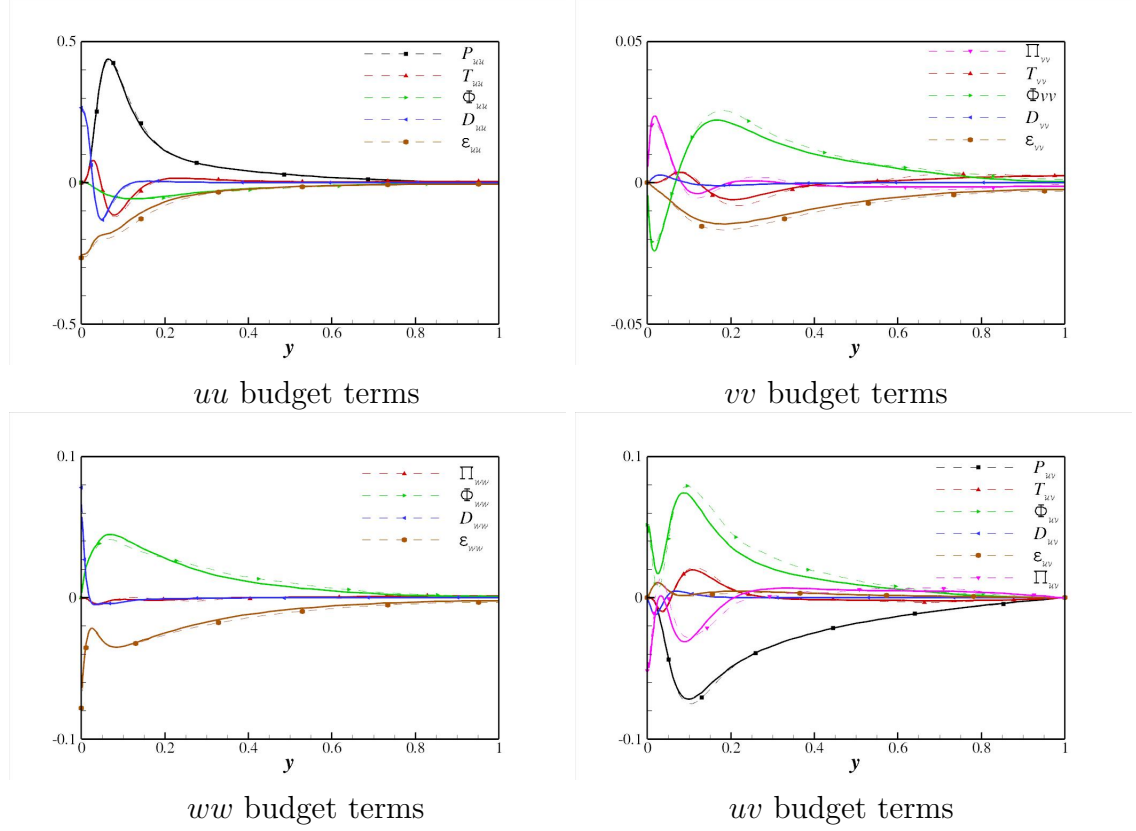


Figure 4.6: The Reynold stress budget profiles in wall units. Steady data (dashed lines with symbols) of Moser et al. (1999) are also included. u_τ^4/ν is used for normalisation.

Reynolds stress anisotropy tensor analysis

Turbulent anisotropy can be analysed through the use of the Reynolds stress anisotropy tensor (τ'_{ij}) (Lumley and Newman, 1977) which is given as:

$$b_{ij} = \frac{\tau_{ij}^a}{\tau_{kk}} = \frac{\overline{u'_i u'_j}}{2k} - \frac{\delta_{ij}}{3}, \quad (4.7)$$

where τ_{ij}^a and τ_{kk} is the anisotropic and isotropic parts of the Reynolds stress tensor respectively and k is the turbulent kinetic energy. The non-dimensional anisotropy tensor b_{ij} has zero trace and its second and third invariants are given as:

$$II = -\frac{1}{2}b_{ij}b_{ji}, \quad (4.8)$$

$$III = \frac{1}{3}b_{ij}b_{jk}b_{ki}. \quad (4.9)$$

In case of axisymmetric turbulence, b_{22} and b_{33} normal components becomes equal and the off-diagonal component must vanish *i.e.*, $b_{12} = 0$ and the invariants reduces to an axisymmetric relationship (Krogstad and Torbergsen, 2000).

$$III = \pm 2 \left(\frac{-II}{3} \right)^{3/2}. \quad (4.10)$$

Lee and Reynolds (1985) proposed a new parameter A to define the axisymmetric turbulence

$$A = \frac{III}{2(-II/3)^{3/2}}. \quad (4.11)$$

Equation 4.10 can be deduced from Equation 4.11 by substituting $A = \pm 1$. Lee and Reynolds (1985) proposed that $A = 1$ indicates the “rod-like” axisymmetric turbulence state which is represented by the dominance of the streamwise component b_{11} over the other two components. On the other hand, $A = -1$ indicates the “disk-like” axisymmetric turbulence state, which is encountered in case if the sum of b_{22}

4.4. TURBULENT STATISTICS

and b_{33} is greater than b_{11} . Two invariant functions are given by

$$F = 1 + 9II + 27III, \quad (4.12)$$

$$G = -(III/2)^2/(II/3)^3, \quad (4.13)$$

where F and G are the two-component and axisymmetric turbulence state parameters respectively. $F = 0$ indicates the two-component turbulence while $F = 1$ represents the isotropic turbulence. The two-component turbulence usually occurs in the viscous sublayer in case of fully-developed turbulent channel where the wall-normal fluctuations are suppressed due to splashing effect (Chung et al., 2002).

Lumley and Newman (1977) proposed the anisotropy invariant maps (AIM) for analysing the turbulent anisotropy. AIM are the cross plots of the invariant functions defined above *i.e.*, $-II$ and III and the bounds of AIM are well explained by Simonsen and Krogstad (2005), as shown in Figure 4.7 showing the different states of turbulence. Turbulence must exist within the bounds of AIM surrounded by three lines which defines the limits of all physically realizable turbulence. One-component turbulence exists where the contribution of the streamwise component is significantly higher than the sum of the other two components. Two-component turbulence exists in the region where contribution from one component is significantly smaller than the other two components. This turbulence state lies in the viscous sublayer where the wall-normal component is suppressed. The rod-like axisymmetric turbulence state exists in the outer layer region where the turbulent shear stress contribution is negligible and contributions from b_{22} and b_{33} are non-trivial. The isotropic turbulence state exists in the centreline region for the turbulent channel where all three normal stress components are approximately equal and shear stress is equal to zero.

Figure 4.8 shows the AIM for the fully-developed turbulent channel flow at several Reynolds numbers, *i.e.*, $Re = 3500, 6900, 11000$ and 15000 . It is clear from the

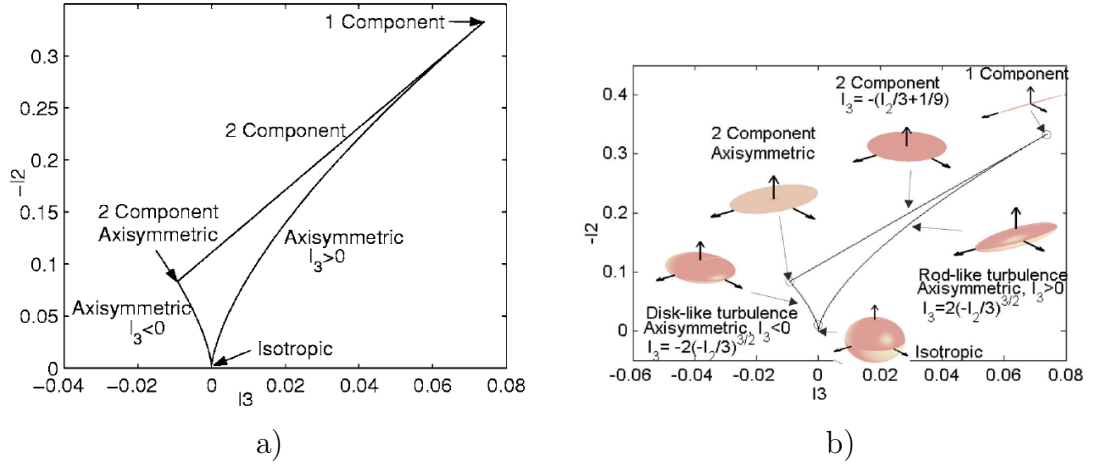


Figure 4.7: Anisotropy invariant map showing the limiting states of turbulence (Simonsen and Krogstad, 2005). The arrows in a) represent the turbulent fluctuations that correspond to each of the limiting states

figure that the near-wall turbulence in viscous sublayer exists in the two-component state due to suppression of the wall-normal stress component. The right hand corner value where the turbulent field is closest to the one-component state is indicative of viscous sublayer boundary (Chung et al., 2002). Turbulence shifts from two-component turbulence to the rod-like axisymmetric state in the buffer layer, and remains a little away from pure axisymmetric line (left lower line) due to the non-trivial turbulent shear stress contribution. As the distance from the channel wall increases and the contribution from the turbulent shear stress component decreases in the outer layer, turbulence becomes more axisymmetric and subsequently, acquires nearly an isotropic state at the channel centre. It is worth noting that the near-wall region becomes more isotropic with an increase in Reynolds number due to smaller near-wall structures at higher Reynolds numbers, resulting in a reduction in the viscous sublayer thickness (in global units). It is also worth mentioning that the distance from the axisymmetric line increases with an increase in Reynolds number which is indicative of an increase in turbulent shear stress contribution in the buffer layer at higher Reynolds numbers.

4.4. TURBULENT STATISTICS

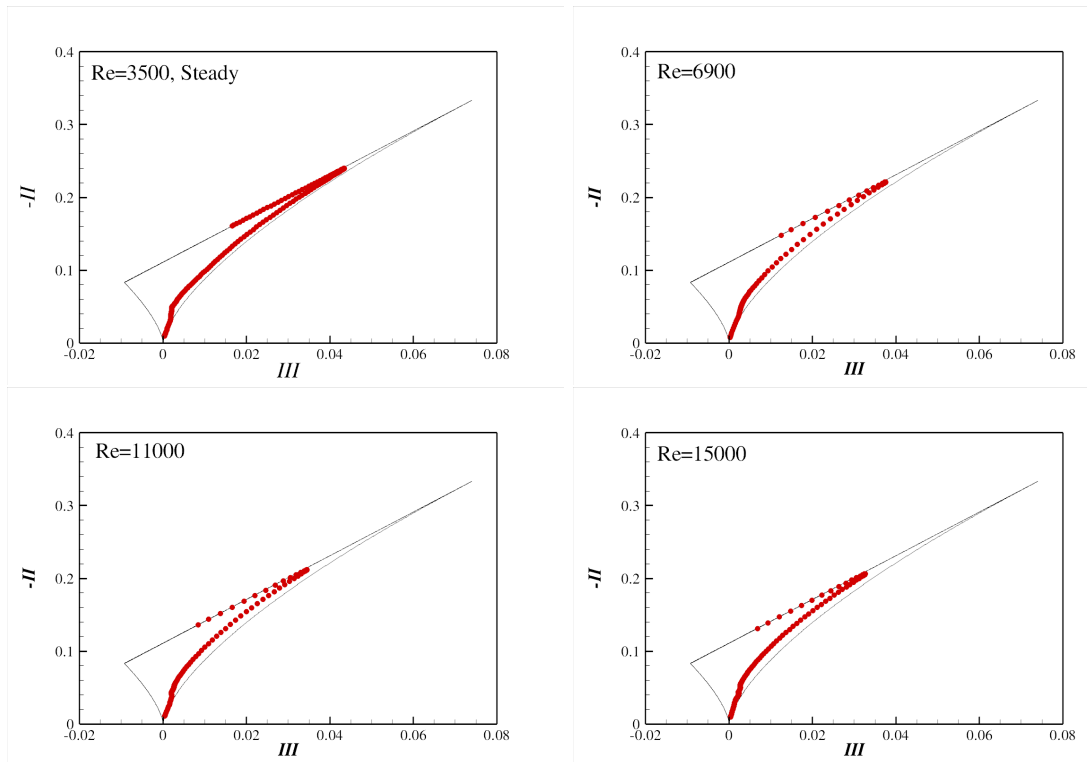


Figure 4.8: AIM for fully-developed turbulent channel flow at several Reynolds numbers.

Vortex identification

Vortex dynamics plays a crucial part in governing the turbulence physics. Substantial efforts have been put in order to define the vortex. Lugt (1979) proposed that a vortex is a multitude of material particle rotating around a common centre while Chong et al. (1990) proposed a more mathematical interpretation of a vortex as a region of complex eigenvalues of velocity gradient tensor (Δu). A comprehensive literature review of vortex identification methods is given in Jeong and Hussain (1995). It is well known that the turbulent shear flow contain spatially-coherent, temporally-evolving structures called *coherent structures* and that the evolution of these coherent structures is governed by the vortex dynamics. Many efforts have been made in the past to identify the coherent structures in turbulent shear flows which include pressure minimum, closed streamlines, and iso-vorticity as discussed by Jeong and Hussain (1995). They proposed a new method to identify coherent structures for the incompressible turbulent flow by using eigenvalues of the symmetric tensor $S^2 + \Omega^2$ where S and Ω are the symmetric and antisymmetric part of the velocity gradient tensor. It was suggested that the negative value for second eigenvalue of $S^2 + \Omega^2$, i.e λ_2 , gives the correct representation of the vortex core. λ_2 represents the local pressure minimum in a plane when the contribution of unsteady irrotational strains and viscous terms are discarded. Vortex geometry and topology are obtained by interconnecting the negative λ_2 values. This method is valid for low as well as high Reynolds numbers due to its ability to successfully capture the pressure minimum and the vortex core.

Jeong et al. (1997) used the λ_2 criteria to study the topology of coherent structures in the fully-developed turbulent channel. Figure 4.9 shows the near-wall coherent structures for the fully-developed turbulent channel at several Reynolds numbers. The iso-surfaces are plotted at the corresponding maximum value of λ_2' . Here “'” denote the rms fluctuations. The size of the near-wall structures decreases consid-

4.4. TURBULENT STATISTICS

erably with the increase in Reynolds number. Figure 4.10 shows the λ'_2 profiles for the fully-developed turbulent channel flow cases at several Reynolds numbers. The maximum λ'_2 in wall units is approximately 0.015 and its maximum wall-normal location is $y^+ \approx 20$.

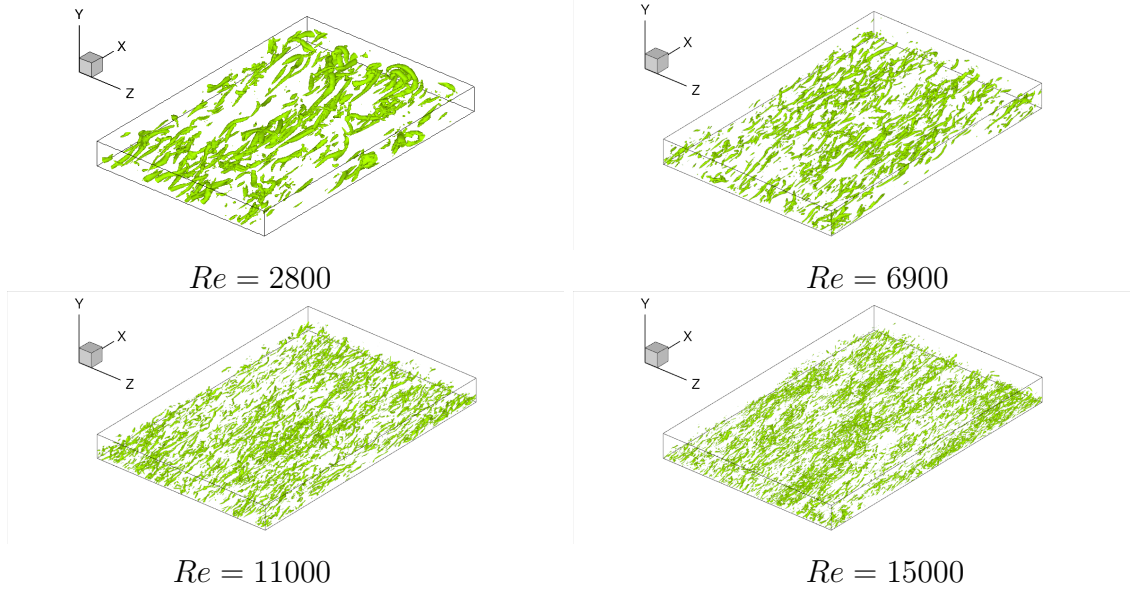


Figure 4.9: λ_2 plots for fully-developed turbulent channel flow at several Reynolds numbers.

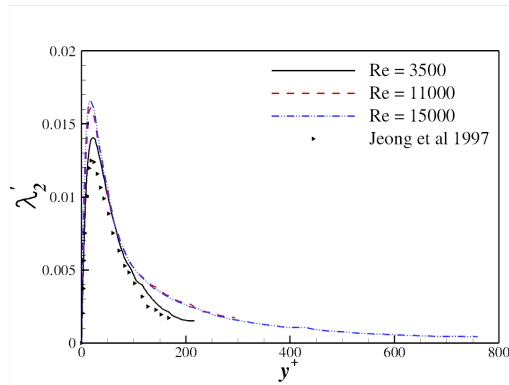


Figure 4.10: Profiles of rms λ_2 fluctuations at several Reynolds numbers.

5

DNS of Temporal Acceleration.

In this chapter, DNS results of a fully-developed turbulent channel subjected to constant temporal acceleration are presented. The effect of the imposed acceleration is clearly shown by comparing the results with the corresponding fully-developed turbulent flow statistics at four Reynolds numbers. The fully-developed turbulent flow simulations were performed at four Reynolds numbers: $Re = 3500, 6900, 11000$ and 15000 . The wall shear stress, mean velocity, rms fluctuations, turbulent kinetic energy budgets and quadrant analysis are discussed in detail.

5.1 Simulation parameters

DNS was performed for a fully-developed turbulent channel flow subjected to constant acceleration. The initial Reynolds number based on the bulk-mean velocity, U_{m0} , and the half-channel height, h , was $Re_0 = 3500$ (or $Re_\tau \approx 215$ based on the friction velocity), and the final Reynolds number was $Re_f = 15000$ (or $Re_\tau \approx 800$). He and Jackson (2000) conducted experimental investigation of a turbulent pipe flow subjected to constant temporal acceleration, in which the initial Reynolds number was $Re_0 = 3500$ and the final Reynolds number used was $Re_f = 22600$ (or $Re_\tau \approx 1100$). The acceleration parameter (f) was set equal to 0.2 in this study which is analogous to $\gamma = 0.61$ in the pipe experiment. Ensemble averaging was taken over 5 independent realisations to improve the flow statistics. The separation between each realisation is approximately $100 (tu_{\tau 0}^2/\nu)$. Simulation parameters used in the present DNS study are shown in Table 5.1.

$L_x \times L_y \times L_z$	$N_x \times N_y \times N_z$	Δx^+	Δy_{min}^+	Δy_{max}^+	Δz^+
$12h \times 2h \times 4h$	$768 \times 384 \times 640$	12.5	0.4	9.7	5.0

Table 5.1: Simulation parameters used in DNS based on $Re_\tau = 800$.

Initial condition

First, a DNS of steady channel flow at $Re = 3500$ was performed to provide the initial conditions for the main simulations. The mean velocity (U) and rms velocity fluctuations ($u_{i,rms}$) compared very well with the DNS results of Kim et al. (1987) for $Re_\tau = 180$. In Kim et al. (1987), $C_f = 8.18 \times 10^{-3}$ at $Re = 2800$; the displacement and momentum thickness are $\delta^*/\delta = 0.141$ and $\theta/\delta = 0.087$, and the shape factor is $H = 1.62$. As shown in Table 5.2, these are very close to the initial values used in this study. The fully-developed turbulent state is confirmed by ensuring a linear

total shear stress profile.

The flow rate of the channel flow was increased linearly in time from the initial value of $Re = 3500$ to the final value of $Re = 15000$ over a total excursion time of $T_e = 16.43h/U_{m0}$. The rate of change of Re during the acceleration is constant:

$$\frac{dRe}{d\xi} = \frac{(Re_f - Re_0)}{T_e}. \quad (5.1)$$

In this study, $dRe/d\xi = 700$, where $\xi = t h/U_{m0}$. Note that the local Reynolds number is equivalent to the time elapsed after the onset of the acceleration since the mass flow rate increases linearly in time:

$$Re = Re_0 + (Re_f - Re_0)\xi/T_e. \quad (5.2)$$

	Present	Kim et al. (1987)
Re	3500	2800
Re_τ	210	180
C_f	8.18×10^{-3}	7.98×10^{-3}
δ^*/δ	0.140	0.141
θ/δ	0.089	0.087
H	1.56	1.62

Table 5.2: Initial mean flow variables of the simulation.

5.2 Wall shear stress

Dean and Bradshaw (1976) proposed an experimental correlation between C_f and Re_m :

$$C_f = 0.073 Re_m^{-0.25}, \quad (5.3)$$

where Re_m is based on the channel height ($H = 2h$), so $Re_m = 2Uh/\nu = 2Re$.

5.2. WALL SHEAR STRESS

Equation 5.3 can be rewritten in terms of Re :

$$C_f = aRe^{-0.25}, \quad (5.4)$$

where $a = 0.073 \times 2^{-0.25} \approx 0.061$. Then, the rate of change of C_f can be calculated using Equation 5.1:

$$\frac{dC_f}{d\xi} = \frac{dC_f}{dRe} \frac{dRe}{d\xi}, \quad (5.5)$$

$$\begin{aligned} &= -0.25aRe^{-1.25} \frac{dRe}{d\xi}, \\ &= -10.7Re^{-1.25}. \end{aligned} \quad (5.6)$$

Similarly, Equation 5.4 can be rewritten for Re_τ :

$$Re_\tau = cRe^{7/8}, \quad (5.7)$$

where $c = \sqrt{a/2} \approx 0.175$. The rate of change of Re_τ can be calculated using Equation 5.1:

$$\frac{dRe_\tau}{d\xi} = \frac{dRe_\tau}{dRe} \frac{dRe}{d\xi}, \quad (5.8)$$

$$\begin{aligned} &= \frac{7}{8}cRe^{-1/8} \frac{dRe}{d\xi}, \\ &= 107.4Re^{-1/8}. \end{aligned} \quad (5.9)$$

$dRe_\tau/d\xi$ is about 38.7 at $Re_0 = 3500$, and reduces to 32.3 at $Re_f = 15000$. From Equation 5.7, U_m^+ can be calculated:

$$U_m/u_\tau = \frac{1}{c}Re^{1/8}. \quad (5.10)$$

Figure 5.1 shows the variations of Re_τ during the acceleration. Four distinct stages

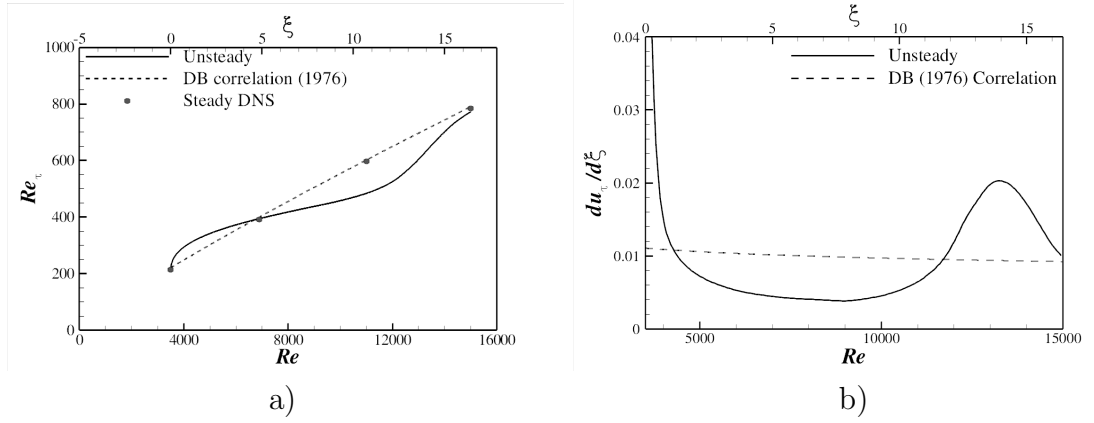


Figure 5.1: Variation of the wall shear stress during the acceleration. a) Re_τ , and b) $du_\tau/d\xi$, the rate of change of Re_τ . Steady DNS data and Dean and Bradshaw (1976) correlation from Equations 5.7 and 5.9 are included for comparison.

of near-wall turbulence response can be observed here: the initial transient (IT) stage (stage I), the weak time-dependence (WT) stage (stage II), and the strong time-dependence (ST) stage (stage III). In chapter 7, it is found that the ST stage is followed by the pseudo-steady (PS) stage (stage IV). The similar response of the wall shear stress was reported in the previous LES study of a pipe flow subjected to temporal acceleration (Jung and Chung, 2007).

At the onset of acceleration, u_τ increases rapidly in the stage I ($3500 < Re < 4300$, or $0 < \xi < 1$). Initially, du_τ/dt is several times larger than the steady corresponding value, and this is due to a uniform increase in the mean velocity across the channel. As a result, u_τ is significantly larger than the steady corresponding values at the same Re numbers. du_τ/dt decreases sharply and the stage I range is defined where the rate of change of u_τ is larger than the steady value calculated in Equation 5.9. In the stage II ($4300 < Re < 12000$, or $1 < \xi < 12$), the rate of change of u_τ is much smaller than the steady values. In the middle of the stage II, du_τ/dt is smaller than half of the steady value. For $\xi \geq 9$, the wall shear stress begins to increase, and at the end of the WT, du_τ/dt is the same as the steady value. In the stage III ($12000 < Re < 16000$, or $12 < \xi < 17$), the wall shear stress increases rapidly.

5.2. WALL SHEAR STRESS

The largest du_τ/dt is observed at $\xi = 13.9$ with its value approximately an order of magnitude smaller than the imposed acceleration rate ($f = 0.2$). The rate of change of u_τ starts decreasing towards the end of the stage III, and Re_τ has almost the steady value at the end of the stage III ($Re = 15000$). In the PS stage ($Re > 15000$, or $\xi > 17$), the near-wall turbulence approaches the pseudo-steady state (this is shown in Chapter 7).

Figure 5.2 shows the variation of the ratio of the bulk-mean velocity to u_τ *i.e.*, ($U_m/u_\tau = U_m^+$) and the skin friction coefficient, $C_f = \tau_w/(\frac{1}{2}\rho U_m^2)$. In the steady flow, the skin friction coefficient decreases with the Re number: $C_f = 0.061Re^{-0.25}$ as in Equation 5.4. C_f decreases by 30% from $C_f = 7.98 \times 10^{-3}$ at $Re = 3500$ to $C_f = 5.54 \times 10^{-3}$ at $Re = 15000$. As the bulk-mean velocity increases linearly during the acceleration, U_m^+ decreases sharply at the start of acceleration and lowest value is reached during the stage I at $Re = 3950$. It starts to increase afterwards due to the subsequent near-wall flow adjustment to the imposed acceleration until the end of the stage II ($Re = 11800$). Finally, U_m^+ decreases towards the steady value during the stage III (Equation 5.10). C_f exhibits exactly the opposite trends as observed for U_m^+ , showing an initial increase during the stage I followed by a reduction in the stage II at exactly the same time as that for U_m^+ during acceleration. This phenomenon of an initial increase and a subsequent reduction in the skin friction coefficient is reported in previous studies of the boundary layer subjected to the acceleration by favourable pressure gradient (FPG) (Sreenivasan, 1982; Fernholz and Warnack, 1998).

Figure 5.3 shows the variation of boundary layer parameters during acceleration. The displacement thickness (δ^*) and the momentum thickness (θ) decrease after the onset of acceleration in an identical manner until both reach a minimum level at $Re = 11350$ and $Re = 11100$ respectively. It is followed by a subsequent increase during the stage III. It is worth noting that the timing for the minimum values of

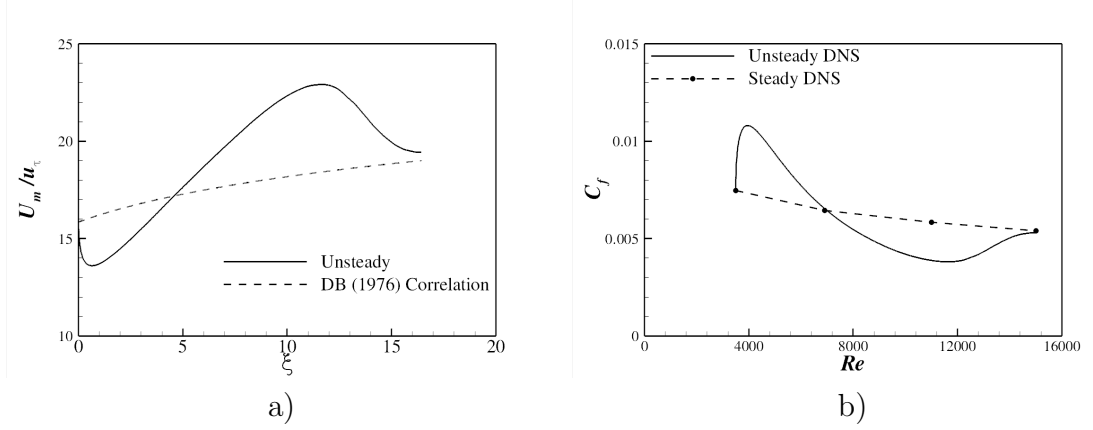


Figure 5.2: Variation of a) $U_m/u_\tau = U_m^+$, and b) C_f during acceleration. Dean and Bradshaw (1976) correlation from Equation 5.10 is included for comparison.

C_f , δ^* and θ occur approximately at the end of the stage II. On the other hand, the shape factor exhibits a different trend; it decreases from the start and reaches its minimum value at $Re = 5500$ and a subsequent gradual increase is observed during the stage II with a local maximum at $Re = 10850$. This two-stage behaviour of shape factor has been reported in several studies of boundary layer subjected to FPG (Blackwelder and Kovasznay, 1972; Fernholz and Warnack, 1998; Bourassa and Thomas, 2009). It is suggested that the flow depicting the two-stage shape factor variation accompanied with a significant reduction in C_f value is representative of a laminar-like mean velocity profile.

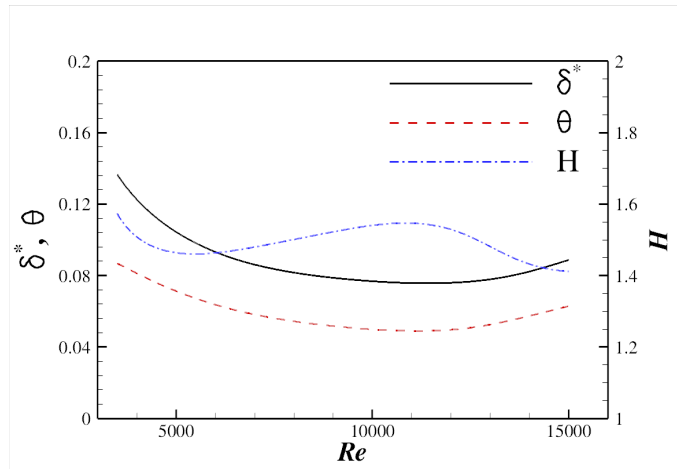


Figure 5.3: Variation of mean flow properties during the acceleration.

5.3 Mean velocity

The wall shear stress and boundary layer parameters provide the velocity information only in the very near-wall region. The mean velocity profiles are plotted at several Reynolds numbers during the acceleration in Figure 5.4. The corresponding steady profiles are also included for comparison. During the stage II at $Re = 7000$, the mean velocity in the near-wall region is larger than the steady value while an opposite trend is observed in the core region. The similar trend was also observed in the pipe experiments of He and Jackson (2000). The flatness of the mean velocity profile is more evident at $Re = 11000$, indicating the lack of response of the near-wall turbulence to the imposed acceleration. Blackwelder and Kovasznay (1972) attributed the flatness of mean velocity profile for boundary layer flow to the rapid acceleration in their FPG study. The mean velocity profile at $Re = 15000$ shows that the near-wall mean velocity has adjusted itself to the acceleration while the centre-line mean velocity is still under-predicted. This slow response of the mean velocity in the core region was also found in boundary layer subjected to FPG (Fernholz and Warnack, 1998). In their case, this effect was attributed to strong upstream history effect affecting the larger structures in outer region while in the present case it is due to the dominance of mean pressure gradient in the core region.

The difference of the mean velocity can be seen more clearly, when plotted in local wall units. The U^+ profiles deviate significantly from the log-law profile during the acceleration. The log-law profile is shifted downward at $Re = 5000$ due to a significantly higher u_τ value during the initial stages of acceleration. A lower value of the wall shear stress during the stage II results in an upward shift of the log-law profile and this upward shift is most prominent at $Re = 12000$. A similar upward shift of the log-law profile was also reported in several turbulent boundary layer experiments subjected to FPG (Escudier et al., 1998; Fernholz and Warnack, 1998). The $U^+ = y^+$ relationship in the viscous sublayer remains valid for $y^+ \leq 2$ at

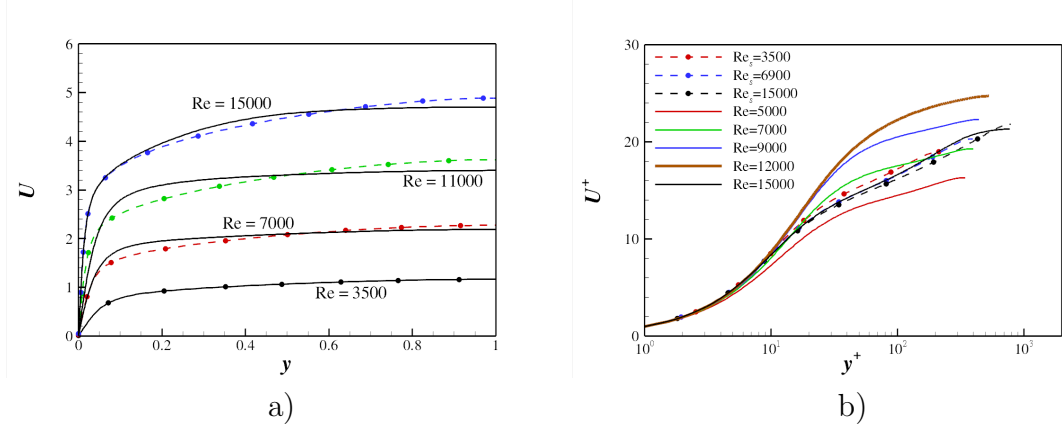


Figure 5.4: Mean velocity profiles at several Re numbers during the acceleration in a) global units, and b) wall units. The local friction velocity (u_τ) is used to calculate U^+ and y^+ . Solid lines indicate the unsteady profiles while symbols indicate the steady profiles.

$Re = 5000$. It is interesting to note that the log-law does not hold at $Re = 7000$ even when the unsteady u_τ is equal to its steady counterpart (cf. Figure 5.1). This is partly due to the delay in turbulence response in the near-wall region resulting in relatively lower velocity gradient and a slug like uniform response of the mean velocity in the core region. The standard log-law profile is approximately recovered towards the end of the stage III at $Re = 15000$.

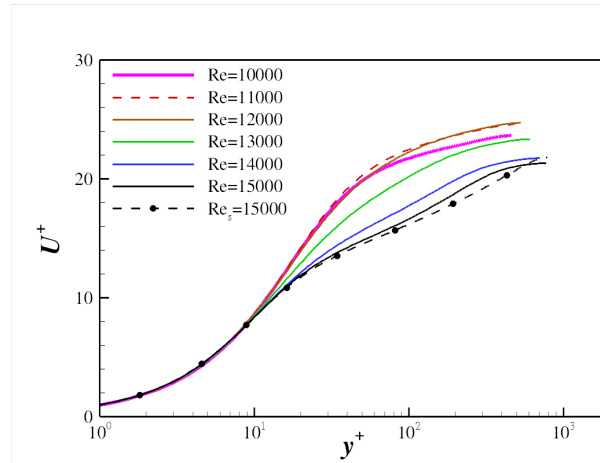


Figure 5.5: Log-law profiles during the stage III. Solid lines denote the unsteady profiles while dashed line with symbols denote the steady profile at $Re = 15000$.

Log-law profiles are plotted in Figure 5.5 at several Re during the stage III to

5.3. MEAN VELOCITY

demonstrate the recovery process. The velocity profile is furthest from the log-law profile towards the end of the stage II ($Re = 11000$), and the log region has a much smaller gradient, indicating that the mean velocity field still has the characteristics of the initial turbulence. The new log-law region begins to develop from $Re = 12000$ with an increase in the friction velocity. The velocity gradient recovers first from the wall region, and then moves outwards as near-wall turbulence is adjusted to the acceleration.

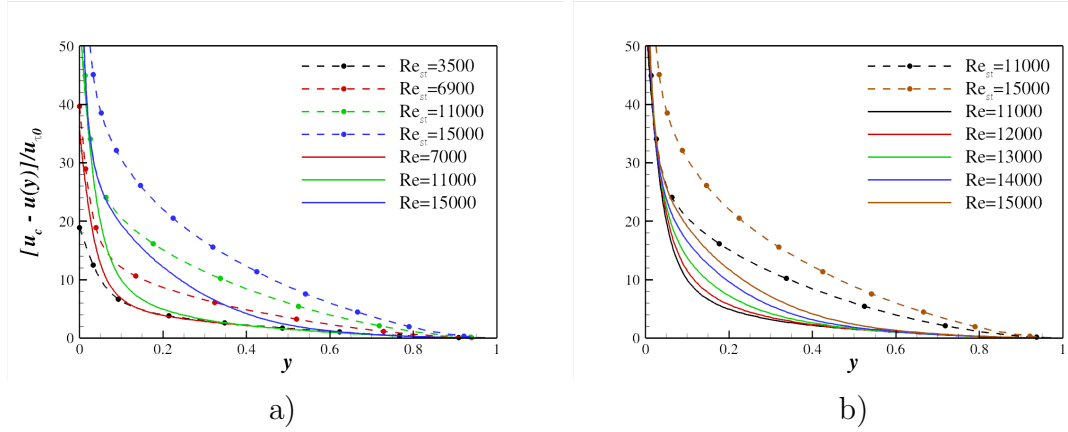


Figure 5.6: Variation of the defect law profiles during the acceleration in a) entire acceleration, and b) the stage III only. The initial friction velocity (u_{τ_0}) is used to calculate defect law profile.

The deviation of the mean velocity from the steady corresponding values in the core region can be clearly seen in the velocity defect law profiles during the acceleration in Figure 5.6. It shows that the mean velocity in the core region increases more uniformly at $Re = 7000$, resulting in significantly lower values than the steady corresponding values. The lower values of defect law were also reported in boundary layer subjected to FPG (Blackwelder and Kovasznay, 1972; Fernholz and Warnack, 1998). The mean velocity gradient in the core region remains largely unchanged during the stage II, and starts to adjust itself rapidly with the generation of new turbulence during the stage III.

Figure 5.7 shows the variation of the mean velocity at several y locations across the

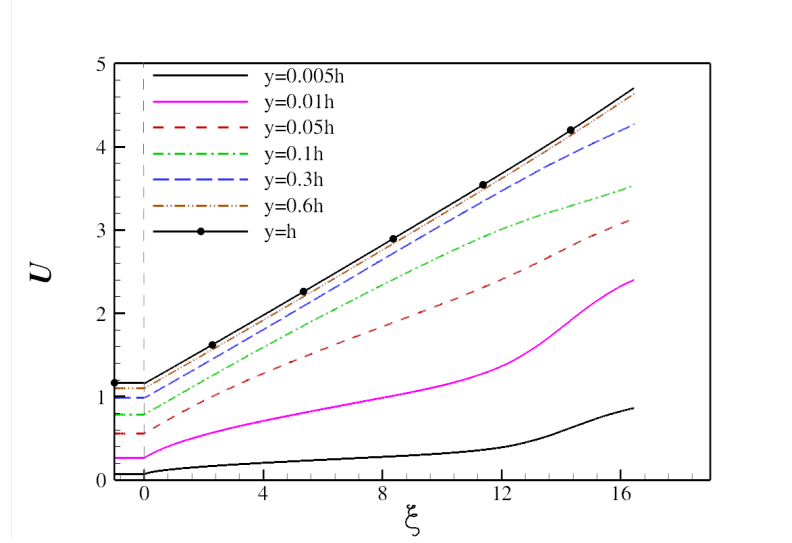


Figure 5.7: Variations of the mean velocity during the acceleration at several y locations across the channel.

channel. It is again evident that the core region velocity is unaffected by the wall effect and increases almost linearly during the acceleration while in the near-wall region this linear increase occurs only at the beginning of the acceleration as the wall effect increases. In the region of $y/h \leq 0.01$, the wall constraint is more prominent and it does not allow the linear increase in the mean velocity. This relatively lower increase of the mean velocity in the near-wall region results in the under-prediction of the wall shear stress towards the end of the stage II and this subsequently results in an abrupt increase in the near-wall mean velocity during the stage III. Similar trends were observed in the pipe flow experiment of He and Jackson (2000). It is interesting to see that the mean velocity increases by the same amount at all y locations in the stage I. Near the wall, the velocity increase soon becomes weaker due to the no-slip condition. On the other hand, the linear increase of the mean velocity away from the wall ($y > 0.3$) is observed throughout the acceleration.

Figure 5.8 shows 2D variation of the wall-normal gradient of the mean velocity, dU/dy , in the near-wall region. Please note that the wall dU/dy value increases 14.5 times during the acceleration. The velocity gradient increases only in the near-

5.3. MEAN VELOCITY

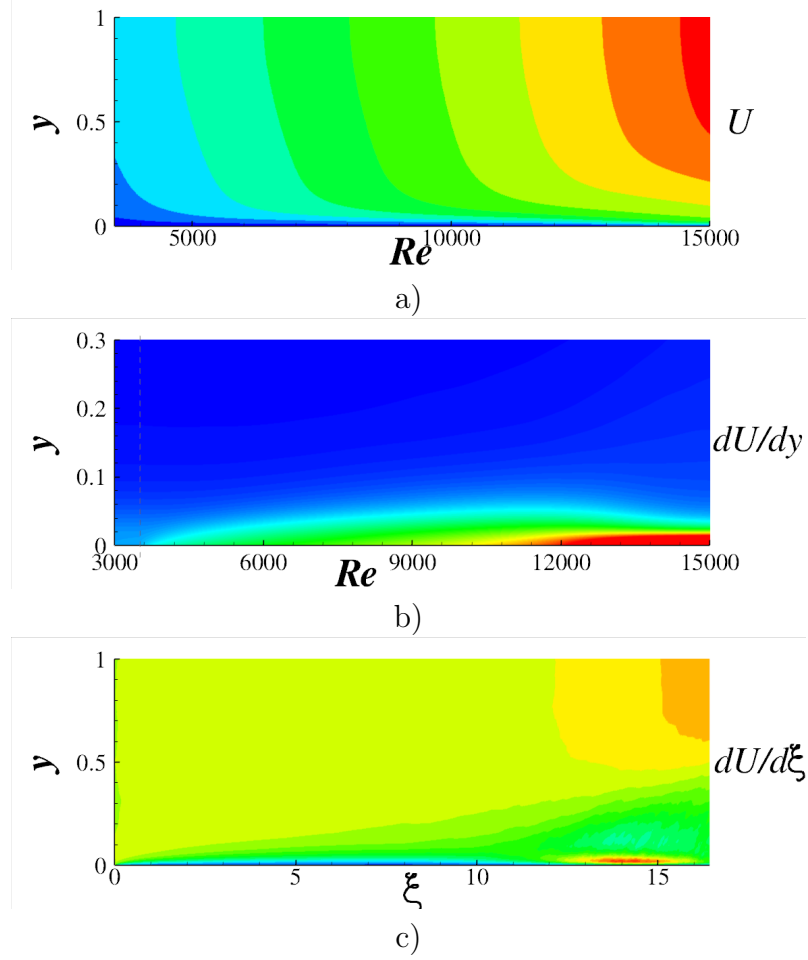


Figure 5.8: Variations of a) the mean velocity, b) the wall-normal gradient of the mean velocity, dU/dy , and c) the rate of change of the mean velocity, $dU/d\xi$, during the acceleration.

wall region during the stage II due to the no-slip condition while it remains largely unchanged in the core region. The near-wall high shear region grows in size with time. This process is mainly due to viscous diffusion and can be approximated by Stokes' first problem. The Stokes layer thickness for $u/U = 0.9$ is $\delta_s \approx 2.32\sqrt{\nu t}$ (White, 2006, pp 131). The Stokes layer thickness at the end of the stage II is roughly $\delta_s = 0.07$. This is very close to the size of the high shear region in Figure 5.8b. At the end of the stage II, the majority of the core region is still insensitive to the acceleration, and dU/dy increases substantially only in a small near-wall region ($y \leq 0.07$). The mean velocity gradient at wall increases rapidly during the stage III, resulting in subsequent change in the mean velocity in the core region. This

indicates that another mechanism other than the viscous diffusion is responsible for the response of turbulence during the stage III.

2D variation of dU/dt during the acceleration is also shown in Figure 5.8c. This shows that the mean velocity changes monotonically in the core region for most part of the imposed acceleration. However, the velocity in the near-wall region remains largely unchanged due to wall constraint, and it increases at a relatively smaller rate during the stage II. There is an abrupt increase in the near-wall mean velocity in the stage III ($13 < \xi < 16$). This abrupt change in the near-wall mean velocity results in a subsequent readjustment of the mean velocity profile in the outer region (as shown in the mean velocity profile at $Re = 15000$ in Figure 5.4).

5.4 RMS velocity fluctuations

The rms velocity fluctuation profiles are shown in Figure 5.9 at several Reynolds numbers during the acceleration. The response of the streamwise fluctuations is delayed at the start, and there is no increase in u_{rms} above the initial steady values at $Re = 5000$. As the acceleration proceeds, u_{rms} starts to increase only in the near-wall region (can be clearly seen in u_{rms} profile at $Re = 7000$), but the response is confined only to the near-wall region. The y location for the maximum u_{rms} remains largely unchanged during the stage II, and it moves much closer to the wall during the stage III. The maximum u_{rms} almost recovers the steady value at $Re = 15000$. The delay in response is even increased in the wall-normal and spanwise fluctuations with a considerable increase only observed during the stage III. v_{rms} and w_{rms} are frozen until $Re = 7000$ and increase very little at $Re = 11000$. Moreover, the maximum v_{rms} and w_{rms} values always remain substantially smaller than the steady corresponding values throughout the acceleration. It is interesting to note that the turbulence intensity is largely unchanged in the core region during the acceleration, and only start to increase after the initiation of the near-wall turbulence propagation in the core region. The insensitivity of core region fluctuations is also reported in the experimental study of boundary layer subjected to FPG (Blackwelder and Kovasznay, 1972).

Figure 5.10 shows the time development of the rms velocity fluctuations at several y locations during the acceleration. It is again clearly seen that u_{rms} responds first only in the near-wall region ($y \leq 0.3$) after an initial delay of approximately 2ξ while it remains unchanged in the core region throughout the acceleration. v_{rms} and w_{rms} exhibit much slower response, and their delay is much longer ($\xi \leq 8$) as compared to the initial delay in u_{rms} response. Similar trends were also observed in the pipe experiment of He and Jackson (2000). The response time of rms fluctuations increases with the distance away from the wall, indicating that the delay in

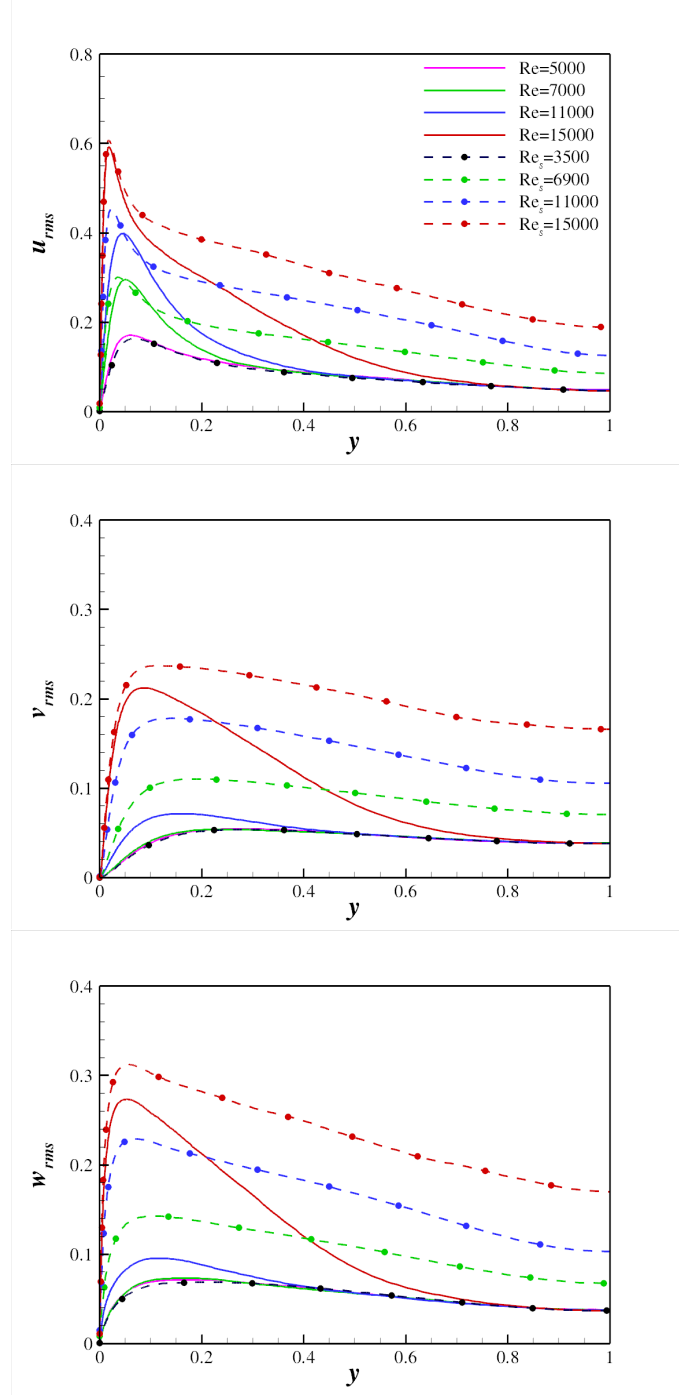


Figure 5.9: RMS velocity fluctuation profiles during the acceleration. Steady profiles (dashed lines with symbols) are included for comparison.

turbulence propagation in the core region. This is consistent with the findings reported in turbulent boundary layer subjected to FPG (Piomelli et al., 2000). There is a noticeable decrease in u_{rms} at $y = 0.05h$ in the near-wall region towards the

5.4. RMS VELOCITY FLUCTUATIONS

end of the stage III. This can be explained by the fact that the energy is extracted from the mean flow by the streamwise component of velocity fluctuations which is subsequently redistributed to the lateral components.

RMS fluctuations normalised by the local mean velocity in Figure 5.10 show interesting trends. Steady data at several time instances are included for comparison. One clear effect of the acceleration is the breakdown of equilibrium of turbulence with the mean flow during the stage I and the stage II. In the very near-wall region ($y = 0.005h$), there is an abrupt decrease in the turbulence intensity, during the stage I and the stage II of the acceleration. This equilibrium breakdown can be attributed partly to the sudden increase in the near-wall mean velocity and partly to the lack of turbulence response at the onset of the acceleration. Similar reduction of $u_{rms,i}/U$ was also reported in FPG experimental study of (Blackwelder and Kovaszny, 1972). u_{rms}/U increases above the corresponding steady value in the near-wall region ($y \leq 0.1$) towards the end of the stage III. The reduction of $u_{rms,i}/U$ below the steady value becomes smaller with an increase in the distance from the wall, and it remains below the steady corresponding values throughout the acceleration. This trend implies the dominance of the acceleration over turbulence in the outer region. On the other hand, the inner layer first regains this equilibrium and it propagates subsequently in the outer region. This behaviour is consistent with the two-layer model proposed by Sreenivasan (1982) for boundary layers subjected to FPG. He suggested that the outer layer flow is largely driven by mean pressure gradient in the initial stages of acceleration while the inner layer flow becomes insensitive (evident from the delay in response) to the imposed acceleration. Moreover, the flow *tends to be laminar but does not necessarily always become laminar* and this stage of flow was referred as *Laminarrescent*. The flow reversion to the fully laminar state is dependent upon the acceleration rate. If the acceleration rate is below the critical value required for relaminarisation, the flow reverts back to the pseudo-steady turbulent state during the acceleration.

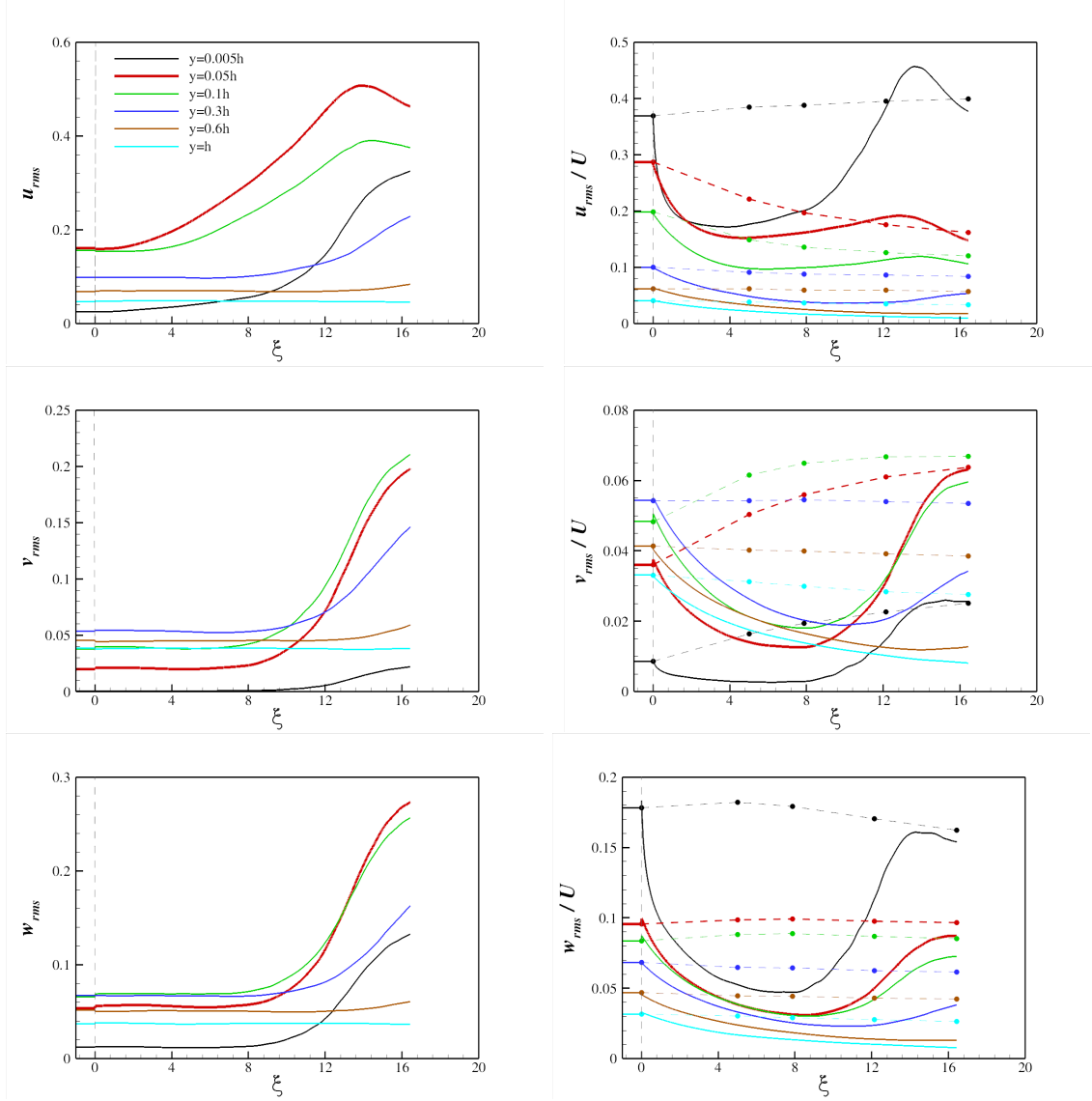


Figure 5.10: Variation of velocity fluctuations at several y locations across the channel during the acceleration.

5.4. RMS VELOCITY FLUCTUATIONS

It is clear from the rms velocity profiles and time histories that turbulence responds first in the near-wall region after exhibiting an initial delay during the stage I and the stage II. This delay in response can be clearly seen in the 2D variation of rms velocity fluctuations, normalised by the local u_τ value, as shown in Figure 5.11. All three components decay at the start of the acceleration due to abrupt increase of u_τ in the stage I as shown in Figure 5.1. This is followed by a subsequent increase of the rms values in an anisotropic manner. The similar variations of normalised turbulent intensities were also reported in boundary layer subjected to FPG (Fernholz and Warnack, 1998). Figure 5.11 clearly shows that the streamwise component responds first in the near-wall region while the other components remain unchanged at that time and starts to respond much later. The pseudo-steady state is achieved only by u'^+ at $Re = 15000$. The delay in the near-wall turbulence response is similar for the wall-normal and spanwise components.

A parameter is introduced in this study to make comparison of different flow variables easy.

$$q^N = (q(t) - M_s)/(M_f - M_s), \quad (5.11)$$

where M_s and M_f are the steady values of flow property “ q ” at the initial and final Reynolds numbers, and the superscript “N” denotes the normalisation by the corresponding steady value difference. The normalisation by steady value difference is performed in order to determine to what extent a flow properly has recovered during the acceleration. The response criterion is denoted by $\xi_{\%n}$, where $\xi_{\%n}$ is the time required for a flow property to reach n percent of the steady values difference. In addition, a parameter R_p is defined to quantify the total recovery with respect to the final steady value.

Table 5.3 shows the time taken by the maximum values of rms velocity fluctuations to reach 50 percent of the respective steady difference. It clearly shows that u'_{max}

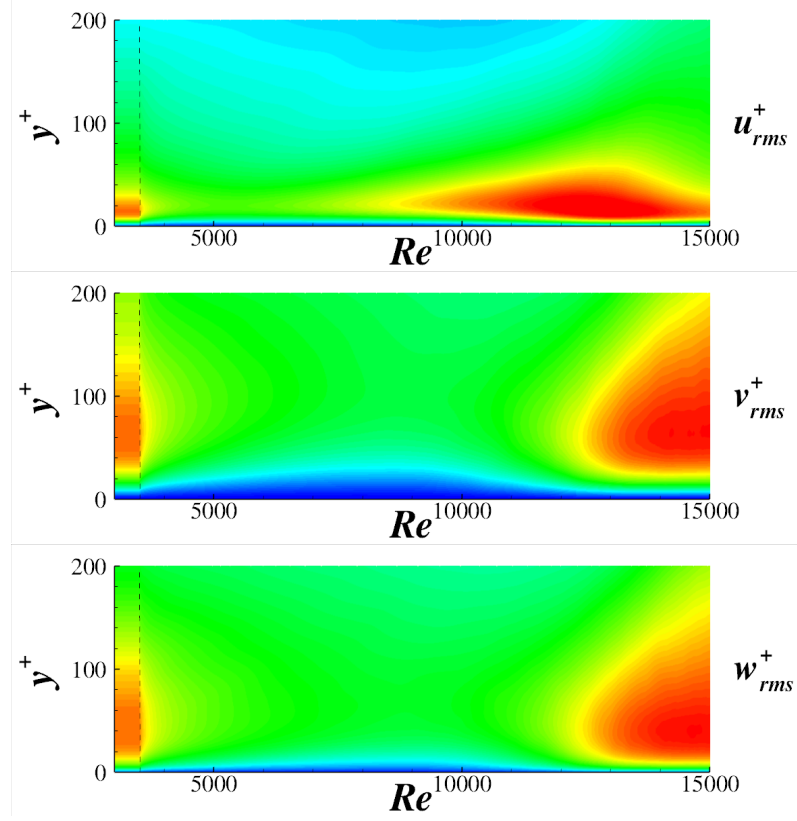


Figure 5.11: Variations of velocity fluctuations in wall units during the acceleration. Initial steady values are included for comparison. The local friction velocity (u_τ) is used for scaling in wall units.

achieves 50 percent of the steady difference first at $\xi = 10.7$ while the response of the other two components is delayed further. The value of R_p shows that only the streamwise component has recovered its maximum intensity towards the final stage of the acceleration. Please note that this quantification of delay is only for the near-wall region. The recovery time of turbulent intensities increases as the distance from the wall increases (cf. Figure 5.9).

The earlier response of u'_{max}^N is also clearly seen in Figure 5.12a showing the variations for maximum rms velocity fluctuations $u'_{i,max}^N$. It is interesting to note that u'_{max}^N overshoots the final steady value towards the end of the stage III ($Re \approx 13500$, or $\xi = 14.4$) and returns below the final steady value afterwards. This behaviour can be clearly seen in u_{rms} profiles in Figure 5.12b where the u'_{max} value at $Re = 15000$

5.4. RMS VELOCITY FLUCTUATIONS

is smaller than the $Re = 14000$ value. This overshooting is indicative of a sudden response of the near-wall turbulence after an initial delay. The subsequent reduction of the maximum streamwise intensity indicates that the energy redistribution from the streamwise component to the other two components becomes more dominant than the energy extraction by u_{rms} from the mean flow. A sharp change in the y location for u'_{max} towards the wall can be clearly seen in Figure 5.12b indicating the production of new turbulence during the stage III.

Flow Property	ξ_{50}^*	R_p	M_s	M_f/M_s
u'_{max}^N	10.7	0.98	0.160	3.7
v'_{max}^N	13.9	0.88	0.053	4.6
w'_{max}^N	14.0	0.86	0.070	4.6

Table 5.3: Response times for maximum values of rms velocity fluctuations during the acceleration.

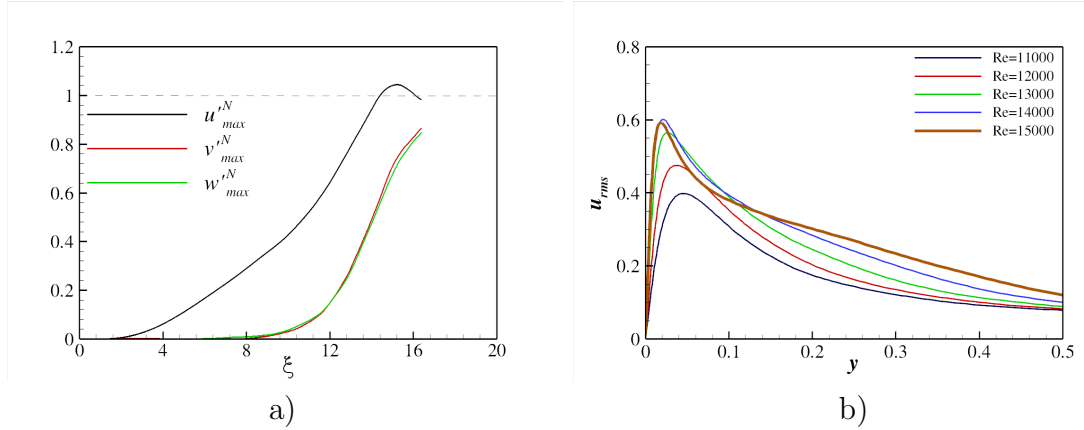


Figure 5.12: Variations of a) maximum velocity fluctuation as defined by Equation 5.11, and b) u_{rms} profiles during the stage III.

The time histories of wall-normal locations for maximum velocity fluctuations are shown in Figure 5.13. The y location for u'_{max} exhibits a decrease in two separate stages. Upon the onset of acceleration, the peak y location remains approximately constant for a short period ($\xi = 1$) in the stage I, followed by a first significant decrease in the stage II ($2 < \xi < 6$). It stops decreasing during the later part of the stage II ($6 < \xi < 11$), followed by a second sharp decrease towards the

corresponding steady value during the stage III. On the other hand, v'_{max} location remains approximately constant, followed by a monotonic decreases towards the steady value during the stage III. It is interesting to note the v'_{max} location moves nearer the wall as compared to the corresponding steady value during the stage III. A similar trend is observed for the w'_{max} location; a long delay followed by a gradual decrease towards the steady value, apart from a small initial increase.

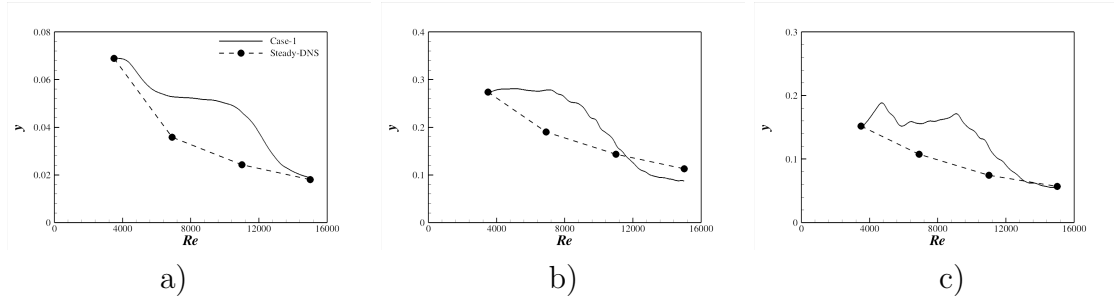


Figure 5.13: Variation of y locations for maximum rms velocity fluctuations. a) u'_{max} , b) v'_{max} and c) w'_{max} .

It is clear from the above results that turbulence starts to increase in the near-wall region first where most of the turbulence production occurs. This newly generated turbulence propagates into the core region afterwards. Please note that the new turbulence is generated after an initial delay (cf. Figure 5.1) and this delay is a function of the initial Reynolds number and the acceleration parameter (this is shown in Chapter 7). He and Jackson (2000) proposed that the characteristics speed of turbulence propagation in the core is proportional to the initial u_τ value. Greenblatt and Moss (2004) used the following criterion in their turbulent pipe experiment subjected temporal acceleration, to characterise the turbulence regeneration and propagation

$$[\phi(t) - \phi(0)]/\phi(0) > a_\phi \quad (5.12)$$

where $\phi(0)$ is the initial steady value and a_ϕ is a constant chosen as 0.15 in their study. The same criterion is applied in the present study to determine the character-

5.4. RMS VELOCITY FLUCTUATIONS

istic propagation speed of u_{rms} into the core region as shown in Figure 5.14, which shows that u_{rms} propagates at a speed of initial u_τ value (u_{τ_0}) in the core region. The effect of different acceleration parameters on the propagation of turbulence is discussed in detail in Chapter 7.

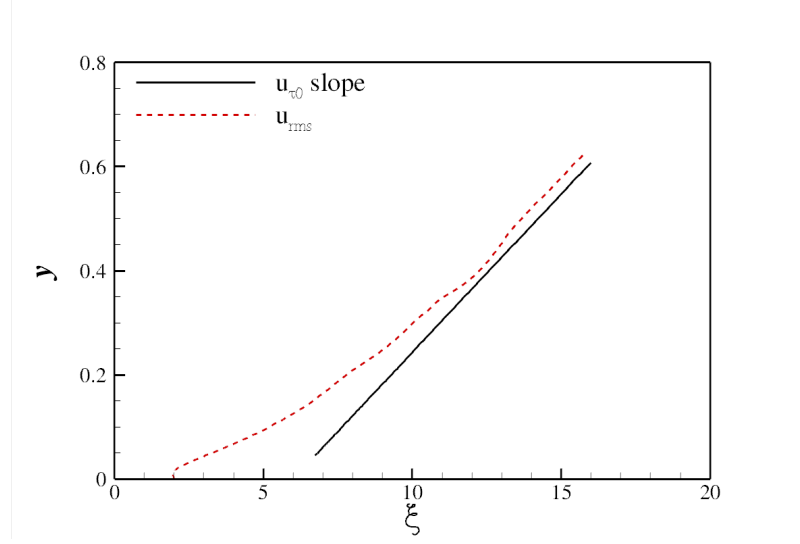


Figure 5.14: The speed of propagation of u_{rms} in the channel core region. x axis is the time taken for u_{rms} during transient process to increase by 15 percent of its initial steady value. *i.e.*, $[u_{rms}(t) - u_{rms}(0)]/u_{rms}(0) > 0.15$ (Greenblatt and Moss, 2004)

5.5 Reynolds stresses

The turbulent shear stress profiles at several Reynolds numbers are plotted in Figure 5.15. The shear stress also exhibits a similar initial delay in response as found for rms velocity fluctuations in Figure 5.9. The turbulent shear stress in the core region is largely unchanged during the acceleration, and its increase from the initial value is observed only in $y < 0.2$ and $y < 0.4$ at $Re = 7000$ and $Re = 11000$ respectively. The maximum value of $-\overline{uv}$ at $Re = 15000$ is approximately 80% of the corresponding steady value. Moreover, the turbulent shear stress decreases sharply away from maximum y location at $Re = 15000$. These trends are also evident from the variations of the turbulent shear stress at several y locations. The lack of increase in the turbulent stress in the core region again shows the lack of turbulence response in the core region. The lack of turbulent shear stress response in the core region was also reported by Fernholz and Warnack (1998). The response times for various terms of Reynolds stresses (as calculated using criterion introduced in Equation 5.11) are tabulated in Table 5.4. This table shows that the turbulent shear stress responds after the \overline{uu} component and before the \overline{vv} and \overline{ww} components.

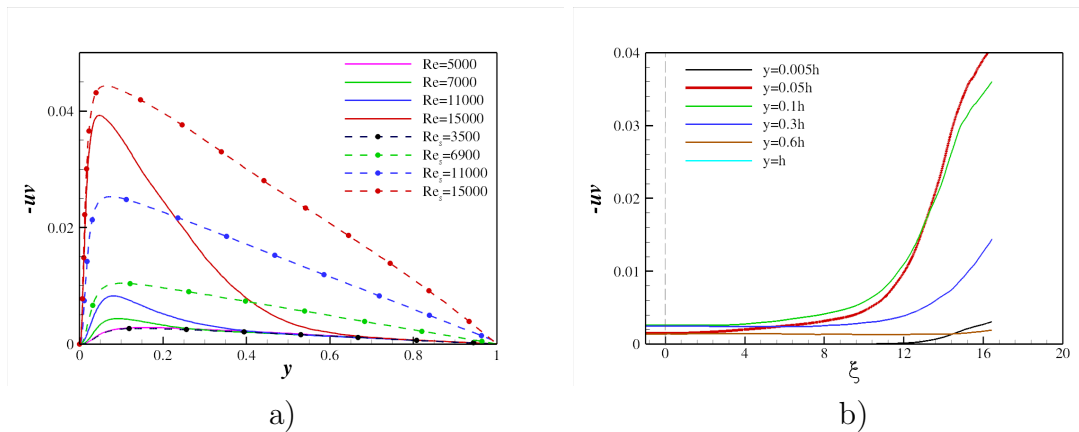


Figure 5.15: Variation of turbulent shear stress ($-\overline{uv}$) during acceleration a) y profiles, and b) time histories at several y locations across the channel. Steady data are also included for comparison.

5.5. REYNOLDS STRESSES

Flow Property	$\xi_{\%50}^*$	R_p	M_s	M_f/M_s
\overline{uu}_{max}^N	11.8	0.97	0.0270	13.8
$-\overline{uv}_{max}^N$	13.9	0.92	0.0026	16.5
\overline{vv}_{max}^N	14.6	0.81	0.0029	21.1
\overline{ww}_{max}^N	14.7	0.78	0.0049	21.6

Table 5.4: Response times for maximum values of Reynolds stresses using $\xi_{\%50}$ criteria (cf. Table 5.3).

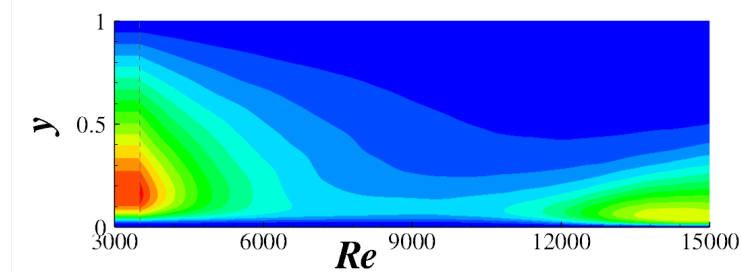


Figure 5.16: Variation of the turbulent shear stress, $-\overline{uv}/U_m^2$, during the acceleration.

2D variation of the turbulent shear stress is shown in Figure 5.16. This supports the earlier findings (in Subsection 5.4) of break down of the local equilibrium between turbulence and mean flow during the stage I and the stage II. The ratio, $-\overline{uv}/U_m^2$, decreases gradually after the onset of the acceleration and reaches a minimum value during the stage II. It starts to increase in the stage III towards the steady values due to generation of new turbulence. However, the value $Re = 15000$ is still smaller than the steady value. This figure clearly indicates that the flow is derived largely by the imposed mass incursion in the stage I and the stage II while turbulence takes a subdued role in affecting the flow field characteristics. It is only when the new turbulence is generated during the stage III that the flow recovers the pseudo-steady turbulent state.

Figure 5.17 shows the variation of the Reynolds stress structure parameter ($a_1 = -\overline{uv}/2k$) at several wall-normal locations. Steady data are also included for comparison purpose. $-\overline{uv}/2k$ ratio decreases in the near-wall region significantly as compared to its steady corresponding value, due to the early response of the turbu-

lent kinetic energy over the turbulent shear stress. Schwarz and Bradshaw (1994) found the similar reduction of structure parameter in their experiment of a turbulent duct flow subjected to a mean spanwise strain. They suggested that this decrease is due to the fact that turbulence becomes less efficient in extracting energy from the mean flow due to the applied strain. This argument is also relevant to the present case, indicating that the additional streamwise pressure gradient weakens the ability of turbulence to extract energy from the mean flow.

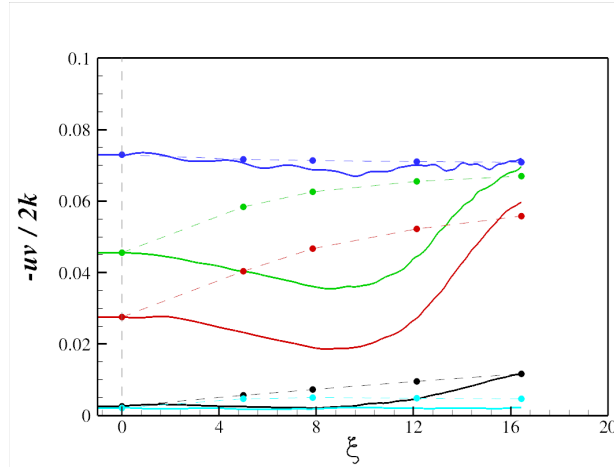


Figure 5.17: Variation of $-\overline{uv}/2k$ at several wall-normal locations across the channel during the acceleration. Legends are the same as in Figure 5.10.

Figure 5.18 shows the variation of the structure parameter and the ratio of the eddy viscosity to the kinematic viscosity. The 2D variation of the structure parameter shows the reduction of the turbulent shear stress to turbulent kinetic energy ratio after the onset of the acceleration. This ratio decreases in the stage II throughout the channel cross section before reaching its minimum value at the end of the stage II. This indicates the inability of near-wall turbulent structures to extract Reynolds shear stress during the WT stage. The reduction in structure parameter was also reported in numerical investigation of turbulent boundary layer subjected to FPG (Piomelli et al., 2000). This is, then, followed by a relatively sudden increase first in the very near-wall region. The 2D variation of the turbulent viscosity $\nu_t/\nu = [-\overline{uv}/(dU/dy)]/\nu$ shows a similar reduction until the end of the stage II.

5.5. REYNOLDS STRESSES

This implies that the turbulent shear stress is not extracting enough energy from the mean velocity field. This results in higher dU/dy values in the near-wall region originating from the no-slip wall constraint. This higher velocity gradient moves away from the wall as the acceleration proceeds (cf. Figure 5.8b), resulting in a subsequent reduction in turbulent viscosity. ν_t/ν increases during the stage III as the mean velocity gradient adjust itself to the new turbulence generation.

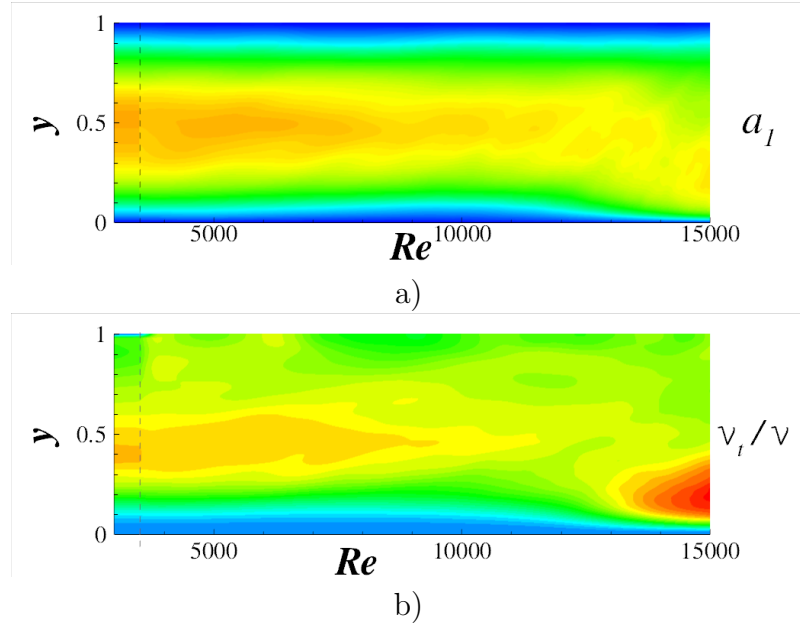


Figure 5.18: Variation of a) the Reynolds stress structure parameter, $a_1 = -\overline{uv}/2k$, b) the ratio of the turbulent viscosity to the molecular viscosity (ν_t/ν), during the acceleration.

5.6 RMS vorticity fluctuations

Although the rms velocity fluctuations provide comprehensive information about turbulence response during acceleration, yet the understanding of near-wall vortical structures response can be best understood by rms vorticity fluctuations analysis. Figure 5.19 shows the rms vorticity fluctuation profiles at several Reynolds numbers during the acceleration. A log scale is used for abscissa to demonstrate near-wall variations more clearly. ω'_x profile appears to be completely frozen at $Re = 7000$. ω'_x remain largely unchanged until the end of the stage II and it starts to increase during the stage III, only in the near-wall region. This delay indicates the delay in response of near-wall turbulent structures in the stage I and the stage II. On the other hand, ω'_y and ω'_z profiles show relatively early increase in comparison to ω'_x and recover the maximum steady corresponding values at $Re = 15000$. The rms vorticity fluctuations in the core region are largely unchanged during the acceleration again supporting the earlier findings in Subsection 5.4.

The time histories of local minimum and maximum values for rms vorticity fluctuations (as calculated using Equation 5.11) are shown in Figure 5.20. $\omega'_{x,wall}$ value was also included. These time histories are consistent with the trends observed in Figure 5.19 that $\omega'_{y,max}$ and $\omega'_{z,wall}$ increase earlier than $\omega'_{x,max}$ during the stage II after a delay of $\xi \approx 3$. On the other hand, all three values for ω'_x show an initial delay of $\xi \approx 10$. These values, afterwards, begin to increase at a similar rate as that of $\omega'_{z,wall}$ during the stage III. Maximum rms vorticity values of the three components recover almost 90% of the corresponding steady values at $Re = 15000$.

It is well known (Kim et al., 1987) that the center of streamwise vortices is located at $y^+ \approx 20$ for a fully-developed turbulent channel flow, which is represented by the local maximum in the ω'_x profile. The y location of the edge of the streamwise vortices, represented by local minimum in the ω'_x profile, is located at $y^+ \approx 5$. The

5.6. RMS VORTICITY FLUCTUATIONS

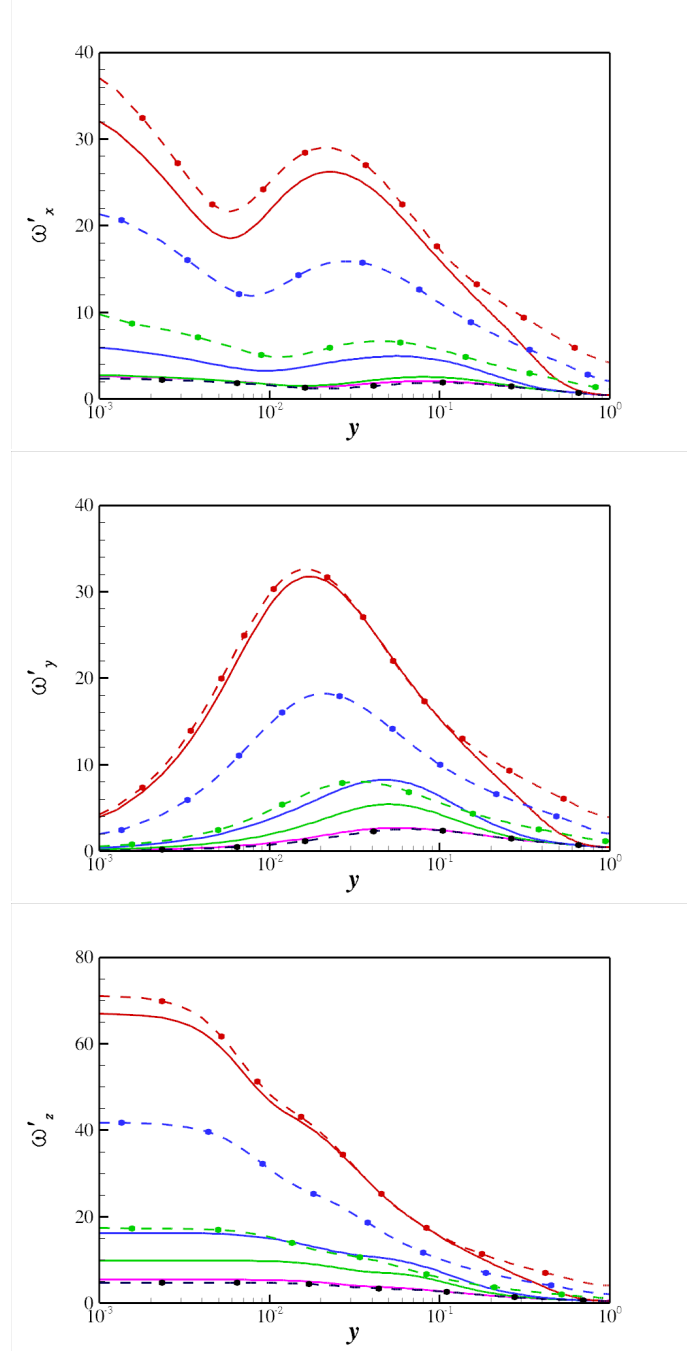


Figure 5.19: Vorticity fluctuation profiles during the acceleration. a) ω'_x , b) ω'_y and c) ω'_z . Steady values are included for comparison. For legend see Figure 5.9.

y location of maximum ω'_y lies in the vicinity of y location of maximum turbulent kinetic energy production *i.e.*, $y^+ \approx 15$. All these y locations move towards the wall as the Reynolds number increases for fully-developed turbulent channel flow, due to the scaling of near-wall structures in wall units.

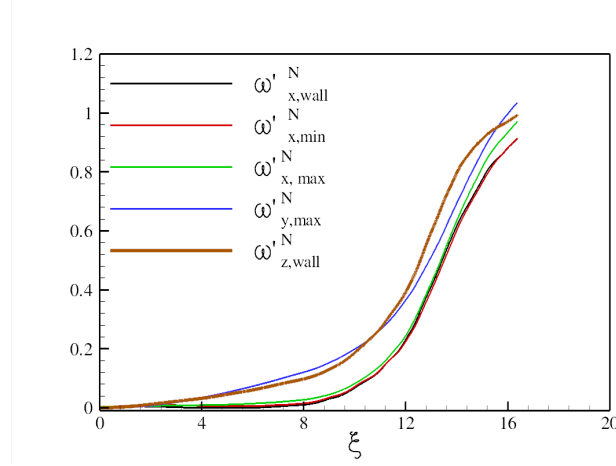


Figure 5.20: Time histories of local minimum, local maximum and wall values of rms vorticity fluctuations.

Figure 5.21 shows the time variations of these three vorticity y locations during the acceleration. The corresponding y locations from fully-developed steady turbulent channel flow at several Re numbers are also included. The three y global locations remain significantly higher than the steady corresponding locations in the stage I and the stage II. These y locations decrease sharply towards the steady y locations during the stage III with the generation of new turbulence. The variations of y locations are more prominent in the graphs plotted using wall units.

All three y locations show a two-stage reduction during the acceleration. The $\omega'_{x,min}$ and $\omega'_{x,max}$ wall-normal locations decrease slightly until $\xi \approx 3$. These locations cease to decrease during the stage II ($3 \leq \xi \leq 8$), and exhibit a sharp decrease towards the steady y locations during the stage III. Time history of $\omega'_{y,max}$ wall-normal location in global units shows the similar two-stage trend as for u'_{max} (cf. Figure 5.13). These two-stage changes in vorticity maximum and minimum locations can be explained that the temporal acceleration only changes the mean velocity gradient in the wall region without affecting the near-wall structures significantly during the stage I. The generation of new turbulence is delayed in the stage II, resulting in constant locations for the vorticity maximum and minimum. Finally, these y locations move

5.6. RMS VORTICITY FLUCTUATIONS

rapidly towards the wall during the stage III with the generation of new turbulence and approximately attain the steady corresponding values at $Re = 15000$.

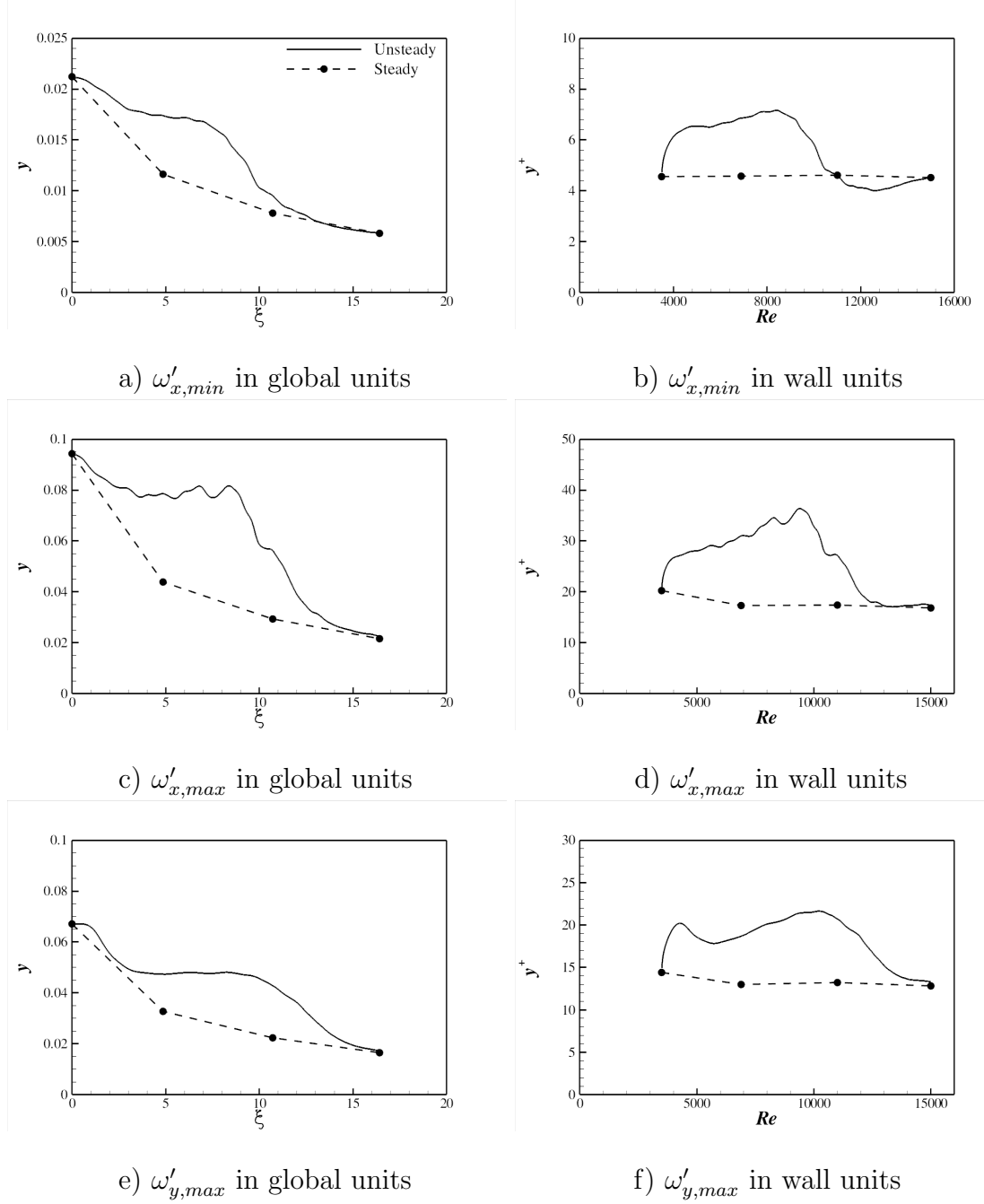


Figure 5.21: Time histories of y locations of $\omega'_{x,min}$, $\omega'_{x,max}$ and $\omega'_{y,max}$ during the acceleration.

5.7 Turbulent kinetic energy (TKE) budgets

Turbulent kinetic energy budget analysis is very helpful in investigating the flow physics. As it is shown in Chapter 4, the kinetic energy budget terms have significant contribution in the near-wall region only where most of the turbulent production occurs. Time histories of maximum values for several budget terms (the turbulent production, the pressure-strain and the dissipation terms), calculated using Equation 5.11, are shown in Figure 5.22a. Please note that log scale is used for ordinate in order to clearly see the response in the beginning of acceleration. The transport equation terms for \overline{uu} respond first of all. The production term for \overline{uu} increases first, followed by the dissipation and pressure-strain terms respectively. It is worth noting that all transport terms increase at a similar rate during the stage III as shown in 5.22b. All the budget terms in the near-wall region recover the final steady value at $Re = 15000$. The production term for \overline{uu} overshoots the steady value and the overshoot of production term explains the overshoot of u'_{max} during the stage III (cf. Figure 5.12a).

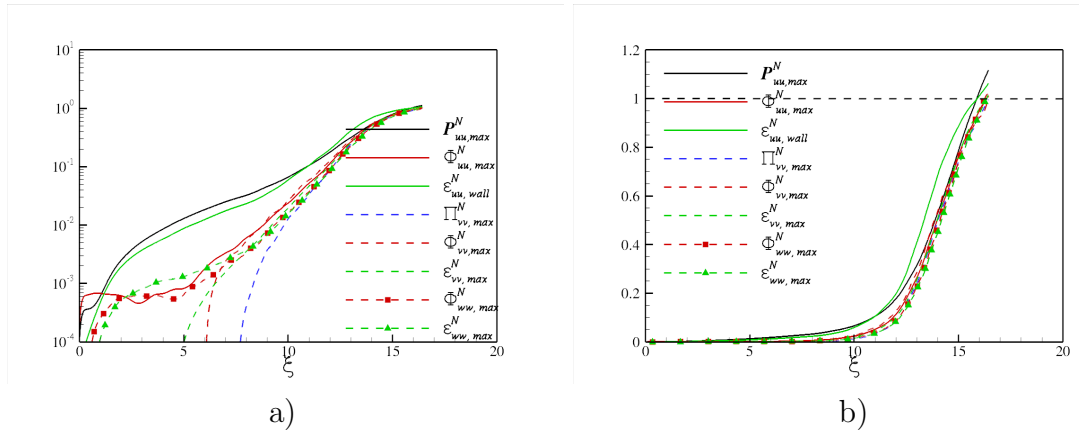


Figure 5.22: Time histories of maximum values of several budget terms. a) in log scale for ordinate, and b) in normal scale. Solid lines show the budget terms of \overline{uu} transport equation, dashed lines for \overline{vv} and dashed lines with symbols for \overline{ww} transport equation.

2D time variations of turbulent kinetic energy budget terms for \overline{uu} transport equa-

5.7. TURBULENT KINETIC ENERGY (TKE) BUDGETS

tion are shown in Figure 5.23. Steady initial profiles are included in the plots and the local u_τ is used for normalisation (ν^2/u_τ^4). It is clearly evident from the plots that all transport terms exhibit an initial delay in adjusting to the imposed acceleration, and the production term is the first one to acquire the pseudo-steady state. The increase in the production term results in a subsequent increase in u_{rms} . The dissipation term is delayed further as compared to the production term as shown clearly in 5.23f, with the production term dominating the dissipation term during the stage II. The pressure-strain term shows a sudden increase towards the end of the stage III, indicating the initiation of the newly generated turbulence propagation in the core region. Generally, all other terms lag behind the production term to certain extent in the stage II and increase at a similar rate during the stage III.

Wall-normal profiles of the several budget terms in the near-wall region are shown in Figure 5.24. Steady data at $Re = 15000$ is also included for comparison. All budget terms achieve the corresponding steady maximum values in the near-wall region at $Re = 15000$. The rapid increase in the \overline{uu} production term during the stage III is evident, and the production term does not increase in the region of $0.04 \leq y \leq 0.08$ at $Re = 15000$. This trend explains an unexpected reduction of u_{rms} intensity at $Re = 15000$ below $Re = 14000$ at the same y location (cf. Figure 5.12b). This behaviour is due to a rapid increase in pressure-strain terms for all three transport equations in this region. This sharp increase in the pressure-strain terms during the later part of the stage III is an indication of energy redistribution to the lateral components and subsequent turbulence propagation in the core region.

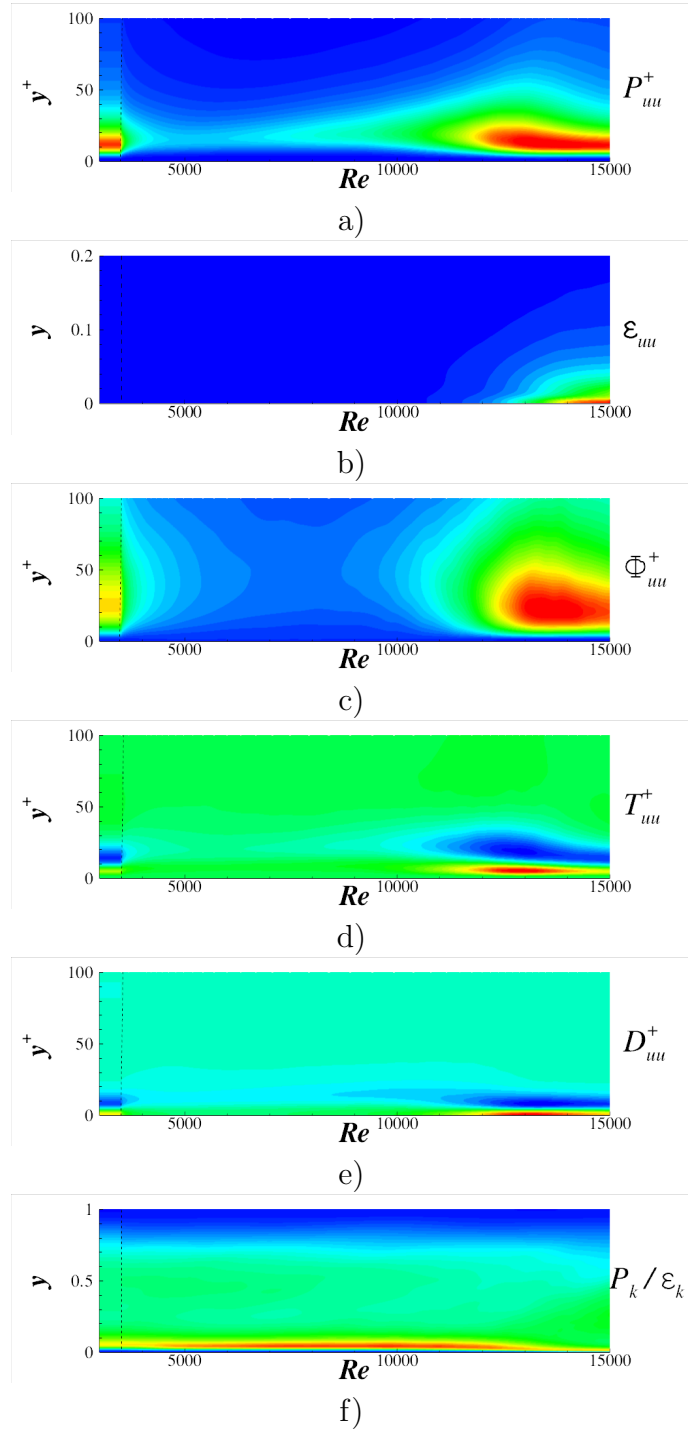


Figure 5.23: Budget terms of \overline{uu} transport equation during the acceleration. a) the production, b) viscous dissipation, c) pressure-strain, d) turbulent transport e) viscous diffusion terms, and f) the ratio of the turbulent production to the viscous dissipation term. Local u_τ is used for normalisation

5.7. TURBULENT KINETIC ENERGY (TKE) BUDGETS

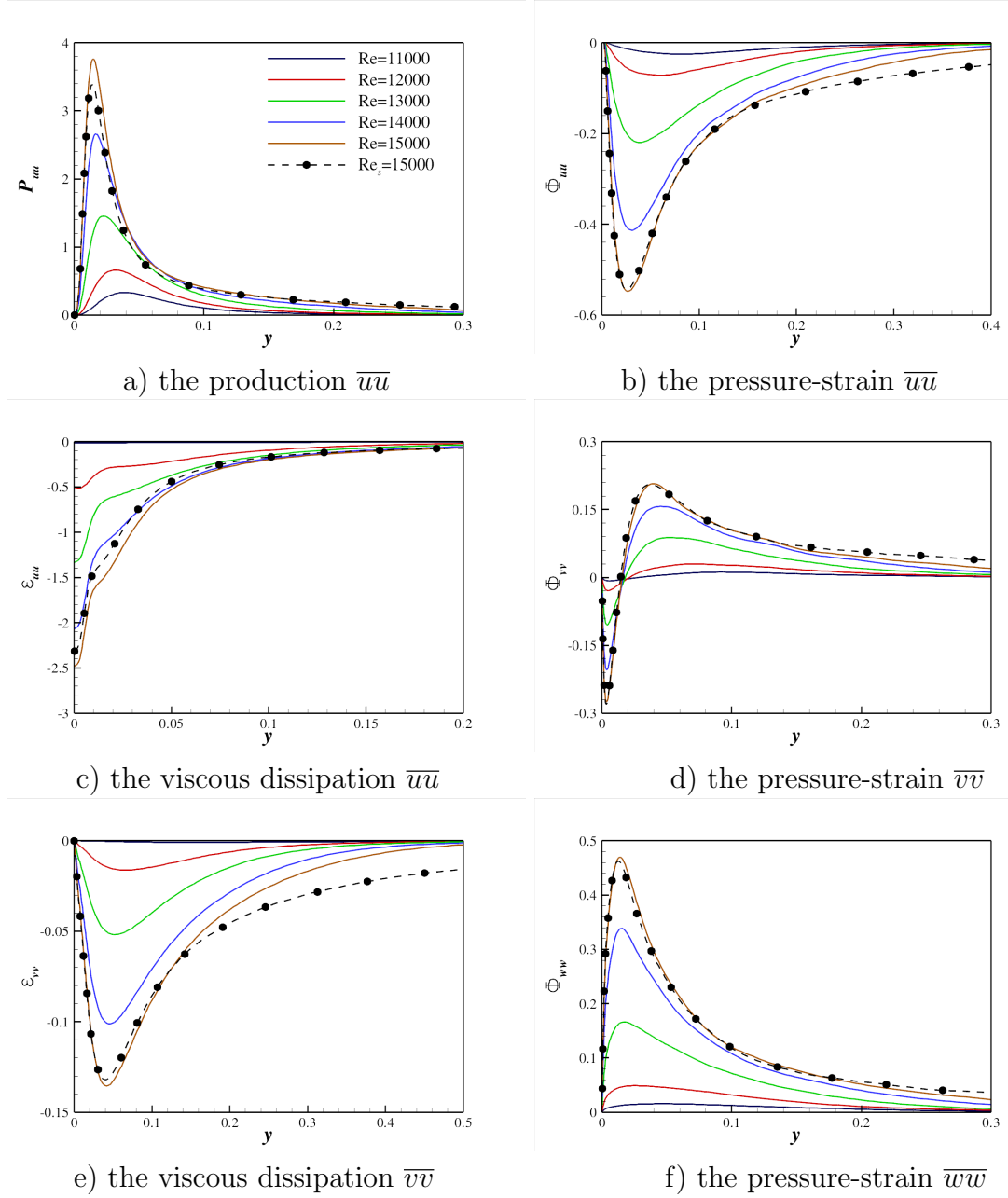


Figure 5.24: Variation of the various transport budget terms profiles in the stage III from $Re = 11000$ to $Re = 15000$.

5.8 Probability density function (pdf) analysis

Probability density function (pdf) analysis for the streamwise and wall-normal velocity fluctuations (u', v') is performed to investigate instantaneous Reynolds stress producing events during the acceleration. Please note that “'” denote fluctuations in this section. Robinson (1991) suggested that these Reynolds stress producing motions are actually the consequence of the dynamics of the near-wall coherent structures. These events are divided into four different quadrants according to the different signs of (u' and v') (Lu and Willmarh, 1973). The first quadrant (Q_1), $u' > 0$ and $v' > 0$, represents the outward motion of high speed fluid, the second quadrant (Q_2), $u' < 0$ and $v' > 0$, represents the outward motion of low speed fluid, the third quadrant (Q_3), $u' < 0$ and $v' < 0$, represents the inward motion of low speed fluid and finally the fourth quadrant (Q_4), $u' > 0$ and $v' < 0$, is associated with events related to inward motion of high speed fluids. The second quadrant events are generally referred as *ejection*, while the fourth quadrant events are referred as *sweep*. Both of these events account for positive production in turbulent flows. Ejections are considered as the events responsible for the occurrence of turbulent bursts (Kim et al., 1971). These turbulent bursts, in turn, are mainly responsible for the turbulent kinetic energy production.

The pdf contours at several y^+ locations are shown in Figure 5.25 for a fully-developed turbulent channel at $Re = 3500$ ($Re_\tau \approx 215$) and the corresponding number of events (in percentage) for each quadrant is tabulated in Table 5.5. Please note that all the pdf data presented in this section are prepared from approximately 4 million points of velocity information for each y^+ location. The 2D bin size to calculate the probabilities is kept constant in wall units as 0.1. Since the wall-normal fluctuations are significantly small in the near-wall region due to its limiting behaviour, the bin size for v' is reduced to 0.05 for the pdf at $y^+ = 3$. The pdf graphs and quadrant contributions for fully-developed channel are in very good agreement

5.8. PROBABILITY DENSITY FUNCTION (PDF) ANALYSIS

with the data in literature (Kim et al., 1987). In the very near-wall region ($y^+ = 3$), the magnitude of sweep events is much larger than the ejection events. Contribution from Q_2 quadrant becomes equal to the Q_4 quadrant contribution in buffer layer and Q_2 contributions become large in the outer layer. On the other hand, the frequency of ejection events is greater than the sweep events in the viscous sublayer. Number of Q_2 events reduces in the buffer layer and number of Q_4 events increases in the outer layer region. The number of events from all quadrant becomes approximately equal in the core region.

Location (y^+)	Magnitude				Frequency			
	Q_1	Q_2	Q_3	Q_4	Q_1	Q_2	Q_3	Q_4
3	-22.1	45.5	-19.0	95.6	15.0	33.7	22.2	29.1
10	-10.3	52.6	-8.9	66.6	14.3	34.8	16.2	34.7
20	-12.4	68.0	-10.3	54.7	18.2	32.5	13.5	35.8
50	-13.8	75.7	-14.0	52.1	18.2	30.1	15.9	35.8
100	-12.1	74.9	-12.3	49.5	17.3	29.4	16.0	37.3
200	-96	209	-132	119	25.2	24.4	22.5	27.9

Table 5.5: Percentage contribution of magnitude and frequency in the quadrant analysis at several wall normal locations for a fully-developed turbulent channel flow at $Re = 3500$.

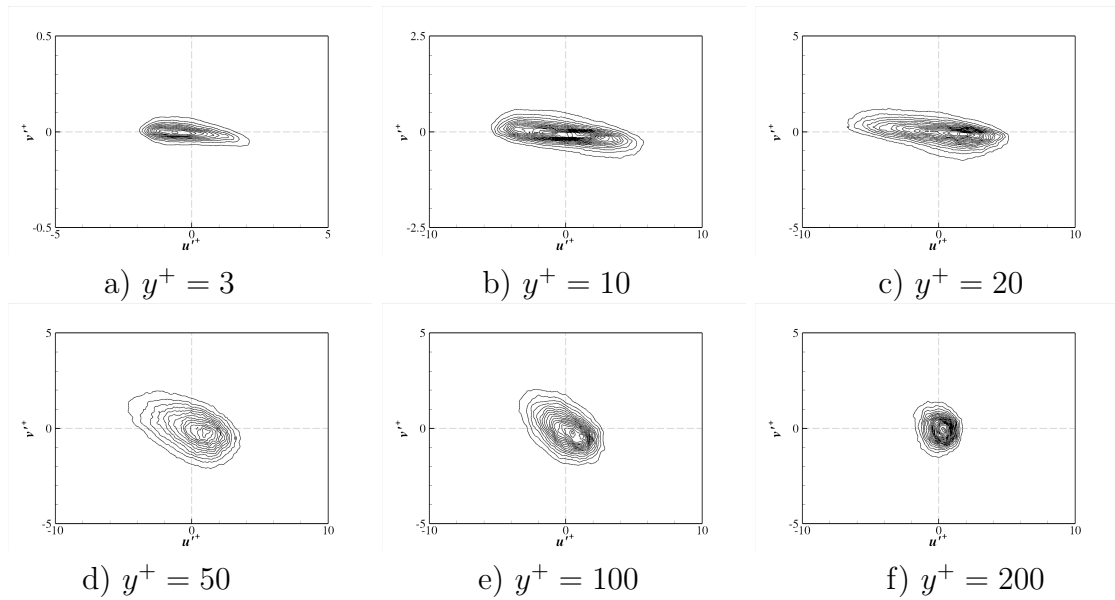


Figure 5.25: PDF of u' and v' at several y locations for a fully-developed turbulent channel flow at $Re = 3500$.

5.8. PROBABILITY DENSITY FUNCTION (PDF) ANALYSIS

Figure 5.26 shows the time histories of number of quadratic events (in percentage) at several wall-normal locations during the acceleration. The number of Q_4 events starts to decrease considerably after $Re = 8000$ in the very near-wall region at $y^+ = 3$, accompanied with an increase in Q_3 events. Q_4 events reduce below Q_3 events during the stage III and recovers approximately its initial value at $Re = 15000$. This reduction implies the reduction in number of sweep events during the stage III. It is interesting to note that this reduction of Q_4 events, in the present case, happens towards the end of the stage II, where the local u_τ value is significantly smaller than the steady value (cf. Figure 5.1a). It is worth noting that Q_1 events also increase during the stage III with corresponding reduction in Q_2 at $y^+ = 3$ and $y^+ = 10$. The deviation of frequency of quadratic events from the initial values is also evident at $y^+ = 10$ and $y^+ = 20$. The quadratic contributions are less effected by acceleration at $y^+ = 50$ as shown in Figure 5.26d.

This increase in the number of Q_3 events at the expense of Q_4 events is also reported by Bourassa and Thomas (2009) in their experiment of boundary layer subjected to acceleration. They suggested that the decrease in the Q_4 events is due to effective aliasing of Q_4 events. This effective aliasing occurs due to large near-wall streamwise mean velocity, which may make the inward moving high speed fluid Q_4 event as a Q_3 event. This large near-wall streamwise velocity occurred in their experiments because of relatively large positive streamwise mean velocity gradients in the near-wall region due to relaminarisation of boundary layer. In the present study, an abrupt increase in the mean velocity results in large near-wall streamwise mean velocity as clearly seen in Figure 5.8c during $13 < \xi < 16$ (or $12600 \geq Re \leq 14700$).

They also suggested that in case of mild acceleration, this increase in the Q_2/Q_4 ratio (as ejections events are largely insensitive to acceleration in the present study) would result in more vigorous wall-normal transport of fluid in order to satisfy mass conservation. It implies that the reduction in the number of Q_4 events results in

less frequent, highly energetic inrush of fluid having large amplitude of fluctuations, resulting in a subsequent increase in the skin friction (this can be seen in pdf graphs during the stage III in Figures 5.29 and 5.30) .

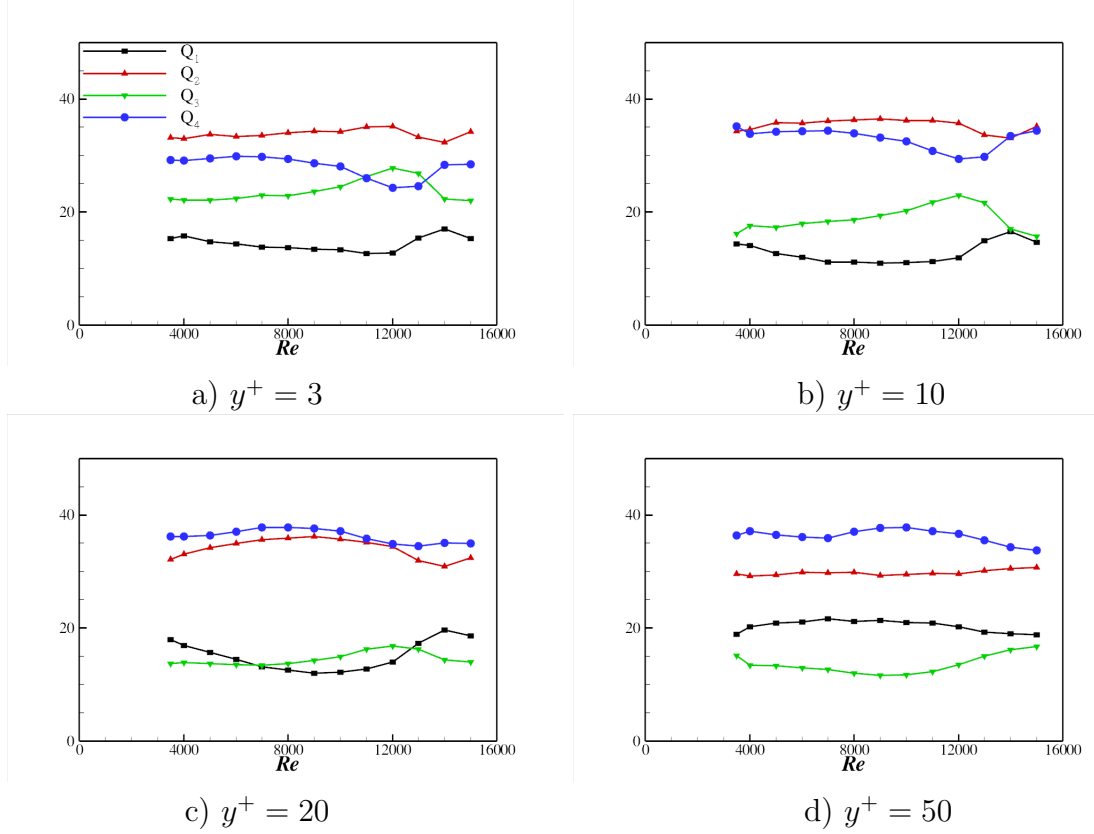


Figure 5.26: Frequency of quadratic events at several y locations (in percentage) during the acceleration.

The time histories of quadratic contributions at several y locations are shown in Figure 5.27. The deviation of quadratic contributions from the initial values increases as the distance from the wall reduces, which can be clearly seen from the time histories at $y^+ = 3$ having maximum deviation and $y^+ = 50$ having minimum deviation. Contributions from Q_1 and Q_4 events increase while Q_2 and Q_3 contributions decrease in the range of ($8000 < Re < 14000$) before returning towards the steady quadratic contributions at $Re = 15000$. The contribution of sweep events increases significantly at $y^+ = 3$ during the stage III, resulting in subsequent increase in the wall shear stress. It is interesting to note that the number of sweep

5.8. PROBABILITY DENSITY FUNCTION (PDF) ANALYSIS

events decrease in the start of the stage III as shown in Figure 5.26a, while the quadratic contribution from sweep events increases. This implies the occurrence of less frequent, strong sweep events during the stage III.

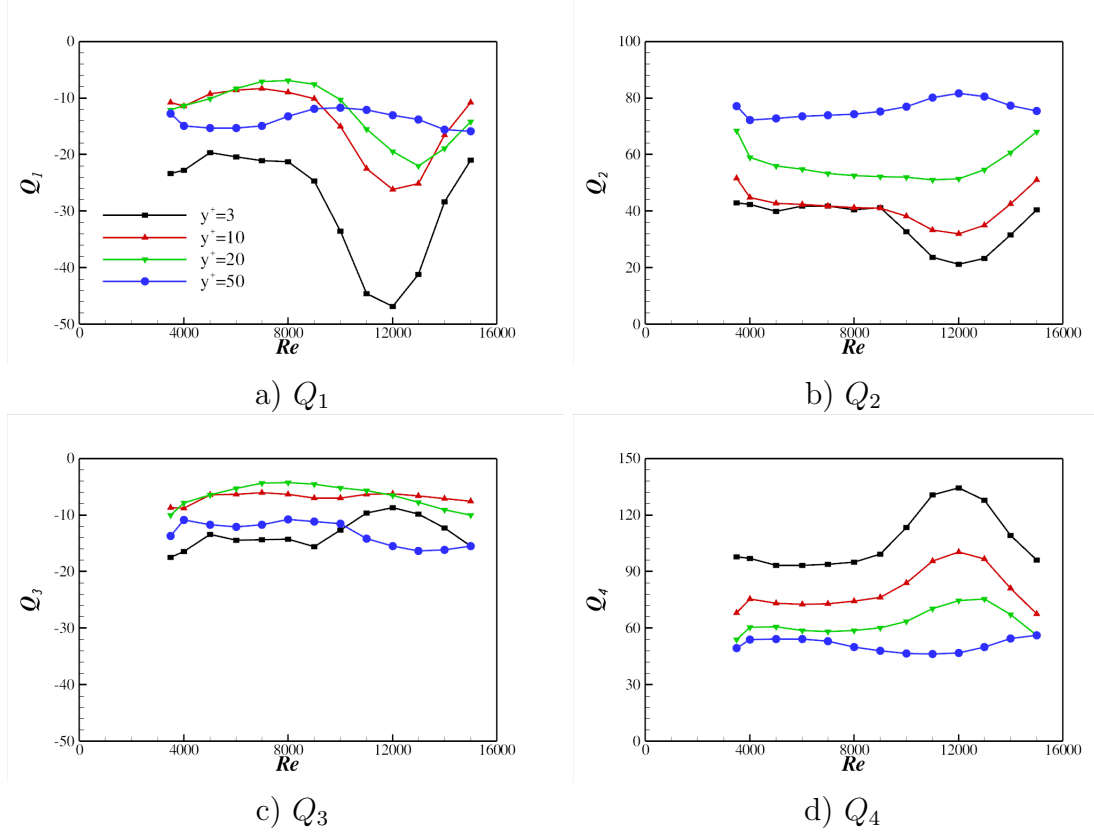


Figure 5.27: Time histories of magnitude of quadratic contributions $y^+ = 3$ (in percentage) during the acceleration.

The increase in quadratic contributions from Q_1 and Q_4 events accompanied with corresponding reduction in Q_2 and Q_3 in the near-wall region is clearly seen in Figure 5.28. This increase implies an increase in positive streamwise fluctuations. The increase in the contribution of the positive streamwise fluctuations can be explained by the fact that the mean velocity in the very near-wall region remains relatively low during the initial part of the stage III due to the imposition of no-slip constraint (cf. Figure 5.7). The rapid increase in the near-wall turbulence results in a subsequent abrupt increase in the near-wall mean velocity. This explains the decrease in magnitude of Q_1 and Q_4 and the corresponding increase in the number of Q_1 and

Q_4 events towards later part of the stage III ($Re > 12000$). It is worth noting that the quadratic contributions from Q_1 and Q_2 becomes approximately equal during the stage III at $y^+ = 10$ in Figure 5.28b .

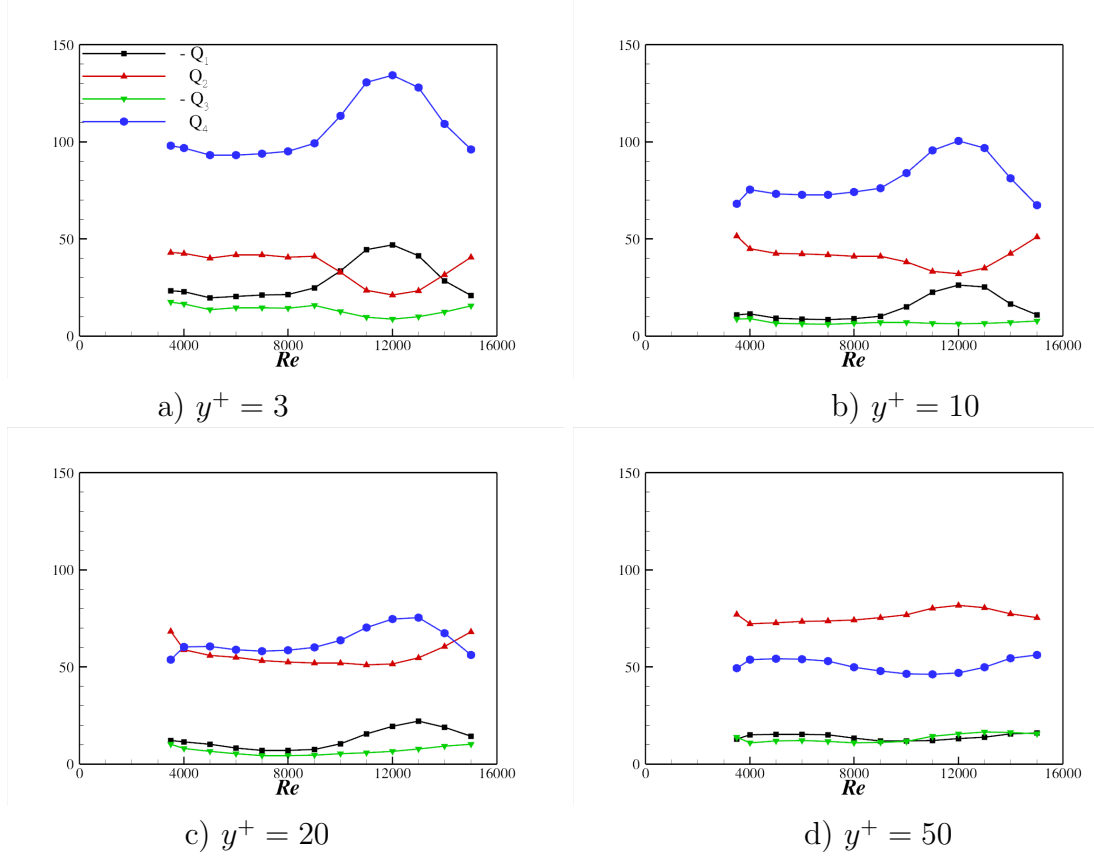


Figure 5.28: Magnitude of quadratic contributions (in percentage) at during the acceleration.

PDF contours are helpful in analysing the individual contributions from u' and v' separately in each quadrant. Figure 5.29 shows the weighted pdf in the viscous sublayer at $y^+ = 3$ at several Reynolds numbers during the acceleration. The pdf are produced by using the same contour levels for all graphs and fluctuations are normalised by the rms velocity fluctuations at each y location. PDF contours in the stage II show a reduction of high amplitude v' events while the number of strong u' events remain largely unchanged. Large number of weak v' events occur at $Re = 12000$ to $Re = 14000$ contour plots in the third quadrant in Figure 5.29f-h which supports the variations of frequency of Q_3 events in Figure 5.26a. On the

5.8. PROBABILITY DENSITY FUNCTION (PDF) ANALYSIS

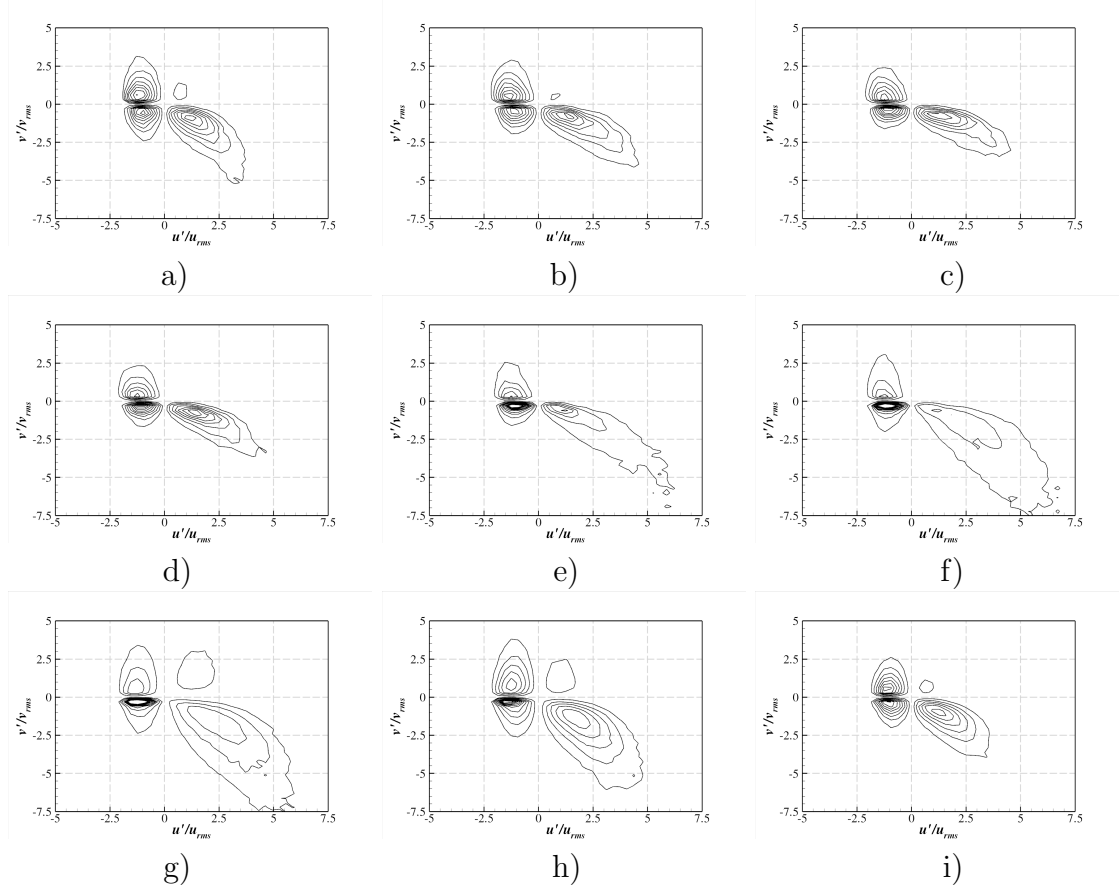


Figure 5.29: Weighted pdf of u' and v' at $y^+ = 3$ at several Reynolds numbers during the transient. For captions, From top left row wise: a) $Re = 3500$, b) $Re = 5000$, c) $Re = 7000$, d) $Re = 9000$, e) $Re = 11000$, f) $Re = 12000$, g) $Re = 13000$, h) $Re = 14000$ and i) $Re = 15000$. Same contour levels are used for all the figures.

other hand less frequent, high amplitude sweep events also occur during the stage III ($Re = 11000$ and onwards). It is interesting to note that the occurrence of these strong sweep events is coincident with the rapid increase in the wall shear stress (cf. Figure 5.1). The increase in contribution from less frequent, strong v' events during the later part of the stage III, indicates a vigorous wall-normal transport of the fluid through highly energetic v' events. The pdf contributions approximately attain the steady pdf shape as the initial pdf at $Re = 3500$.

Figure 5.30 shows the pdf contours at $y^+ = 10$ to study quadrant analysis in the region of maximum turbulent production. There is no significant suppression of v' during the stage II as found in the viscous sublayer in Figure 5.29. The amplitude of

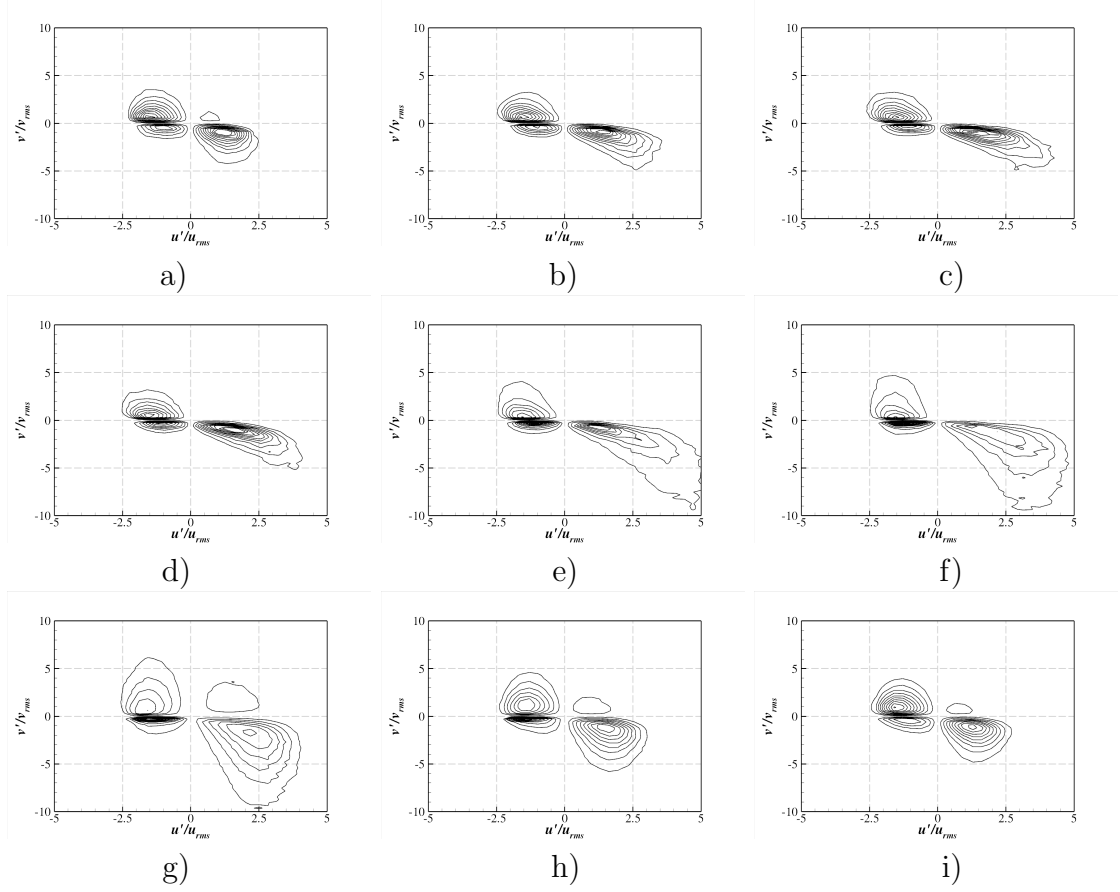


Figure 5.30: Weighted pdf of u' and v' at $y^+ = 10$ at several Reynolds numbers during the acceleration. For captions, see Figure 5.29. Same contour levels are used for all the figures.

positive u' events increases gradually during the stage II and there is a rapid increase in less frequent, strong sweep events at $Re = 11000$. These pdf again supports the observation of vigorous wall-normal transport of fluid through less frequent, strong sweep events during the stage III. It is interesting to note that the pdf contour at $Re = 14000$ almost acquire the initial pdf contour values at $Re = 14000$ whereas the steady pdf shape is acquired at $Re = 15000$ indicating the earliest response of this region during the acceleration. Figure 5.31 shows the similar variations of pdf contours at $y^+ = 50$. Less frequent, strong v' events increase during the stage III. This increase is more prominent at $Re = 11000$ and $Re = 12000$. It is interesting to note that the strength of u' and v' increase significantly in the second quadrant indicating an increase in the ejection events during the acceleration.

5.8. PROBABILITY DENSITY FUNCTION (PDF) ANALYSIS

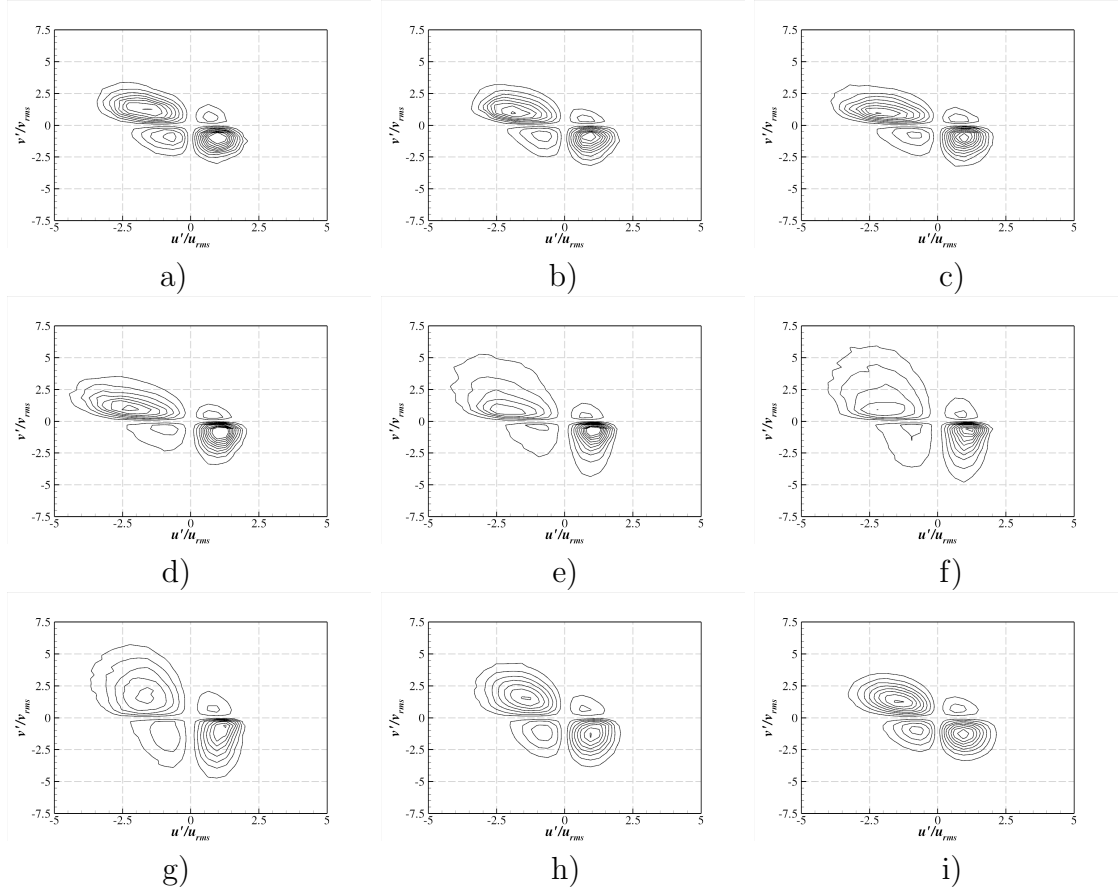


Figure 5.31: Weighted pdf of u' and v' at $y^+ = 50$ at several Reynolds numbers during the acceleration. For captions, see Figure 5.29. Same contour levels are used for all the figures.

5.9 Conclusions

Comprehensive turbulent statistics for DNS of temporal acceleration are presented in this chapter. Response of the wall shear stress, mean velocity and rms velocity fluctuations has been discussed in detail. The rms vorticity profiles has been presented with a detailed discussion of time histories of vorticity maximum values and wall-normal locations. The turbulent kinetic energy budget analysis has been presented. Finally, the quadrant analysis is presented to investigate the dynamics of energy producing Reynolds stress events. The findings of this chapter are as following

1. Four distinct stages of the wall shear stress response are found: the initial transient (IT) stage (stage I), the weak time-dependence (WT) stage (stage II), the strong time-dependence (ST) stage (stage III) and the pseudo-steady (PS) stage (stage IV). But, the PS stage is not included in the DNS. The IT stage is representative of tendency of uniform increase of the mean velocity across the channel after the onset of acceleration, the WT stage is the stage where rate of change of wall shear stress is lower than the steady value and finally the turbulence responds rapidly to the acceleration during the ST stage which is characterised by a sharp du_τ/dt increase over the steady value.
2. The displacement and momentum thickness reduce in the stage I and the stage II and recover in the stage III. The shape factor shows a two-stage variation: an initial reduction in the stage I is followed by a subsequent sharp increase during the stage II and a monotonic reduction during the stage III.
3. The mean velocity increase linearly in the core region due to flow inertia while it remains below the steady corresponding values in the near-wall region during the stage II. The near-wall mean velocity increases rapidly, afterwards, during the stage III resulting in adjustment of the mean velocity profile across the

5.9. CONCLUSIONS

channel.

4. The relation of the mean velocity and the wall shear stress (log-law) is broken during the acceleration exhibiting an under-prediction in the stage I and an over-prediction during the stage II before reverting back to the standard log-law profile at $Re = 15000$.
5. The rms velocity fluctuations exhibit a two-layer response to the imposed acceleration. Inner layer fluctuations respond first in the near-wall region after an initial delay, while the outer region intensities remain largely frozen for extended period of time.
6. \overline{uu} responds first in the near-wall to the acceleration, followed by $-\overline{uv}$ while \overline{vv} and \overline{ww} respond in the last.
7. The local equilibrium between turbulence and mean flow shows a distinct deviation from the steady values during the stage I and the stage II due to inability of turbulence to extract energy effectively from the mean flow during this period.
8. The rms vorticity fluctuations exhibit the similar delay in response as reported for rms velocity fluctuations. Wall-normal locations of $\omega'_{x,min}$, $\omega'_{x,max}$ and $\omega'_{y,max}$ show a two-stage decrease towards the steady y location due to an initial delay in response for the near-wall turbulent structures.
9. The turbulent production term for \overline{uu} transport equation extracts kinetic energy from mean flow in the near-wall region. Turbulent kinetic energy is redistributed among the lateral components by the pressure-strain term.
10. The number of events from fourth quadrant (Q_4) decreases during the stage II which is balanced by a corresponding increase in number of third quadrant events (Q_3) in the very near-wall region during the stage III. This deviation

of quadratic contributions from initial values reduces as the distance from the wall is increased and the outer layer region remains largely unchanged.

11. The quadratic contributions from Q_1 and Q_4 quadrants increase in the near-wall region during the stage III while vice versa is true for the Q_2 and Q_3 quadratic contributions.
12. The amplitude of v' fluctuations reduces significantly in the near-wall region during the later part of the stage II and increases rapidly afterwards during the stage III.

6

Effect of acceleration on turbulent structures.

Detailed turbulence statistics for turbulent channel flow subjected to temporal acceleration has been presented in Chapter 5. It was found that the near-wall region responds first during the acceleration, so it is imperative to analyse the response of near-wall structures. The effect of acceleration on the near-wall structures during the acceleration is analysed in detail with the help of low-speed streaks and λ_2 plots. Conditionally-averaged statistics are presented to clearly show two distinct flow regions during the acceleration and the new turbulence generation is discussed.

Turbulent structure response during the acceleration is determined with the help of Reynolds stress anisotropy analysis.

6.1 Low-speed streaks

It is well known that high- and low-speed streak patterns exist in the near-wall region of turbulent wall bounded flows. The low-speed streaks are the result of the counter-rotating streamwise vortices (Robinson, 1991). Extensive efforts have been made in the past to investigate the characteristics of the low-speed streaks. Kim et al. (1971) proposed that the turbulent kinetic energy is produced by “bursting”, which involves uplifting, oscillations and subsequent breakdown of the low-speed streaks. It is generally accepted that the near-wall mean spanwise spacing (λ_z^+) of these streaky structures is approximately 100 in wall units (Kline et al., 1967), and the streamwise extent of these streaks is reported to be approximately 1000 in wall units (Blackwelder and Eckelmann, 1979). λ_z^+ is found to increase linearly with the distance away from the wall in the buffer region ($2 \leq y^+ \leq 30$) (Smith and Metzler, 1983). Kim et al. (1987) used the two-point spanwise correlation of the streamwise fluctuations to determine the mean streak spacing in the log-layer. They verified the experimental observation of Smith and Metzler (1983) that the streak spacing increases linearly in the log-layer.

Figure 6.1a shows the variation of the mean streak spacing in y direction for a fully-developed turbulent channel at $Re = 3500$. The data in the present study are in good agreement with the data in literature, and it shows that the mean low-speed streak spacing increases linearly in the log-layer as the distance from the wall is increased. Figure 6.1b shows the two-point correlation coefficient for $u'u'$ in the spanwise direction at $y^+ = 10$ for several Reynolds numbers during the acceleration. The location of a local minimum at $Re = 3500$ is approximately at 50.

6.1. LOW-SPEED STREAKS

The streak spacing is generally taken as twice the distance to the local minimum of $R_{<u,u>}$. Therefore, λ_z^+ is approximately equal to 100 at the initial Reynolds number ($Re = 3500$). The location of the local minimum of two-point correlations is shifted away from the wall at $Re = 7000$ and $Re = 10000$, indicating a slight increase in the mean streak spacing in the stage II. The mean streak spacing recovers the steady value at $Re = 15000$. It is very interesting to note that the local minimum shifts above zero during the stage III ($Re = 12000$ and $Re = 13000$).

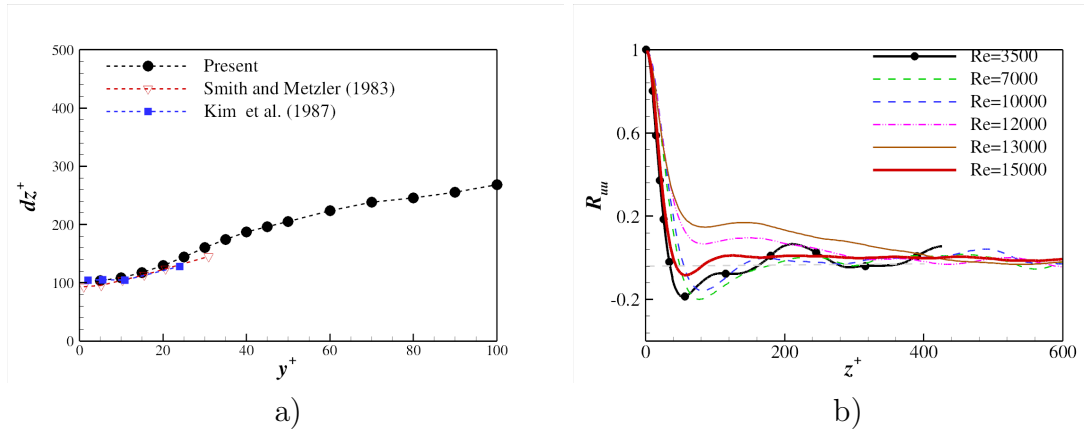


Figure 6.1: a) Variation of low-speed streak spacing in y direction for fully-developed turbulent channel flow at $Re = 3500$, and b) two-point spanwise correlation for $<u, u>$ at several Reynolds numbers during the acceleration. The DNS data of Kim et al. (1987) and experimental data of Smith and Metzler (1983) are included for comparison.

Figure 6.2 shows the instantaneous 2D contours of low-speed streaks in the near-wall region at several Reynolds numbers during the acceleration. It clearly shows that the low-speed streaks exist in two distinct length scales during the stage III (for example, $Re = 13000$). The streak patterns with smaller length scale are evolved during the stage III ($Re = 11000$ and onwards) as the new turbulence seems to scale with the local Reynolds number. The existence of low-speed streaks in two distinct length scale explains the shifting of two-point correlation during the stage III in Figure 6.1b. The streaks become slightly weaker in the early stages of the acceleration ($Re = 5000$), due to relatively higher corresponding mean velocity in the

CHAPTER 6. EFFECT OF ACCELERATION ON TURBULENT STRUCTURES.

near-wall region. It is worth noting that the streaks are elongated and straightened in the streamwise direction in the stage II ($Re = 7000$ and 9000). The streamwise elongation of low-speed streaks is also reported in the LES of accelerating boundary layer (Piomelli et al., 2000).

It is very interesting to note that these small-scale streaks have high amplitude u' (this can be clearly seen in Figure 6.14b), again supporting the already made observation that these streaks are from newly generated turbulent structures during the acceleration. It implies that there is a significant delay in the generation of the new turbulent structures in the near-wall region during acceleration, resulting in a subsequent delay in turbulence response. The large-scale streaks reduce rapidly during the stage III with the evolution of the new small-scale streaks. It is worth noting that the new streak patterns evolve in form of patches during the stage III. At $Re = 15000$, almost the entire wall is filled with the new streaks.

6.1. LOW-SPEED STREAKS

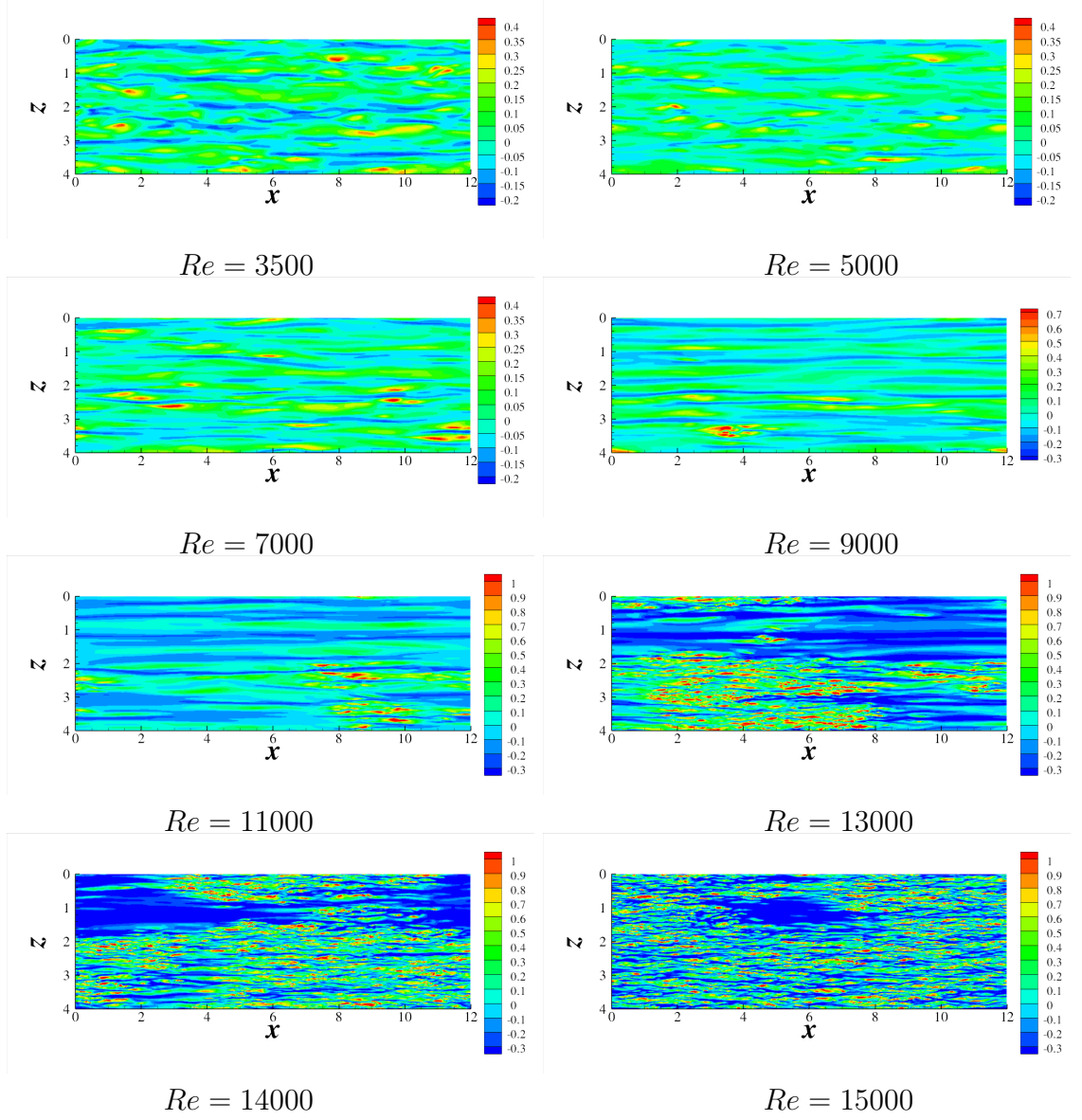


Figure 6.2: Instantaneous low-speed streak plots at $y^+ = 5$ during the acceleration for a realisation.

6.2 Structures visualisation

Jeong and Hussain (1995) proposed the λ_2 -criterion to visualise the near-wall turbulent structures. RMS of λ_2 , λ'_2 , gives an indication of the strength of the turbulent structures. λ'_2 profiles for fully-developed turbulent channel flow at several Reynolds numbers are already shown in Chapter 4 (cf. Figure 4.10). The y location of the maximum λ'_2 , $\lambda'_{2,max}$, lies in the near-wall region at $y^+ \approx 20$ (Jeong et al., 1997). Figure 6.3a shows the variation of $\lambda'_{2,max}$ at several Reynolds numbers during the acceleration. Please note that the $\lambda'_{2,max}$ is non-dimensionalised based on the initial bulk-mean velocity for the steady values. This figure clearly shows that the near-wall turbulent structures exhibit an initial delay in the stage II. $\lambda'_{2,max}$ increases initially at relatively smaller rate until $Re = 8000$ and starts to increase rapidly afterwards, with the initiation of new turbulence generation. The rate of increase of $\lambda'_{2,max}$ is highest during the stage III. This trend indicates that turbulence generation is strong during the stage III. It is worth noting that the rate of increase for $\lambda'_{2,max}$ acquires the pseudo-steady value towards the end of the stage III ($Re = 15000$). The breakdown of equilibrium between the near-wall turbulent structures and the mean flow is clearly seen by replotting the $\lambda'_{2,max}$ values normalised by the local bulk-mean velocity. The ratio $\lambda'_{2,max}/U_m^2$ decreases in the early part of the stage II and starts to increase afterwards rapidly during the stage III.

The generation of new turbulence during the acceleration can be better visualised using iso-surface contour plots of λ_2 as shown Figures 6.4 and 6.5. Please note that the λ_2 contour value increase with increase in Re during the acceleration. $\lambda'_{2,max}$ is chosen as the λ'_2 contour values as suggested by Dubief and Delcayre (2000). The λ_2 contour plot at $Re = 3500$ contains familiar turbulent structures for the fully-developed turbulent channel flow. After a substantial initial delay, the new turbulence generation is clearly seen at $Re = 10000$. The newly generated turbulent structures are much smaller than the initial structures. On the other hand, the

6.2. STRUCTURES VISUALISATION

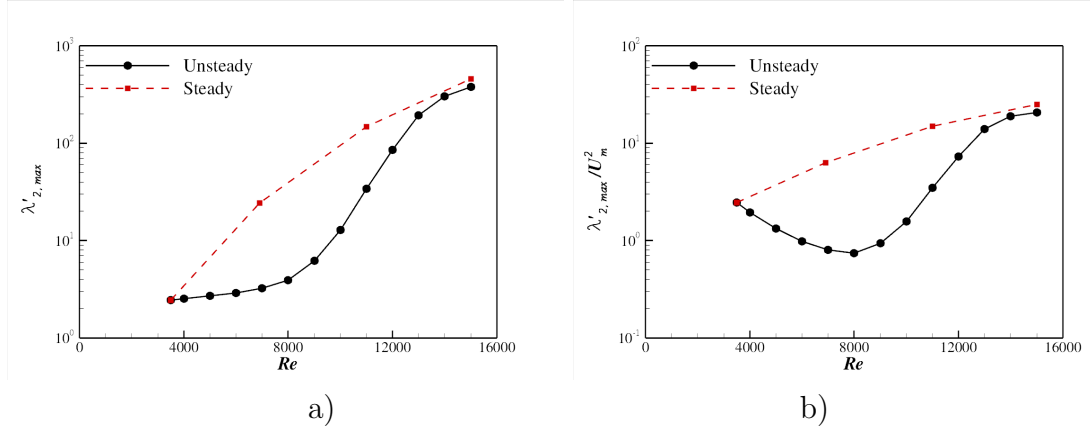


Figure 6.3: Time histories of a) $\lambda'_{2,max}$, and b) $\lambda'_{2,max}/U_m^2$ during the acceleration. Steady DNS data are also included for comparison.

corresponding λ_2 contour value at $Re = 10000$ is significantly higher than the value at $Re = 3500$, indicating that the the new turbulence structures are much stronger than the initial structures. This is consistent with the observations made in the low-speed streak plots in Figure 6.2. The newly generated turbulent structures result in the small-scale streaks during the stage III.

The turbulent structures remain largely unchanged during the stage I of the acceleration, and are slightly elongated in the streamwise direction during the stage II ($Re = 6000$ and onwards). The streamwise elongation of turbulent structures is also reported in turbulent boundary layer subjected to FPG studies (Warnack and Fernholz, 1998; Piomelli et al., 2000). The local equilibrium between turbulence and the mean flow is weakened in the stage II with the mean flow being dominant. This results in a substantial initial delay in the generation of new turbulent structures during the stage II. The flow field can be thought of existing in laminarescent state during the stage I and the stage II, as suggested by Sreenivasan (1982).

The turbulence generation process becomes stronger during the stage III as shown in Figure 6.5. The new turbulent structures cover approximately the entire wall area at $Re = 15000$. The rapid generation of new structures results in a sharp increase of the $\lambda'_{2,max}$ value during the stage III (cf. Figure 6.3). It is worth noting that the strong

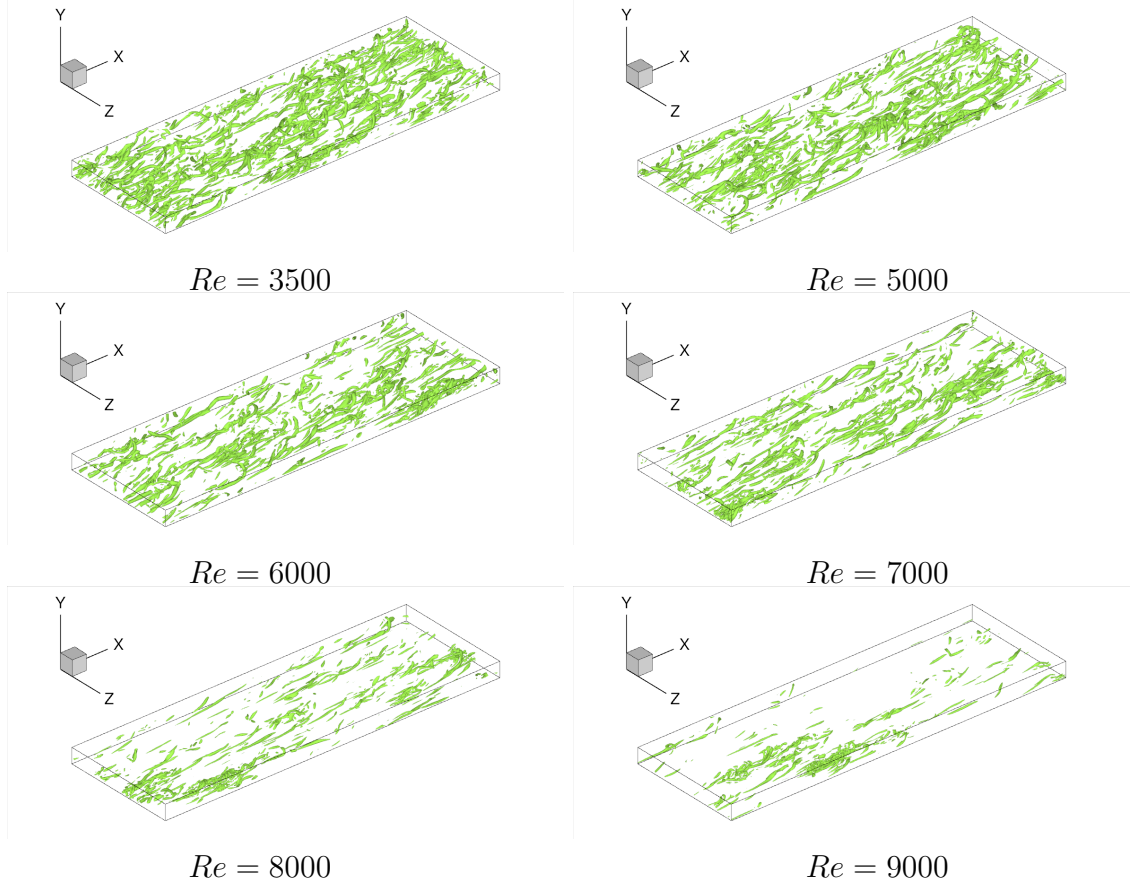


Figure 6.4: λ_2 iso-surfaces during the acceleration during the stage I and the stage II.

turbulence evolves in the form of patches during the stage III, while weak large-scale streaks are found in the rest of the wall area. This evolution trend for the stronger structures can be clearly seen in Figure 6.6, which shows the 2D instantaneous streamwise vorticity contours at several instances during the acceleration. The size of the turbulent structures remain largely unchanged in the stage II at $Re = 7000$ while it reduces sharply at $Re = 12000$. The new turbulent structures are evolved in the very near-wall region. It is clearly seen at $Re = 15000$ that the new turbulent structures have much smaller length scales as compared to the initial turbulence. It is interesting to note that the wall shear stress at this Reynolds number is the same as the steady value while τ_w is significantly lower than the steady values for much of the acceleration (cf. Figure 5.1a).

6.2. STRUCTURES VISUALISATION

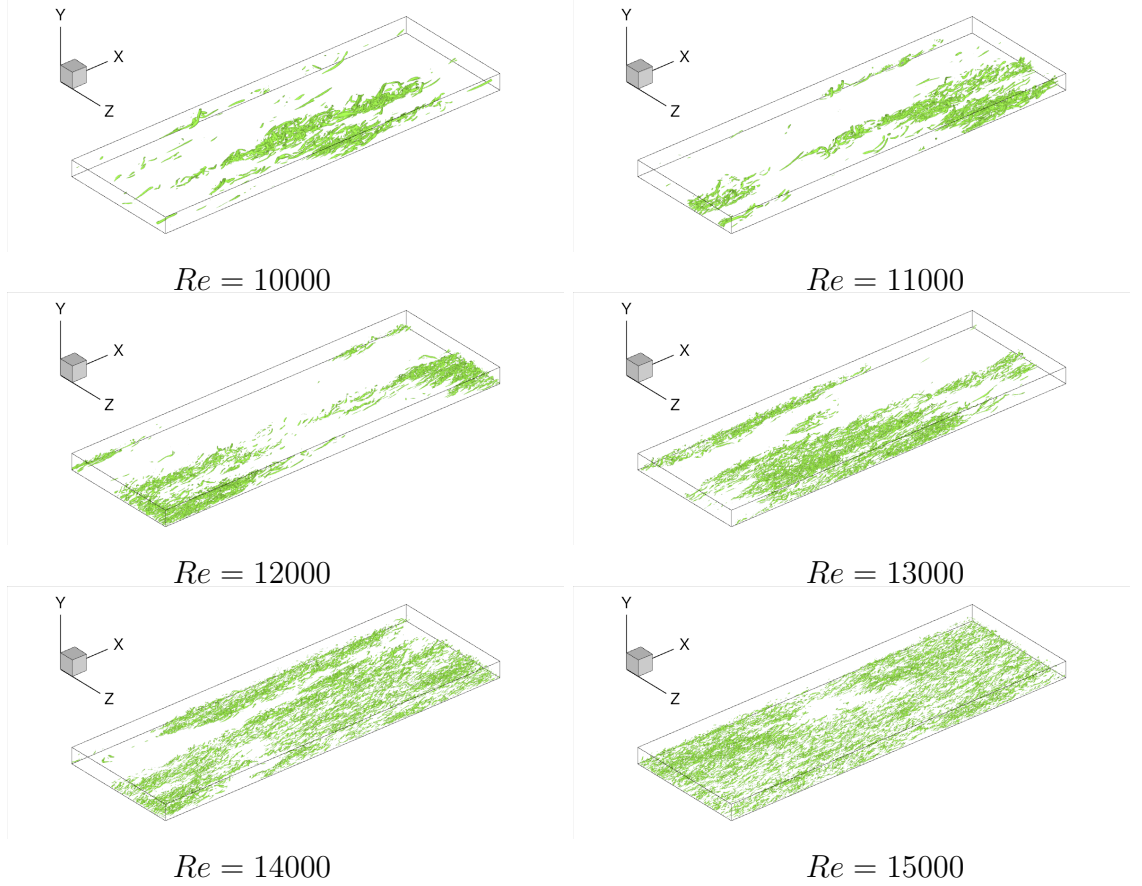


Figure 6.5: λ_2 iso-surfaces during the acceleration during the stage III.

The new turbulent structures evolution in distinct patches during the stage III is clearly seen in Figure 6.5. Figure 6.7 shows the iso-surfaces for four realisations at $Re = 11000$. Two contour levels are used: the local $\lambda'_{2,max}$ (red, dark contour lines) and the initial $\lambda'_{2,max}$ (blue, bright contour lines). Please note that the red contour lines show turbulent structures approximately 12 times stronger than the initial structures at $Re = 3500$. The stronger structures in all the plots are significantly smaller in size again supporting the earlier observation that these structures are generated during the acceleration. It is interesting to note that the smaller structures generation is accompanied with the breakdown of the relatively large weaker structures, indicating the possible evolution of the smaller structures from the larger structures.

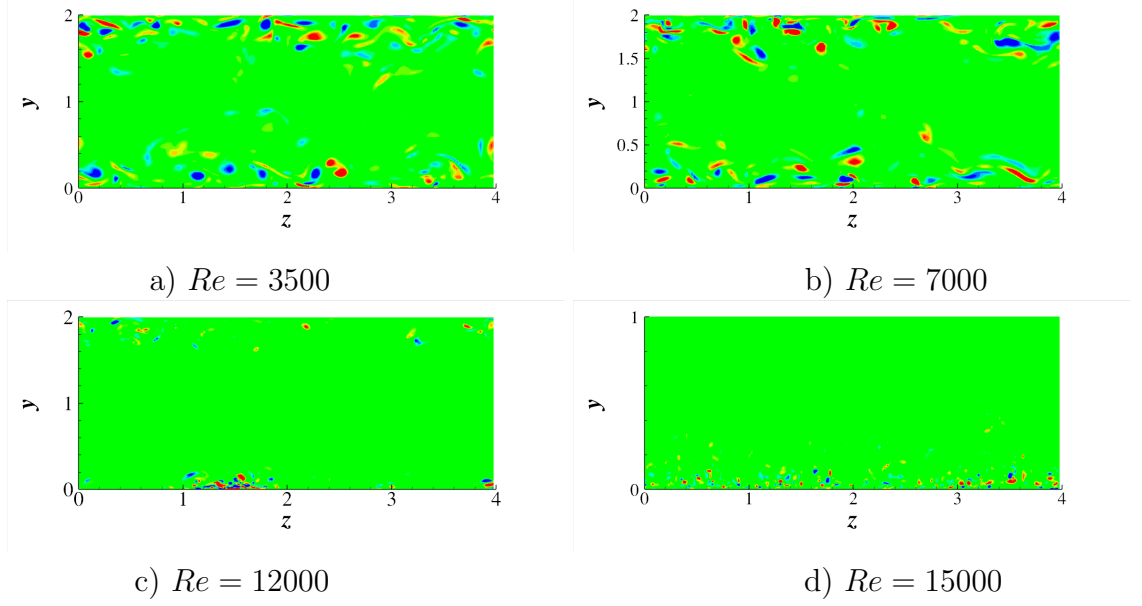


Figure 6.6: Contour plots of the instantaneous streamwise vorticity at several instances during the acceleration.

Flow visualisations presented in this subsection have revealed many interesting trends for the near-wall structures response during the acceleration. Turbulent structures are elongated in the streamwise direction during the stage II. New turbulence is generated during the stage III in forms of distinct patches while the rest of the wall area remains at significantly less turbulent intensity. The relatively weak turbulent structures in the stage III have a size comparable to the initial structures. The new turbulent structures are probably evolved from within the old turbulent structures.

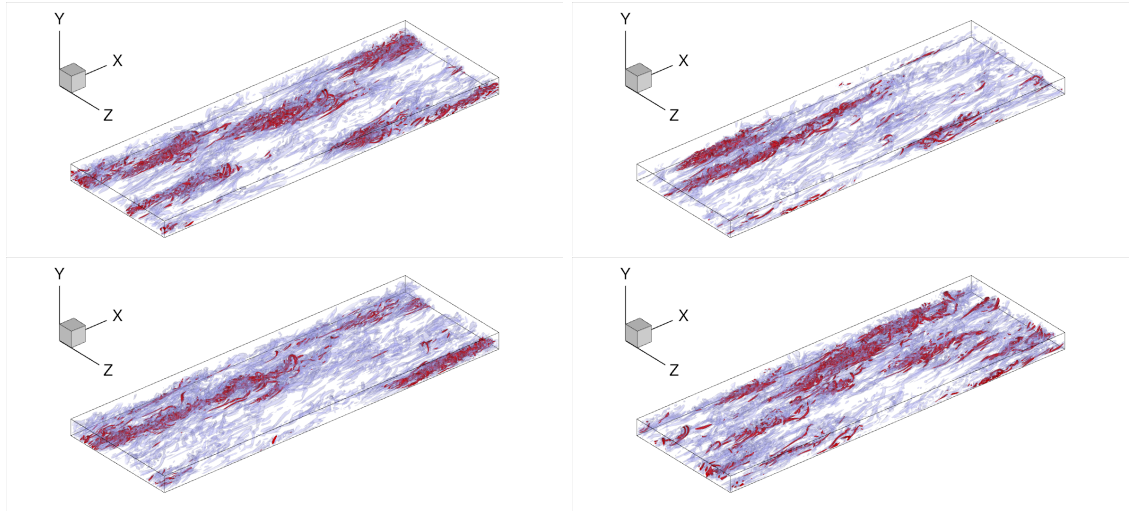


Figure 6.7: Iso-surfaces of λ_2 at $Re = 11000$ for four different realisations. Blue (bright) contour lines denote the iso-surfaces at the initial $\lambda'_{2,max}$ value while red (dark) contour lines denote the iso-surfaces at the local $\lambda'_{2,max}$.

6.3 Active area quantification procedure

Figure 6.7 show the evolution of the new turbulence in form of distinct patches during the stage III. It is worth noting that only a fraction of wall area is filled with the new turbulence during the initial part of the stage III ($Re = 11000$) while the rest of the area can still be characterised by the initial turbulent flow. This particular observation motivates to quantify and study the characteristics for these two distinct regions using conditional averaging. The terms *active* and *non-active* areas are used to indicate the new turbulent area and the less turbulent area respectively. The conditionally-averaged statistics are then used to characterise the turbulence in the active and non-active areas.

λ'_2 is used for this active area quantification procedure (AAQP), where “'” indicates the absolute fluctuations. Jeong et al. (1997) used the absolute fluctuations of λ_2 in their turbulent structures eduction scheme for determining the size and shape of the coherent structures in the near-wall region. They argued that the λ'_2 is a better choice for eduction of coherent structures than $\overline{\lambda_2}$ because of the cancellation of positive λ_2 values with the negative counterpart in the buffer region ($10 \leq y^+ \leq 30$). PDF of λ'_2 is shown in Figure 6.8 for steady turbulent channel flow at $Re = 3500$ and for accelerating channel flow at $Re = 7000, 11000$ and 15000 . Please note that the pdf is constructed using fluctuations data four realisations (top as well as bottom halves). Figure 6.8 shows that the negative and positive fluctuations are symmetric for steady equilibrium turbulence as well as for the present acceleration case.

As new turbulence is generated in form of patches during the stage III, the criterion for AAQP should be capable of separating the active areas from the non-active areas as a whole rather than an individual control volume. Therefore, the criterion is based on the comparison of 3D average λ'_2 value around each control volume with a *base* value (this is discussed later). The size of this window in xz plane is chosen

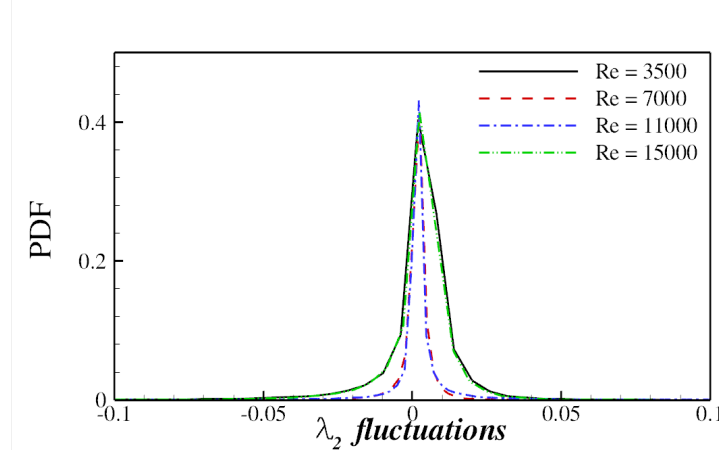


Figure 6.8: PDF of λ_2 fluctuations at the y location for the maximum λ_2' at several Re numbers during the acceleration. Steady data at $Re = 11000$ are also included.

as $(\Delta x^+, \Delta z^+) = (150, 40)$. Jeong et al. (1997) used the same window size for the cross-correlation calculations in their structures eduction scheme. It is important to note that the averaging in xz plane is performed in order to separate regions of active area rather than individual control volumes in the near-wall region, and the averaging in the y direction is also performed. Jeong et al. (1997) employed a wall-normal window size of $0 \leq y^+ \leq 40$ for the eduction of the near-wall structures. Stanislas et al. (2008) found in their experimental study of turbulent boundary layer that the near-wall region is richly populated with the eddy structures in the range of $y^+ \leq 150$. Therefore, the wall-normal integral window size of $y^+ = 150$ is chosen in the current study.

The *base* value is chosen as the xz plane-averaged λ_2' value *i.e.*, $\lambda_{2, plane}'$, for comparison with the 3D local-averaged value *i.e.*, $\lambda_{2, l}'$ at each control volume in the near-wall region. The relationship of $\lambda_{2, l}'$ to the $\lambda_{2, plane}'$ is determined from the fully-developed channel flow at several Reynolds numbers. The near-wall region in the fully-developed turbulent flow is assumed to be completely filled with structures (suppose 99%). Therefore, pdf for $\lambda_{2, l}'$ are produced at several Reynolds numbers for fully-developed turbulent cases in order to determine relation between $\lambda_{2, l}'$ and $\lambda_{2, plane}'$. The 3D window size used for $\lambda_{2, l}'$ is $(\Delta x^+, \Delta y^+, \Delta z^+) = (150, 150, 40)$ as

CHAPTER 6. EFFECT OF ACCELERATION ON TURBULENT STRUCTURES.

discussed previously. Data sampling convergence is ensured by taking data from approximately two million control volumes for the pdf at $Re = 3500, 6900$ and 11000 , as shown in Figure 6.9. Please note that all λ'_2 values are in local wall units. The respective ratio of the *cut-off* $\lambda'_{2,l}$ to the corresponding $\lambda'_{2,plane}$ are tabulated in Table 6.1. The *cut-off* $\lambda'_{2,l}$ value is chosen as the $\lambda'_{2,l}$ value comprising 1% of pdf. The ratio of the *cut-off* $\lambda'_{2,l}$ to $\lambda'_{2,plane}$ is in the range of 0.14 to 0.2. Based on this ratio, the criterion for active area is formulated as follows: if $\lambda'_{2,l}$ value for a control volume is greater than 10% of the corresponding $\lambda'_{2,plane}$ value, the control volume would be regarded as part of active area. It can be mathematically written as

$$\begin{aligned} \lambda'_{2,l} &\geq \frac{0.1}{N_y} \sum_{j=1}^{N_y^*} \lambda'_{2,plane} \Rightarrow \text{Active area,} \\ \lambda'_{2,l} &< \frac{0.1}{N_y} \sum_{j=1}^{N_y^*} \lambda'_{2,plane} \Rightarrow \text{Non-Active area,} \end{aligned} \quad (6.1)$$

where N_y^* are the number of control volumes in the the wall-normal direction.

Re	$\lambda'_{2,plane}$	<i>cut-off</i> $\lambda'_{2,l}$	Ratio
3500	8.0×10^{-3}	1.1×10^{-3}	0.14
6900	8.5×10^{-3}	1.7×10^{-3}	0.20
1100	1.0×10^{-2}	1.5×10^{-3}	0.15

Table 6.1: Ratio of cut-off λ'_2 to the $\lambda'_{2,plane}$. 3D integral $\lambda_{2,plane}$ and *cut-off* λ'_2 are shown in Figure 6.9. All values are in local wall units.

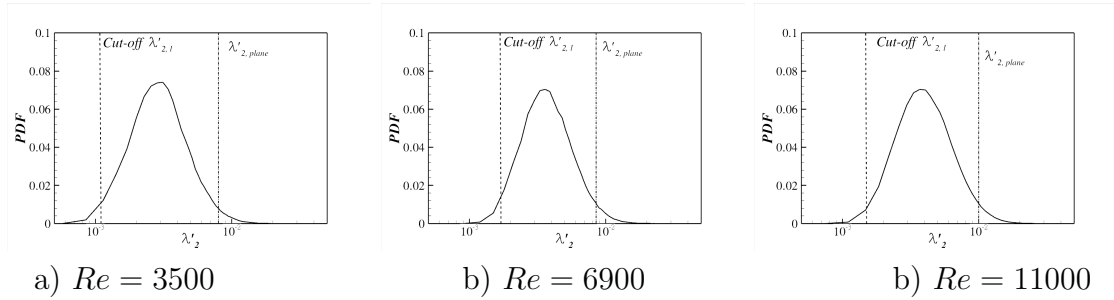


Figure 6.9: PDF of λ'_2 for fully-developed turbulent channel flow at several Reynolds numbers.

6.3. ACTIVE AREA QUANTIFICATION PROCEDURE

Figure 6.10 shows an instantaneous 3D snapshot of λ_2 iso-surfaces during the acceleration at $Re = 12000$. It clearly shows that the local xz plane averaging indeed plays a smoothing role in the AAQP and facilitates the core objective of separating the patches of turbulent areas from non-active ones. A parametric study was conducted by increasing the window sizes separately in each direction with no significant change found from the base window size, *i.e.*, ($\Delta x^+ = 150$, $\Delta z^+ = 40$) for several realisations. Figure 6.10b shows that there is very little change beyond $y^+ \geq 150$. This trend is consistent with the findings of Stanislas et al. (2008) that the near-wall region is richly populated with structures in the region $y^+ \leq 150$.

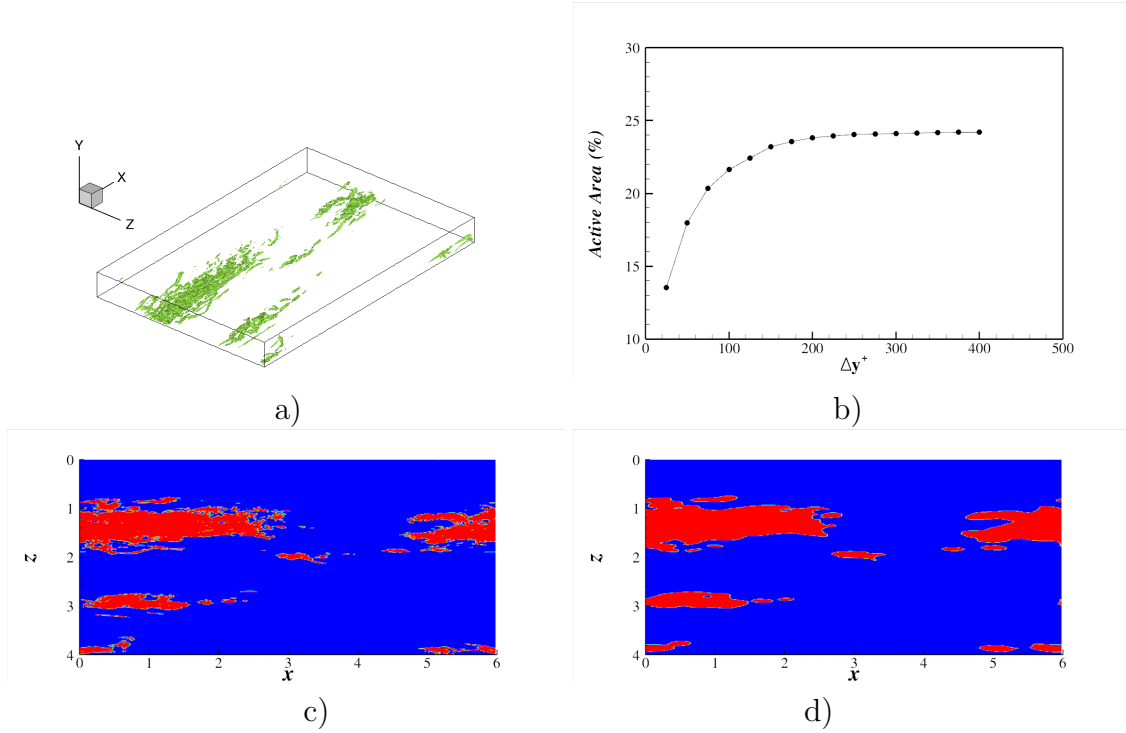


Figure 6.10: Instantaneous iso-surface contour plot of λ_2 during the acceleration at $Re = 12000$. b) effect of wall-normal integration window on the AAQP for the snapshot shown in a), c) the AAQP without xz plane averaging, d) the AAQP with xz plane averaging. Red contour lines show the active area while the blue lines represent non-active area.

The size of near-wall structures decreases during the acceleration at high Reynolds numbers. Therefore, the local u_τ value is used to determine the 3D test window size. The conditionally-averaged u_τ value from the active area is employed in the current

CHAPTER 6. EFFECT OF ACCELERATION ON TURBULENT STRUCTURES.

study because of the high u_τ value in the active area. Since, the conditionally-averaged u_τ value is unknown at the start of the AAQP, the following iterative procedure is used to update u_τ .

1. Use plane-averaged u_τ value.
2. Determine the physical size of the test window *i.e.*, $150 \times 150 \times 40$ in wall units based on the u_τ value from Step 1.
3. Calculate $\lambda'_{2,l}$ and $\lambda'_{2,plane}$.
4. Identify the active areas by using the criterion in Equation 6.1.
5. Calculate conditionally-averaged value of u_τ for each region.
6. Repeat the procedure until the convergence of u_τ is achieved.

Less than ten iterations were needed to achieve the convergence of the conditionally-averaged u_τ value. Based upon the formulated AAQP, the active area has been quantified at several Reynolds numbers during the acceleration. Please note that this procedure is applied to five realisations with both bottom and top halves of the channels used. Figure 6.11 shows the variation of active area during the acceleration. At $Re = 11000$, almost 75% of the wall area still contains old turbulence. The active area increases rapidly with the generation of new turbulence exhibiting approximately an exponential trend during the stage III, and it achieves the pseudo-steady value at $Re = 15000$. This is consistent with the turbulence generation shown using iso-surfaces for λ_2 in Figure 6.5. The rapid increase in active area during the stage III shows the generation of new turbulence.

It is important to note that the criterion introduced in Equation 6.1 separates the non-active area from the active area based on the assumption that almost the entire wall area is active in case of fully-developed turbulent channel case. Therefore,

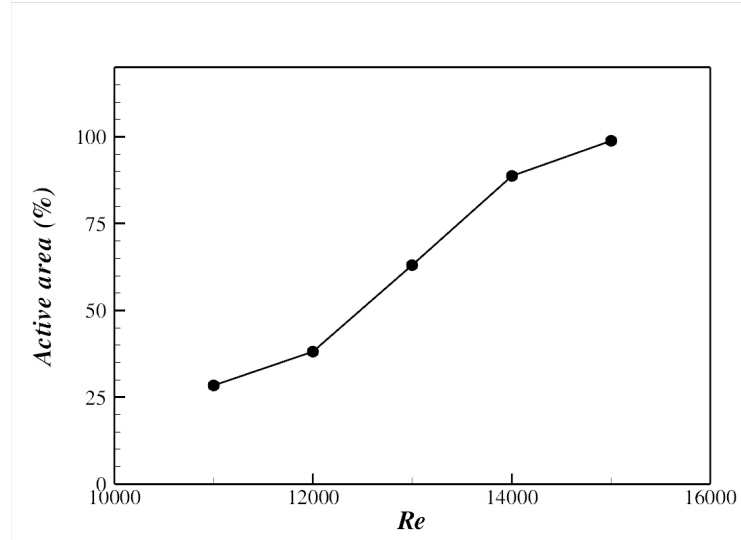


Figure 6.11: Active area at different stages of acceleration.

this criterion separates the weak turbulent regions effectively. The conditionally-averaged statistics for both active and non-active areas are presented in Subsection 6.4.

6.4 Conditional average statistics

Turbulence statistics are calculated for the active and non-active areas in order to investigate flow characteristics for active and non-active areas. Figure 6.12 shows the conditionally-averaged λ'_2 profiles at $Re = 11000$ for the two flow regions. The log scale is used for the abscissa to show the statistics in the near-wall region clearly. The difference between the λ'_2 levels in the near-wall region is very large for the two areas. It is worth mentioning that the ratio of the maximum λ'_2 for the active and non-active areas is almost 12, which is consistent with the ratio of higher λ_2 contour value (red lines) to the lower λ_2 contour value (blue lines) in Figure 6.7. It is interesting to note that the strength of near-wall structures in the non-active area is approximately similar to the initial turbulence. This implies that the turbulent structures in approximately 75% of the near-wall region at $Re = 11000$ (cf. Figure 6.11) are comparable to the initial structures at $Re = 3500$.

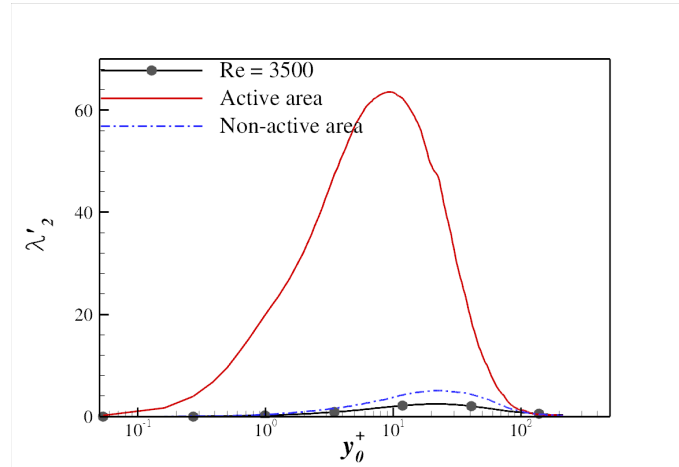


Figure 6.12: Conditionally-averaged λ'_2 profiles at $Re = 11000$ for the active and non-active areas. λ'_2 profile at the initial Reynolds number ($Re = 3500$) is also included for comparison.

Figure 6.13a shows the time histories of maximum λ'_2 in the two areas. Corresponding steady profiles are also included in each graph for comparison. Please note that the time histories are shown from $Re = 9000$ where the active area has reduced to

6.4. CONDITIONAL AVERAGE STATISTICS

80% of the whole near-wall region (cf. Figure 6.11). The difference between the strengths of turbulent structures can be clearly seen. It is interesting to note that the rate of increase of λ'_2 is similar for both areas, when they are plotted using log scale. The u_τ variation for both areas in Figure 6.13b clearly demonstrates that the active area has higher wall shear stress values as compared to the non-active area. It is worth noting that the rate of increase of the wall shear stress in the active area is higher than in the non-active area.

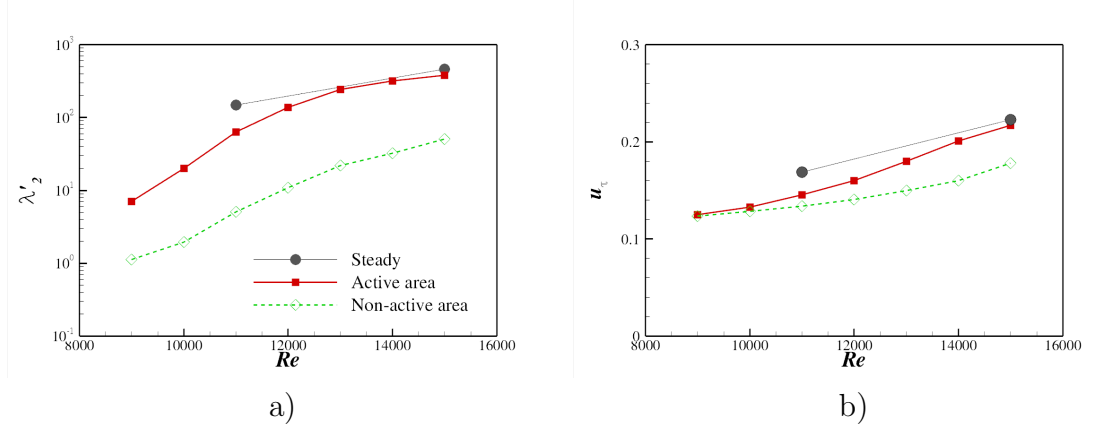


Figure 6.13: Time histories of conditionally-averaged a) maximum λ'_2 b) u_τ at several Reynolds numbers during the acceleration.

Figure 6.14 shows the conditionally-averaged profiles for the mean velocity and rms velocity fluctuations at $Re = 11000$. Steady DNS profiles are also included for comparison. The mean velocity in the near-wall region is higher for the active area in Figure 6.14a. This near-wall trend of the mean velocity in the active area is consistent with the higher u_τ value in Figure 6.13. It is interesting to note that the mean velocity in the active area is still less than the steady value in the near-wall region. The mean velocity in the core region is quite similar for active and non-active areas which indicates that the effect of the new turbulence is only confined to the near-wall region. The rms velocity fluctuation profiles exhibit much significant difference between the active and non-active areas while the outer layer intensities are again similar for both areas. The significant level of difference between the

turbulent intensities during the acceleration supports the earlier observation of new turbulent generation in form of patches during the stage III. It is interesting to note that the u_{rms} maximum value for the active area is greater than the corresponding steady value in Figure 6.14b indicating much stronger response of turbulence after initial delay. The y locations of all three fluctuations is nearer to the wall for the active area indicating the existence of newly generated turbulence nearer to the wall.

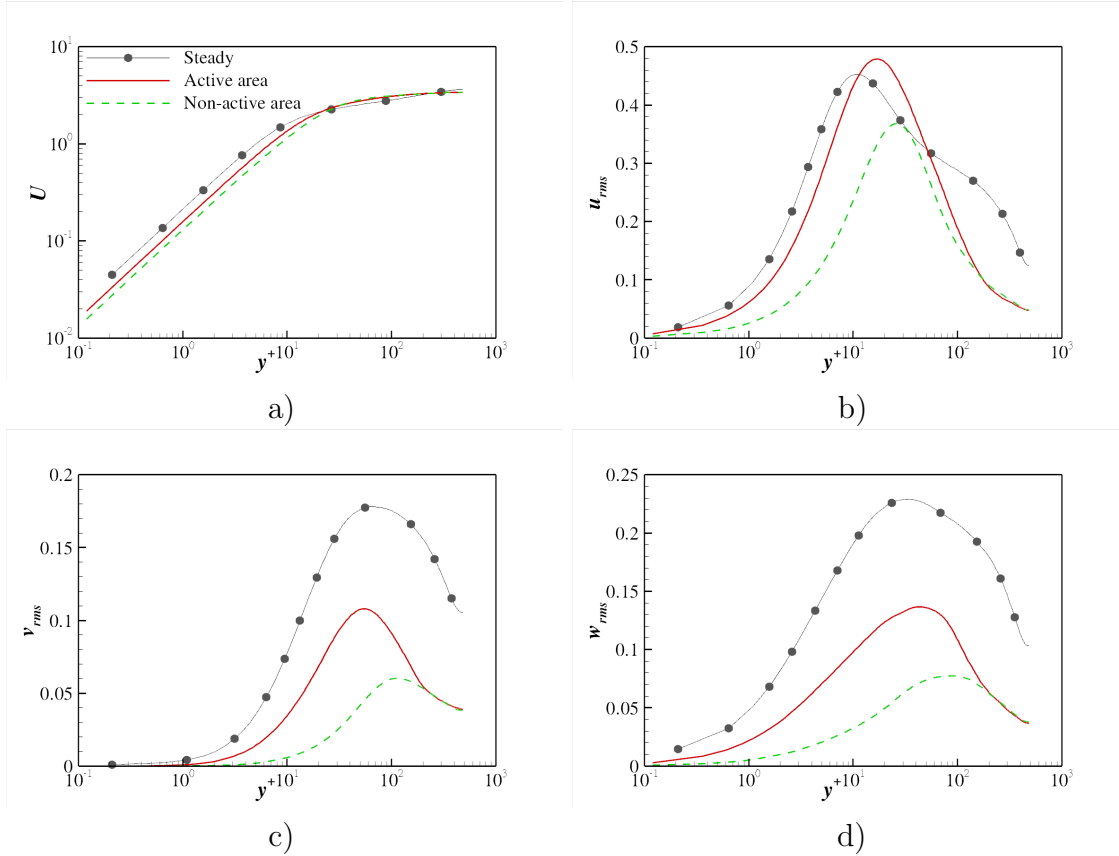


Figure 6.14: Conditionally-averaged profiles for a) mean velocity, b) u_{rms} , c) v_{rms} and d) w_{rms} during the stage III at $Re = 11000$. Local plane averaged u_τ is used for y^+ calculation.

The effect of conditional averaging on the rms vorticity fluctuations is shown in Figure 6.15 which shows conditionally-averaged rms vorticity profiles. A log scale is used for the abscissa to clearly see the near-wall trends. The much higher values for all three vorticity components in the active area again confirms the earlier observation of turbulent structures of two different strengths during the acceleration.

6.4. CONDITIONAL AVERAGE STATISTICS

Please note that the vorticity fluctuations in the active area is still less than the the corresponding steady values in the very near-wall region at this stage. The strength of ω'_y and ω'_z for active area is comparable with the corresponding steady vorticity values in the buffer layer indicating the new turbulence generation.

It is interesting to note that the y locations for $\omega'_{x,min}$ and $\omega'_{x,max}$ in the active area are nearer to wall as compared to the non-active area as shown in Figure 6.15. This behaviour indicates that the new turbulence stays nearer to the wall while the non-active area contains turbulent structures further away from the wall. The location of ω'_x in the non-active area can be seen more clearly in Figure 6.16. The initial ω'_x profile at $Re = 3500$ is also included for comparison. Figure 6.16 shows that the y locations of $\omega'_{x,min}$ and $\omega'_{x,max}$ at $Re = 9000$ in the non-active area is approximately the same as those y locations at initial Reynolds number ($Re = 3500$). It is also very interesting to note that the vorticity level for the non-active area is less than the initial level in the near-wall region, indicating the weakening of turbulent structures in the stage II. The similar near-wall vorticity values also indicate that the turbulence in the non-active area has the characteristics of the initial turbulence.

The near-wall vorticity value increases in the non-active area during the stage III, and $\omega'_{x,min}$ and $\omega'_{x,max}$ locations move towards the wall as well. The time histories of $\omega'_{x,min}$ and $\omega'_{x,max}$ are shown for the active and non-active areas in Figure 6.17. The y location of the streamwise vorticity decreases sharply in the stage III and the non-active mean vorticity y location remains away from the wall as compared to the active area value. The higher y location for $\omega'_{x,min}$ indicates that the thickness of the viscous sublayer in the non-active area is greater, as $\omega'_{x,min}$ location represents the edge of the viscous sublayer (Kim et al., 1987).

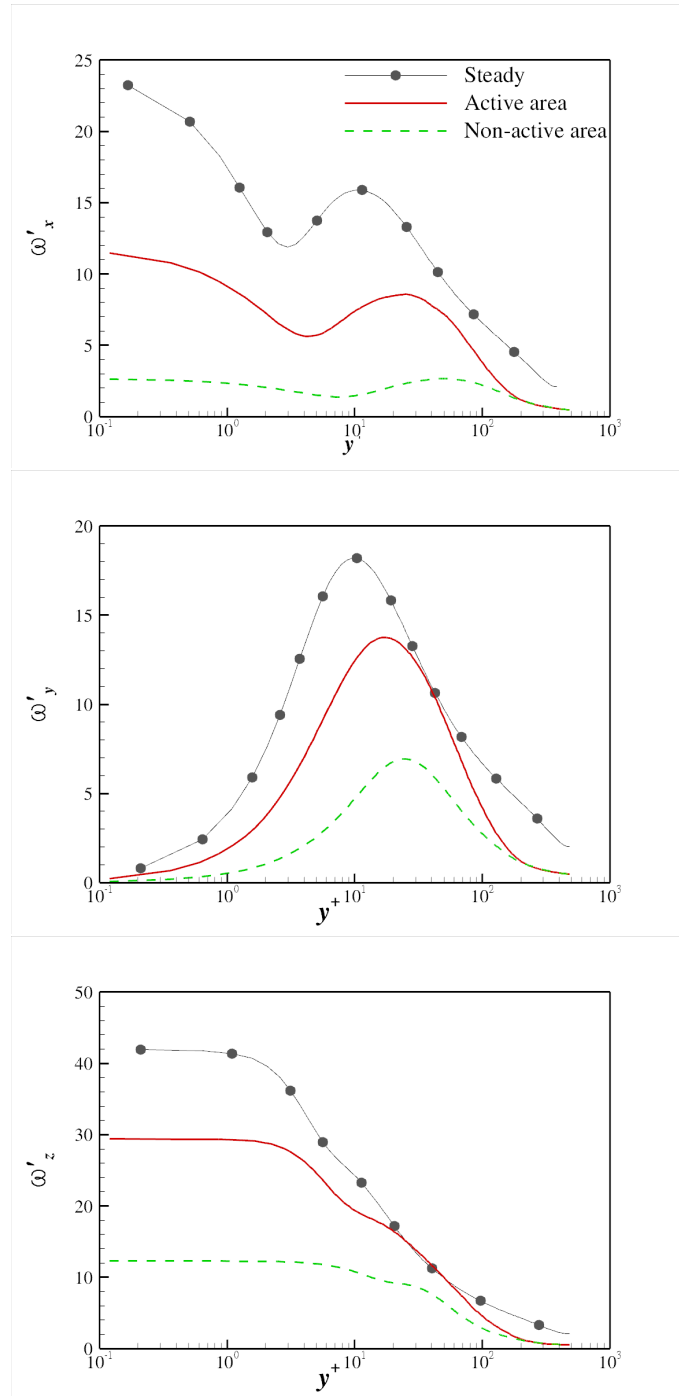


Figure 6.15: Conditionally-averaged rms vorticity profiles during the stage III at $Re = 11000$. Local plane averaged u_τ is used for y^+ calculation.

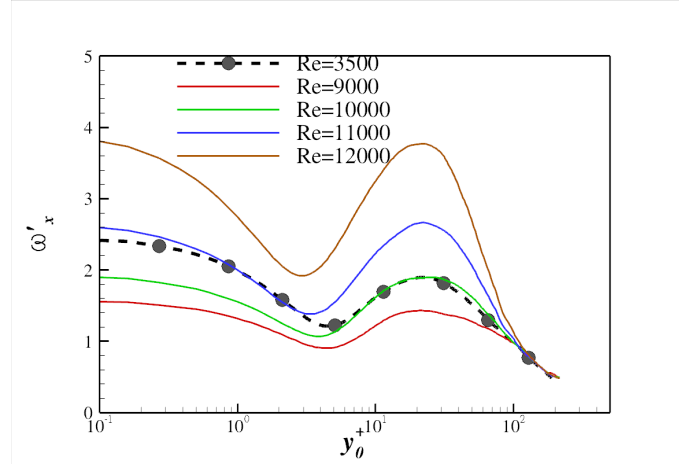


Figure 6.16: ω'_x profiles for the non-active area at several Reynolds numbers during the acceleration.

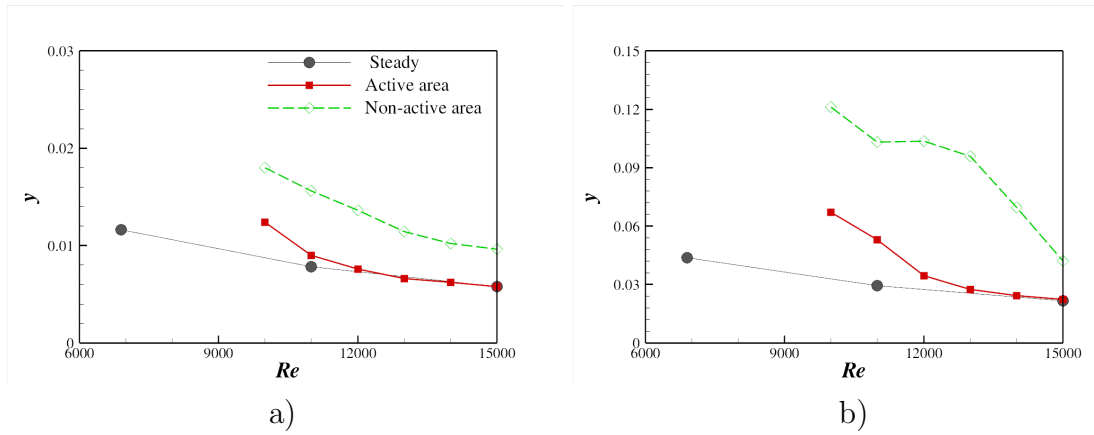


Figure 6.17: Time histories of a) $\omega'_{x,min}$, and b) $\omega'_{x,max}$ for the conditionally-averaged data.

6.5 Reynolds stress anisotropy tensor analysis

The response of the Reynolds stresses during the temporal acceleration has been investigated using the response times and rms velocity fluctuations profiles and time histories for each component in Chapter 5. The earlier response of \overline{uu} component is observed in the near-wall region, followed by $-\overline{uv}$, \overline{vv} , and \overline{ww} . In this section, the anisotropic response of turbulent flow is investigated using the Reynolds stress anisotropy tensor analysis.

Figure 6.18 shows the time histories of the anisotropy tensor at several y locations. The streamwise component of the anisotropy tensor, b_{11} , exhibits an initial increase in the near-wall region, followed by a significant decrease during the stage III. The initial increase of b_{11} is consistent with the fastest response time for \overline{uu} (cf. Table 5.4). b_{33} also becomes more anisotropic during the stage II in the near-wall region. The wall-normal component b_{22} is largely unchanged at $y = 0.005h$ and it is attributed to the suppression of v' in the viscous sublayer (Kim et al., 1987). The near-wall anisotropy for b_{22} and b_{33} decreases during the stage III with the rapid increase in v' and w' . The absolute value of b_{12} exhibits an initial decrease in the stage II followed by a subsequent increase in the stage III. The initial decrease in b_{12} indicates the unresponsiveness of turbulence in the stage II. Time histories of b_{12} are consistent with the time histories of the structure parameter a_1 (cf. Figure 5.17) with shear stress lagging behind the kinetic energy.

The anisotropy remains largely unaffected in the channel core during the acceleration as observed in Figure 6.18. Therefore, the anisotropy tensor profiles are plotted in the near-wall region in Figure 6.19 to study the near-wall variations of turbulence structure. The increase in anisotropy is clearly seen in the stage I and the stage II. On the other hand, the turbulent isotropy exhibit an increase during the stage III with the initiation of turbulence generation, and attains approximately the steady

6.5. REYNOLDS STRESS ANISOTROPY TENSOR ANALYSIS

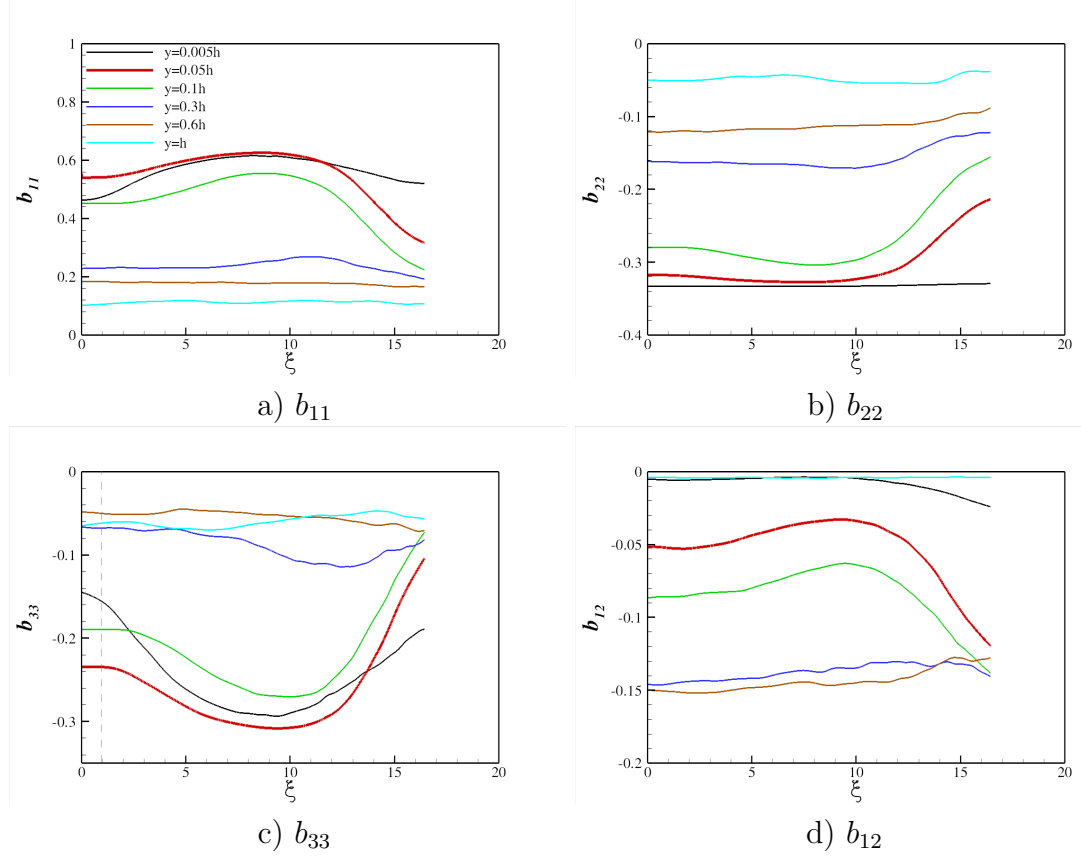


Figure 6.18: Time histories of anisotropy stress tensor terms at several y locations during the acceleration.

isotropy values at $Re = 15000$. Chung et al. (2002) reported an increase in the turbulence anisotropy due to suppression of transverse (v' and w') fluctuations in case of a localised suction in a DNS study of turbulent channel flow whereas an increase in isotropy was found in case of a localised blowing due to enhanced turbulent motions. The same reasons may be attributed to explain the turbulence anisotropy increase during the stage I and the stage II, and a subsequent reduction during the stage III.

Figure 6.20 shows the 2D variation of the second (II) and third (III) invariants of anisotropy tensor. The data at the initial Re are also included. A substantial increase in the anisotropy can be seen more clearly during the stage I and the stage II. The turbulence anisotropy increases until approximately $Re = 10000$. Turbulent

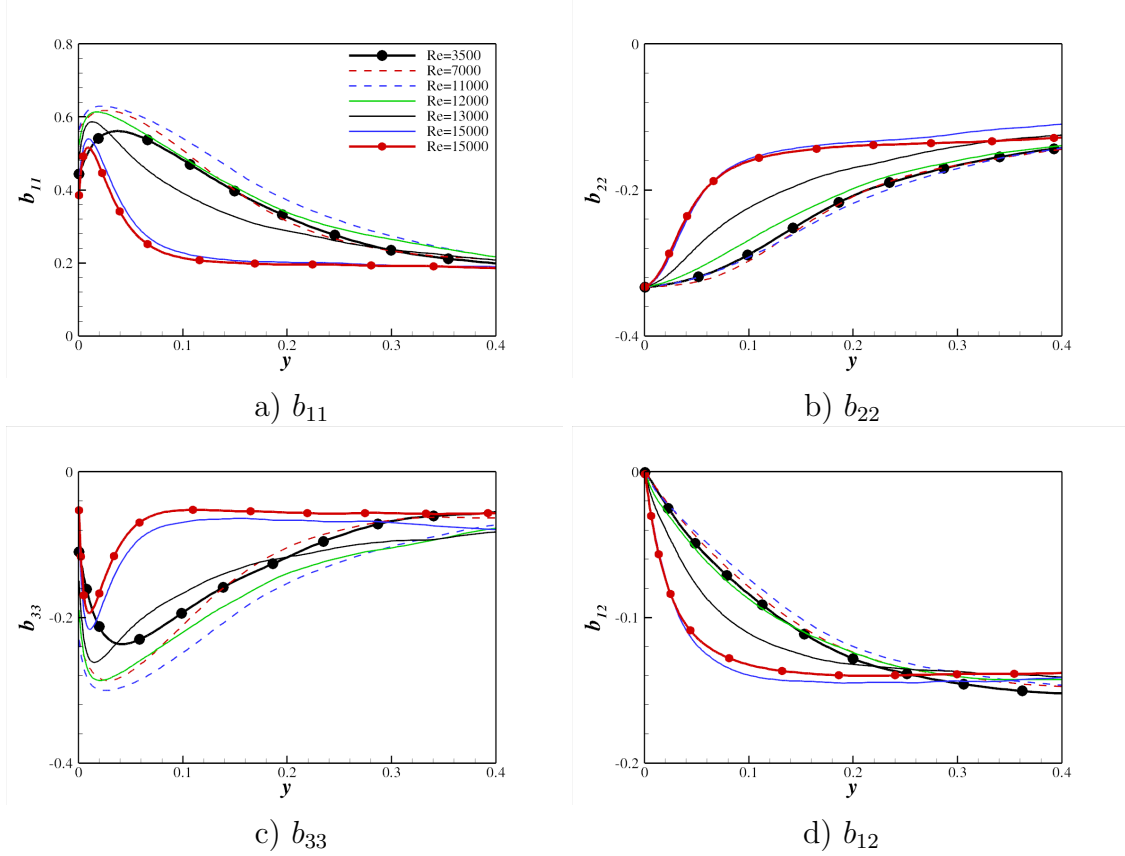


Figure 6.19: Profiles of anisotropy stress tensor terms at several stages during the acceleration. Steady profiles (lines with symbols) at initial and final stages are also included for comparison.

structures become more isotropic during the stage III and the y location of the maximum anisotropy moves towards the wall (clearly seen from $Re = 12000$ onwards in Figure 6.20).

Figure 6.21 shows the profiles of F and G invariant functions, representing the two-component turbulence and axisymmetric turbulence states respectively. F invariant profiles show that the turbulence stays in two-component state during the stage I and the stage II of the acceleration which again supports the already made observation of the suppression of wall-normal fluctuations. The reduction in F below the initial profile in the near-wall region is maximum during the later part of the stage II at $Re = 10000$. Turbulence moves away from the two-component state during the stage III. Figure 6.21b shows that turbulence becomes more axisymmetric in the

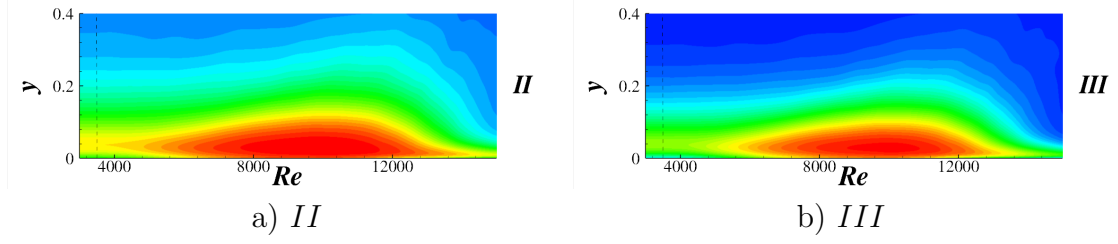


Figure 6.20: Variations of anisotropy invariants during the acceleration.

inner-layer region during the stage II. This behaviour is due to the lack of response of the turbulent shear stress during the stage II. It is worth noting that G invariant profile at $Re = 15000$ remains significantly towards the axisymmetric state in the outer region ($y = 0.4h$) as compared to the corresponding steady value. This can be explained by the earlier propagation of u_{rms} in the outer region, while the transverse velocity fluctuations and turbulent shear stress remain largely unchanged in the outer region during the stage III.

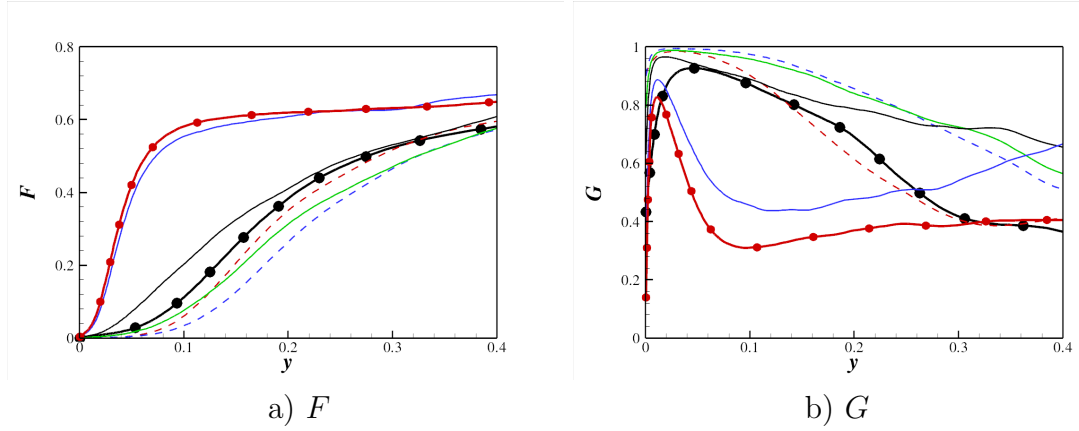


Figure 6.21: Wall-normal profiles of anisotropy invariants during the acceleration. Legend are the same as that for Figure 6.19.

The turbulent structures can also be analysed using anisotropy invariants maps (AIM) analysis (Lumley and Newman, 1977) as described in Chapter 4. Figure 6.22 shows several interesting variations of the turbulence structure during the acceleration. The turbulence structure shifts towards the one-component state in the stage I and the stage II (as clearly seen by the rightwards shift of the right top corner

CHAPTER 6. EFFECT OF ACCELERATION ON TURBULENT STRUCTURES.

point on the two-component line). This shift is due to the dominance of u_{rms} over the other components in the stage II. The one-component turbulence is maximum at the edge of the viscous sublayer (Chung et al., 2002). The one-component turbulence state decreases with the rapid response of v' and w' fluctuations in the stage III, and the top right point moves leftwards (this can be clearly seen in AIM from $Re = 11000$ to $Re = 13000$).

The shift of turbulence towards the one-component state can be seen more clearly by following the time histories of maximum values of II and $-III$ as shown in Figure 6.23a. The wall-normal location for the maximum II are shown in initial and local wall units in Figure 6.23b. The variation of this location is similar to the two-stage variation of $\omega'_{x,min}$ (cf. Figure 5.21).

The lower right line of the AIM represents the axisymmetric state of turbulence. The turbulence usually stays away from axisymmetric state due to non-trivial contributions from all the Reynolds stress components in the buffer-layer and log-layer for fully-developed turbulent channel flow. It is very interesting to note that the turbulence becomes completely axisymmetric at $Re = 11000$ and $Re = 13000$ in Figure 6.22, again supporting the observation of earlier increase in the streamwise fluctuations in the near-wall region. The turbulence axisymmetry reduces in the near-wall region during the stage III and turbulence shifts substantially away from the axisymmetry line at $Re = 15000$. The core region remains largely isotropic during the acceleration

6.5. REYNOLDS STRESS ANISOTROPY TENSOR ANALYSIS

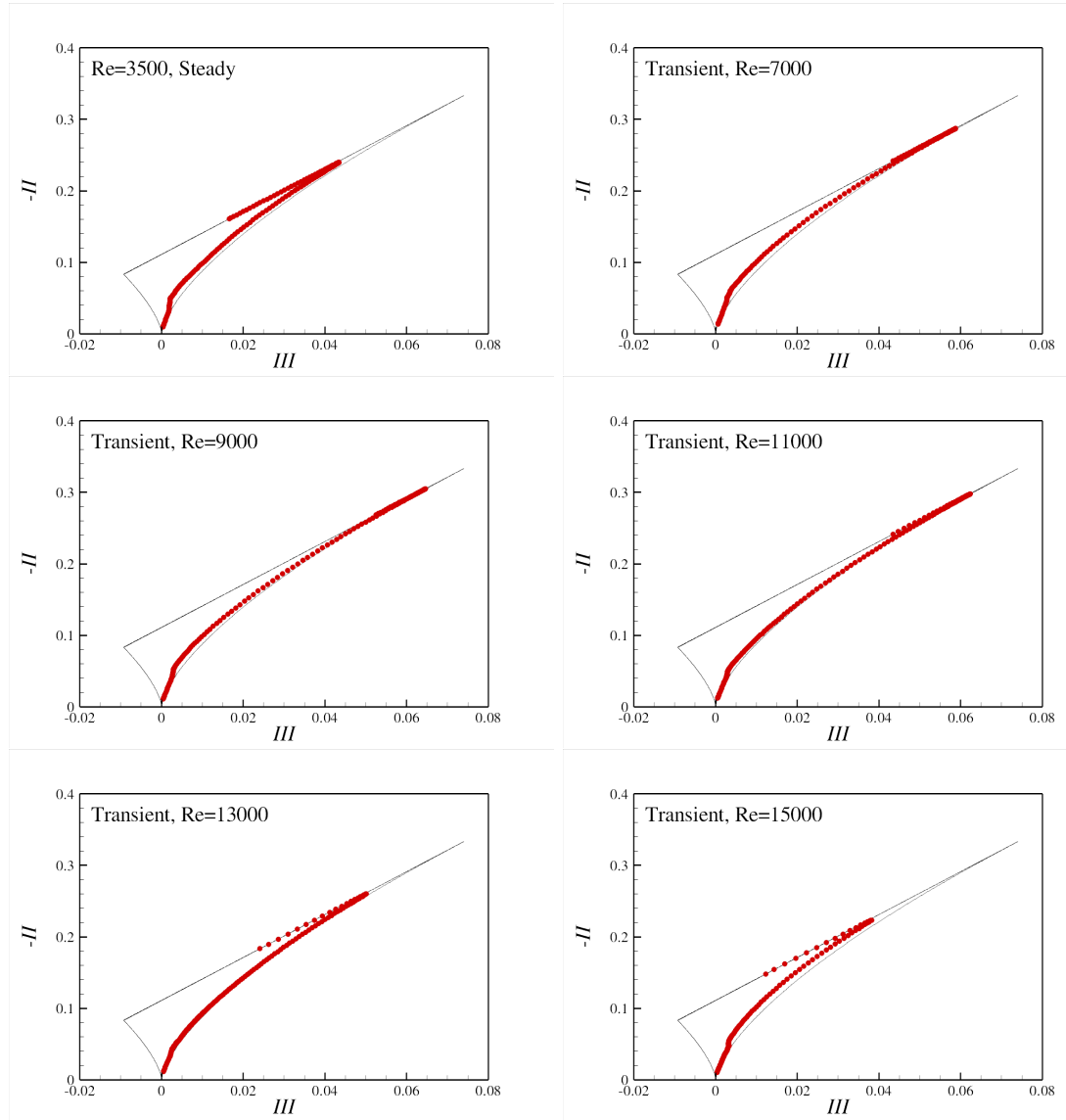


Figure 6.22: Anisotropy invariant maps at several Reynolds numbers during the acceleration.

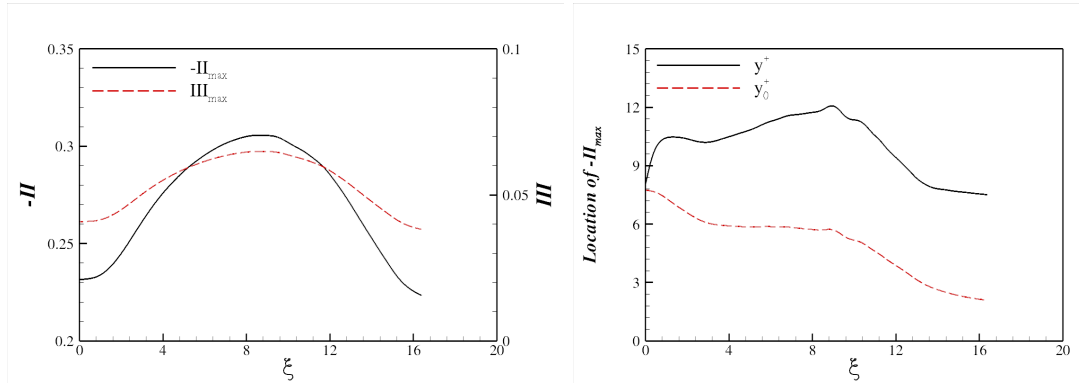


Figure 6.23: Time histories of a) the maximum values of $-II$ and III at right top corner for AIM, and b) the wall-normal location for the maximum $-II$.

6.5.1 Energy spectra analysis

Energy spectra analysis is being performed in this section to study the energy transfer between large and small scales during the acceleration. Figure 6.24 shows the energy spectra at several Reynolds numbers in the near-wall region ($y^+ = 5$). Please note that these spectra are constructed from 5 realisations. The energy spectra clearly demonstrate the adequacy of the grid resolutions employed for the present DNS as there is no energy pile up towards the higher frequency modes. The energy spectrum in the streamwise direction at $Re = 7000$ shows a substantial initial reduction for the energy of smaller scales below the initial values ($Re = 3500$). This clearly indicates that the temporal acceleration results in weakening of the smaller scales. As acceleration proceeds, the energy starts to build up in relatively larger scales throughout the acceleration and energy in the large scales is highest at $Re = 13000$. The energy in the large scales starts to decrease afterwards but still there is substantial difference between the energy levels of steady and unsteady large scales at $Re = 15000$. It indicates that the temporal acceleration disturbs the energy cascade.

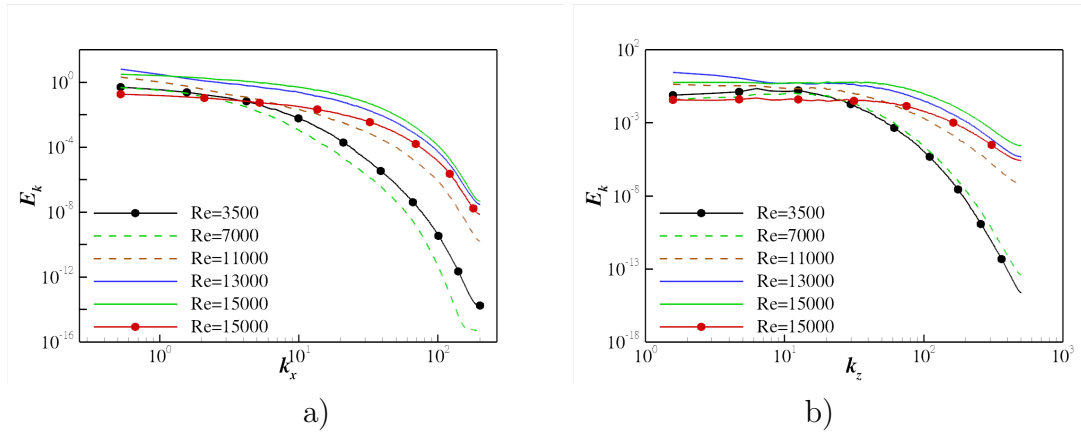


Figure 6.24: Variations of energy spectra at $y^+ = 5$ of turbulent kinetic energy in a) the streamwise direction, and b) the spanwise direction at several Reynolds number.

Figure 6.24b shows the energy spectra in the spanwise direction. There is an initial

CHAPTER 6. EFFECT OF ACCELERATION ON TURBULENT STRUCTURES.

reduction in the energy level for the low frequency modes at $Re = 7000$ whereas there is no reduction below the initial steady values for the high frequency modes. The energy build up of the low frequency modes in the spanwise direction is similar as observed in the streamwise energy spectra. Figure 6.25 shows the energy spectra at the channel centreline. The streamwise spectrum at $Re = 700$ also exhibits an initial decrease in the energy for the smaller scale. However, the weakening effect is not as prominent as in the near-wall region. The energy builds up in large scales until the final stage of acceleration, indicating that the core region is largely dominated by the flow acceleration.

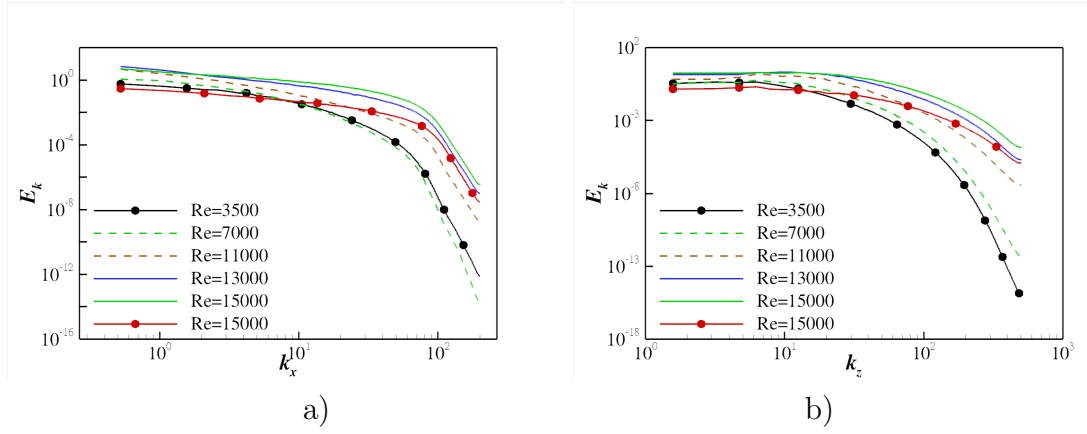


Figure 6.25: Variations of energy spectra at $y = h$ of turbulent kinetic energy in a) the streamwise direction, and b) the spanwise direction at several Reynolds number.

6.6 Conclusion

The effect of acceleration on the near-wall structures has been investigated in this chapter using low-speed streaks and λ_2 iso-surfaces. The new turbulence is found to evolve in distinct patches after showing a substantial delay. The conditional averaging has been performed on the newly generated turbulent region to study its characteristics. Finally, the response of turbulent structures during the acceleration has been analysed in detail with the help of Reynolds stress anisotropy analysis and AIM analysis. The major findings of this chapter are as following,

1. The low-speed streaks exist in two distinct length scales during the stage III of the acceleration. The larger streaks are from the old turbulence while the smaller patterns are from the new turbulence.
2. The new turbulence generation process exhibits a substantial initial delay during the stage II.
3. The near-wall structures are elongated in the streamwise direction during the stage II.
4. The generation of new turbulent structures starts to occur during the later part of the stage II and it increases rapidly during the stage III.
5. The rapid new turbulence generation results in a sharp increase of the wall shear stress during the stage III.
6. The new turbulent structures evolve in form of distinct patches during the acceleration.
7. The turbulence characteristics in the areas devoid of new turbulence are comparable to the initial turbulence during the stage II.

CHAPTER 6. EFFECT OF ACCELERATION ON TURBULENT STRUCTURES.

8. The newly generated turbulent structures remain closer to the wall as compared to the weaker structures.
9. The turbulence anisotropy increases in the viscous sublayer during the stage II. The turbulence structure shifts towards one-component state due to the dominance of u_{rms} .
10. Flow in the buffer layer and some part of the log-layer becomes completely axisymmetric during the early part of the stage III due to the early propagation of u_{rms} in this region, and the core region remains largely isotropic during the acceleration.
11. Temporal acceleration results in a substantial turbulent kinetic energy build-up in low frequency modes in the near wall region during the stage II.

7

Effect of Different Acceleration Rates.

The DNS of temporal acceleration has shown many interesting aspects of turbulence response during the acceleration, but the computational cost of performing DNS is very high due to stringent grid resolutions. At the final stage of DNS calculations at $Re_f = 15000$, the wall shear stress has not fully recovered while the rms velocity fluctuations are in the process of recovery after exhibiting an initial delay, and hence the turbulence propagation in the core region has not completed. Therefore, LES investigation is performed to study the effect of different acceleration rates as well as the turbulence response after the ST stage (stage III) and turbulence propagation characteristics in the core region. The final Reynolds number for DNS was restricted

to ($Re_f = 15000$) due to stringent grid resolution requirements and approximately 190 million computational cells were required to perform the DNS. In LES, the final Reynolds number of the calculations is increased to $Re_f = 22600$.

7.1 Simulation parameters

Three f values are used in this chapter to investigate the effect of acceleration rate on the turbulence development during the acceleration. The details of LES performed in the present study are tabulated in Table 7.1. The Dynamic SGS model (Germano et al., 1991; Lilly, 1992) is used to account for unresolved SGS scales, and the test filtering is applied in the streamwise and spanwise directions only. An LES of the fully-developed turbulent channel flow was performed at the initial Reynolds number ($Re = 3500$) in order to obtain the initial conditions for the temporal acceleration simulations. The initial data are in good agreement with the steady DNS data (Kim et al., 1987).

Case	Re_0	Re_f	f	T_e	$dRe/d\xi$	γ	Experiment time
Case-1	3500	22600	0.20	$27.3 h/U_{m0}$	700	6.1	5
Case-2	3500	22600	0.33	$16.3 h/U_{m0}$	1170	10.3	3
Case-3	3500	22600	0.50	$10.9 h/U_{m0}$	1750	15.3	2

Table 7.1: Details of LES calculations performed. Captions are same as of Table 4.1.

LES validation

It is imperative to validate the LES results before any results would be presented. There are a few studies for transient turbulent flows using LES. Piomelli et al. (1997) studied the SGS stresses response to the imposed impulsive transition for two separate cases for channel flow with *a priori* test. It was found that the SGS stresses

7.1. SIMULATION PARAMETERS

are less sensitive to flow transient as compared to the large resolved scale. Moreover, the dynamic SGS model is found to be suitable for their transient calculations. Since in the present study, the flow field is subjected to temporal acceleration, LES results are compared with the DNS data presented in Chapter 5 for $f = 0.2$ case to validate the accuracy of the present LES.

Figure 7.1 shows the comparison of Re_τ time history, showing an excellent agreement between DNS and LES results. It is worth noting that the LES grid resolution is comparable to DNS grid resolution in the initial stages of the acceleration with the negligible contribution of the SGS viscosity. The SGS contribution increases towards the later stages of the acceleration.

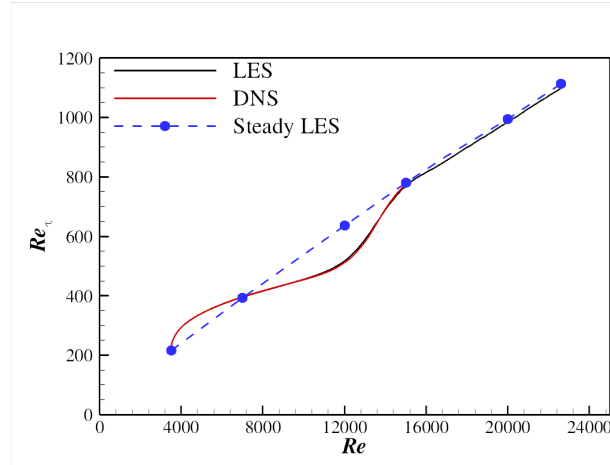


Figure 7.1: Re_τ time history comparison for DNS and LES calculations during the acceleration for $f = 0.2$ case.

Since the wall shear stress provides the data comparison only adjacent to the wall, the mean velocity and rms velocity fluctuation profiles at several Reynolds number during the acceleration are shown in Figure 7.2. All profiles show good agreement with the corresponding DNS data. Figures 7.1 and 7.2 demonstrate that the present LES produce reliable results for the temporal acceleration case.

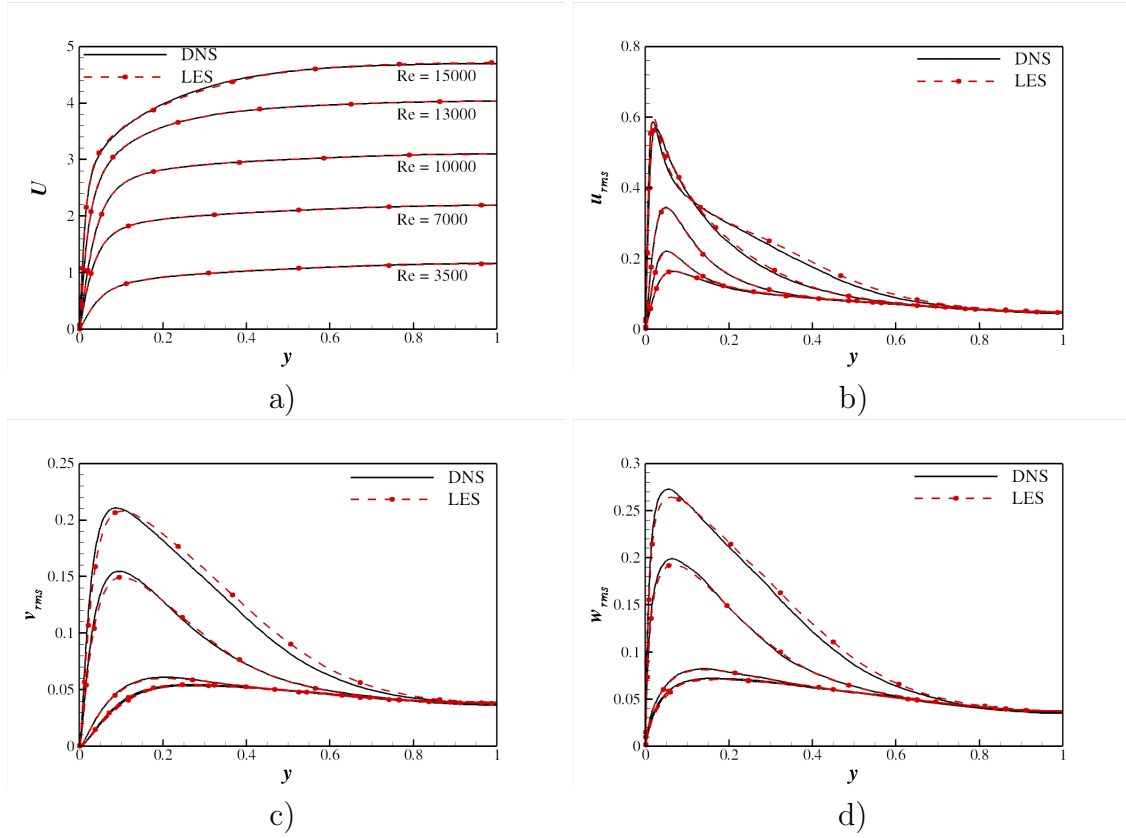


Figure 7.2: Comparison of a) the mean velocity, b) u_{rms} , c) v_{rms} , and d) w_{rms} profiles for DNS and LES at several Reynolds number during the acceleration.

7.2 Wall shear stress

Figure 7.3 shows the time history of the wall shear stress for three f values during the acceleration. The wall shear stress attains a pseudo-steady equilibrium state (PS stage or stage IV) at the end of the stage III and increases monotonically afterwards as the acceleration proceeds. This behaviour was also reported in pipe flow LES by Jung and Chung (2007). The offset of the Re_τ value from the pseudo-steady Re_τ value increases at higher acceleration during the stage I and the stage II. This increase in deviation is due to an increase in the inertia at higher acceleration rate. The stage IV is achieved for $f = 0.2$ and $f = 0.33$ cases only at $Re = 22600$. The wall shear stress for $f = 0.5$ case is in the stage III of acceleration at $Re = 22600$.

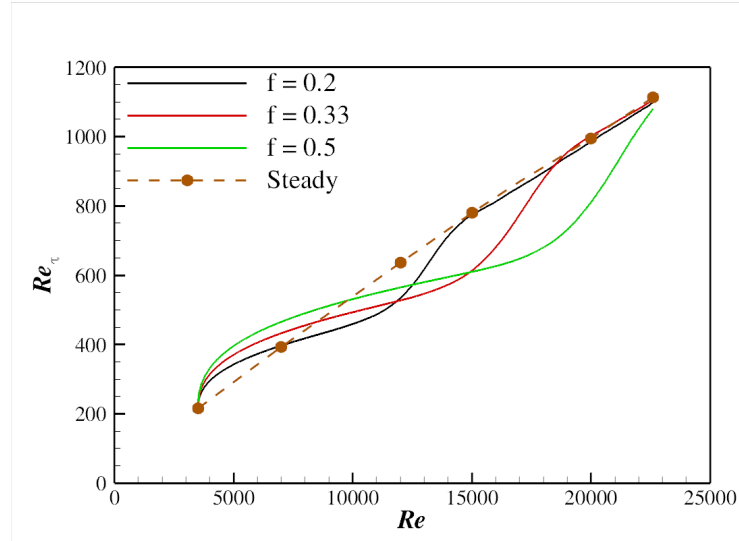


Figure 7.3: Variation of the wall shear stress during the acceleration for the three cases. Steady LES values are included for comparison.

The comparison of ratios of final values to the initial steady values, for the three acceleration cases with the corresponding steady values for Re_τ , Re_c and C_f is tabulated in Table 7.2. Here Re_c denotes the Reynolds number based on the centreline velocity. All the properties for $f = 0.5$ case are considerably smaller than the steady corresponding values.

Flow Property	Steady	$f = 0.2$	$f = 0.33$	$f = 0.5$
Re_τ	5.18	5.15	5.15	5.03
Re_c	6.38	6.39	6.18	5.97
C_f	0.645	0.630	0.638	0.608

Table 7.2: The comparison of ratio of final values to the initial steady values for different flow properties.

The final Reynolds numbers and the time for the different stages of acceleration are tabulated in Table 7.3. It is worth noting that the final Reynolds numbers for the first two stages *i.e.*, the stage I and stage II, increase for higher f values. A similar increase in critical Reynolds number at higher acceleration rates is also reported in the experimental studies of laminar to turbulent transition (Lefebvre and White, 1989, 1991). Please note that the final Reynolds number and time ranges are determined where the unsteady $du_\tau/d\xi$ crosses the steady $du_\tau/d\xi$ value in Figure 7.4, and the steady $du_\tau/d\xi$ is calculated from Dean and Bradshaw (1976) correlation (cf. Equation 5.9). It is clear from Table 7.3 that the time for all the three stages reduces with increase in the f value, implying the quicker response of the wall shear stress for higher acceleration rates. The reduction of transition time is also found in laminar to turbulent transition studies (Nakahata et al., 2007; Annus and Koppel, 2011).

Stage	$\xi_{\text{case-1}}$	$\xi_{\text{case-2}}$	$\xi_{\text{case-3}}$	$Re_{\text{case-1}}$	$Re_{\text{case-2}}$	$Re_{\text{case-3}}$
stage I	1.0	0.85	0.7	4200	4500	4800
stage II	11.4	9.5	8.6	11500	14600	18500
stage III	16.2	13.8	-	14900	19700	-

Table 7.3: Reynolds number and time ranges for different stages of wall shear stress variations. “ ξ ” and “ Re ” indicates the final time and Reynolds number for each stage.

Figure 7.4 shows the time histories of $dRe_\tau/d\xi$ for the three cases, and the corresponding steady $dRe_\tau/d\xi$ time histories are also included. The wall shear stress response during the stage II and Re_τ recovery rate during the stage III increase for

7.2. WALL SHEAR STRESS

higher f values. The maximum overshoot of $dRe_\tau/d\xi$ above the steady value during the stage III also increases with increase in acceleration rate. It is worth noting that the maximum $du_\tau/d\xi$ value during the stage III is approximately 10 % of the corresponding f values which are shown by 3 dashed lines in 7.4b.

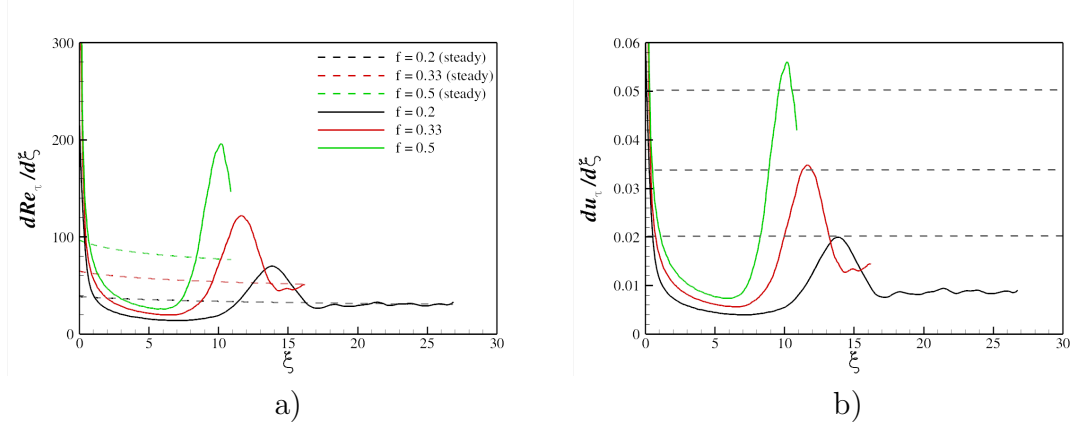


Figure 7.4: Variation of rate of change of wall shear stress during the constant acceleration for the three cases. a) $dRe_\tau/d\xi$ and b) $du_\tau/d\xi$, the rate of change of Re_τ and u_τ . Steady values from Dean and Bradshaw (1976) correlation are included for comparison.

Figure 7.5 shows the time histories of boundary layer parameters. During acceleration, the boundary layer thickness and displacement thickness decrease below the steady values and this deviation increases at higher f values. It is interesting to note that the boundary layer thickness and displacement thickness exhibit a slow recovery as compared to the wall shear stress (cf. Figure 7.3). The shape factor shows the similar two-stage behaviour as reported in DNS case in Chapter 5. The pseudo-steady equilibrium values for the shape factor is only achieved for the two lower f values. All the above results and statistics indicate that the mass flow incursion dominates the initial stages of acceleration. Higher acceleration rates result in earlier adjustment of the near-wall mean velocity to the imposed acceleration.

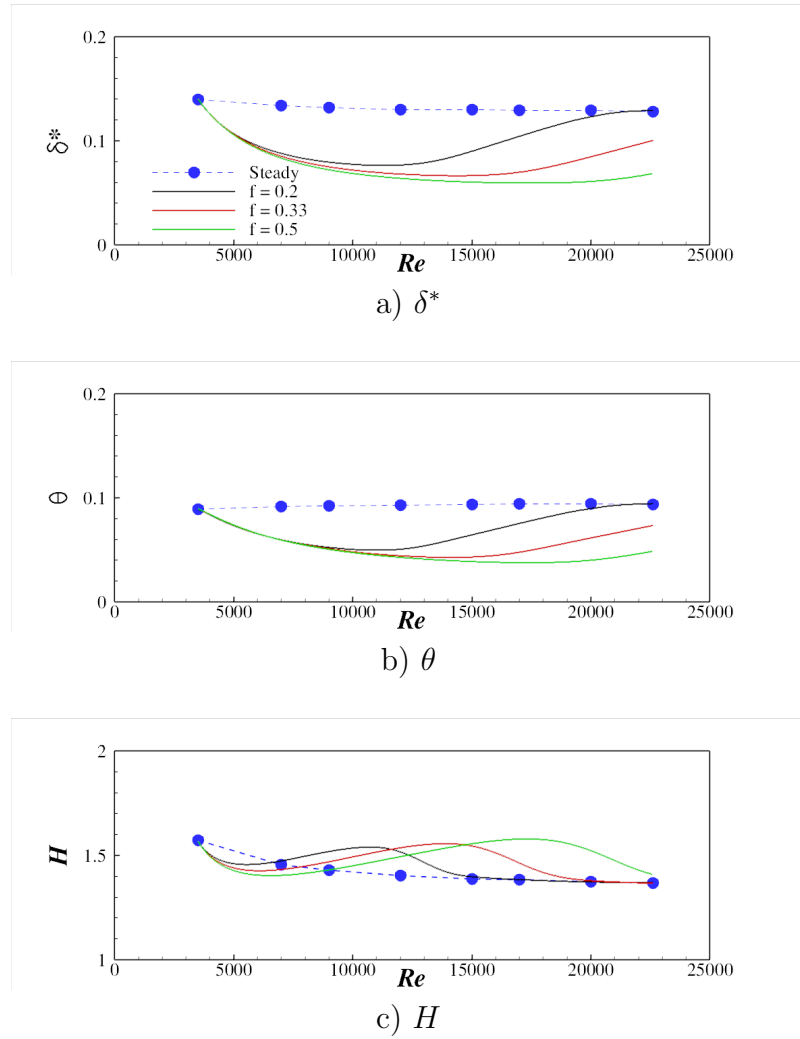


Figure 7.5: Variation of boundary layer parameters during the acceleration for the three cases.

7.3 Mean velocity

Figure 7.6 shows the mean velocity profiles at several Reynolds numbers for $f = 0.2$ and $f = 0.5$ cases. The corresponding steady profiles are also included to clearly show the difference of acceleration from the fully-developed equilibrium state. As the mean velocity response until $Re = 1500$ for $f = 0.2$ case is discussed in detail in Chapter 5, the main focus of attention here is the variation of the mean velocity in the stage IV. It is clearly seen in Figure 7.6a that the mean velocity profiles revert back to the steady profiles during the stage IV and achieves the steady profile values at $Re = 22600$.

It is interesting to note that the mean velocity deviation from the steady values increases with an increase in f during the stage II and the stage III. This behaviour is evident from Figure 7.6b where the departure of mean velocity profiles from the steady profiles for $f = 0.5$ case is significantly larger as compared to $f = 0.2$ case in Figure 7.6a. The mean velocity profile at $Re = 22600$ for $f = 0.5$ case is still different from the steady profile implying a much longer delay in the mean velocity profile adjustment.

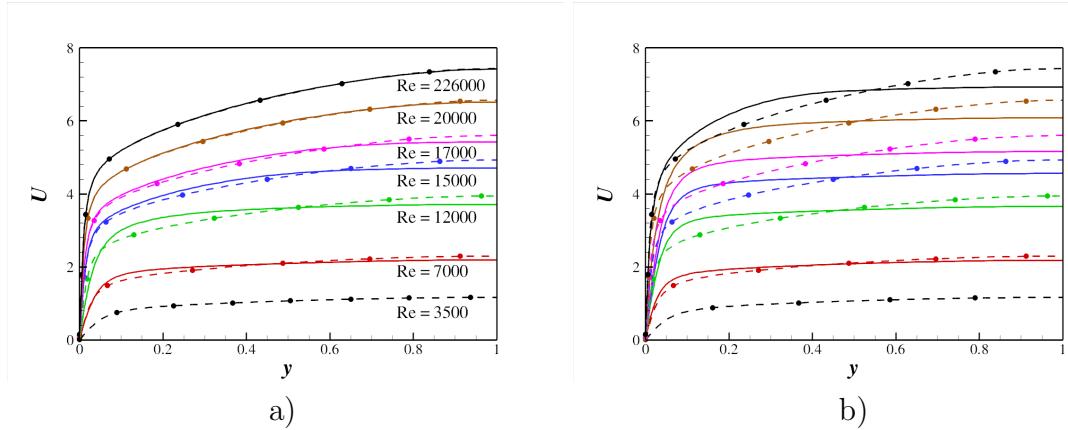


Figure 7.6: Variation of the mean velocity profiles during the acceleration for a) $f = 0.2$, and b) $f = 0.5$. Dashed lines with symbols are steady LES profiles.

Figure 7.7 shows the mean velocity profiles in wall units for $f = 0.2$ and $f = 0.5$

cases. Please note that the local u_τ is used for calculation of U^+ . The effect of different acceleration rates on the variation of the log-law is clearly evident in the figure. The deviation of the log-law increases with f . As discussed earlier in Chapter 5, the mean velocity profile shifts downwards during the stage I while it moves upwards during the stage II. The mean velocity profile starts to recover the log-law profile during the stage III with the generation of the new turbulence, and subsequently achieves the log-law profile in the stage IV for $f = 0.2$ case as shown in Figure 7.7a. It is worth noting that the log-law profile first starts to recover in the near-wall region. The log-law profile has not recovered for $f = 0.5$ case at $Re = 22600$.

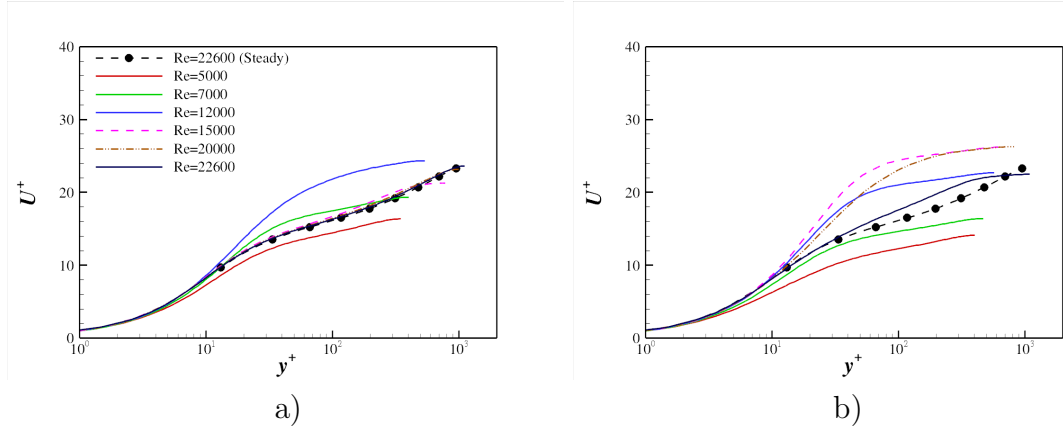


Figure 7.7: Variation of the log-law profile during the acceleration for a) $f = 0.2$ case, and b) $f = 0.5$ case. The log-law profile at $Re = 22600$ is included.

Figure 7.8 shows the time histories of the mean velocity at several wall-normal locations for the three acceleration cases. It is interesting to note that the effect of the no-slip wall constraint in the stage II weakens with increasing acceleration rate. Moreover, the near-wall mean velocity adjustment delay time in the near-wall region ($y = 0.005h$) is decreased with increase in f . This earlier adjustment of the near-wall mean velocity is consistent with the time histories of the wall shear stress (cf Figure 7.3) and this is indicative of earlier response of the near-wall turbulence.

Figure 7.9 shows the 2D contour plot for the variation of rate of change of mean

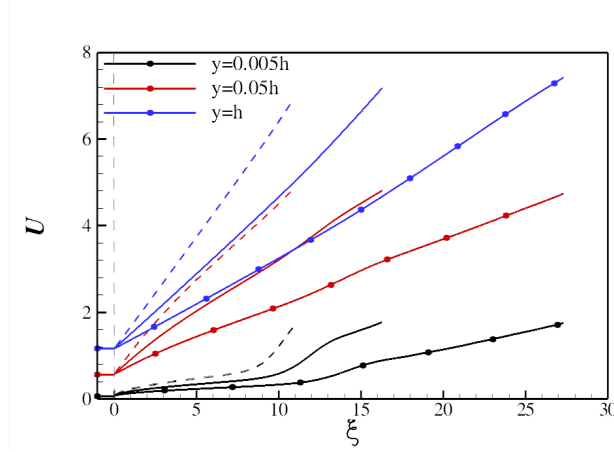


Figure 7.8: Variation of the mean velocity at three y locations during the acceleration. Lines with symbols indicates $f = 0.2$ case, solid lines without symbols indicates $f = 0.34$ case while dashed lines represent $f = 0.5$ case.

velocity *i.e.*, dU/dt . The adjustment of the mean velocity in the near-wall region, during the stage III is clearly seen for the three cases. The increase in acceleration rate results in the earlier adjustment of the near-wall mean velocity. It was found in the DNS analysis in Chapter 5 that this rapid adjustment of the mean velocity is an indicator of near-wall turbulence generation and this figure implies that the delay in the near-wall turbulence generation decreases with increase in f . The effect of different acceleration rates on the near-wall turbulence generation is discussed in detail in Subsection 7.4.

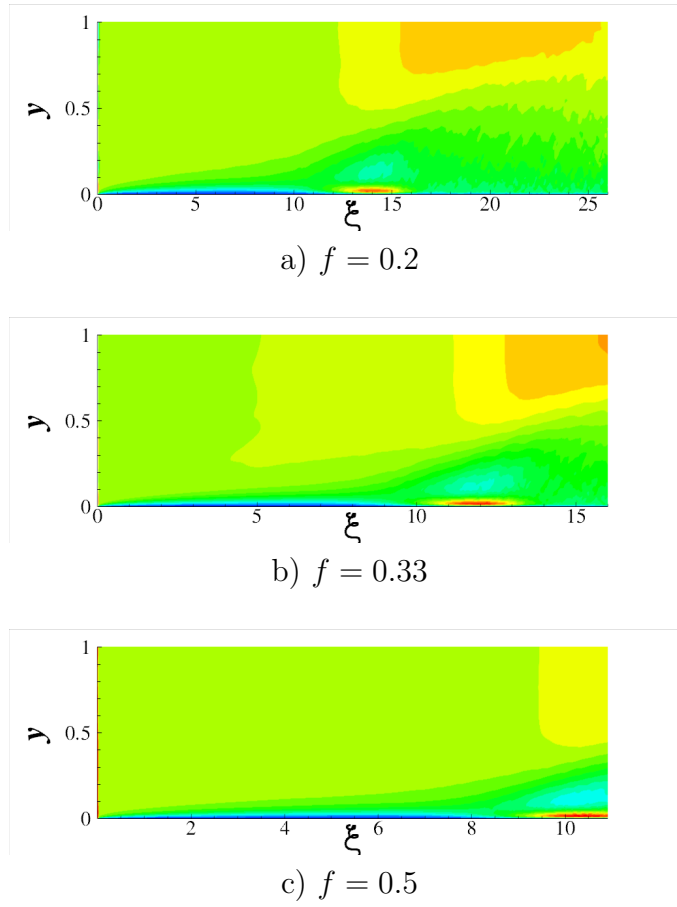


Figure 7.9: Variations of rate of change of mean velocity (dU/dt) during the acceleration.

7.4 RMS velocity fluctuations

Figure 7.10 shows the rms velocity profiles for $f = 0.2$ case and $f = 0.5$ case. The rms velocity is frozen on the centreline at $y = h$ even during the earlier part of the stage IV at $Re = 17000$ for $f = 0.2$ case (Figure 7.10a). The maximum u_{rms} values in the stage IV are comparable with the steady values while the core region intensities are significantly smaller. This trend indicates the delay in turbulence propagation in the core region. The maximum v_{rms} and w_{rms} values in the stage IV are significantly smaller than the steady maximum values, indicating the delay in turbulence redistribution.

RMS velocity profiles for $f = 0.5$ case shows that the turbulence intensity remains largely unchanged from its initial value even at the final stage of calculations. It is interesting to note that the maximum u_{rms} value at $Re = 22600$ in Figure 7.10b is greater than the steady maximum values. This overshoot of maximum u_{rms} signifies a sudden response of turbulence after a period of dormancy. Moreover, maximum u_{rms} value at $Re = 22600$ decreases sharply in the core region indicating lack of turbulence propagation in the core region. The maximum v_{rms} value also exhibits a rapid increase during the stage III, and it remains below the steady corresponding value at $Re = 22600$. The changes in v_{rms} and w_{rms} are very similar to each other during the acceleration.

Figure 7.11 shows the 2D contours of u_{rms} and v_{rms} in wall units. It clearly show the effect of acceleration rate on the near-wall evolution of rms velocity. Steady equilibrium contour values at the initial Reynolds number $Re = 3500$, are also shown. The stage IV of the acceleration is clearly seen in u'^{+} for $f = 0.2$ and $f = 0.33$ cases. All v'^{+} plots show higher turbulence activity in extended region in the outer layer. This effect is due to the fact that the v'^{+} has relatively smoother profile distribution around the maximum location and the location for the maximum

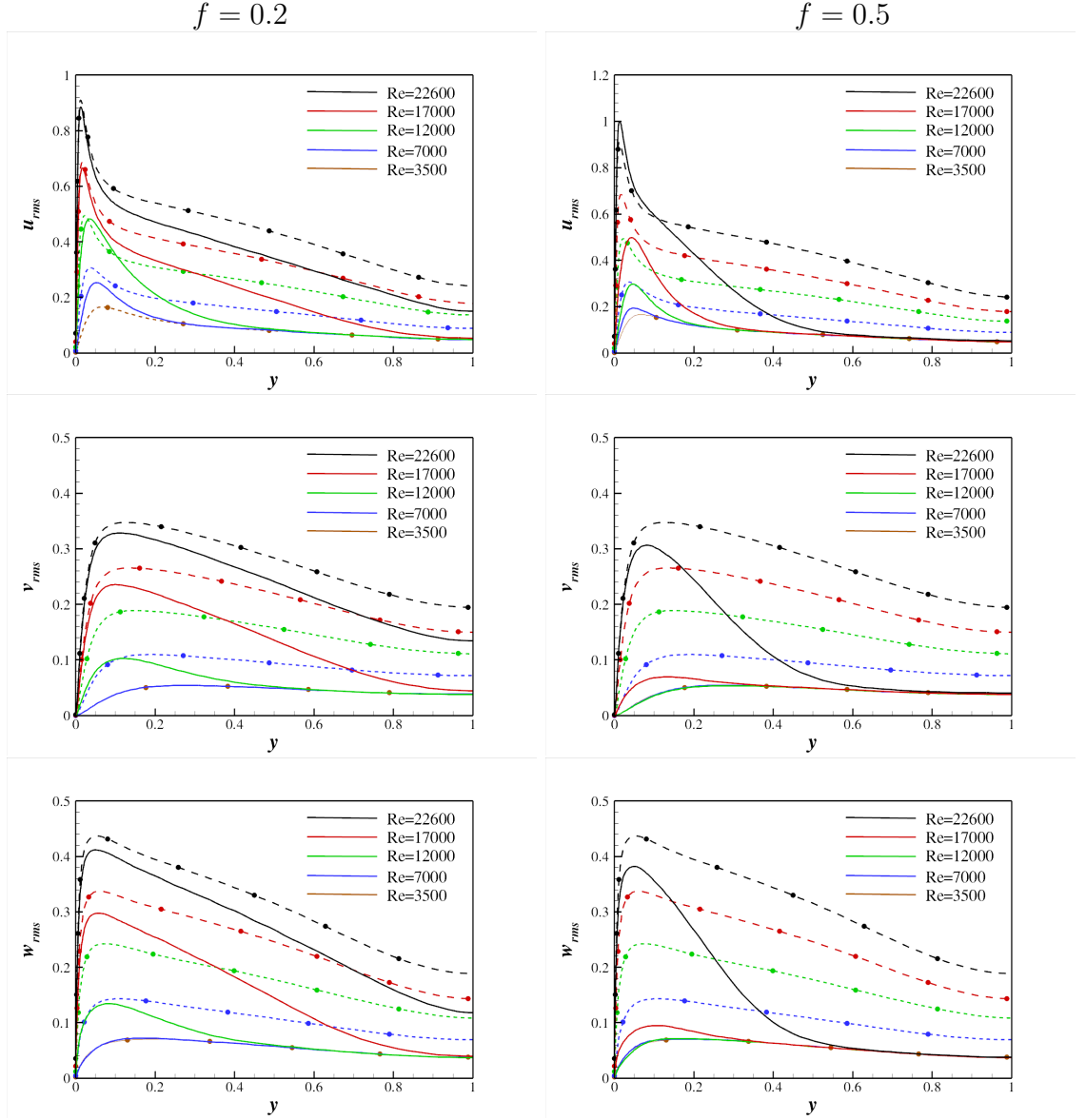


Figure 7.10: Variation of the rms velocity fluctuations during the acceleration. Dashed lines with symbols denote the steady LES data.

is located away from the wall as compared to u'^+ . This extended region of higher turbulence activity is also evident during the stage III for u'^+ contour plots for all three cases. The delay in response for rms velocity, in terms of Reynolds number, increases with f .

The response of turbulence in the near-wall region for the three acceleration cases is investigated using the time histories of the maximum values of rms velocity. The

7.4. RMS VELOCITY FLUCTUATIONS

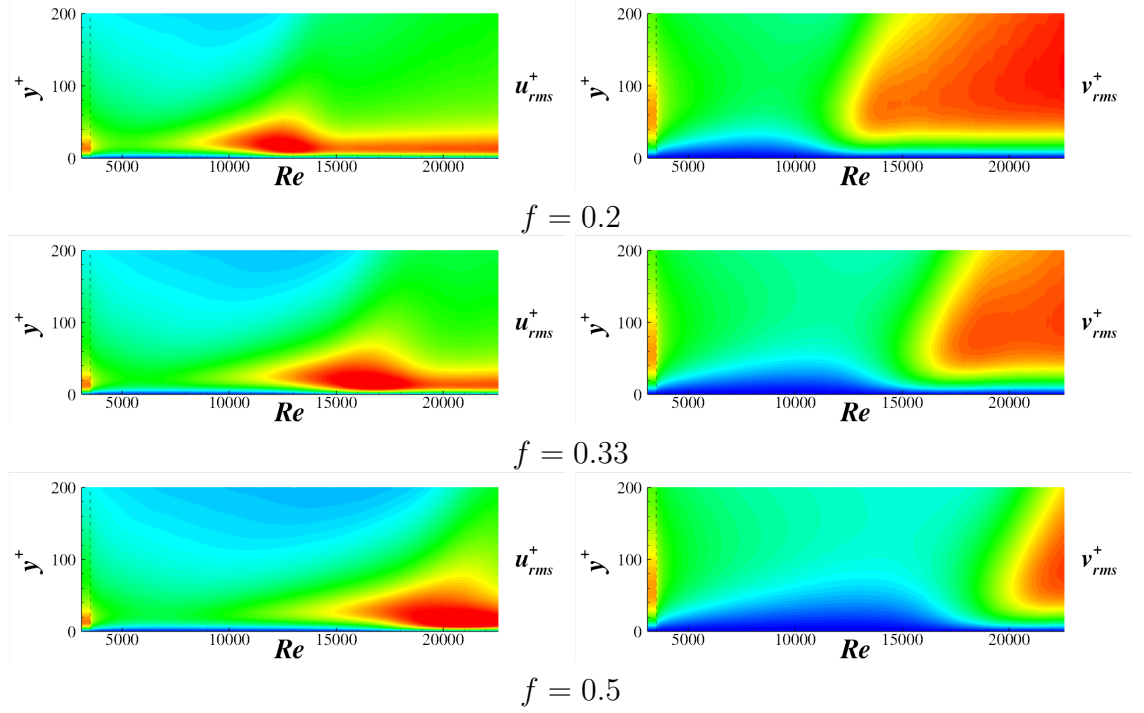


Figure 7.11: 2D contours of u'^+ and v'^+ for the three cases. The local u_τ is used for normalisation. The steady initial data are also included.

criterion introduced in the DNS analysis in Chapter 5 (cf. Equation 5.11) is used. Figure 7.12 shows the variations of u_{rms} and v_{rms} maximum values. Their steady values (calculated using LES) at several Reynolds numbers are also included. The deviation (reduction) from the steady values is increased during the stage II for large f , due to a delay in turbulence response. u'_{max} overshoot over the steady value during the stage III is clearly seen for all cases in Figure 7.12a which is consistent with the increase of maximum u_{rms} value at $Re = 22600$ in Figure 7.10b. The amount of overshoot increases with f . The overshoot of maximum u_{rms} is also evident in Figure 7.10b. It is interesting to note that u'_{max} increases at the same rate as its steady rate in the stage IV. However, u_{rms} for acceleration cases remains relatively low as compared to the corresponding steady values, due to the delay in turbulent kinetic energy production as shown in Figure 7.13.

v'_{max} time histories, in Figure 7.12b, also exhibit the similar patterns of delay and sudden response during the acceleration as observed for u'_{max} . It is interesting to

note that the difference between the steady and unsteady v'_{max} values in the stage IV is greater than the corresponding difference of u'_{max} values. This greater difference during the stage IV is due to an additional delay in turbulence redistribution from the streamwise component to the other two components.

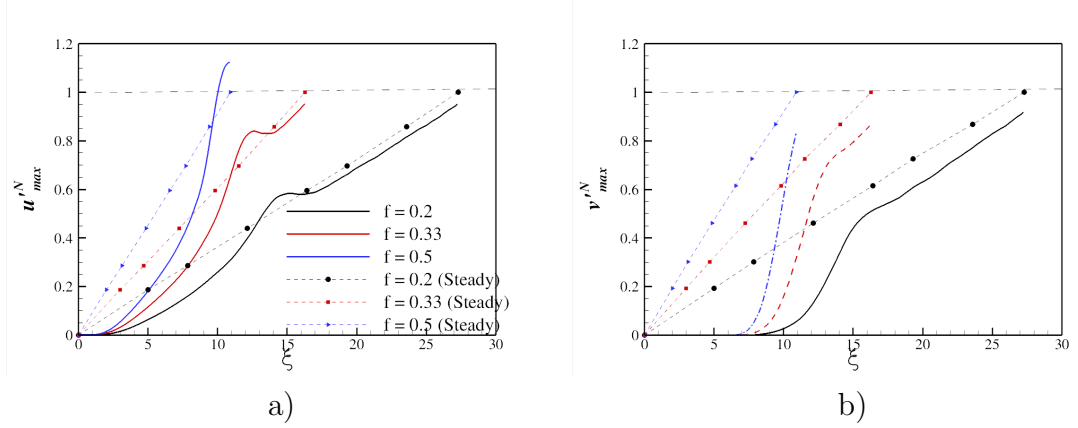


Figure 7.12: Variation of maximum values of a) u'_{rms} , and b) v'_{rms} .

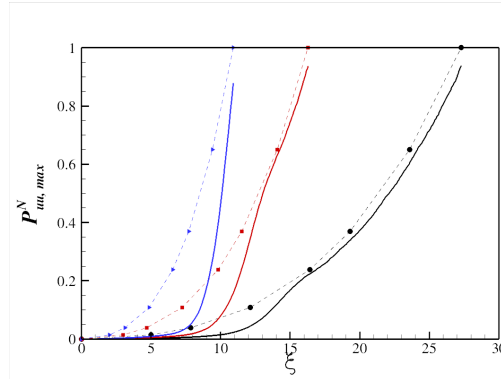


Figure 7.13: Time history of maximum value of production term in \overline{uu} budget equation. Legends are the same as in Figure 7.12.

Figure 7.14 shows the turbulent kinetic energy profiles in the near-wall region ($y \leq 0.4$) at $\xi = 5$ and at $\xi = 10$ for the three cases. It is clearly seen that the delay in turbulence response in early stages decreases with increase in acceleration rate. It is interesting to note that the turbulent kinetic energy profiles at $\xi = 10$ exhibit greater increase of kinetic energy in the outer region for higher acceleration rates, implying the earlier turbulence propagation in the core region at higher acceleration

7.4. RMS VELOCITY FLUCTUATIONS

rates.

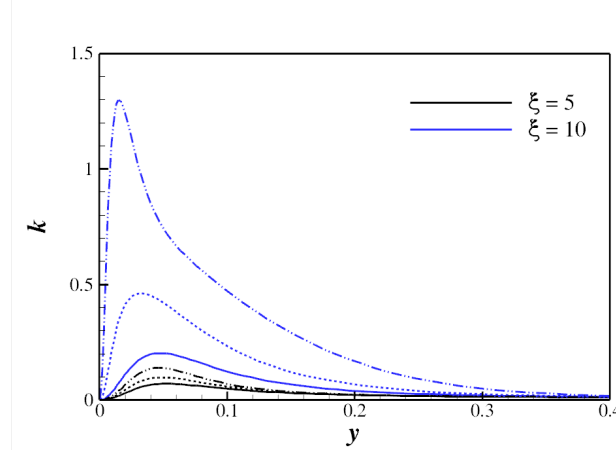


Figure 7.14: Turbulent kinetic energy profiles at two time instances during the acceleration. Solid lines correspond to $f = 0.2$ case, dashed to $f = 0.33$ case and dash-dott-dott to $f = 0.5$ case.

Table 7.4 shows the delay time of maximum values for different Reynolds stress terms using criterion introduced in Chapter 5 (cf. Equation 5.11). This table clearly shows that turbulence responds earlier at higher f values.

Flow Property	$f = 0.2$		$f = 0.33$		$f = 0.5$		M_s	M_f/M_s
	ξ_{50}^*	$R_p \times 100$	ξ_{50}^*	$R_p \times 100$	ξ_{50}^*	$R_p \times 100$		
\overline{uu}_{max}^N	18.8	94.5	10.7	93.9	8.9	121	2.7×10^{-2}	30.9
\overline{vv}_{max}^N	20.5	89.2	12.6	80.9	10.1	77.3	2.9×10^{-3}	42.5
\overline{ww}_{max}^N	20.3	89.2	12.6	80.0	10.1	76.5	4.9×10^{-3}	40.2
$-\overline{uv}_{max}^N$	18.9	94.1	11.8	90.6	9.6	95.0	2.8×10^{-2}	32.8

Table 7.4: Response times for maximum values of Reynolds stresses.

In Chapter 5, the breakdown of the local equilibrium between turbulence and the mean flow was reported (cf. Figure 5.10). Figure 7.15 shows the variations of the ratio of the turbulent kinetic energy to the mean velocity at several y locations. The steady ratios at several Reynolds number are included. At the onset of the acceleration, the k/U^2 ratio decreases significantly across the channel due to imposed mass incursion. This ratio remains below the steady value during the stage II,

followed by an abrupt increase during the stage III only in the near-wall region. This ratio remains below the steady ratio during the stage IV. The deviation from steady ratio increases with f during the stage II. In the outer region, k/U^2 exhibits an extended period of delay due to the dominance of the mean flow, and it only starts to increase with the propagation of new turbulence from the near-wall region.

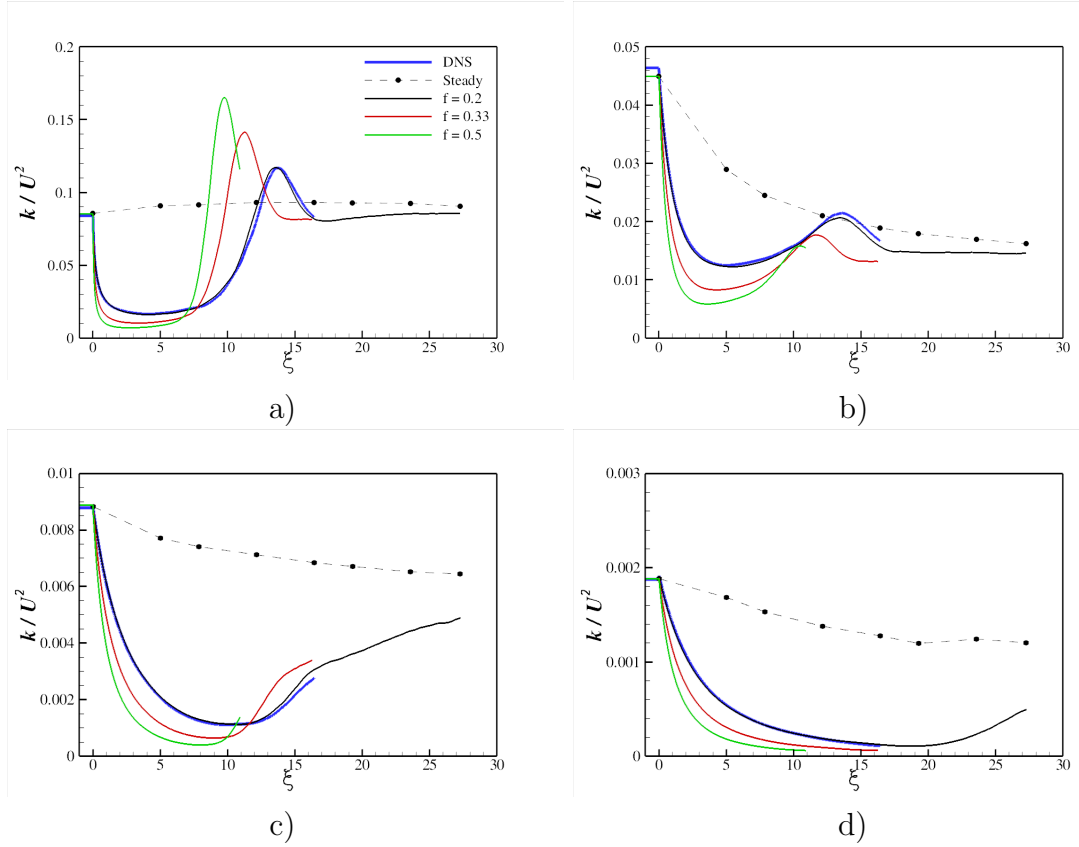


Figure 7.15: Time histories of kinetic energy normalised by the corresponding mean velocity at a) $y = 0.005h$, b) $y = 0.05h$, c) $y = 0.3h$ and d) $y = h$ for the three cases. Steady values are included for comparison.

Propagation of new turbulence can be clearly seen in Figure 7.16, which shows the 2D contour graphs of the rate of change of rms velocity fluctuations for $f = 0.2$ case. The newly generated turbulence during the stage III propagates subsequently into the core region after approximately $\xi \approx 10$. It is interesting to note that the turbulence starts to increase at a relatively smaller rate during the stage II for u_{rms} .

7.4. RMS VELOCITY FLUCTUATIONS

The significant turbulence generation, redistribution and propagation occurs during the stage III and the stage IV. u_{rms} increases first during the stage III, resulting in a subsequent increase in v_{rms} and w_{rms} and these findings support earlier observation, as reported in Chapter 5, about the anisotropic response of turbulence during the acceleration.

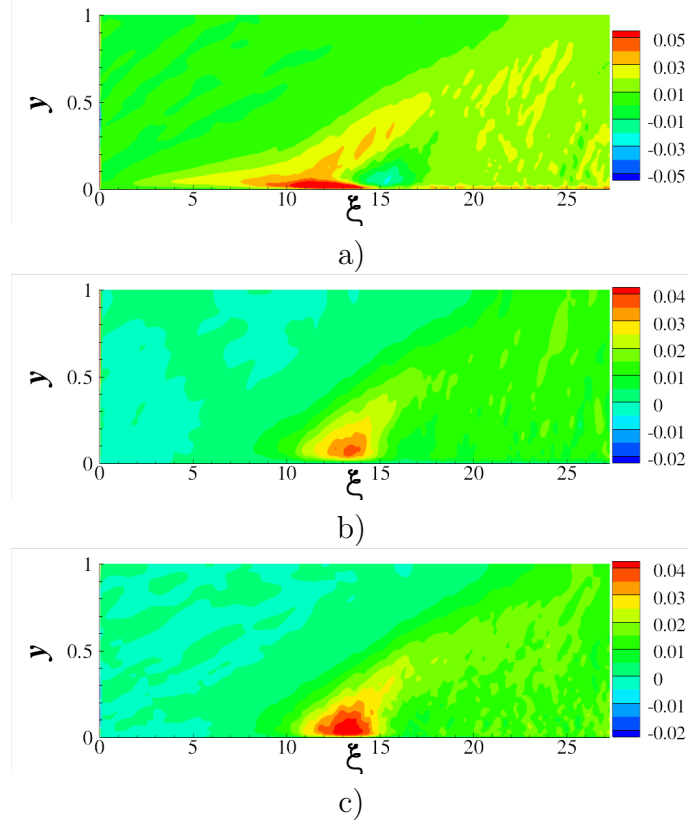


Figure 7.16: Rate of change of rms velocity fluctuations a) $du_{rms}/d\xi$, b) $dv_{rms}/d\xi$, and c) $dw_{rms}/d\xi$ for $f = 0.2$ case.

The effect of different acceleration rates on turbulence propagation in the core region is investigated using the same criterion as introduced in Chapter 5 (cf. Equation 5.12). The characteristic speed for u_{rms} propagation in the core region was found proportional to the initial u_τ value using $a_\phi = 0.15$ criterion (Greenblatt and Moss, 2004). However, turbulence propagation in the core region could not be studied in detail due to the relatively low final Reynolds number ($Re_f = 15000$). The choice of a_ϕ is arbitrary, therefore it is important to study the effect of different values of a_ϕ on

turbulence propagation. Figure 7.17 clearly shows that this criterion is independent of the value of a_ϕ . $a_\phi = 0.5$ is used in the present study to investigate the effect of different acceleration rates on turbulence propagation in the core region.

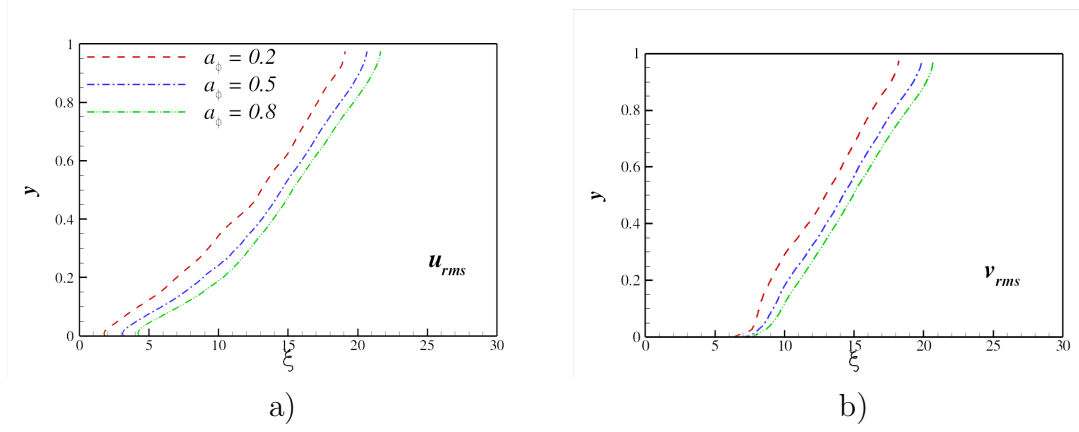


Figure 7.17: Propagation of a) u_{rms} , and b) v_{rms} for several a_ϕ values for $f = 0.2$ case.

Figure 7.18 shows the propagation of the rms velocity fluctuations and the turbulent shear stress in the core region. It shows that the propagation speed of all properties investigated here, is proportional to the initial u_τ value. The turbulence propagation is limited in only part of the core region for the two higher f values. This is due to relatively extended delay in turbulence response in terms of Reynolds number (cf. Table 7.3). The turbulence propagation speed is found to be largely independent of the acceleration rate.

7.4. RMS VELOCITY FLUCTUATIONS

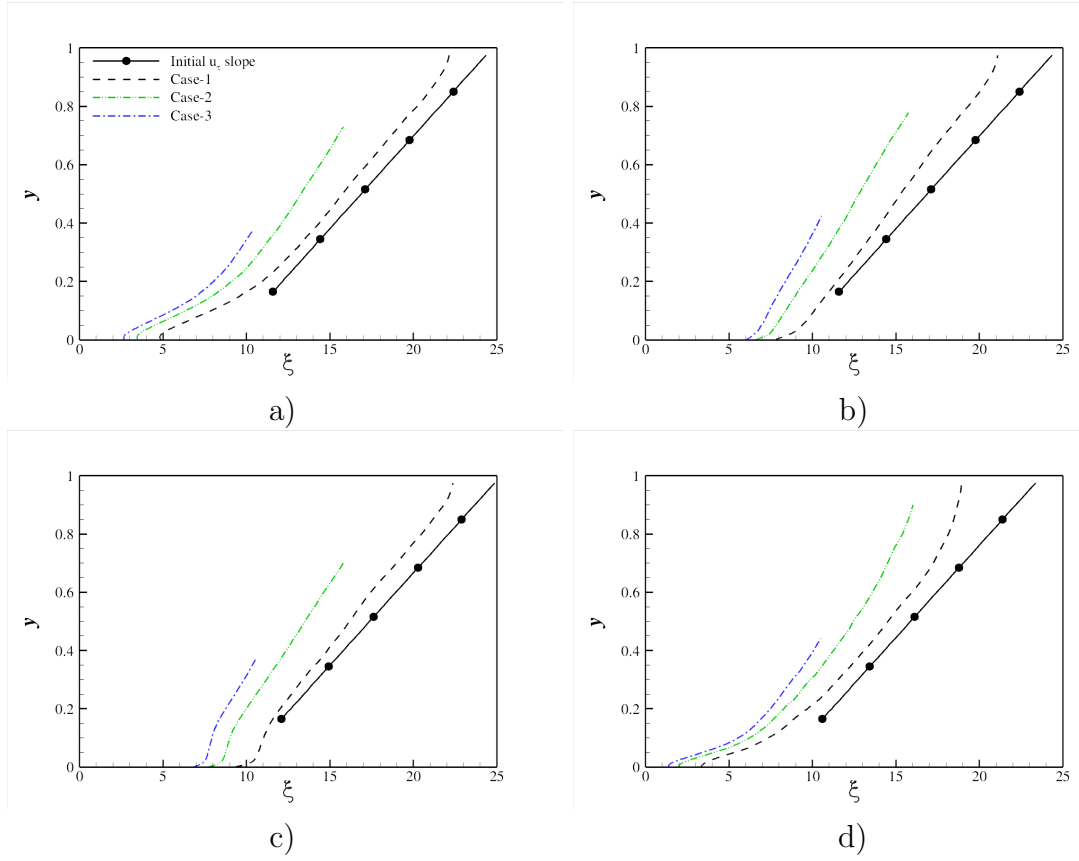


Figure 7.18: Comparison of turbulence propagation of a) u_{rms} , b) v_{rms} , c) w_{rms} and d) $-\overline{u'v'}$ in the core region for the three acceleration cases.

7.5 RMS vorticity fluctuations

RMS vorticity fluctuations analysis is helpful in investigating the response of near-wall structures. In the DNS of temporal acceleration presented in Chapter 5, it was found that like rms velocity fluctuations, rms vorticity fluctuations respond first in the near-wall region. The effect of different acceleration rates on the near-wall structures response can be investigated using the time histories of the maximum rms vorticity fluctuations. Figure 7.19 shows the variation of $\omega'_{x,max}$, $\omega'_{y,max}$ and $\omega'_{z,wall}$ with time for the three f cases. $\omega'_{x,max}$ and $\omega'_{y,max}$ for $f = 0.5$ case have not achieved the stage IV of acceleration at $Re = 22600$. On the other hand, $\omega'_{z,wall}$ exhibits a significant overshoot for $f = 0.5$ case, and a similar overshoot was also reported in u'_{max} history graph (cf. Figure 7.12a). It is worth noting that a sudden increase is evident for all three cases, and rate of change appears to be independent of f , suggesting that the turbulence response during the stage III is largely independent of the acceleration rate. It is also interesting to note that $\omega'_{x,max}$ remains below the steady values during the stage IV indicating that the strength of streamwise vortices during the stage IV is less than the steady strength. This is due to the delayed production of turbulent kinetic energy during the stage IV (cf. Figure 7.13).

In Chapter 5, the rms vorticity y locations of $\omega'_{x,min}$, $\omega'_{x,max}$, and $\omega'_{y,max}$ exhibited interesting trends during the acceleration (cf. Figure 5.21) although the trends in the stage IV were not be presented. Figure 7.20 shows the time variations of the y locations from LES. Steady LES data are included to elaborate the effect of acceleration on vorticity locations in comparison with the steady locations. The LES results exhibit similar trends as the DNS study, again validating the accuracy of LES calculations. The monotonic decrease of all three vorticity locations during the stage IV is clearly seen in the figure.

7.5. RMS VORTICITY FLUCTUATIONS

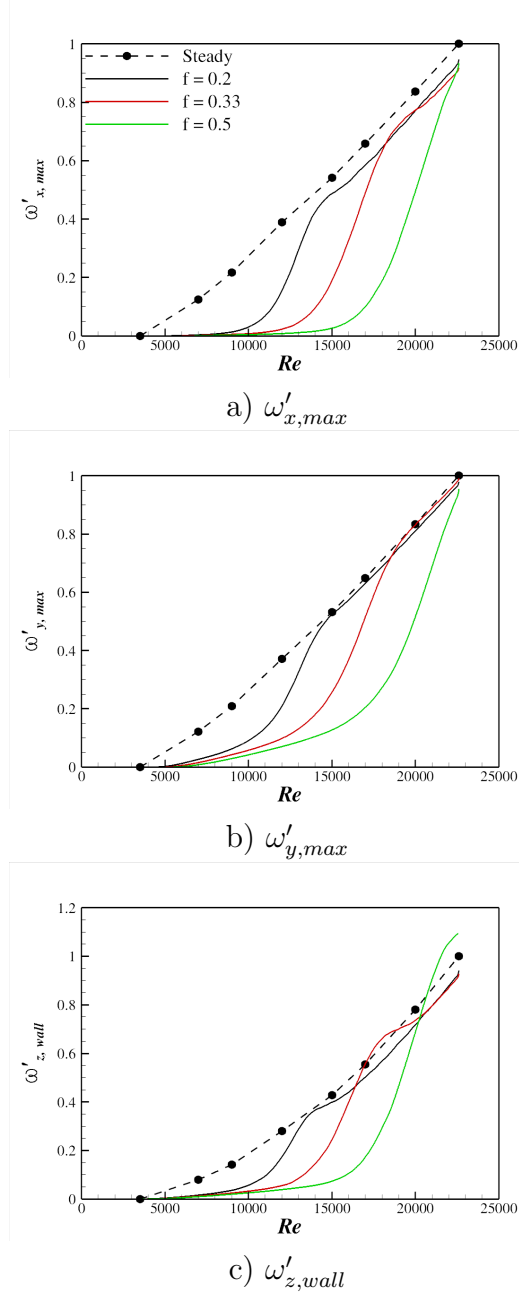
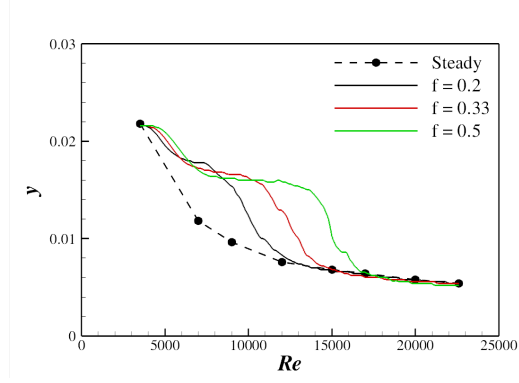
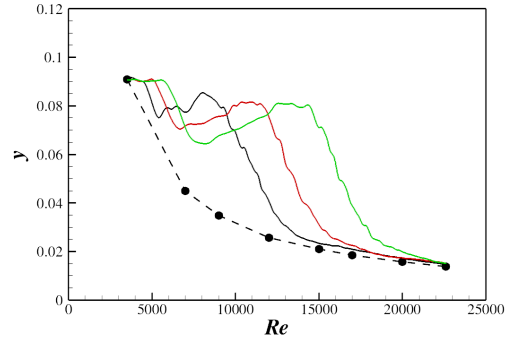


Figure 7.19: Maximum values of rms vorticity fluctuations variations during the constant acceleration for the three cases. Steady value are included for comparison.

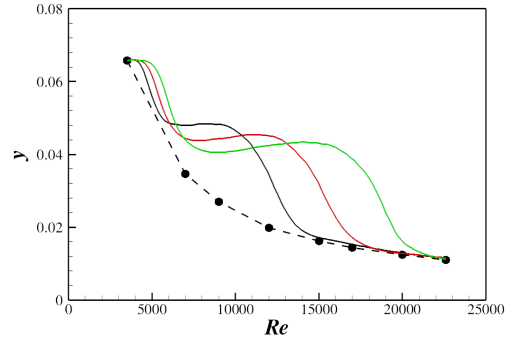
Figure 7.21 shows the 2D contour plots of $\omega'_x{}^+$ and $\omega'_y{}^+$ for the three acceleration cases. The delay in response for these two vorticity components is evident. Please note that the local u_τ value is chosen for the normalisation. This delay decreases with increase in the acceleration rate. The strength of the near-wall structures during the stage II remains approximately the same as the initial strength. The



a) $\omega'_{x,min}$



b) $\omega'_{x,max}$



c) $\omega'_{y,max}$

Figure 7.20: Variation of y locations for rms vorticity fluctuations during the acceleration for the three f values.

turbulent structures exhibit an abrupt response in the near-wall region during the stage III.

7.5. RMS VORTICITY FLUCTUATIONS

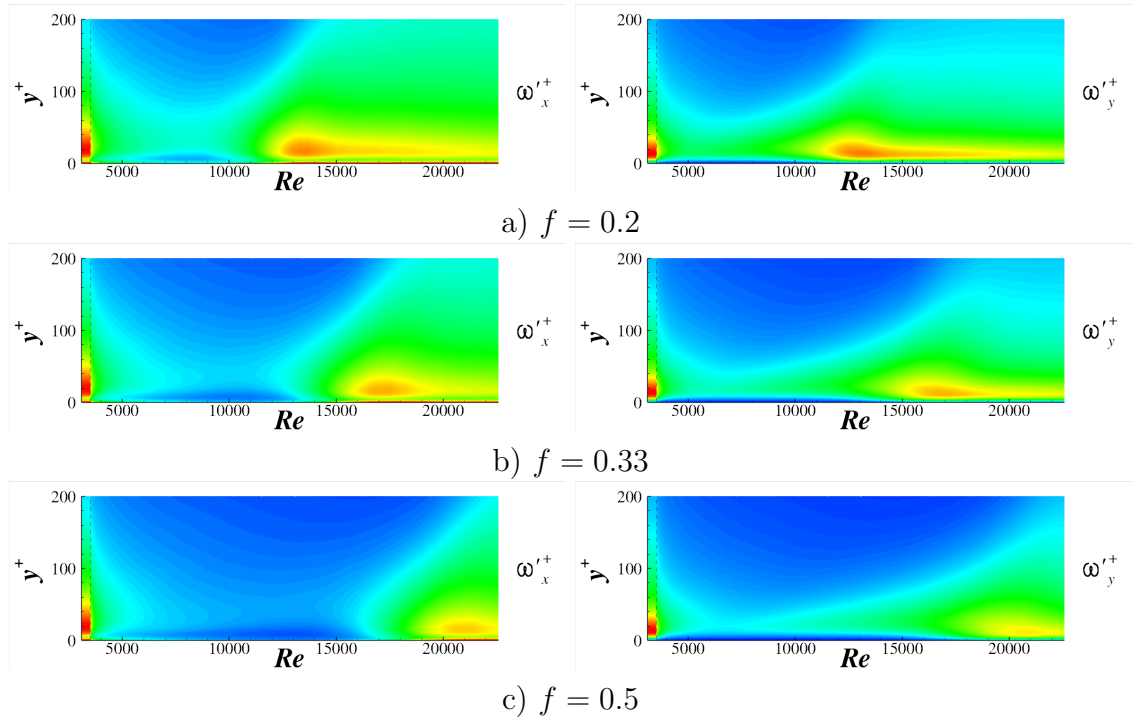


Figure 7.21: ω'_x and ω'_y contour plots for the three cases. Local u_τ value is used for the normalisation.

7.6 PDF analysis

The DNS of temporal acceleration revealed many interesting trends for the quadrant contributions (cf. Subsection 5.8). Quadratic contribution analysis is performed for the three acceleration cases in order to study the effect of acceleration rate and variations of quadratic contributions during the stage IV. Figure 7.22 shows the quadratic contribution (in percentage) for the four components at $y^+ = 3$. Approximately 2 million grid cell information from 5 realisations is used to collect this quadratic contribution at each time instant, represented by symbols in the time history graphs. Time history from the DNS for $f = 0.2$ case is also included and there is good agreement between DNS and LES. The deviation from the steady values increases with f .

Figure 7.23 shows 2D pdf contours during the stage II in the very near-wall region ($y^+ = 3$). Steady pdf results at $Re = 3500$ are included to show the differences between the steady and acceleration cases. It clearly shows that the v' contributions are reduced significantly during the stage II, and the suppression of wall normal fluctuations increases with f .

The suppression of wall-normal fluctuations in the stage II of the acceleration, is more prominent at $y^+ = 20$ in Figure 7.24. It is interesting to note that the pdf contributions for positive u' in the fourth quadrant increase in the later stage II, shown in Figures 7.24a, 7.24c and 7.24e. This indicates an increase in number of large amplitude positive u' events at higher acceleration rates. The pdf contours in the stage III are shown in Figure 7.24b, 7.24d and 7.24f. It is worth noting that the majority of events in the fourth quadrant, in the steady pdf at $Re = 3500$, shift significantly towards the second and third quadrant during the acceleration. This indicates an increase in the number of negative u' events. This can be attributed to the commencement of the abrupt adjustment of the mean velocity profile towards

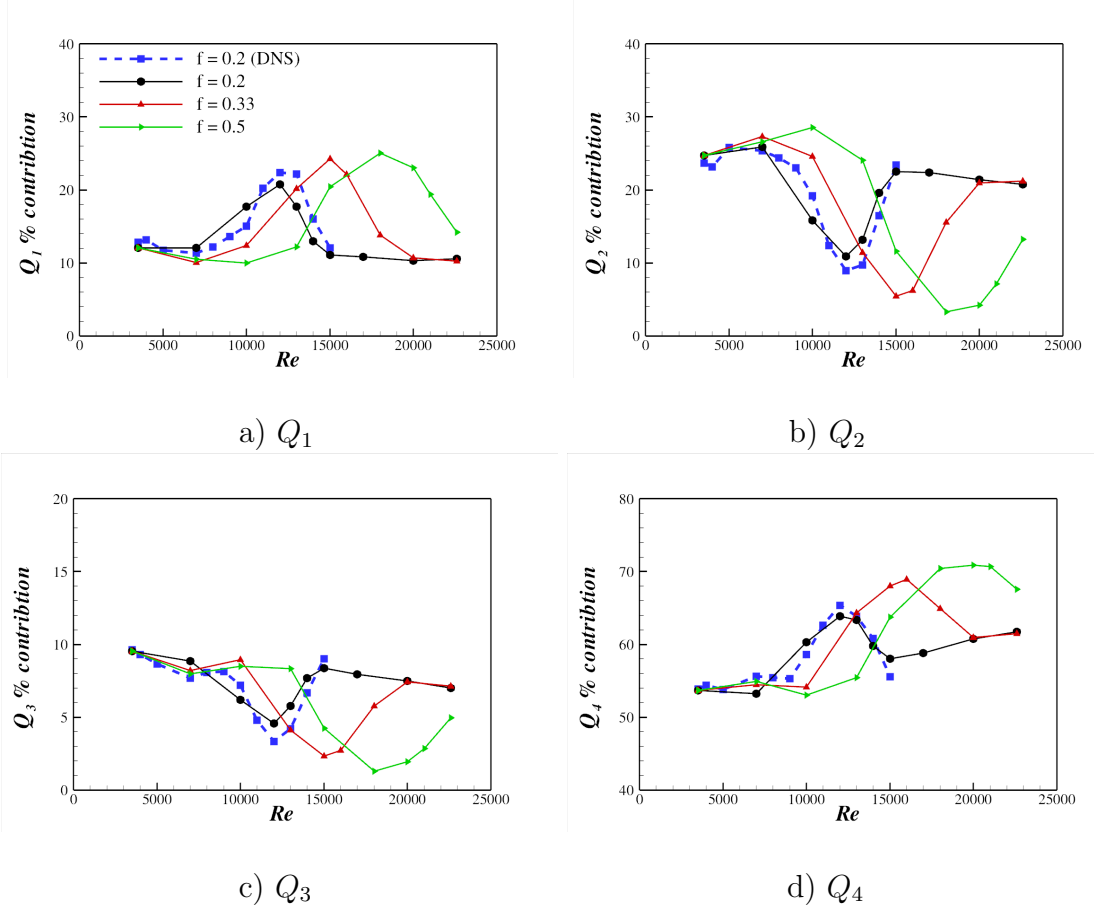


Figure 7.22: Time histories of quadratic contribution (in percentage) for the three acceleration cases at $y^+ = 3$.

the start of the stage III. The amplitude of v' recovers first in the first and fourth quadrants in the stage III.

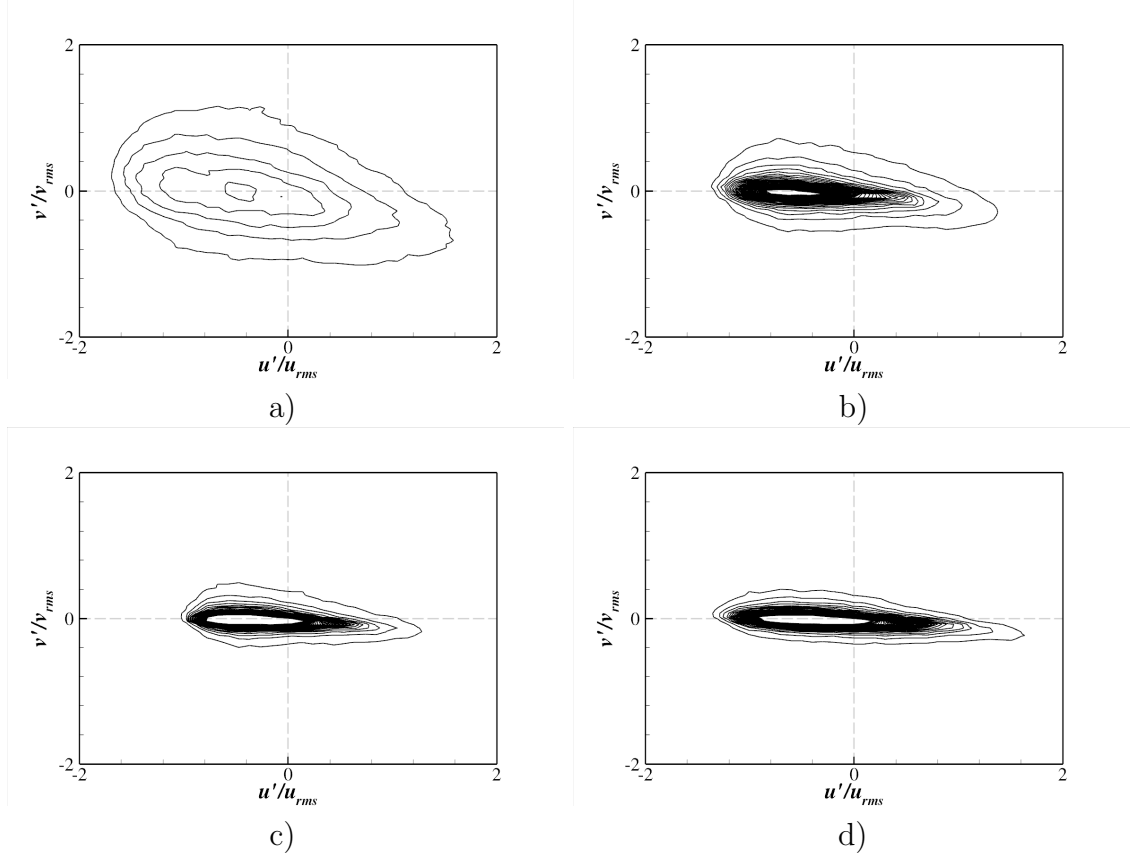


Figure 7.23: Joint pdf of u' and v' at $y^+ = 3$ at a) $Re = 3500$ (steady), b) $Re = 12000, f = 0.2$, c) $Re = 15000, f = 0.33$, and d) $Re = 18000, f = 0.5$ in the stage II. 2D bin size is kept constant as $0.1u_{rms}$ for u' and $0.05v_{rms}$ for v' . Same contour levels are used for all figures.

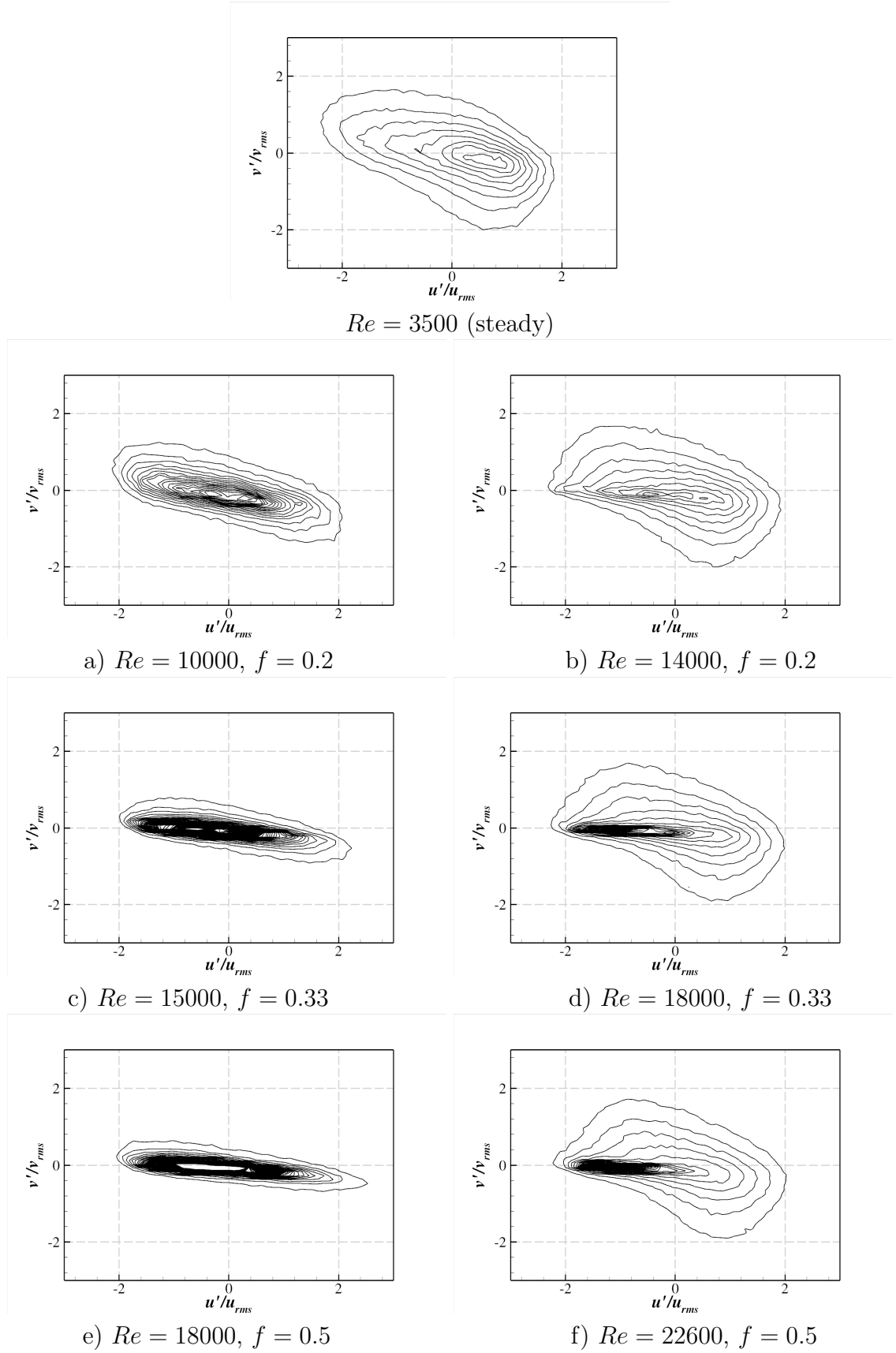


Figure 7.24: Joint pdf of u' and v' at $y^+ = 20$ at several Reynolds numbers in the stage II and the stage III during the acceleration.

7.7 Turbulent structures

In this subsection, the two-point correlation coefficients analysis is employed to study the near-wall structures during various stages of acceleration. Please note that, for this analysis the correlations are constructed with velocity information from 10 xz planes, comprising of approximately 2 million data points. The variation of correlations is shown at $y^+ = 20$ and $y = h$.

Figure 7.25 shows the two-point correlation coefficient variation of u for $f = 0.2$ case and $f = 0.5$ case. There is an increase in the coefficient value during the stage II at $y^+ = 20$ in Figure 7.25a. This increase implies the elongation of near-wall structures in the streamwise direction. The increase in coherence of the near-wall structures was also reported in the pulsating turbulent pipe LES investigation (Manna and Vacca, 2008). The correlation value decreases below the initial value after the generation of new turbulence in the stage III and the stage IV. A large acceleration rate enhances the coherence of near-wall structures in the stage II in the near-wall region. The core region also show an increase in correlation coefficient during the acceleration.

Two-point correlation coefficient of v , in Figure 7.26, also shows a similar increase during the stage II. It is interesting to note that the increase in correlation is not as significant as for u , and this increase is limited in the range of $x \leq 2$ for $f = 0.2$ case and $x \leq 3$ for $f = 0.5$ case, respectively. The correlation value decreases sharply in the stage III (at $Re = 120000$ and $Re = 18000$ for $f = 0.2$ case and $f = 0.5$ case respectively). This sharp decrease may indicate the occurrence of highly energetic wall-normal transport in the near-wall region with the advent of new turbulence generation in the stage III. The correlation coefficient of w exhibits similar trends as for v and is not shown here.

In Chapter 6, the existence of low-speed streaks with two distinct length scales during the acceleration has been reported. The effect of different acceleration rates

7.7. TURBULENT STRUCTURES

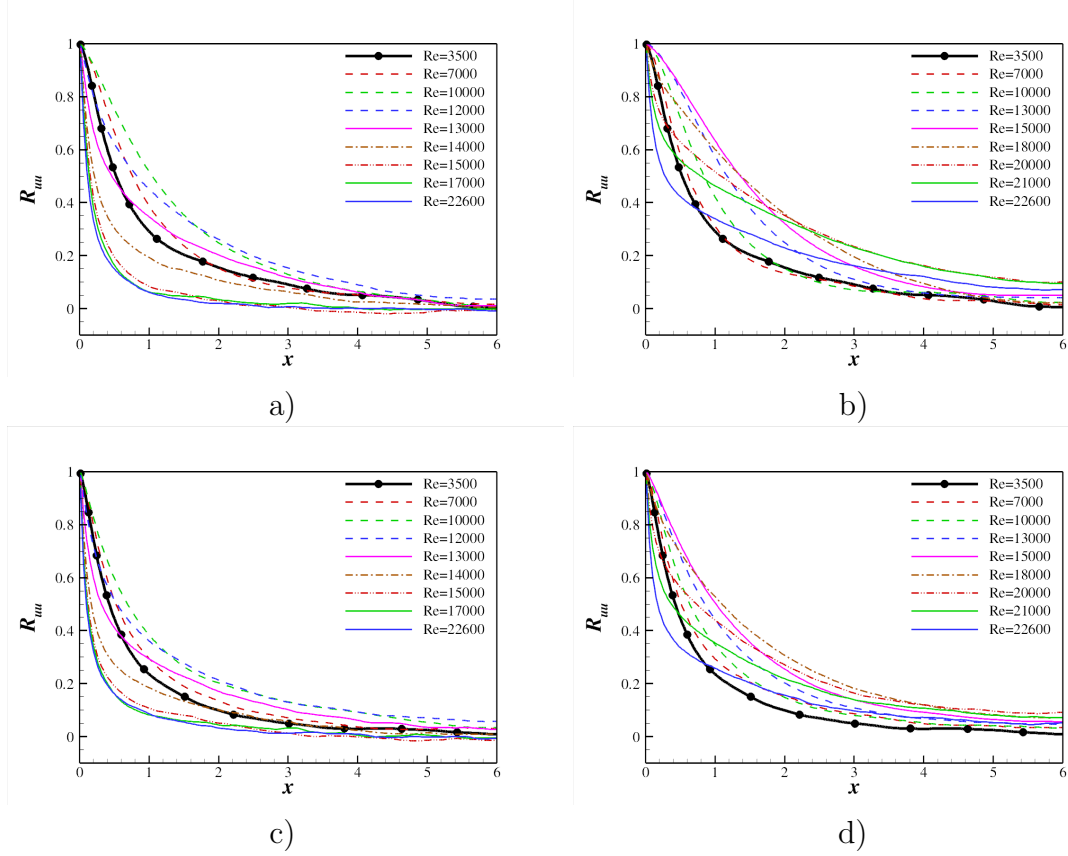


Figure 7.25: Two-point correlation variation of $\langle u, u \rangle$ in the streamwise direction during the acceleration at a) $y^+ = 20$, $f = 0.2$ case, b) $y^+ = 20$, $f = 0.5$ case, c) $y = h$, $f = 0.2$ case, and d) $y = h$, $f = 0.5$ case.

and as well as the low-speed streak patterns in the stage IV can be studied using the correlation coefficient of u in the spanwise direction. Figure 7.27 shows the two-point correlation variations for $f = 0.2$ case and $f = 0.5$ case at $y^+ = 20$. The local minimum value in the near-wall region increases in the stage III, which is consistent with the DNS results in Chapter 6. This increase in local minimum value is very clear in Figure 7.27b at $Re = 21000$. The increase of two-point coefficient above zero increases with f values. Afterwards, the local minimum value decreases in the stage IV for $f = 0.2$, as clearly seen at $Re = 17000$ and $Re = 22600$ in Figure 7.27a.

In the DNS study, the low-speed streak patterns could not be examined in the stage IV. Figures 7.28 and 7.29 show the instantaneous low-speed streak contours at $y^+ = 5$ at several Reynolds numbers for $f = 0.2$ and $f = 0.5$ cases, respectively.

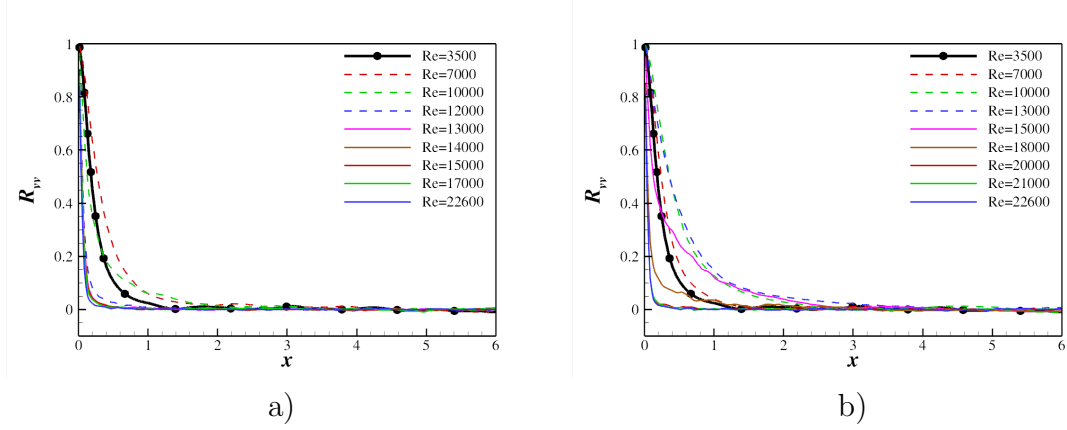


Figure 7.26: Two-point correlation variation of $\langle v, v \rangle$ in the streamwise direction during the acceleration for a) $y^+ = 20$, $f = 0.2$ case, and b) $y^+ = 20$, $f = 0.5$ case.

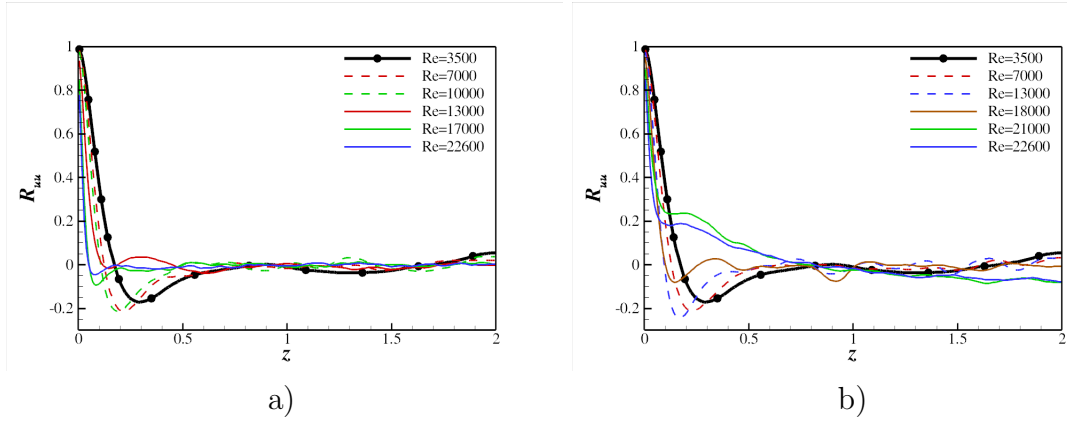


Figure 7.27: Two-point correlation variation of $\langle u, u \rangle$ in the spanwise direction at $y^+ = 20$ during the acceleration for a) $f = 0.2$ case, and b) $y^+ = 5$, $f = 0.5$ case.

Please note that both figures are from the same initial conditions, therefore these figures also show the effect of acceleration rate clearly. Same contour levels are used in the first three plots to show the changes in the streamwise velocity fluctuations strength in the stage II. Low-speed streaks at $Re = 7000$ for both cases show that the strength of streamwise fluctuations reduces with f . Moreover, the elongation of low-speed streaks is clearly seen in the stage II. The reduction in low-speed streak strength is recovered during the stage III. The generation of new low-speed streaks with smaller length scales in terms of distinct patches is evident in the stage III, at $Re = 13000$ and $Re = 14000$ for $f = 0.2$ case in Figure 7.28 and

7.7. TURBULENT STRUCTURES

at $Re = 20000, 21000$ and 22600 for $f = 0.5$ case in Figure 7.29. Similar streak patterns were also found in DNS of temporal acceleration.

Figures 7.30 and 7.31 show the iso-surfaces of λ_2 for $f = 0.2$ case and $f = 0.5$ case respectively. Please note that the iso-surfaces are plotted for the same data as used for low-speed streak plots in Figures 7.28 and 7.29. Maximum rms λ_2 values are chosen as threshold values for the iso-surface plots. The generation of new structures in the stage III is clearly seen from the plots at $Re \geq 10000$ and $Re \geq 15000$ for $f = 0.2$ case and $f = 0.5$ case respectively. The new structures are generated in form of patches in the stage III as observed in DNS case in Chapter 6. The entire wall is filled with the newly generated structures in the stage IV as shown for $f = 0.2$ case in Figure 7.30 at $Re = 17000$ and $Re = 22600$. The final Reynolds number ($Re = 22600$) for $f = 0.2$ case lies in the stage III, therefore, the new turbulence generation is not completed at $Re = 22600$ in Figure 7.30.

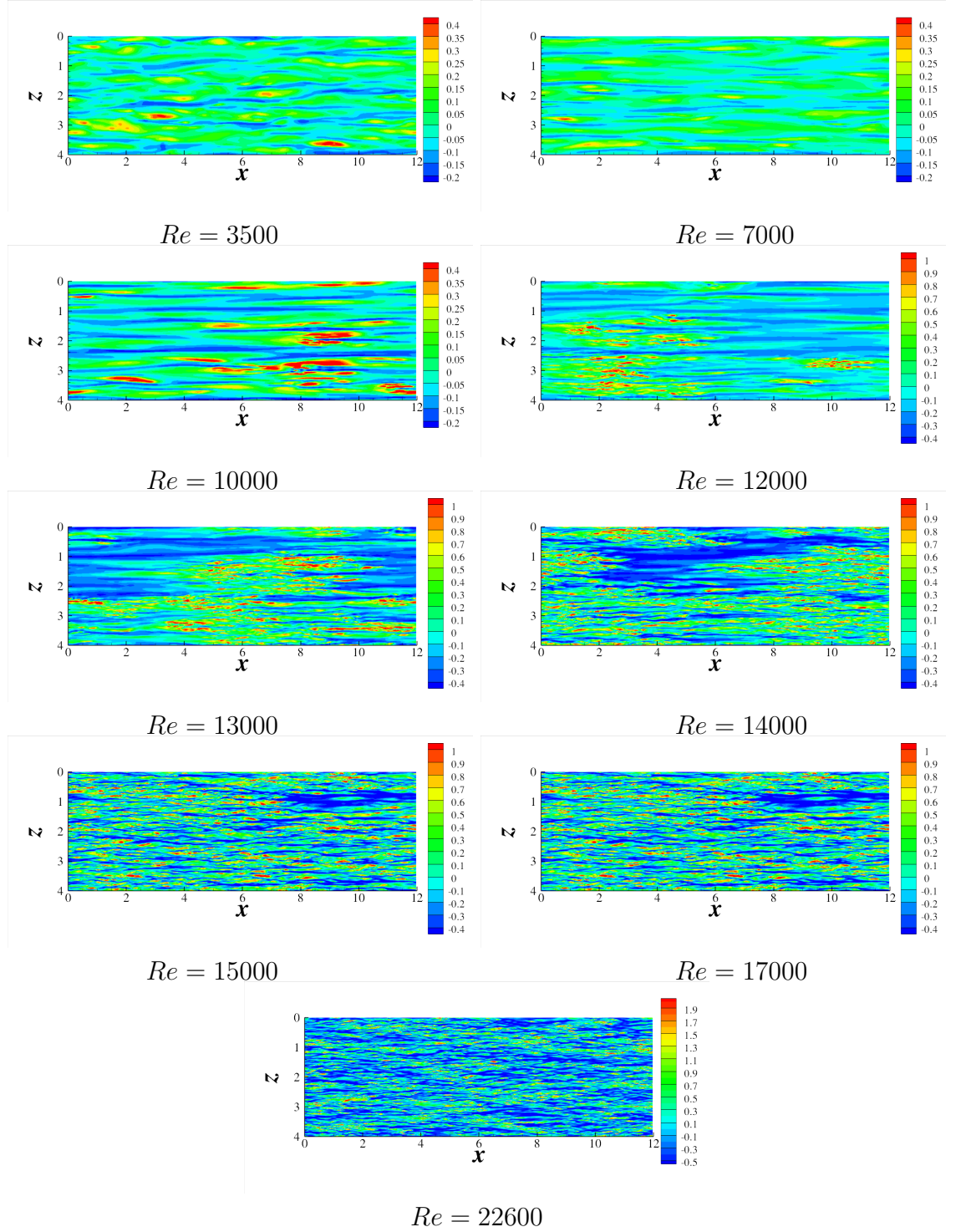


Figure 7.28: Low-speed streaks at $y^+ = 5$ during acceleration at several Reynolds numbers for $f = 0.2$ case.

7.7. TURBULENT STRUCTURES

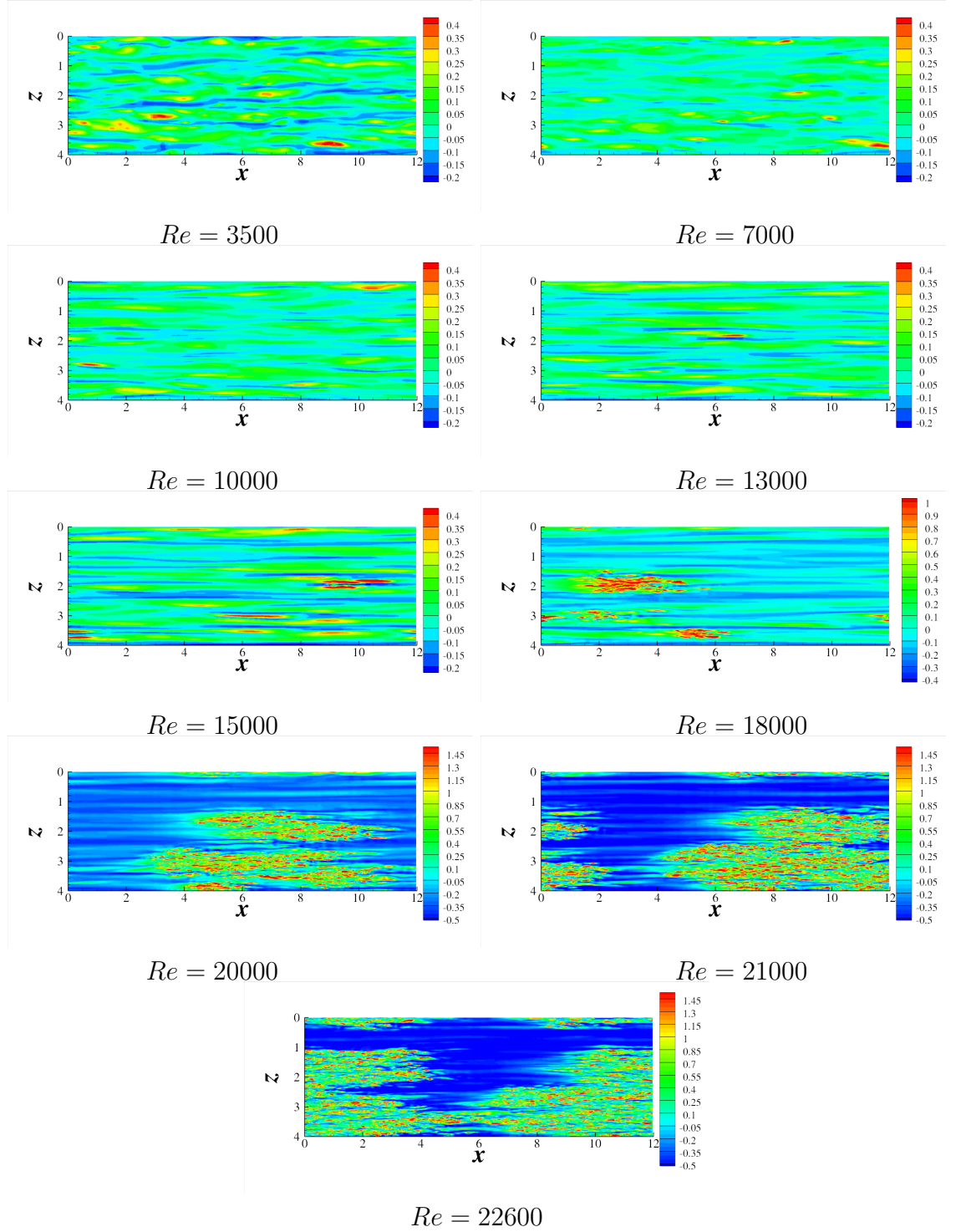


Figure 7.29: Low-speed streaks at $y^+ = 5$ acceleration at several Reynolds numbers for $f = 0.5$ case.

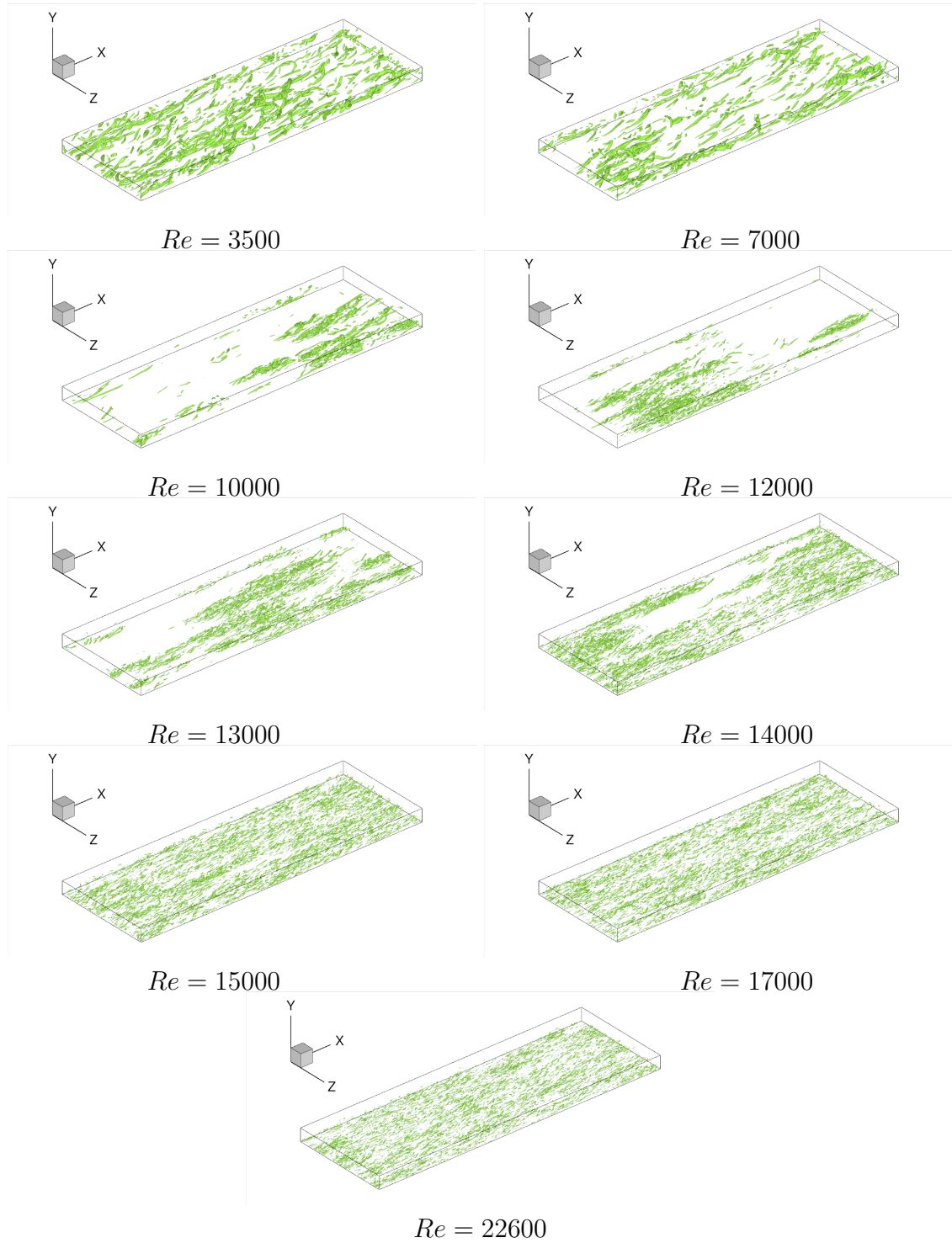


Figure 7.30: λ_2 iso-surfaces at several Reynolds numbers for $f = 0.2$ case.

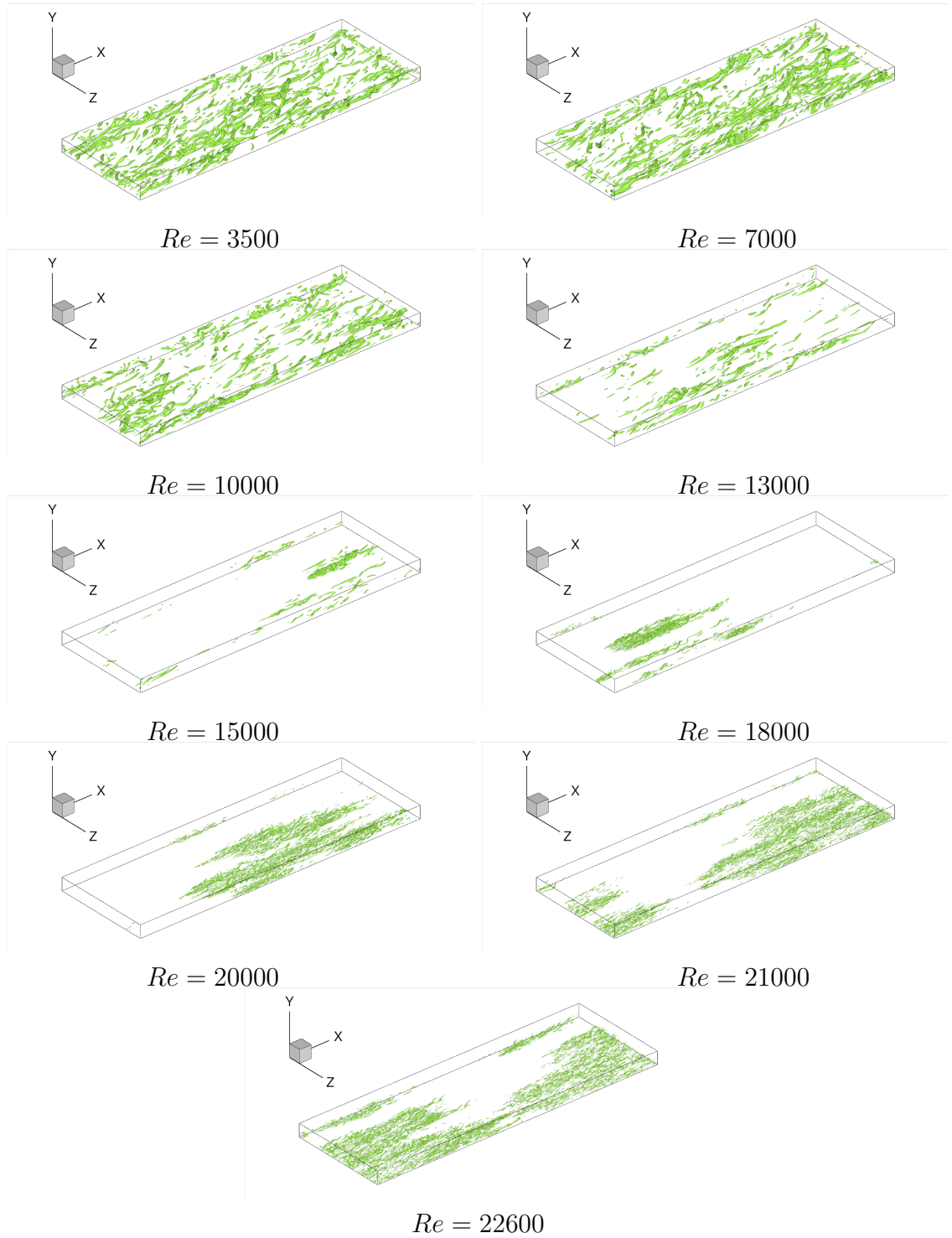


Figure 7.31: λ_2 iso-surfaces at several Reynolds numbers for $f = 0.2$ case.

The active area quantification procedure employed in the DNS study is applied for the three acceleration cases. The percentage of the area filled with new turbulent structures is shown in Figure 7.32. Five LES realisations are used for averaging and data from top and bottom halves are also averaged. LES data for $f = 0.2$ case show good agreement with the DNS data. The rate of new turbulence generation is similar for the three cases as shown in Figure 7.32. This may imply that the turbulence generation process appears to be largely independent of the acceleration rate.

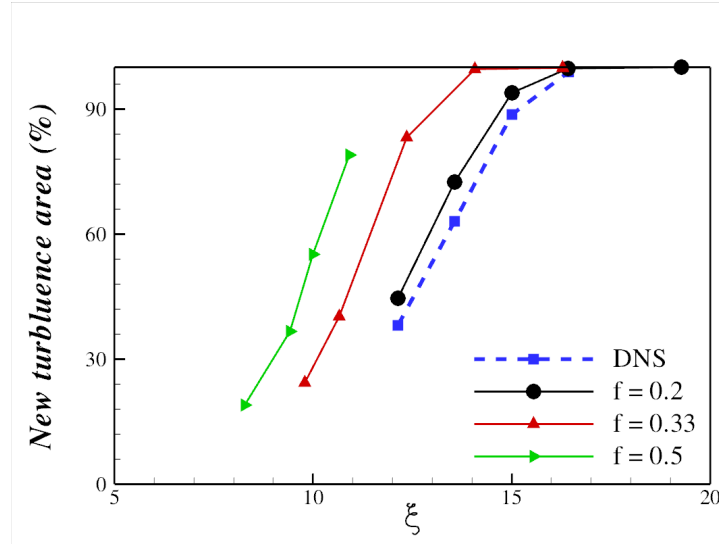


Figure 7.32: Percentage of new turbulent area during acceleration for the three cases. DNS data for $f = 0.2$ case are also included.

Figure 7.33 shows the variation of ω'_x in the non-active flow regions (as introduced in Subsection 6.3) for three acceleration cases. The initial steady ω'_x profile is added for the comparison. It shows that the strength of streamwise vorticity in non-active regions reduces below the initial at $\xi \approx 5$, followed by an increase in the later part of the stage II. $\omega'_{x,max}$ responds earlier than $\omega'_{x,min}$ and the streamwise vorticity attains the same strength as that of initial value in the later stages of the stage II.

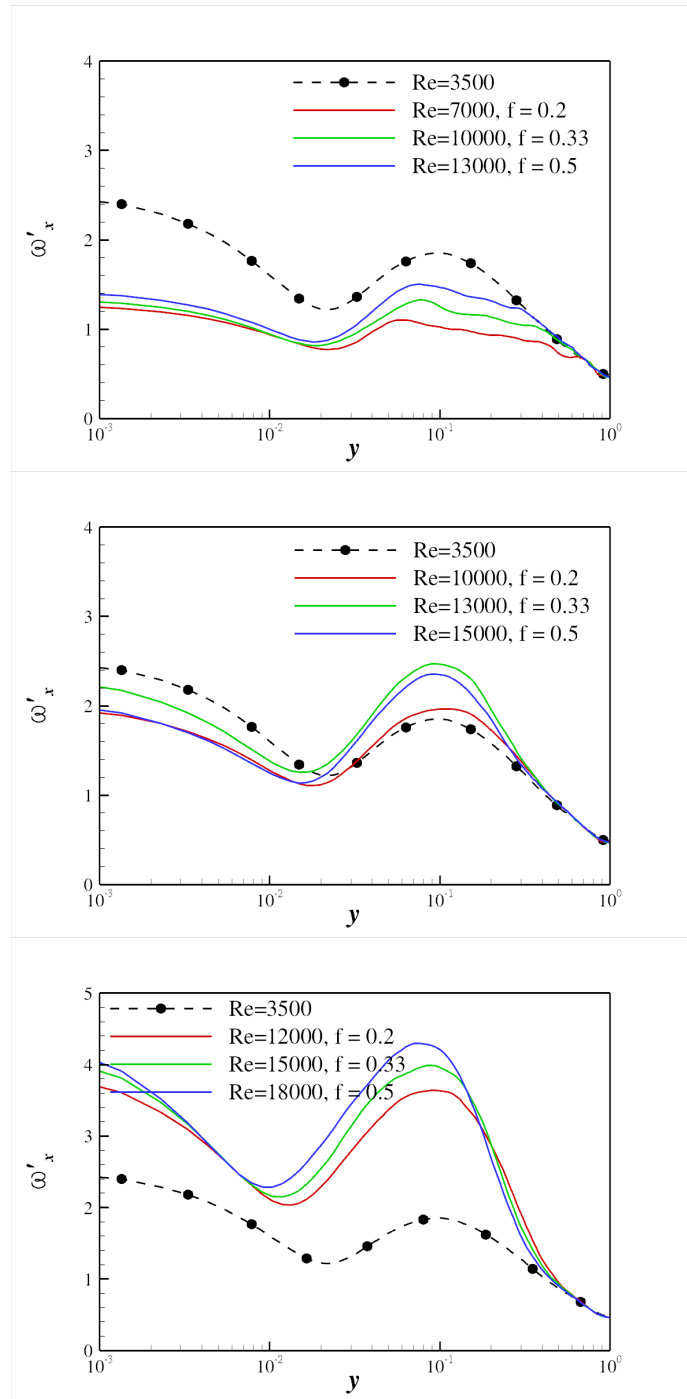


Figure 7.33: Conditionally averaged ω'_x profile in non-active area at different stages of the acceleration for the three f values. Conditionally averaged profiles are plotted at $Re = 7000$ (or $\xi = 5$), $Re = 10000$ (or $\xi = 9.3$) and $Re = 12000$ (or $\xi = 11.9$) for $f = 0.2$ case, while for $f = 0.33$ case $Re = 10,000$ (or $\xi = 5.5$), $Re = 13,000$ (or $\xi = 8.1$) and $Re = 15,000$ (or $\xi = 9.8$), and for $f = 0.5$ case, the graphs are plotted at $Re = 13000$ (or $\xi = 5.4$), $Re = 15,000$ (or $\xi = 6.5$) and $Re = 18,000$ (or $\xi = 8.3$).

7.8 Conclusions

The results presented in this chapter demonstrate that the turbulence returns to the pseudo-steady equilibrium state after exhibiting a certain delay during temporal acceleration. Although the imposed acceleration is linear, its tendency to produce of a uniform increase in the mass flow rate throughout the entire cross-section in the initial stages of acceleration results in streamwise elongation of near-wall turbulent structures and hence causes a certain delay in their response. This initial delay results in subsequent rapid turbulence response until turbulence achieves pseudo-steady state. The findings of this chapter are as following

1. The wall shear stress increases monotonically in the PS stage (stage IV) after exhibiting a significant deviation from the steady values in the first three stages.
2. The deviation of the wall shear stress and the mean velocity from the corresponding steady values increases with f while the duration of the IT stage (stage I), the WT stage (stage II) and the ST stage (stage III) decrease with the increase in the acceleration rate.
3. The delay in response for the rms velocity and vorticity fluctuations decreases with the increase in acceleration rate.
4. The characteristic speed of turbulence propagation in the core region is similar to the initial u_τ value and it is largely independent of the acceleration rate.
5. Degree of breakdown of local equilibrium between turbulence and mean flow increases with f .
6. The pdf analysis supports the findings in the DNS study (Chapter 5), and exhibit an increase in quadratic contribution from first and fourth quadrant

7.8. CONCLUSIONS

and a corresponding reduction in second and third quadrant contribution in the stage III. This trend becomes more prominent with f .

7. The suppression of wall-normal fluctuations in the near-wall region increases with increase in acceleration rate value while the pdf contours show similar trends during the stage II and the stage III for the three cases.
8. The two-point correlation coefficient in the streamwise direction indicates an increase in coherence of near-wall structures. The enhanced coherence increases with f .
9. Low-speed streaks show that the two length scale behaviour of low-speed streaks increases with increase in acceleration rate.
10. Iso-surfaces of λ_2 supports the DNS findings *i.e.*, emergence of new turbulence in form of patches during the stage III. Turbulence generation process is found to be largely independent of the acceleration rate.

8

LES of Temporal Deceleration.

In the previous chapters, the turbulent channel flow subjected to temporal acceleration has been investigated in detail, which has revealed many interesting results. However, turbulent flows subjected to temporal deceleration has received little attention as compared to its acceleration counterpart. He and Jackson (2000) reported the time histories of rms velocity fluctuations for the turbulent pipe flow subjected to temporal deceleration in their experimental study. Chung (2005) investigated the turbulent channel subjected to sudden deceleration at a relatively low Reynolds number range. Coleman et al. (2003) studied the fully-developed turbulent channel flow subjected to a mean streamwise strain. More recently, Ariyaratne et al.

(2010) investigated the temporal deceleration in turbulent pipe by using unsteady RANS approach. LES of turbulent channel flow subjected to temporal deceleration is performed for two deceleration rates in order to study turbulence response during temporal deceleration.

8.1 Simulation parameters

LES was performed for the fully-developed turbulent channel subjected to temporal linear deceleration. The initial and final Reynolds numbers, based on the bulk-mean velocity and the channel half-height (h), are $Re_0 = 22600$ ($Re_\tau \approx 1100$) and $Re_f = 3500$ ($Re_\tau \approx 215$) respectively and these ranges are the same as in Chapter 7 for LES of temporal acceleration. Two deceleration rates were employed in the present study to investigate the effect of different deceleration rates ($f = -0.2$ and $f = -0.5$). Table 8.1 shows the simulation details used. Ensemble averaging was taken over 10 independent realisations to improve the flow statistics. The separation between each realisation is approximately 100 ($tu_{\tau 0}^2/\nu$). Please note that f and ξ are calculated based on the final Reynolds number ($Re = 3500$) same as used for temporal acceleration. The bulk-mean velocity is decreased linearly from 6.46 to 1 based on this scaling.

Case	$L_x \times L_y \times L_z$	f	T_e	$dRe/d\xi$	Realisations
Case-1	$12h \times 2h \times 4h$	-0.20	27.3	-700	10
Case-2	$12h \times 2h \times 4h$	-0.50	10.9	-1750	10

Table 8.1: Details of LES performed for temporal deceleration.

Table 8.2 shows the grid resolution used in the present study. The LES grid resolution in the homogeneous directions were about twice the DNS grid spacing. The Dynamic SGS model (Germano et al., 1991; Lilly, 1992) was used to account for

unresolved SGS stresses. Test filtering was applied in the homogeneous directions only.

$L_x \times L_y \times L_z$	$N_x \times N_y \times N_z$	Δx^+	Δy_{min}^+	Δy_{max}^+	Δz^+
$12h \times 2h \times 4h$	$512 \times 192 \times 384$	25.7	1	27.5	11.4

Table 8.2: Simulation parameters based on $Re_\tau = 1100$.

First, an LES of steady channel flow at $Re = 22600$ was performed to provide the initial conditions for the main simulations. The mean velocity and rms velocity fluctuations are in good agreement with the DNS data of Abe et al. (2004) at $Re_\tau = 1020$ (cf. Figures 3.7 and 3.8).

Domain size independence test

It was found in the domain size independence test for temporal acceleration that a small domain size, $L = 6h$, caused suppression of turbulence response in the near-wall region, and very little difference was found between $L = 12h$ and $L = 18h$ domains. The effect of the domain size in the near-wall region depends upon the size of near-wall structures. This domain size effect was significant for temporal acceleration due to the fact that the initial Reynolds number of the calculations, $Re_\tau \approx 215$, was in relatively a low Reynolds number range. The size of the near-wall structures at this Reynolds number is significantly large as shown in λ_2 iso-surface plots in Chapter 6.

In the present case, a parametric study was conducted to study the effect of the length of the computational domain for turbulent channel flow subjected to temporal deceleration. Two different lengths of the domain were selected as shown in Table 8.3. Computations were performed for two f values (cf. Table 8.1) to determine the sensitivity of the domain size with respect to deceleration rate.

8.1. SIMULATION PARAMETERS

Case	$L_x \times L_y \times L_z$	$N_x \times N_y \times N_z$	Realisations
Len-1	$6h \times 2h \times 4h$	$256 \times 192 \times 384$	20
Len-2	$12h \times 2h \times 4h$	$512 \times 192 \times 384$	10

Table 8.3: Details of simulations for the present study.

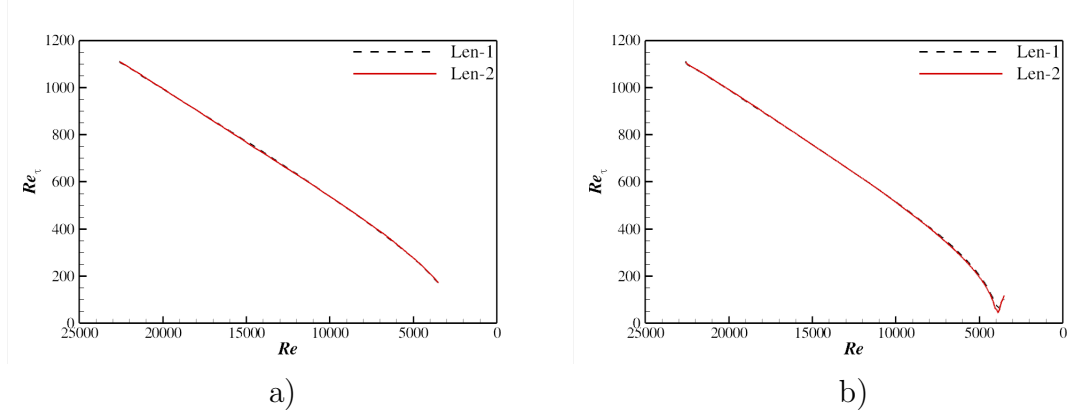


Figure 8.1: Re_τ time history for a) $f = -0.2$ case, and b) $f = -0.5$ case.

Figures 8.1 and 8.2 show a comparison of the wall shear stress and rms velocity fluctuations during the deceleration. The effect of the computational length is found to be less critical for the temporal deceleration, as compared to the temporal acceleration (cf. Figures 4.2 and 4.4). This is not unexpected because the size of near-wall structures is significantly smaller at the initial Reynolds number for flow deceleration ($Re = 22600$), than the initial size for temporal acceleration ($Re = 3500$). The domain length of $L = 12h$ is selected for the present study.

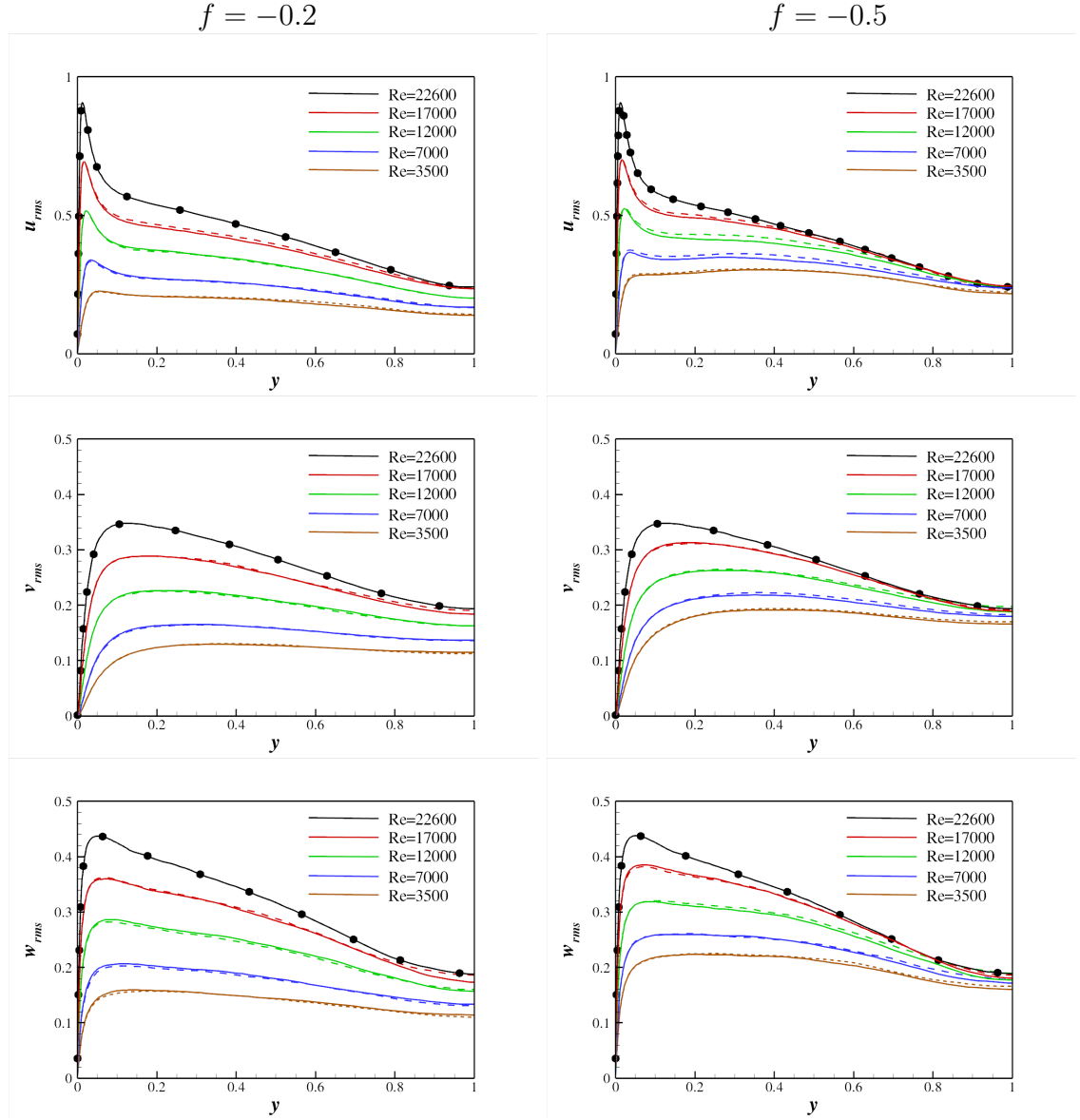


Figure 8.2: The rms velocity fluctuations profiles at several Re numbers during the deceleration. Dashed lines denote ‘Len-1’ case while solid lines denote ‘Len-2’ case.

8.2 Wall shear stress

Figure 8.3 shows the time histories for Re_τ during the deceleration for the two deceleration cases. Steady LES data at several Reynolds numbers are also included for comparison. Re_τ time histories indicate that the initial reduction in Re_τ is in good agreement with the corresponding steady Re_τ values. The wall shear stress decreases in a monotonic fashion and its value reduces below the steady value towards the final stages of the deceleration. Coleman et al. (2003) also reported a similar monotonic decrease of the wall shear stress below the steady value in a DNS study of decelerated turbulent channel flow. Ariyaratne et al. (2010) reported a four-stage response of the wall shear stress during the temporal deceleration. They found a rapid reduction of the wall shear stress in the initial stage of deceleration. The rapid decrease of the wall shear stress in the initial stage of deceleration is more likely to happen in case of turbulent flows involving sudden deceleration, as reported by Chung (2005).

The difference between the steady and unsteady wall shear stress values increases towards the final stages of the deceleration, with this deviation greater for $f = -0.5$ case in Figure 8.3b. It is interesting to note that Re_τ value reaches its minimum ($Re_\tau \approx 65$) at $Re \approx 3800$ for $f = -0.5$ case in Figure 8.3b, followed by a subsequent increase during the final stages of the deceleration.

Time history of skin friction coefficient (C_f) in Figure 8.4a shows a reduction in C_f value from the steady value more clearly towards the end of deceleration. C_f value for $f = -0.5$ decreases at a similar rate as compared to the steady value until $Re = 9000$, while on the other hand, the deviation is more prominent for $f = -0.5$. It is interesting to note that C_f starts to increase towards the final stages of the deceleration for $f = -0.5$ which is indicative of flow separation. Time history graph for the mean pressure gradient during the deceleration in Figure 8.4b

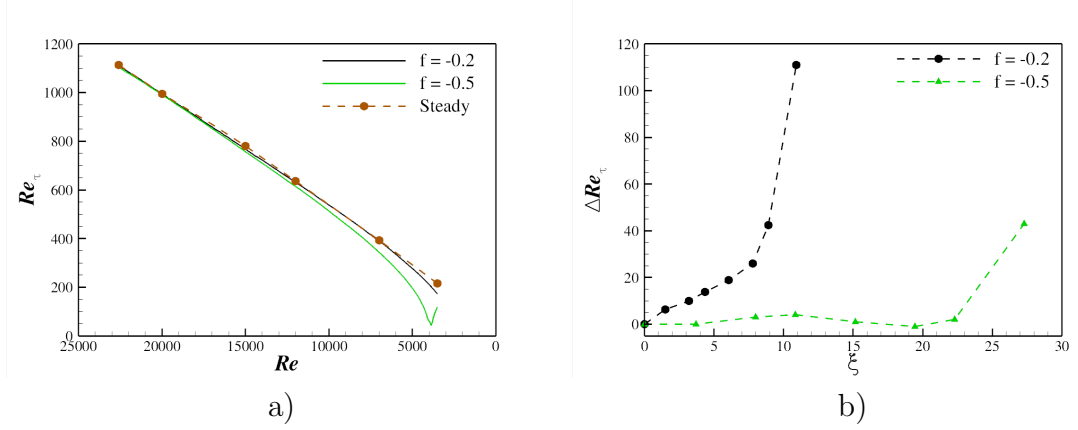


Figure 8.3: Time variations of a) Re_τ , and b) the difference of Re_τ between the steady and unsteady values *i.e.*, $\Delta Re_\tau = Re_{\tau, \text{steady}} - Re_{\tau, \text{unsteady}}$ for the two cases.

shows the evidence of flow reversal. The mean pressure gradient drives the flow and is balanced by the wall shear stress in turbulent channel flow. A positive mean pressure gradient towards the end of deceleration clearly shows a reversal of the mean flow. Flow reversal at wall is also reported by Coleman et al. (2003) towards the final stages of the deceleration.

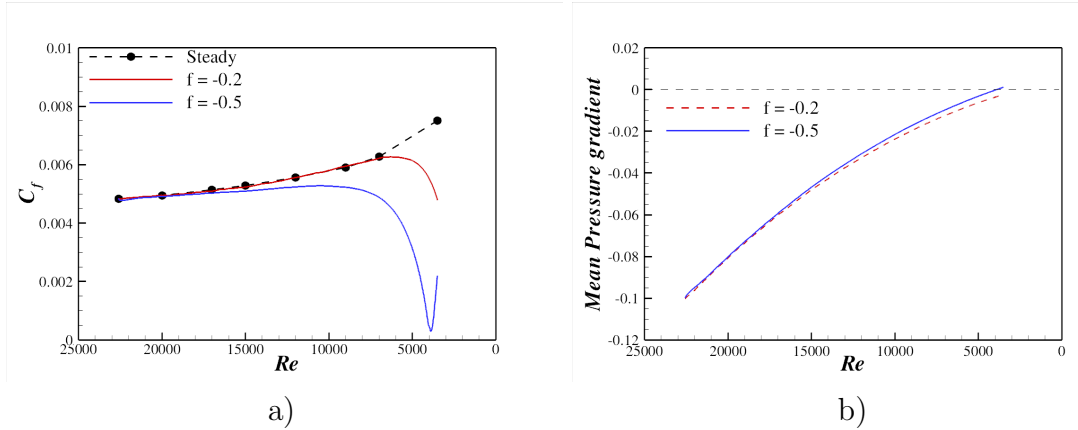


Figure 8.4: Time histories of a) C_f and, b) the mean pressure gradient during the deceleration.

Time histories of boundary layer parameters are plotted in Figure 8.5 to show the variation of the mean velocity in the very near-wall region during the deceleration. The displacement thickness and the boundary layer thickness show a large decrease in the mean velocity. The increase in δ^* and θ becomes larger for $f = -0.5$ case. All

8.2. WALL SHEAR STRESS

boundary layer parameters exhibit a significant deviation from the steady values at $Re = 3500$. The similar trends of boundary layer parameters are also reported in experimental and as well as numerical investigation of boundary layers subjected to adverse pressure gradient (Sparlart and Watmuff, 1993).

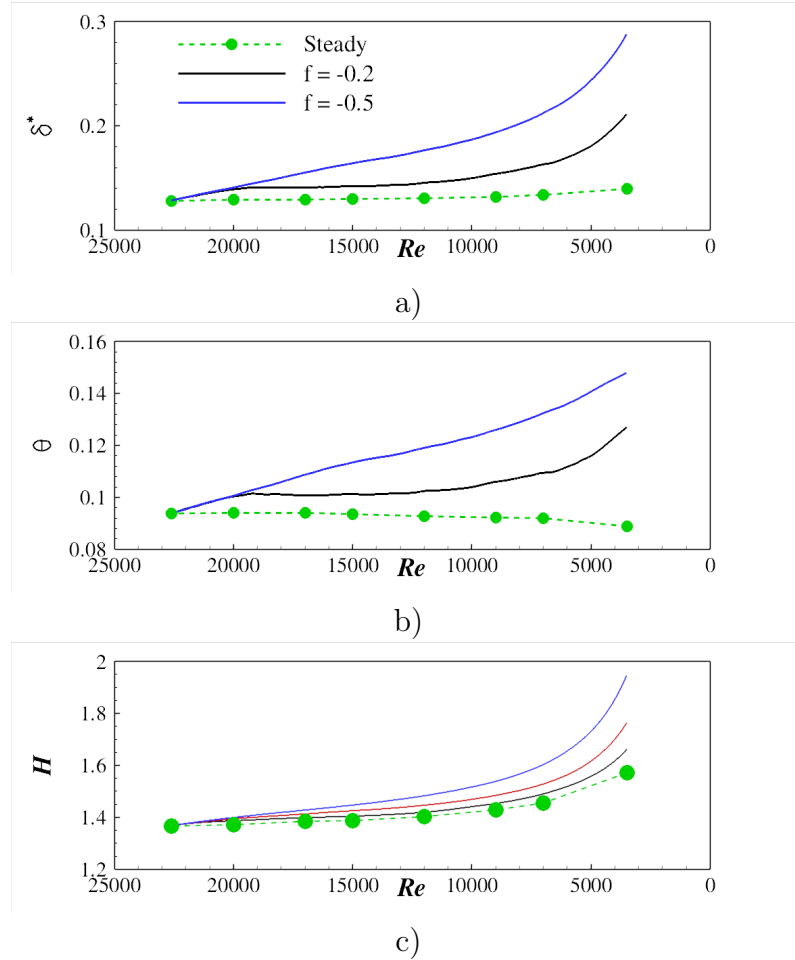


Figure 8.5: Variation of boundary layer parameters during the deceleration for the two cases.

8.3 Mean velocity

The mean velocity profiles at several Reynolds numbers are plotted for $f = -0.2$ and $f = -0.5$ cases in Figure 8.6 to investigate the mean velocity trends during the deceleration. The mean velocity reduces below the steady value in the near-wall region ($y \leq 0.5$) at $Re = 17000$, while it increases in the core region. It is worth noting that the opposite trend has been reported in the initial stages of temporal acceleration case in Chapter 5. A higher deceleration rate increases the deviation of the mean velocity from the corresponding steady value.

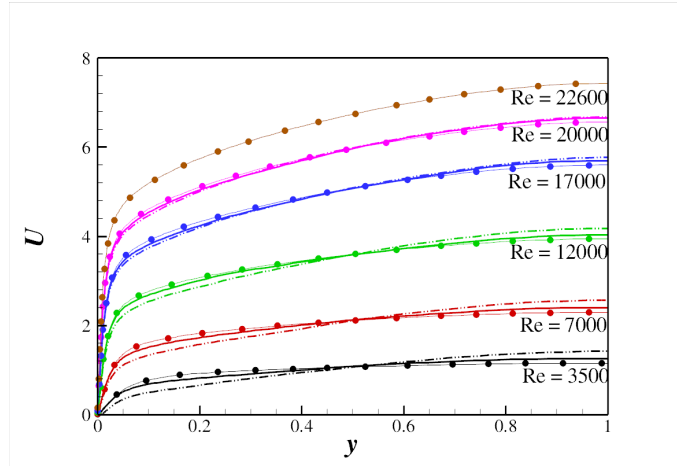


Figure 8.6: Mean velocity profiles during deceleration at several Reynolds numbers for the two cases. Steady values (lines with symbols) are included. Solid lines correspond to the $f = -0.2$ case, and dashed-dott-dott lines correspond to $f = -0.5$ case.

Figure 8.7 shows the variation of the mean velocity gradient dU/dy at several Reynolds numbers during the deceleration for $f = -0.2$ and $f = -0.5$ cases. The mean velocity gradient at the wall for $f = -0.2$ is similar to the corresponding steady values for most part of the deceleration, and this trend is consistent with the wall shear stress plot in Figure 8.3a. On the other hand in the core region, the velocity gradient is larger than the steady values, and this trend is also evident in Figure 8.6. The gradient value at wall decreases below the steady value at

8.3. MEAN VELOCITY

$Re = 3500$ indicating a considerable reduction in the wall shear stress. The effect of deceleration is more clearly seen for $f = -0.5$ case in Figure 8.3b. Please note that the velocity gradient becomes negative in the near wall region at $Re = 3500$, which is not shown due to the choice of log scale for this plot. The deviation from the steady values becomes larger with increase in deceleration rate.

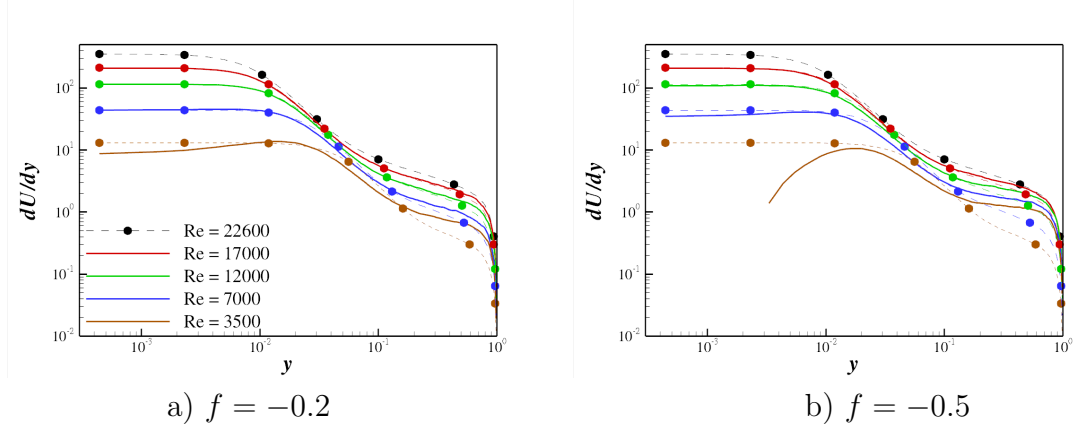


Figure 8.7: dU/dy profiles during the deceleration. Steady values (dashed lines with symbols) are included.

Figure 8.8 shows the variation of the mean velocity in the viscous scales. The law of the wall is followed quite closely for $f = -0.2$ except $Re \leq 5000$. The deviation from the log-law is more prominent for $f = -0.5$. The wake region component increases gradually towards the end of the deceleration due to the smaller local u_τ values.

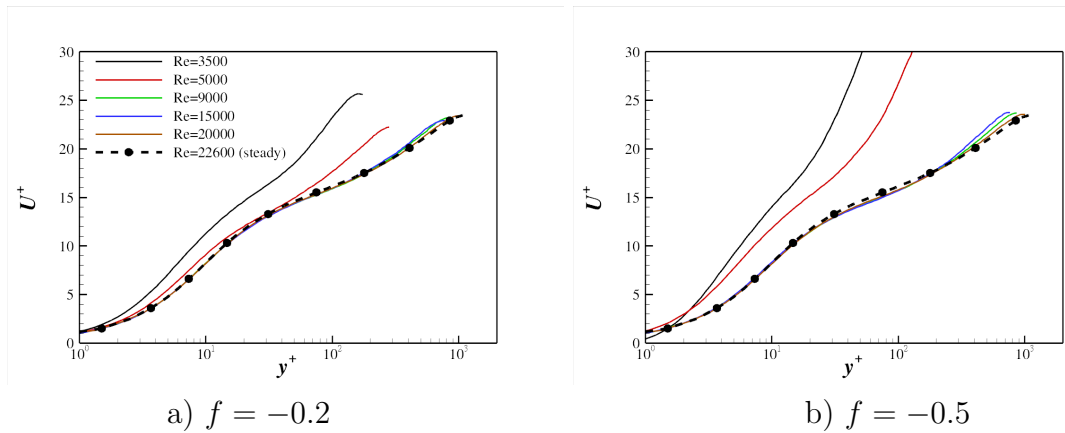


Figure 8.8: Mean velocity profiles in wall units during the deceleration.

Figure 8.9 shows the mean velocity profiles at several Reynolds numbers for $f = -0.5$ case towards the end of the deceleration. It is worth noting that the mean velocity at $Re = 5000$ is approximately equal to the steady value at $Re = 3500$ in the near-wall region ($0.0005 \leq y \leq 0.005$) indicating an excessive reduction in the mean velocity during the later stage of deceleration. The mean velocity keeps on decreasing after $Re = 5000$ and occurrence of back flow in the near-wall region is clearly seen at $Re = 3500$.

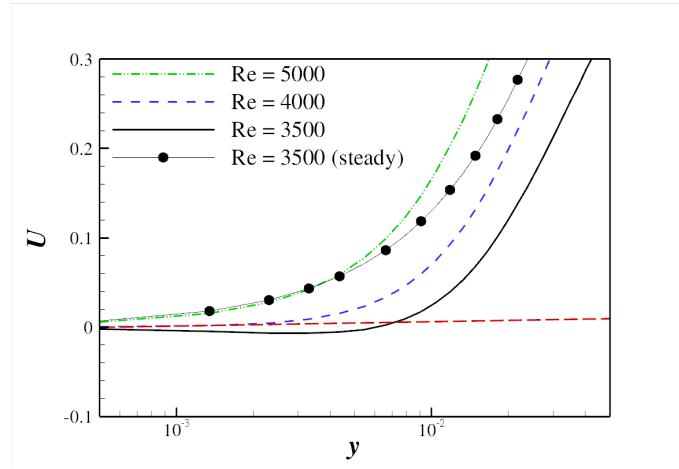


Figure 8.9: Near-wall profiles of the mean velocity for $f = -0.5$ during the final stages of the deceleration.

8.4 Turbulence intensities

Figure 8.10 shows the rms velocity fluctuation profiles at several instants for the two cases. u_{rms} exhibits reduction first in the near-wall region in the initial stage of the deceleration ($Re = 17000$) for both cases. On the other hand, the u_{rms} intensity is largely unchanged in the core region at this stage and remains frozen in the core region, for $y \geq 0.9$ and $y \geq 0.5$ for $f = -0.2$ and $f = -0.5$ cases, respectively. The frozen state of rms velocity fluctuations in the core region is also observed for the temporal acceleration. It is interesting to note that the peak values for v_{rms} and w_{rms} profiles stay above the corresponding steady value at $Re = 17000$ indicating an earlier relaxation of u_{rms} in the near-wall region during the deceleration. The anisotropic relaxation of turbulence is also reported in Chung (2005).

As the deceleration proceeds, the peak value of u_{rms} also starts to remain above the corresponding steady value in Figure 8.10a. This trend shows that turbulence in the near-wall region exhibits a relatively slow relaxation during the later stages of the deceleration. The lack of turbulence response during the later stage of deceleration is also evident in the core region, and the near-wall peaks in each profile start to diminish towards the final stage of deceleration. This results in flat rms velocity profiles at $Re = 3500$. The deviation of turbulence from the corresponding steady values increase with f .

Figure 8.11 shows the time histories of various flow properties at several wall-normal locations during the deceleration for $f = -0.2$ case. All three components decrease sharply in the very near-wall region ($y = 0.005$), while away from the wall ($y = 0.1$), the velocity fluctuations show little reduction immediately after the deceleration is applied. The delay becomes longer in the core region. This trend supports the findings from the wall-normal profiles of rms velocity fluctuations in Figure 8.10. The development of velocity fluctuations with respect to mean velocity is shown in

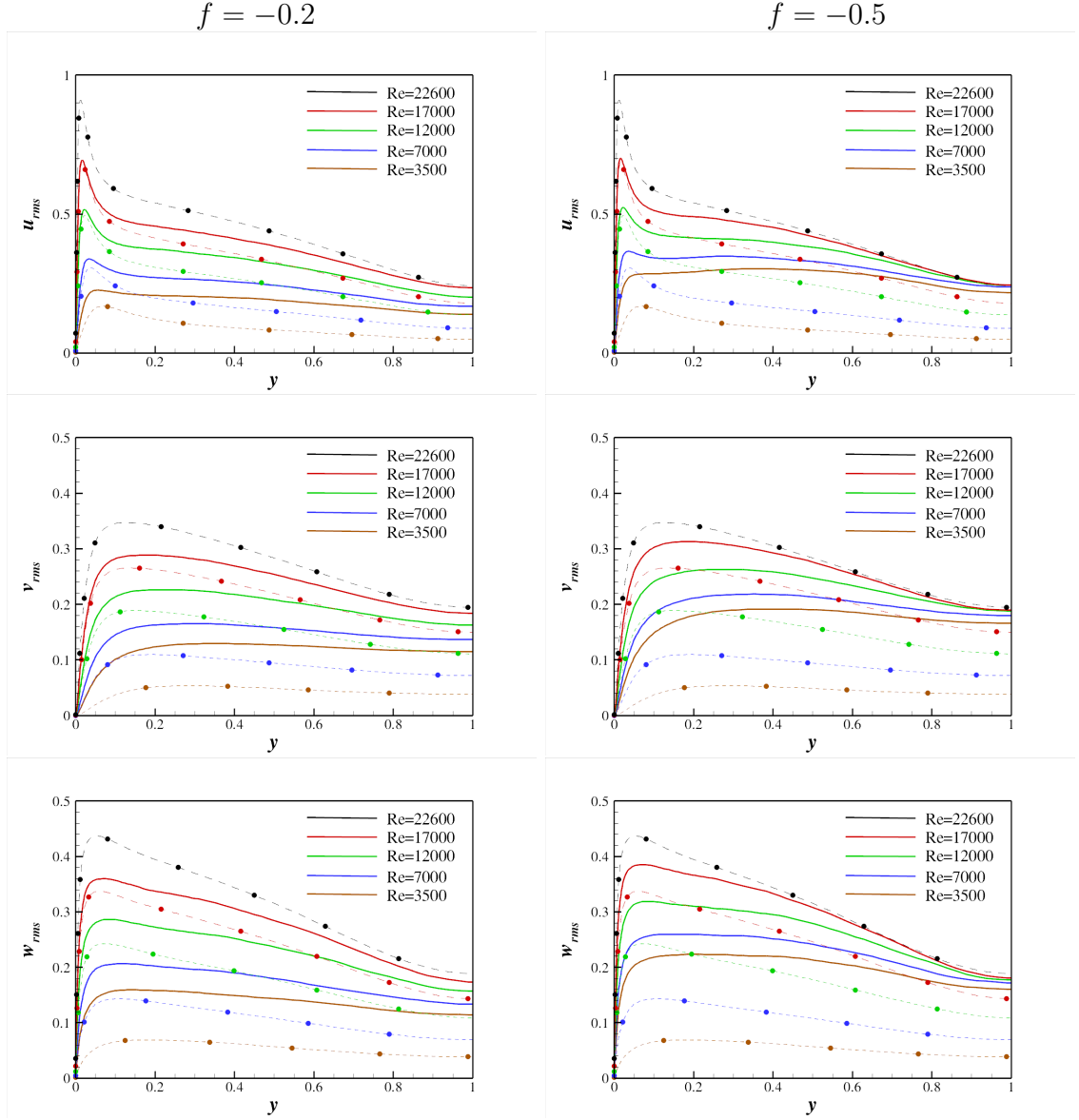


Figure 8.10: The rms velocity fluctuation profiles during the deceleration. Corresponding steady profiles (dashed lines with symbols) are included for comparison.

Figure 8.11. The steady data are also included for comparison. The time histories of $u_{i,rms}/U$ clearly show the delay in turbulence relaxation with respect to the mean velocity. This deviation from the steady values is larger in the near-wall region. The departure from the steady values is larger for $f = -0.5$ (not shown here).

Figure 8.12 shows the profiles of the turbulent shear stress and the structure parameter for $f = -0.2$ case. The turbulent shear stress is frozen in the core region

8.4. TURBULENCE INTENSITIES

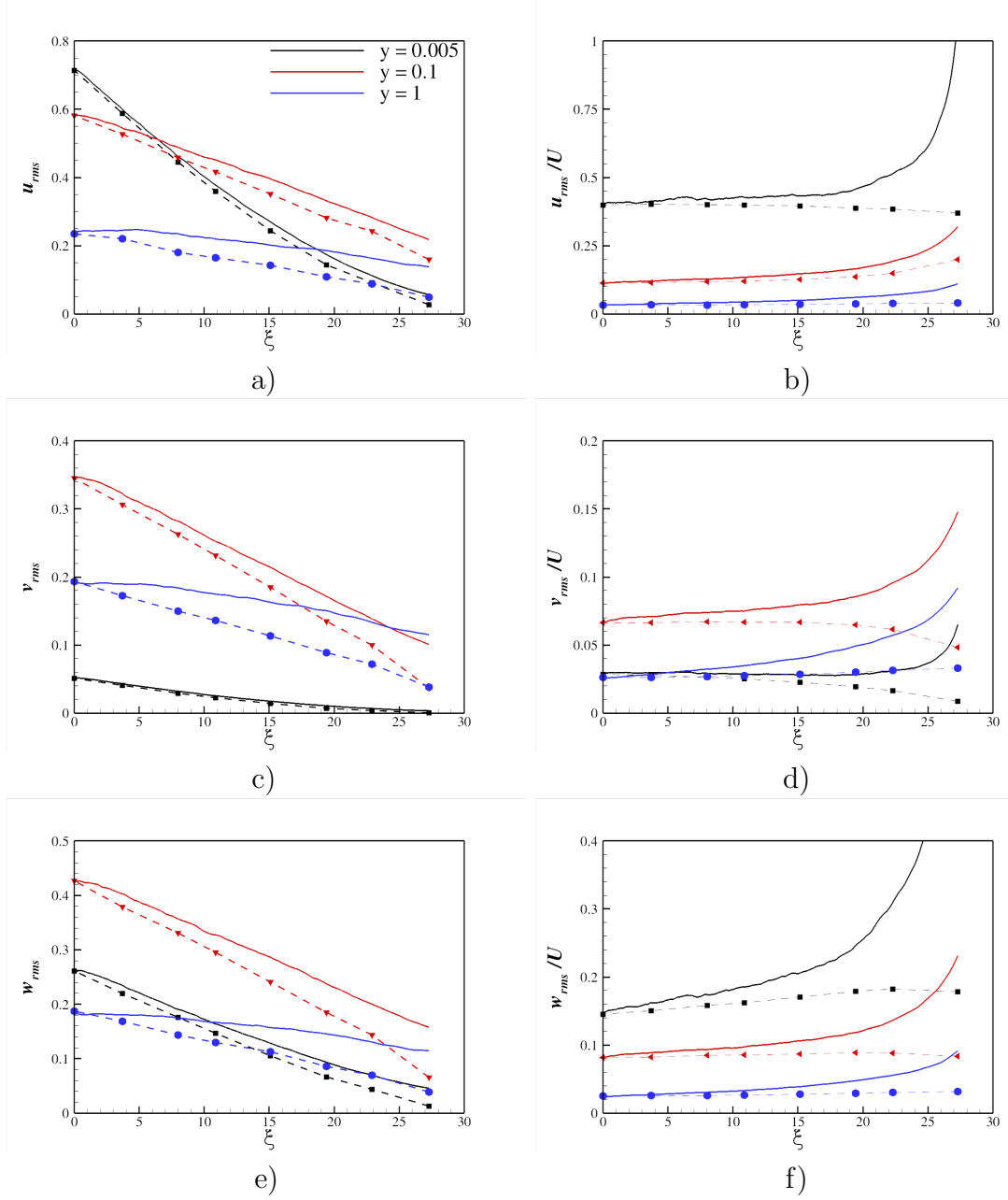


Figure 8.11: Time histories of a) u_{rms} , b) u_{rms}/U , c) v_{rms} , d) v_{rms}/U , e) w_{rms} , and f) w_{rms}/U at several y locations during deceleration for $f = -0.2$ case.

($y \geq 0.7$) at $Re = 17000$ in Figure 8.12a. The turbulent shear stress decreases more rapidly in the near-wall region as compared to the outer region, resulting in diminishing of the turbulent shear stress peak. It is interesting to note the turbulent shear stress is larger in the outer region at the final stage of calculations. An increase in the outer layer turbulent shear stress is also reported in the DNS study of Coleman et al. (2003). The ratio of the shear stress to kinetic energy ($a_1 = -\overline{uv}/2k$)

in Figure 8.12b shows the effect of temporal deceleration on the structure of the Reynolds-stress tensor. The structure parameter remains largely unchanged in the core region ($y \geq 0.6h$) during the early stages of the deceleration due to similar delay in response for the turbulent shear stress and kinetic energy. It is interesting to note that a_1 remains higher than the steady value in the near-wall region indicating an earlier relaxation of the turbulent kinetic energy over the turbulent shear stress while it drops below the steady value in the outer region at $Re = 3500$ due to relatively smaller reduction of turbulent kinetic energy.

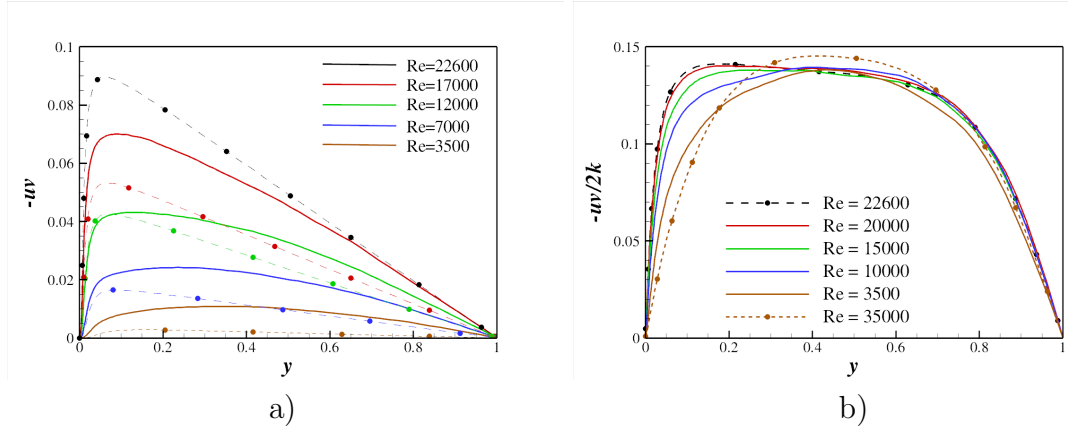


Figure 8.12: Variation of the a) $-\overline{uv}$, and b) $-\overline{uv}/2k$ during the deceleration for $f = -0.2$ case. Steady LES data (dashed lines with symbols) are also included.

Response times for the different terms of Reynolds stresses in the near-wall region are quantified using the criterion introduced for temporal acceleration in Subsection 5.4. Table 8.13 shows the response times for the Reynolds stress tensor terms. Please note that for temporal deceleration, M_s and M_f denote the maximum values at $Re = 22600$ and $Re = 3500$ respectively. \overline{uu} terms is affected first from the deceleration followed by $-\overline{uv}$, \overline{vv} and \overline{ww} and the similar pattern of response was found for temporal acceleration. The turbulence relaxation for all terms increases with f . It is important to note that turbulence relaxation is delayed for $f = -0.5$ case in terms of Reynolds number as shown in Figure 8.10 while the turbulence relaxation is higher for this case in terms of time as clearly seen in Table 8.13. This

8.4. TURBULENCE INTENSITIES

is because of relatively smaller time taken for temporal deceleration for $f = -0.5$ case (cf. Table 8.1).

Flow Property	$f = -0.2$		$f = -0.5$		M_f	M_s/M_f
	ξ_{50}^*	$R_p \times 100$	ξ_{50}^*	$R_p \times 100$		
\overline{uu}_{max}^N	9.5	96.9	3.9	92.0	2.7×10^{-2}	30.9
\overline{vv}_{max}^N	12.4	88.1	6.9	71.2	2.9×10^{-3}	42.5
\overline{ww}_{max}^N	12.6	88.7	6.4	75.4	4.9×10^{-3}	40.2
$-\overline{uv}_{max}^N$	11.3	90.8	5.7	75.8	2.8×10^{-2}	32.8

Table 8.4: Response times for maximum values of Reynolds stresses calculated using criterion introduced in Chapter 5 (cf. Equation 5.11).

Figure 8.13 shows the time histories of the maximum values of u_{rms} and v_{rms} during the deceleration. w'_{max} time history is similar to v'_{max} and is not shown here. Figure 8.13 shows that higher deceleration rate results in earlier turbulence relaxation in the near wall region. Moreover, the anisotropic response of turbulence is clearly seen with extended delay for v'_{max} . One of the major difference between turbulence response in the acceleration and deceleration cases is that, in the temporal acceleration all fluctuation components show an initial delay in response due to acceleration and then recovers in the ST and PS stages. On the other hand, u_{rms} exhibits no significant delay in the near-wall region in the early stage of the deceleration, while v_{rms} and w_{rms} exhibit a considerable initial delay in the near-wall region due to delay in energy redistribution. Turbulence relaxation in the near-wall region slows down during the later stages of the deceleration resulting in a large deviation from the steady value at the final stage of the deceleration. This trend indicates a two-stage turbulence relaxation process in the near-wall region during the deceleration with turbulence undergoing fast reduction in the first phase followed by a slow relaxation phase. This two-stage turbulence relaxation is also reported by Chung (2005).

It is obvious from the response of rms velocity fluctuations that deceleration affects first the near-wall region, and the effect propagates gradually in the core region. This behaviour implies that the turbulence response to the temporal deceleration can be

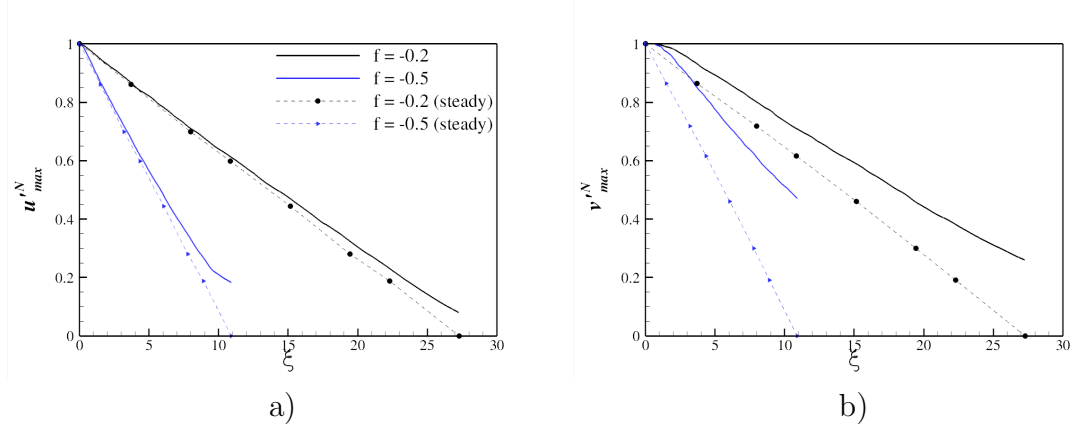


Figure 8.13: Variation of a) the streamwise and b) the wall-normal maximum rms velocity fluctuations calculated using Equation 5.11.

separated into two regions namely: the inner layer response and the outer layer response. Turbulence responds to the deceleration first in the near-wall region while the outer layer exhibits largely negligible change in the turbulence intensity during the early stage of deceleration. It was first proposed by Smits and Wood (1985), that the outer layer dynamics are largely unaffected by the sudden change in the mean pressure gradient and it remains unchanged until the near-wall turbulence changes propagate in the core region. The propagation speed of the the turbulence reduction from the near-wall region to the core region for the rms velocity fluctuations and the turbulent shear stress is calculated using the same criterion employed in Subsection 7.4 (cf. Equation 5.12). The propagation speed for the rms velocity fluctuations and the turbulent shear stress is plotted in Figure 8.14. It shows that turbulence propagation is largely insensitive to the deceleration rate. It is worth noting that the propagation speed is smaller than the initial u_τ value calculated from fully-developed turbulent channel flow at $Re = 22600$, indicating relatively gradual relaxation of the core region turbulence.

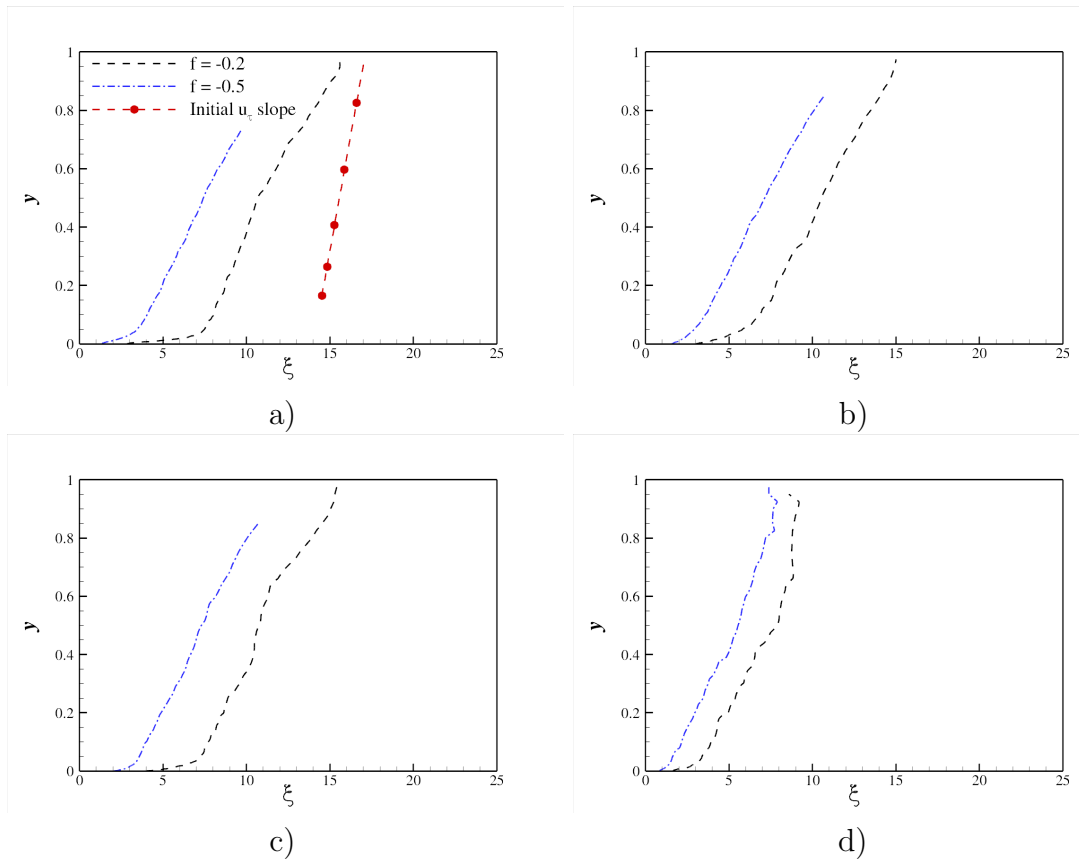


Figure 8.14: Comparison of turbulence relaxation of a) u_{rms} , b) v_{rms} , c) w_{rms} and d) $-\overline{uv}$ in the core region for the two deceleration cases.

8.5 RMS vorticity fluctuations

The response of turbulence during temporal deceleration is investigated in detail in Subsection 8.4, and in this subsection the vorticity analysis is performed to investigate the response of near-wall structures during temporal deceleration. Figure 8.15 shows the rms vorticity fluctuations at several Reynolds numbers during the deceleration for $f = -0.2$ case. The rms vorticity fluctuations exhibit the similar delay in response as the rms velocity fluctuations. ω'_y responds first out of the three components with reduction confined only in the near wall region. While away from the wall, ω'_x remains at significantly higher level than the steady values. This trend indicates that the streamwise vortical structures strength does not decrease considerably during the temporal deceleration, and vortices remain more energetic as compared to the vortices in fully-developed flow. It is interesting to note that in the initial stage of the deceleration at $Re = 20000$ and $Re = 17000$, the wall value of ω'_z , is slightly higher than the steady value. On the other hand, the ω'_z values are quite similar for steady and the deceleration cases in the region of $0.001 \leq y \leq 0.01$, which is the region of maximum turbulent kinetic energy production. As the deceleration proceeds, ω'_z value in $0.001 \leq y \leq 0.01$ region also exhibits a delay in response in the slow relaxation phase.

Figure 8.16 shows the time histories of the maximum values of the rms vorticity fluctuations. All three components exhibit a monotonic decrease in the near-wall region during the deceleration. $\omega'_{x,max}$ shows a delay from the start of the deceleration and stays below the steady value, supporting the trends observed in vorticity profiles in Figure 8.15. It indicates that the strength of streamwise vortices remains higher compared to the fully-developed flow. The evidence of existence of more energetic structures during the temporal deceleration can be clearly seen in iso-surfaces of λ_2 for both deceleration cases at $Re = 3500$ in Figure 8.18. It is interesting to note that the sizes of the near-wall structures remain significantly small in the deceleration

8.5. RMS VORTICITY FLUCTUATIONS

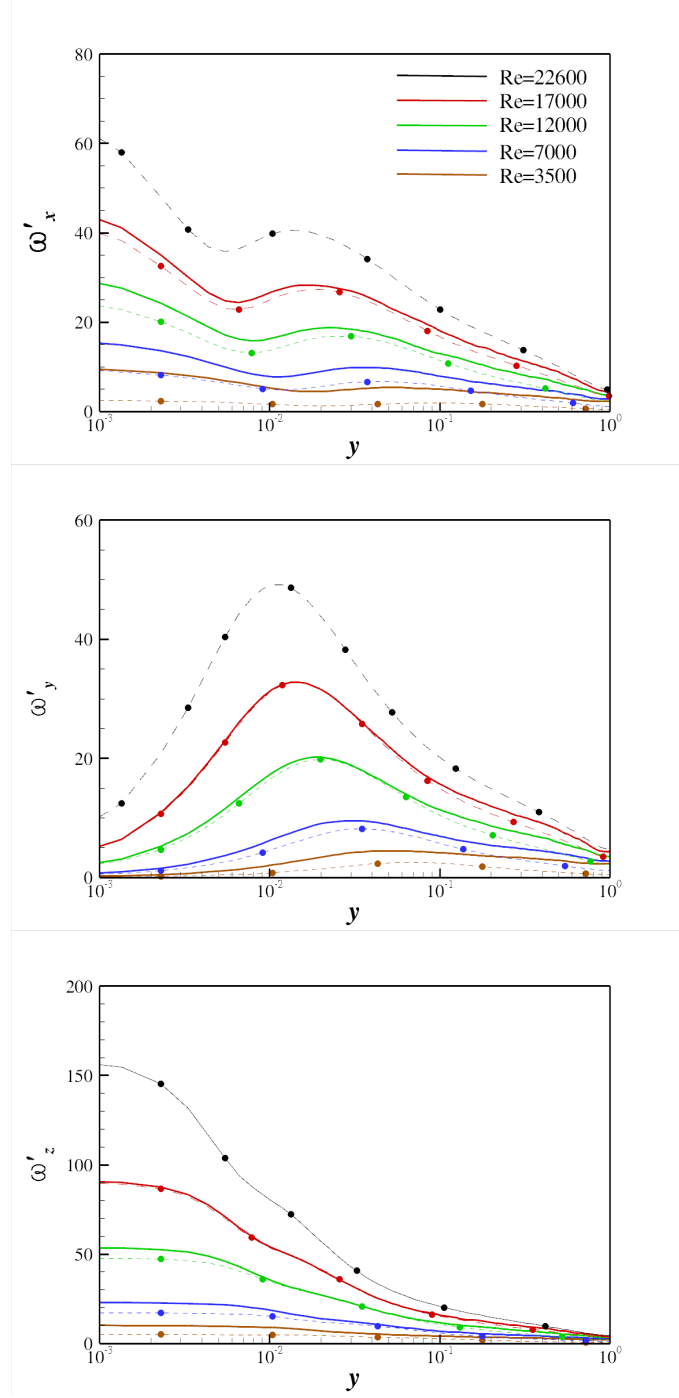


Figure 8.15: Profiles of RMS vorticity fluctuations during deceleration for $f = -0.2$ case.

flow. This indicates that the near-wall structures exhibit a considerable delay in responding to the temporal deceleration. A large delay is found with increase in deceleration rate.

The other two components of vorticity also exhibit monotonic reduction in the near-wall region as shown in Figure 8.16. The deviation from the corresponding steady values increases towards the final stages of the deceleration indicating a slower relaxation phase. It is worth noting that $\omega'_{y,max}$ is rather insensitive to the deceleration rate. The time histories of $\omega'_{x,min}$, $\omega'_{x,max}$ and $\omega'_{y,max}$ locations in Figure 8.17 show that the maximum vorticity locations stay nearer to wall during the deceleration. These trends are consistent with the fact that the size of turbulent structures during the deceleration does not increase significantly as evident from Figure 8.18.

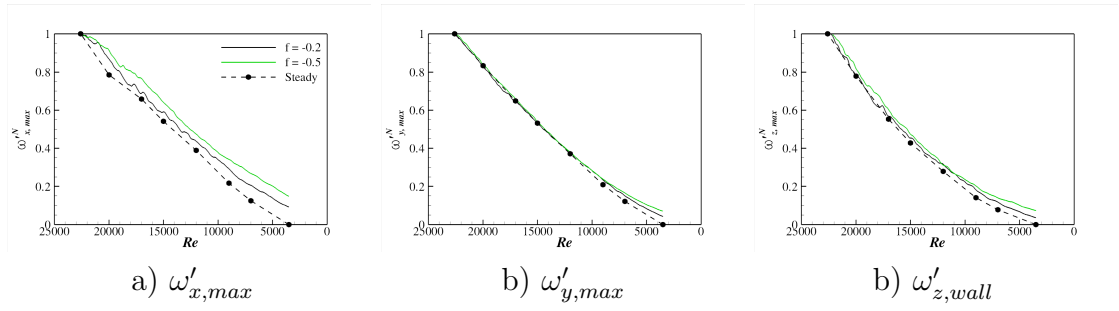


Figure 8.16: Time histories of normalised maximum values of rms vorticity fluctuations during the deceleration for the two cases. Steady value are included for comparison.

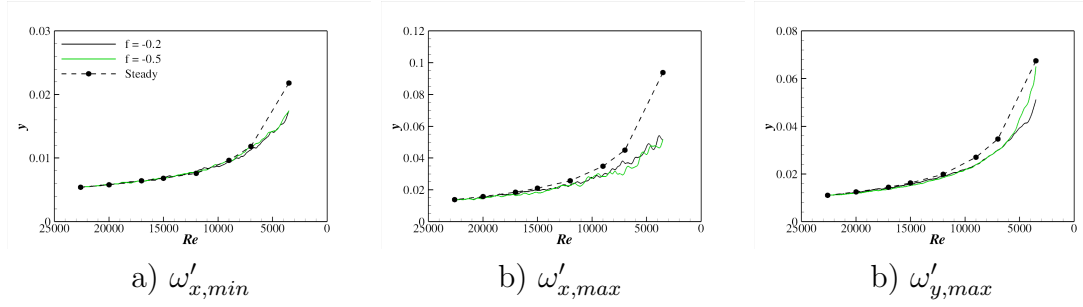


Figure 8.17: Time histories of locations for rms vorticity fluctuations during the deceleration for the two cases. Steady value are included for comparison.

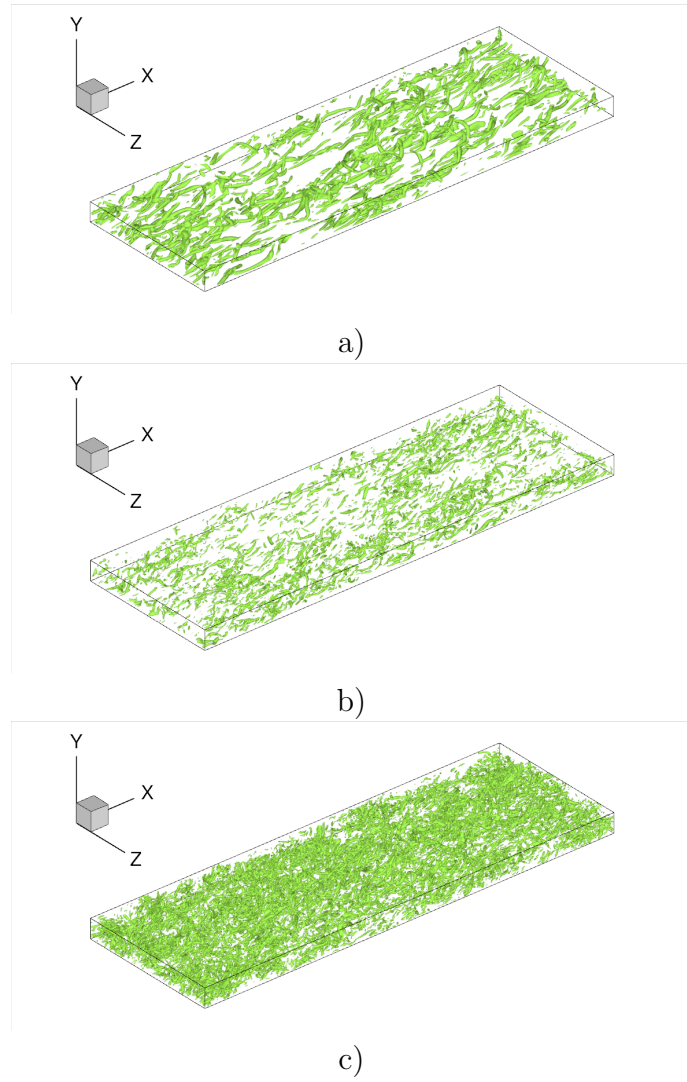


Figure 8.18: Iso-surfaces of λ_2 at $Re = 3500$ for a) a fully-developed channel, b) $f = -0.2$ case and c) $f = -0.5$ case.

8.6 TKE budgets

The near-wall response of \overline{uu} , \overline{vv} and \overline{ww} budget terms can be better understood by analysing the time histories of their maximum values. Figure 8.19 shows the time histories of the maximum values of the turbulent production, viscous dissipation and pressure transport terms. The viscous dissipation term for \overline{uu} responds earliest to the deceleration. This earlier response of ε_{uu} can be explained due to the early response of the wall-normal gradient of the streamwise fluctuations, $\partial u'/\partial y$. The turbulent production of \overline{uu} responds after ε_{uu} , followed by the velocity pressure gradient terms for the three budget equations. The viscous dissipation terms for \overline{vv} and \overline{ww} decreases in the last. It is interesting to note that the budget terms show relatively rapid response in the early stage of the deceleration, followed by a slow response. This trend again supports the earlier observation of two-stage turbulence relaxation in the near-wall region during temporal deceleration.

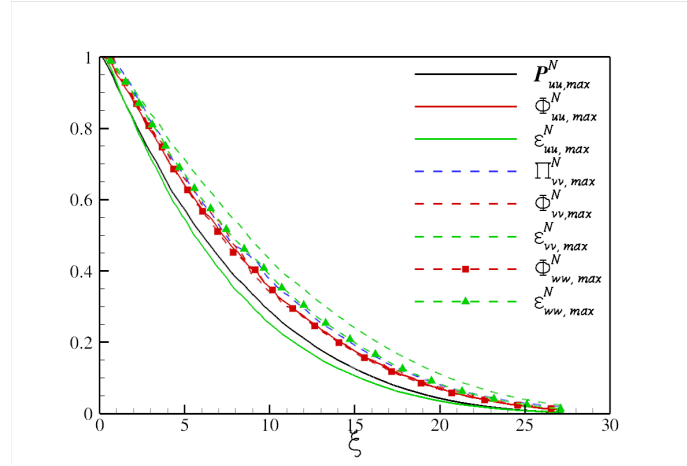


Figure 8.19: Time histories of maximum values of various budget terms for \overline{uu} , \overline{vv} and \overline{ww} transport equation. Maximum values are calculated using Equation 5.11.

The response time for the budget terms of \overline{uu} , \overline{vv} and \overline{ww} transport equations is quantified using the criterion defined in Subsection 5.4. Budget terms of the \overline{uu} equation generally respond first during the deceleration, while \overline{vv} and \overline{ww} budget

8.6. TKE BUDGETS

terms exhibit approximately similar response times. The near-wall response times for all budget terms decrease with the increase in deceleration rate.

Flow Property	$f = -0.2$	$f = -0.5$	M_s	M_f/M_s
$P_{uu,max}$	6.0	2.5	2.2×10^{-2}	784
$T_{uu,max}$	5.5	2.4	4.1×10^{-3}	1614
$T_{uu,min}$	6.1	2.5	-6.2×10^{-3}	679
$\Phi_{uu,min}$	7.2	3.2	-2.8×10^{-3}	686
$D_{uu,wall}$	5.5	2.5	1.4×10^{-3}	1301
$D_{uu,min}$	5.7	2.5	-1.4×10^{-3}	978
$\epsilon_{uu,wall}$	5.5	2.4	1.3×10^{-2}	1235

Table 8.5: Response time (ξ_{50}) for \overline{uu} budget terms. ξ_{50} is the time taken for each property during deceleration to reach 50% of the difference between corresponding initial (M_s) and final (M_f) steady values.

Flow Property	$f = -0.2$	$f = -0.5$	M_s	M_f/M_s
$T_{vv,max}$	6.0	3.1	2.1×10^{-4}	1254
$\Pi_{vv,max}$	7.4	3.7	1.2×10^{-3}	955
$\Phi_{vv,min}$	7.4	3.5	-1.2×10^{-3}	1008
$\Phi_{vv,max}$	7.6	3.6	1.2×10^{-3}	538
$D_{vv,max}$	7.4	3.5	1.3×10^{-4}	858
$\epsilon_{vv,min}$	8.7	4.0	-8.0×10^{-4}	375

Table 8.6: Response time (ξ_{50}) for \overline{vv} budget terms.

Flow Property	$f = -0.2$	$f = -0.5$	M_s	M_f/M_s
$\Phi_{ww,max}$	7.1	3.4	1.6×10^{-3}	935
$D_{ww,wall}$	7.5	3.7	-8.9×10^{-3}	419
$\epsilon_{ww,wall}$	7.6	3.7	-8.0×10^{-3}	375
$\epsilon_{ww,local,max}$	7.6	3.6	-1.1×10^{-3}	901

Table 8.7: Response time (ξ_{50}) for \overline{ww} budget terms.

The turbulent kinetic energy budget terms are plotted at three Reynolds numbers in Figure 8.20 in order to show core region variations. Steady LES data are also included for comparison. All budget terms exhibit approximately an equivalent decrease, as compared to the steady data, in the initial stage of the deceleration ($Re = 20000$), indicating instant initial turbulence response. It is only after a

substantial time, the turbulence relaxation starts to slow down as clearly seen in the profiles at $Re = 12000$ and $Re = 3500$. The production and dissipation terms exhibit a significant delay across the channel during final stage of the deceleration. On the other hand, the turbulent transport and viscous diffusion terms are delayed only in the near-wall region.

8.6. TKE BUDGETS

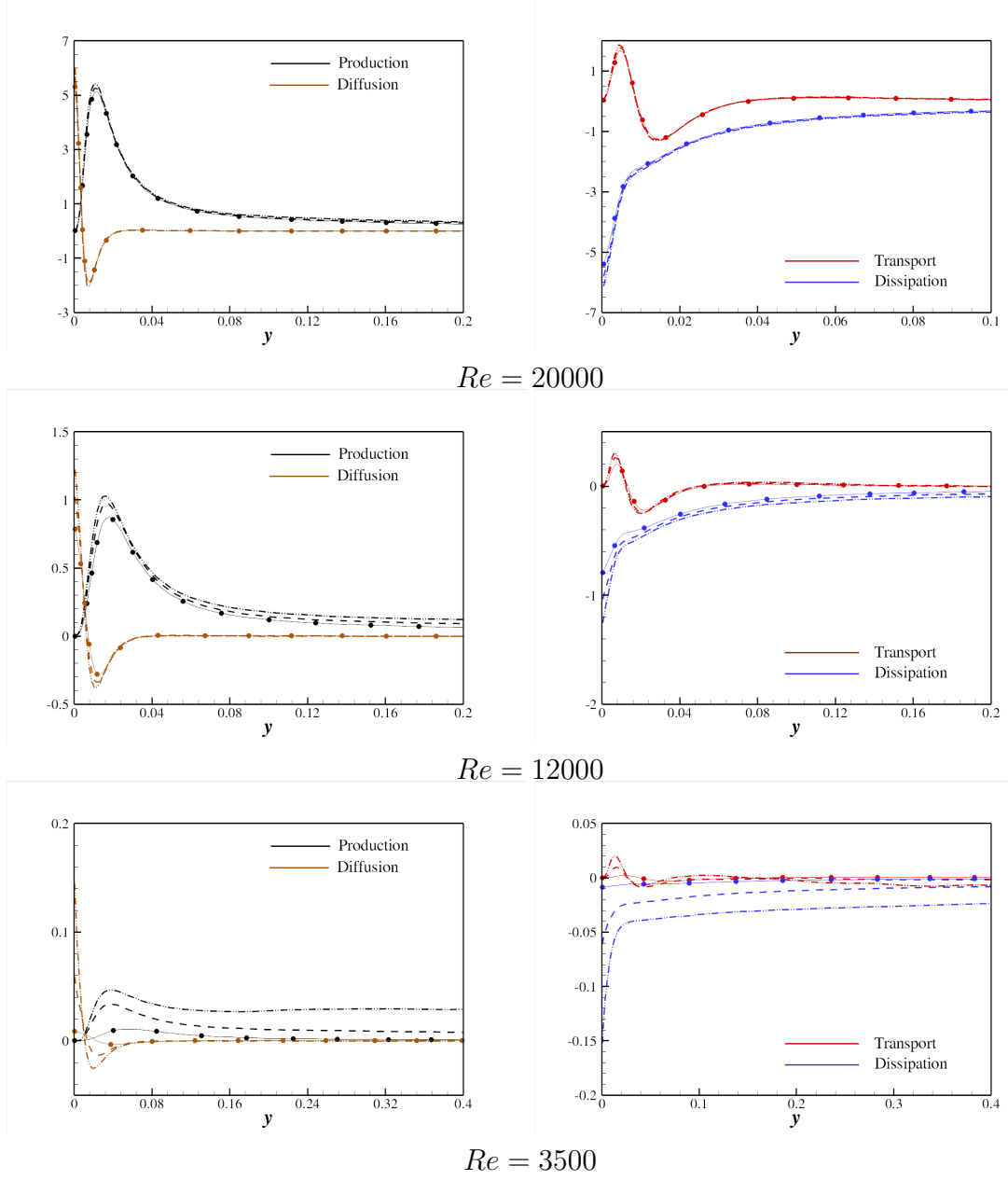


Figure 8.20: Turbulent kinetic energy budget terms profiles in near wall region at several Reynolds number. Solid lines with symbols is for denote profiles. Dashed lines and dashed-dotted-dotted lines denote profiles from $f = -0.2$ and $f = -0.5$ respectively.

8.7 Reynolds stress anisotropy tensor analysis

The response of different terms of Reynolds stress can be studied in terms of anisotropy tensor analysis. The near-wall behaviour of different terms is analysed in Figure 8.21. Figure 8.21 shows the profiles of the second invariant of the anisotropy tensor (II), and two invariant functions, F and G for $f = -0.2$ case. Steady LES data at the initial and final Reynolds numbers are also included. It is clear from Figure 8.21a that the near-wall anisotropy decreases during the temporal deceleration. The profiles at $Re = 3500$ show the clear difference in the isotropy of the deceleration from the steady profile. This increase in isotropy can be attributed to the relatively larger reduction of the streamwise intensity as compared to the other two components. The anisotropy of outer layer region is largely unaffected during the deceleration.

The invariant function F shows the degree of two-component turbulence state and $F = 0$ indicates a two-component turbulence state of flow. The two-component turbulence state usually occurs in the viscous sublayer for turbulent channel flow due to the suppression of the wall-normal intensity. The F profiles shift towards right in the near-wall region with the reduction of flow Reynolds number as shown in Figure 8.21b. This shift is due to an increase in the viscous sublayer thickness. It is interesting to note that F profile shows the opposite trend in the near-wall region from $Re = 7000$ to $Re = 3500$ during deceleration indicating the significant reduction in the two-component state in the viscous sublayer. The invariant function G shows that the flow axisymmetry reduces considerably during the deceleration in the logarithmic region due to relatively slow relaxation of turbulent shear stress as compared to the streamwise intensity. It is interesting to note that the G value increases rapidly at $Re = 3500$ indicating an increase in axisymmetry in the viscous sublayer.

The effect of deceleration on the turbulence structures isotropy can also be analysed

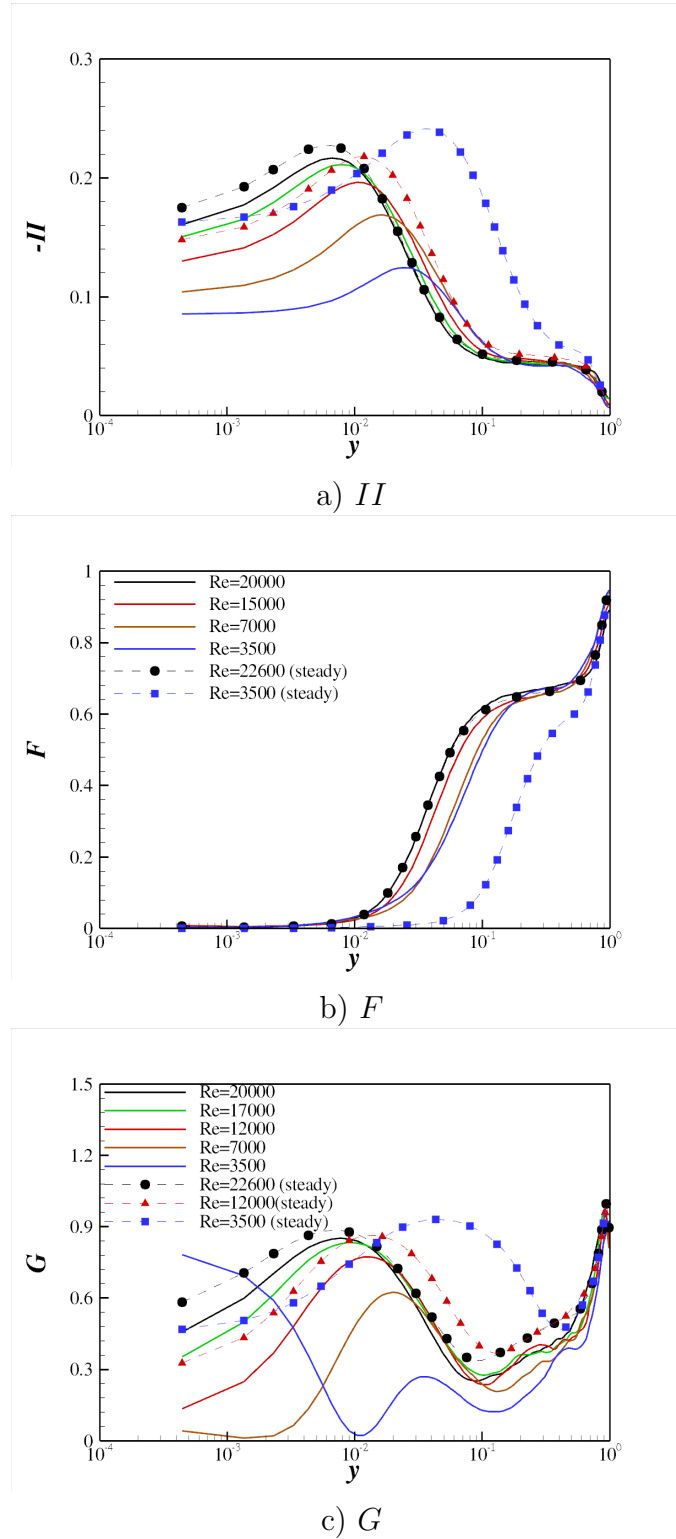


Figure 8.21: Variations of a) II , b) F and c) G at several Reynolds numbers for $f = -0.2$ case during the deceleration. Steady LES profiles (dashed lines with symbols) are also included for comparison.

using anisotropy invariant map (AIM) analysis. Figure 8.22 shows the AIM at several Reynolds numbers during the deceleration for $f = -0.2$ case. Turbulence in the viscous sublayer shifts from the one-component turbulence towards the two-component state in the initial stages of deceleration. This shift is due to slower relaxation of v_{rms} and w_{rms} in comparison with u_{rms} . This trend is maintained in the viscous sublayer until turbulence becomes two-point axisymmetric (left top corner of the AIM) at the final stage of the deceleration ($Re = 3500$). This state indicates the dominance of the overall contribution from b_{22} and b_{33} over b_{11} in the viscous sublayer. The turbulence shifts away from the axisymmetric state in the outer layer region. This trend is due to the increase in contribution from the off-diagonal component b_{12} during the later stages of the deceleration.

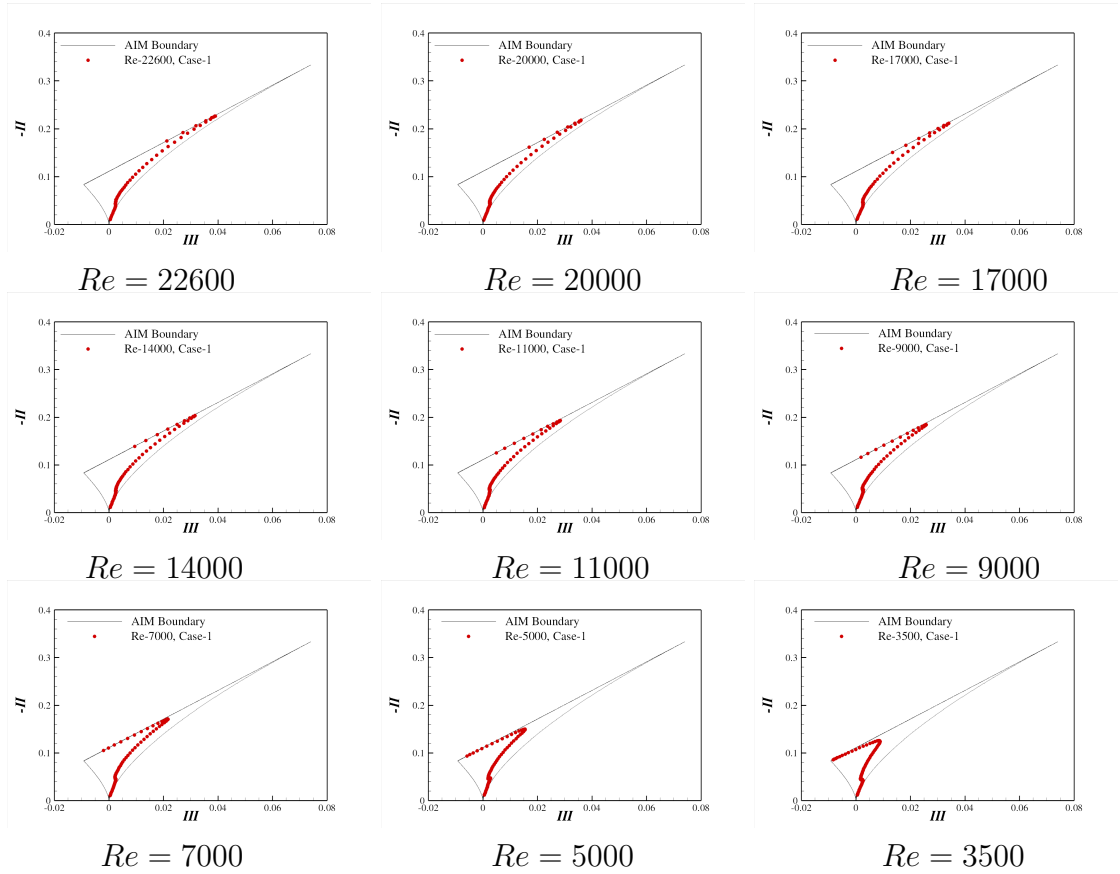


Figure 8.22: Anisotropy invariant maps (AIMs) for $f = -0.2$ case at several Reynolds numbers during deceleration.

8.8 Conclusions

1. Wall shear stress remains similar to the steady value during the initial stages of temporal deceleration. It starts to reduce below the steady value in the later stages of the deceleration.
2. The reduction below the steady value increases with f and rapid deceleration results in flow separation at the wall.
3. The mean velocity exhibits two-layer behaviour in the deceleration. The mean velocity in the inner layer remains below the steady value during the deceleration while the vice versa is true for the outer layer. The law of wall holds good for most parts of the deceleration.
4. Turbulence also exhibits a similar two-layer response, and decreases first in the near wall region with the outer layer virtually frozen during the initial stages of the deceleration.
5. In the near-wall region, turbulence exhibits a two-stage relaxation with an initial fast reduction followed by a slow relaxation.
6. Local equilibrium between the mean flow and turbulence is disturbed during the later stages of the deceleration with turbulence being at higher level. The deviation from the corresponding steady value is more prominent in the near-wall region.
7. RMS vorticity fluctuations in the near-wall region remains at higher level than the corresponding steady values, indicating the existence of high strength near-wall vortices.
8. The viscous dissipation term in \overline{uu} transport equation decreases first of all, followed by the turbulent production and pressure strain terms.

9. The budget terms of \overline{vv} of \overline{ww} transport equations decrease after a further delay.
10. The one-component turbulence state is reduced during the deceleration due to higher decrease in u_{rms} than the other two components, and flow becomes two-point axisymmetric towards the final stage of the deceleration. This behaviour shows that the contribution from b_{11} falls below the overall contribution from b_{22} and b_{33} in the viscous sublayer.
11. In the buffer layer and some part of the log layer, flow shifts away from the axisymmetry because of relatively slower relaxation of the turbulent shear stress.

9

Conclusions.

In the present study, a fully-implicit, fractional step method based on Crank-Nicolson temporal discretisation (Kim et al., 2002) has been implemented. Three test cases have been employed to validate the accuracy of the code. Two SGS models namely, the dynamic SGS model (Germano et al., 1991; Lilly, 1992) and the wall-adapting local eddy viscosity (WALE) SGS model (Nicoud and Ducros, 1999) are considered in the present study. LES results validated by the comparison with the corresponding DNS data at several Reynolds numbers for fully-developed turbulent channel. The domain length of $L = 12h$ is found to be appropriate for temporal acceleration. Calculations using domain length of $L = 6h$ exhibited a suppression of the near-wall

turbulence response during the acceleration. On the other hand, the turbulence response for domain lengths $L = 6h$ and $L = 12h$ for temporal deceleration is found similar.

DNS of temporal acceleration has revealed many interesting trends for response of the wall shear stress, the mean velocity and turbulence. The turbulent statistics are generated using approximately 190 million grid cells and can be used as benchmark for unsteady turbulence modelling. The wall shear stress response during temporal acceleration can be divided into four distinct stages namely: the initial transient (IT) stage (stage I), the weak time-dependence (WT) stage (stage II), the strong time-dependence (ST) stage (stage III), and the pseudo-steady (PS) stage (stage IV). The delays in turbulence production and redistribution are quantified in the near-wall region, and the streamwise velocity component is found to respond first during acceleration. The structure parameter (a_1) reduces during the WT stage and increases rapidly in the ST stage. The rms vorticity fluctuations also exhibit an initial delay in responding to the acceleration, and wall-normal locations of the maximum vorticity are found to exhibit a two-stage reduction trend. The production term for \overline{uu} increases first of all in the near-wall region resulting in a subsequent increase in u_{rms} , and the turbulent kinetic energy is redistributed among the other two components by the velocity pressure gradient term. The quadratic contributions from Q_1 and Q_4 increase in the near-wall region during the ST stage, accompanied with a corresponding reduction of contributions from Q_2 and Q_3 .

The near-wall structures also exhibit an initial delay in responding to the temporal acceleration. Two different types of flow structures have been found in the present study. Old turbulent structures are associated with the initial flow field, while new turbulent structures are generated during acceleration. A novel procedure to identify regions of new turbulence has been developed, and the rate of new turbulence generation occur approximately at an exponential rate. The conditionally-averaged

statistics from active and non-active areas clearly indicate the emergence of new turbulence in distinct patches. The turbulence anisotropy is found to increase during the IT and WT stages while it decreases in the ST stage.

LES of temporal acceleration is performed to study the turbulence response after the ST stage and to investigate turbulence propagation in the core region. The effect of acceleration rates on turbulence evolution is also studied. LES results show good agreement with the DNS results in Chapter 5, validating the accuracy of the present LES. The deviation of the wall shear stress and the mean velocity from the corresponding steady values increases while the delay in turbulence response decrease at a high acceleration rate. The characteristic speed of turbulence propagation in the core region is found to be similar to the initial u_τ value, and it is largely independent of the acceleration rate. An initial increase in coherence of near-wall structures has been found and this enhanced coherence increases at higher acceleration rates.

LES of temporal deceleration has been performed to study turbulence response. Two deceleration rates are employed to investigate the effect of different deceleration rates. The wall shear stress decreases monotonically during the deceleration. The mean velocity exhibits a two-layer response with the inner layer flow decreasing below the steady corresponding values, and the outer layer mean velocity remains higher than the steady mean velocity. Turbulence also shows an earlier decrease in the near-wall region while the core region remains in a frozen state. Near-wall turbulent structures remain at relatively smaller size during the deceleration as compared to the corresponding steady structures. The turbulence anisotropy decreases in the near-wall region during the deceleration.

Bibliography

- H. Abe, H. Kawamura, and Y. Matsuo. Direct numerical simulation of a fully developed turbulent channel flow with respect to the Reynolds number dependence. *ASME: Journal of Fluids Engineering*, 123(2):382–393, 2001.
- H. Abe, H. Kawamura, and Y. Matsuo. Surface heat-flux fluctuations in a turbulent channel flow up to $Re_\tau = 1020$ with $Pr = 0.025$ and 0.71 . *International Journal of Heat and Fluid Flow*, 25(3):404–419, 2004.
- A. E. Alving and H. H. Fernholz. Turbulence measurements around a mild separation bubble and downstream of reattachment. *Journal of Fluid Mechanics*, 322:297–328, 1996.
- I. Annus and T. Koppel. Transition to turbulence in accelerating pipe flow. *ASME: Journal of Fluids Engineering*, 133(7):071202, 2011.
- C. Ariyaratne, S. He, and A. E. Vardy. Wall friction and turbulence dynamics in decelerating pipe flows. *Journal of Hydraulic Research*, 48(6):810–821, 2010.
- C. D. Aubertine and J. K. Eaton. Turbulence development in a non-equilibrium turbulent boundary layer with mild adverse pressure gradient. *Journal of Fluid Mechanics*, 532:345–364, 2005.

BIBLIOGRAPHY

- R. M. Beam and R. F. Warming. An implicit factored scheme for the compressible Navier-Stokes equations. *AIAA Journal*, 16:393–402, 1978.
- R. F. Blackwelder and H. Eckelmann. Streamwise vortices associated with the bursting phenomenon. *Journal of Fluid Mechanics*, 94(3):577–594, 1979.
- R. F. Blackwelder and L. S. G. Kovasznay. Large-scale motion of a turbulent boundary layer during relaminarization. *Journal of Fluid Mechanics*, 53(1):61–83, 1972.
- C. Bourassa and F. O. Thomas. An experimental investigation of a highly accelerated turbulent boundary layer. *Journal of Fluid Mechanics*, 634:359–404, 2009.
- M. E. Brachet, D. I. Meiron, S. A. Orszag, B. G. Nickel, R. H. Morf, and U. Frisch. Small-scale structure of the Taylor-Green vortex. *Journal of Fluid Mechanics*, 130:411–452, 1983.
- P. Bradshaw and N. Pontikos. Measurements in the turbulent boundary layer of an ‘infinite’ swept wing. *Journal of Fluid Mechanics*, 159:105–130, 1985.
- H. Choi and P. Moin. Direct numerical simulation of turbulent flow over riblets. *Journal of Fluid Mechanics*, 255:503–539, 1993.
- H. Choi and P. Moin. Effects of the computational time step on numerical solutions of turbulent flow. *Journal of Computational Physics*, 113(1):1–4, 1994.
- M. S. Chong, A. E. Perry, and B. J. Cantwell. A general classification of three-dimensional flow fields. *Physics of Fluids A*, 2(5):765–777, 1990.
- A. J. Chorin. A numerical method for solving incompressible viscous flow problems. *Journal of Computational Physics*, 2(1):12–26, 1967.
- Y. M. Chung. Unsteady turbulent flow with sudden pressure gradient changes. *International Journal for Numerical Methods in Fluids*, 47(8-9):925–930, 2005.

- Y. M. Chung and T. Talha. Effectiveness of active flow control for turbulent skin friction drag reduction. *Physics of Fluids*, 23(2):025102, 2011.
- Y. M. Chung, H. J. Sung, and P.-Å. Krogstad. Modulation of near-wall turbulence structure with uniform wall blowing and suction. *AIAA Journal*, 40(8):1529–1535, 2002.
- G. N. Coleman, J. Kim, and A. T. Le. A numerical study of three-dimensional wall-bounded flows. *International Journal of Heat and Fluid Flow*, 17(3):333–342, 1996.
- G. N. Coleman, J. Kim, and P. R. Spalart. A numerical study of strained three-dimensional wall-bounded turbulence. *Journal of Fluid Mechanics*, 416:75–116, 2000.
- G. N. Coleman, J. Kim, and P. R. Spalart. Direct numerical simulation of a decelerated wall-bounded turbulent shear flow. *Journal of Fluid Mechanics*, 495:1–18, 2003.
- G. N. Coleman, Federov D., P.R. Spalart, and J. Kim. A numerical study of laterally strained wall-bounded turbulence. *Journal of Fluid Mechanics*, 639:443–478, 2009.
- M. A. Cotton. Resonant responses in periodic turbulent flows: computations using a k-epsilon eddy viscosity model. *Journal of Hydraulic Research*, 45(1):54–61, 2007.
- R. B. Dean and P. Bradshaw. Measurements of interacting turbulent shear layers in a duct. *Journal of Fluid Mechanics*, 78(part 4):641–676, 1976.
- J. W. Deardorff. On the magnitude of the subgrid scale eddy coefficient. *Journal of Computational Physics*, 7(1):120–133, 1971.
- Y. Dubief and F. Delcayre. On coherent-vortex identification in turbulence. *Journal of Turbulence*, 1:1–22, 2000.

BIBLIOGRAPHY

- J. K. Dukowicz and A. S. Dvinsky. Approximate factorization as a high order splitting for the implicit incompressible flow equations. *Journal of Computational Physics*, 102(2):336–347, 1992.
- M. P. Escudier, A. Abdel-Hameed, M. W. Johnson, and C. J. Sutcliffe. Laminarisation and re-transition of a turbulent boundary layer subjected to favourable pressure gradient. *Experiments in Fluids*, 25(5-6):491–502, 1998.
- H. H. Fernholz and D. Warnack. The effects of a favourable pressure gradient and of the Reynolds number on an incompressible axisymmetric turbulent boundary layer. Part 1: The turbulent boundary layer. *Journal of Fluid Mechanics*, 359:329–356, 1998.
- M. Germano. Averaging invariance of the turbulent equations and similar subgrid scale modeling. CTR Manuscript 116. Stanford University, USA, 1990.
- M. Germano, U. Piomelli, P. Moin, and W. H. Cabot. A dynamic subgrid-scale eddy viscosity model. *Physics of Fluids A*, 3(7):1760–1765, 1991.
- S. Ghosal and P. Moin. The basic equations of the large eddy simulation of turbulent flows in complex geometry. *Journal of Computational Physics*, 118(1):24–37, 1995.
- S. Ghosal, T. S. Lund, P. Moin, and K. Akselvoll. A dynamic localization model for large eddy simulation of turbulent flows. *Journal of Fluid Mechanics*, 286:229–255, 1995.
- D. Greenblatt and E. A. Moss. Pipe-flow relaminarization by temporal acceleration. *Physics of Fluids*, 11(11):3478–3481, 1999.
- D. Greenblatt and E. A. Moss. Rapid transition to turbulence in pipe flows accelerated from rest. *ASME: Journal of Fluids Engineering*, 125(6):1072–1075, 2003.
- D. Greenblatt and E. A. Moss. Rapid temporal acceleration of a turbulent pipe flow. *Journal of Fluid Mechanics*, 514:65–75, 2004.

- P. M. Gresho. On the theory of semi-implicit projection methods for viscous incompressible flow and its implementation via a finite element method that also introduces a nearly consistent mass matrix. Part 1: Theory. *International Journal for Numerical Methods in Fluids*, 11(5):587–620, 1990.
- F. H. Harlow and J. E. Welch. Numerical calculation of time-dependent viscous incompressible flow of fluid with free surface. *Physics of Fluids*, 8(12):2182–2189, 1965.
- S. He and J. D. Jackson. A study of turbulence under conditions of transient flow in a pipe. *Journal of Fluid Mechanics*, 408:1–38, 2000.
- S. He and J. D. Jackson. An experimental study of pulsating turbulent flow in a pipe. *European Journal of Mechanics B/Fluids*, 28(2):309–320, 2009.
- S. He, C. Ariyaratne, and A. E. Vardy. A computational study of wall friction and turbulence dynamics in accelerating pipe flows. *Computers and Fluids*, 37(6):674–689, 2008.
- A. Holstad, H. I. Andersson, and B. Pettersen. Turbulence in a three-dimensional wall-bounded shear flow. *International Journal for Numerical Methods in Fluids*, 62:875–905, 2010.
- R. J. A. Howard and N. D. Sandham. Simulation and modelling of a skewed turbulent channel flow. *Flow, Turbulence and Combustion*, 65(1):83–109, 2000.
- S. Huang and Q. S. Li. A new dynamic one-equation subgrid-scale model for large eddy simulations. *International Journal for Numerical Methods in Engineering*, 81:835–865, 2010.
- M. Ichimiya, I. Nakamura, and S. Yamashita. Properties of a relaminarizing turbulent boundary layer under a favorable pressure gradient. *Experimental Thermal and Fluid Science*, 17(1-2):37–48, 1998.

BIBLIOGRAPHY

- J. Jeong and F. Hussain. On the identification of a vortex. *Journal of Fluid Mechanics*, 285:69–94, 1995.
- J. Jeong, F. Hussain, W. Schoppa, and J. Kim. Coherent structures near the wall in a turbulent channel flow. *Journal of Fluid Mechanics*, 332:185–214, 1997.
- J. Jiminez and P. Moin. The minimal flow unit in near-wall turbulence. *Journal of Fluid Mechanics*, 225:213–240, 1991.
- S. Y. Jung and Y. M. Chung. LES of transient turbulent flow in a pipe. In *11th European Turbulence Conference*, page 781, 2007.
- S. Y. Jung and Y. M. Chung. Large-eddy simulation of accelerated turbulent flow in a pipe. In *Turbulence and Shear Flow Phenomena -6*, volume 1, pages 277–282, 2009.
- W. J. Jung, N. Mangiavacchi, and R. Akhavan. Suppression of turbulence in wall-bounded flows by high-frequency spanwise oscillations. *Physics of Fluids A*, 4(8):1605–1607, 1992.
- T. Kajishima and T. Nomachi. One-equation subgrid scale model using dynamic procedure for the energy production. *Journal of Applied Fluid Mechanics*, 73(3):368–373, 2006.
- K. Kataoka, T. Kawabata, and K. Miki. The start-up response of pipe flow to a step change in flow rate. *Journal of Chemical Engineering Japan*, 8(4):266–271, 1975.
- H. T. Kim, S. J. Kline, and W. C. Reynolds. The production of turbulence near a smooth wall in a turbulent boundary layer. *Journal of Fluid Mechanics*, 50(1):133–160, 1971.
- J. Kim and P. Moin. Application of a fractional-step method to incompressible Navier-Stokes equations. *Journal of Computational Physics*, 59(2):308–323, 1985.

- J. Kim, P. Moin, and R. Moser. Turbulence statistics in fully developed channel flow at low Reynolds number. *Journal of Fluid Mechanics*, 177:133–166, 1987.
- K. Kim, S.-J. Baek, and H. J. Sung. An implicit velocity decoupling procedure for the incompressible Navier-Stokes equations. *International Journal for Numerical Methods in Fluids*, 38(2):125–138, 2002.
- S. J. Kline, W. C. Reynolds, F. A. Schraub, and P. W. Runstadler. The structure of turbulent boundary layers. *Journal of Fluid Mechanics*, 30(4):741–773, 1967.
- P.-Å. Krogstad and P. E. Skare. Influence of a strong adverse pressure gradient on the turbulent structure in a boundary layer. *Physics of Fluids*, 7(8):2014–2024, 1995.
- P.-Å. Krogstad and L. E. Torbergsen. Invariant analysis of turbulent pipe flow. *Flow, Turbulence and Combustion*, 64(3):161–181, 2000.
- J. Kurokawa and M. Morikawa. Accelerated and decelerated flows in a circular pipe (1st report, velocity profiles and friction coefficient). *Bulletin of Japanese Society of Mechanical Engineers*, 29:758–765, 1986.
- B. E. Launder. Laminarization of the turbulent boundary layer in a severe acceleration. Technical Report 71, MIT Gas Turbine Laboratory, Cambridge, MA, USA, 1964.
- A. T. Le, G. N. Coleman, and J. Kim. Near-wall turbulence structures in three-dimensional boundary layers. *International Journal of Heat and Fluid Flow*, 21(5):480–488, 2000.
- H. Le and P. Moin. An improvement of fractional step methods for the incompressible Navier-Stokes equations. *Journal of Computational Physics*, 92(2):369–379, 1991.

BIBLIOGRAPHY

- J. H. Lee and H. J. Sung. Structures in turbulent boundary layers subjected to adverse pressure gradients. *Journal of Fluid Mechanics*, 639:101–131, 2009.
- M. J. Lee and C. W. Reynolds. Numerical experiments on the structure of homogenous turbulence. Report TF-24, Thermosciences Division, Department of Mechanical Engineering, Stanford University, USA, 1985.
- P. J. Lefebvre and F. M. White. Experiments on transition to turbulence in a constant-acceleration pipe flow. *ASME: Journal of Fluids Engineering*, 111(4):428–432, 1989.
- P. J. Lefebvre and F. M. White. Further experiments on transition to turbulence in constant-acceleration pipe flow. *ASME: Journal of Fluids Engineering*, 113(2):223–227, 1991.
- A. Leonard. Energy cascade in large-eddy simulations of turbulent fluid flows. *Advances in geophysics*, 18(1):237–249, 1974.
- D. K. Lilly. On the application of eddy viscosity concept to in the inertial subrange of turbulence. NCAR MS 123, National Centre for Atmospheric Research, USA, 1966.
- D. K. Lilly. A proposed modification of the Germano subgrid-scale closure method. *Physics of Fluids A*, 4(3):633–635, 1992.
- S. S. Lu and W. W. Willmarh. Measurements of the structure of the reynolds stress in a turbulent boundary layer. *Journal of Fluid Mechanics*, 60:481–511, 1973.
- H. J. Lugt. *The dilemma of defining a vortex*, pages 309–321. Recent developments in theoretical and experimental fluid mechanics: Compressible and incompressible flows. Berlin, Springer-Verlag, 1979.
- J. L. Lumley and G. R. Newman. The return to isotropy of homogeneous turbulence. *Journal of Fluid Mechanics*, 82:161–178, 1977.

- M. Manhart and R. Friedrich. DNS of a turbulent boundary layer with separation. *International Journal of Heat and Fluid Flow*, 23(5):572–581, 2002.
- R. R. Mankbadi and J. T. C. Liu. Near-wall response in turbulent shear flows subjected to imposed unsteadiness. *Journal of Fluid Mechanics*, 238:55–71, 1992.
- M. Manna and A. Vacca. Spectral dynamic of pulsating turbulent pipe flow. *Computers and Fluids*, 37(7):825–835, 2008.
- N. N. Mansour, J. Kim, and P. Moin. Reynolds-stress and dissipation-rate budgets in a turbulent channel flow. *Journal of Fluid Mechanics*, 194:15–44, 1988.
- Z.-X. Mao and T. J. Hanratty. Studies of the wall shear stress in a turbulent pulsating pipe flow. *Journal of Fluid Mechanics*, 170:545–564, 1986.
- T. Maruyama, T. Kuribayashi, and T. Mizushima. The structure of the turbulence in transient flows. *Journal of Chemical Engineering Japan*, 9:431–439, 1976.
- S. Mehdi, S. He, and A. E. Vardy. A comparative study of turbulence in ramp-up and ramp-down unsteady flows. *Flow, Turbulence and Combustion*, 86(3-4):439–454, 2011.
- C. Meneveau, T. S. Lund, and P. Moin. A lagrangian dynamic subgrid-scale model of turbulence. *Journal of Fluid Mechanics*, 319:353–385, 1996.
- T. Mizushima, T. Maruyama, and Y. Shiozaki. Pulsating turbulent flow in a tube. *Journal of Chemical Engineering Japan*, 6:487–494, 1973.
- T. Mizushima, T. Maruyama, and H. Hirasawa. Structure of the turbulence in pulsating pipe flows. *Journal of Chemical Engineering Japan*, 8, 1975.
- P. Moin. Advances in large eddy simulation methodology for complex flows. *International Journal of Heat and Fluid Flow*, 23(5):710–720, 2002.

BIBLIOGRAPHY

- P. Moin and J. Kim. Numerical investigation of turbulent channel flow. *Journal of Fluid Mechanics*, 118:341–377, 1982.
- P. Moin and K. Mahesh. Direct numerical simulation: A tool in turbulence research. *Annual Review of Fluid Mechanics*, 30:539–578, 1998.
- P. Moin, T. H. Shih, D. M. Driver, and N. N. Mansour. Direct numerical simulation of a three dimensional turbulent boundary layer. *Physics of Fluids A*, 2(10):1846–1853, 1990.
- R. Moser, J. Kim, and N. Mansour. Direct numerical simulation of turbulent channel flow up to $Re_\tau = 590$. *Physics of Fluids*, 11(4):943–945, 1999.
- R. Mukund, P. R. Viswanath, R. Narasimha, A. Prabhu, and J. D. Crouch. Relaminarization in highly favourable pressure gradients on a convex surface. *Journal of Fluid Mechanics*, 567:97–155, 2006.
- Y. Na and P. Moin. Direct numerical simulation of a separated turbulent boundary layer. *Journal of Fluid Mechanics*, 374:379–405, 1998.
- Y. Nakahata, C. W. Knisely, K. Nishihara, Y. Sasaki, and M. Iguchi. Propagation of turbulence in constant-acceleration pipe flow. *Journal of the Japanese Society for Experimental Mechanics*, 7(2):148–154, 2007.
- M. A. Narayanan and V. Ramjee. On the criteria for reverse transition in a two-dimensional boundary layer flow. *Journal of Fluid Mechanics*, 35(2):225–241, 1969.
- F. Nicoud and F. Ducros. Subgrid-scale stress modelling based on the square of the velocity gradient tensor. *Flow, Turbulence and Combustion*, 62(3):183–200, 1999.
- N. Park, S. Lee, J. Lee, and H. Choi. A dynamic subgrid-scale eddy viscosity model with a global model coefficient. *Physics of Fluids*, 18(12):125109, 2006.

- J. B. Perot. An analysis of the fractional step method. *Journal of Computational Physics*, 108(1):51–58, 1993.
- U. Piomelli, P. Moin, and J. H. Ferziger. Model consistency in large eddy simulation of turbulent channel flows. *Physics of Fluids*, 31(7):1884–1891, 1988.
- U. Piomelli, T. A. Zang, C. G. Speziale, and M. Y. Hussaini. On the large-eddy simulation of transitional wall-bounded flows. *Physics of Fluids A*, 2(2):267–275, 1990.
- U. Piomelli, G. N. Coleman, and J. Kim. On the effects of nonequilibrium on the subgrid-scale stresses. *Physics of Fluids*, 9(9):2740–2748, 1997.
- U. Piomelli, E. Balaras, and A. Pascarelli. Turbulent structures in accelerating boundary layers. *Journal of Turbulence*, 1(1):001, 2000.
- M. Quadrio and P. Ricco. Critical assessment of turbulent drag reduction through spanwise wall oscillations. *Journal of Fluid Mechanics*, 521:251–271, 2004.
- M. Quadrio, P. Ricco, and C. Viotti. Streamwise-travelling waves of spanwise wall velocity for turbulent drag reduction. *Journal of Fluid Mechanics*, 627:161–178, 2009.
- M. Rai, , and P. Moin. Direct simulations of turbulent flow using finite-difference schemes. *Journal of Computational Physics*, 96(1):15–53, 1991.
- B. R. Ramaprian and S. W. Tu. Fully developed periodic turbulent pipe flow. Part 2: The detailed structure of the flow. *Journal of Fluid Mechanics*, 137:59–81, 1983.
- W. C. Reynolds. *The potential and limitations of direct and large eddy simulations*, pages 313–343. *Wither Turbulence? Turbulence at the Crossroads*. Berlin, Springer-Verlag, 1990.

BIBLIOGRAPHY

- S. K. Robinson. Coherent motions in the turbulent boundary layer. *Annual Review of Fluid Mechanics*, 23:601–639, 1991.
- M. Rosenfeld. Uncoupled temporally second-order implicit solver of incompressible Navier-Stokes equations. *AIAA Journal*, 34:1829–1834, 1996.
- W. R. Schwarz and P. Bradshaw. Turbulence structural changes for a three-dimensional turbulent boundary layer in a 30 bend. *Journal of Fluid Mechanics*, 274:183–210, 1994.
- A. Scotti and U. Piomelli. Numerical simulation of pulsating turbulent channel flow. *Physics of Fluids*, 13(5):1367–1384, 2001.
- A. Scotti and U. Piomelli. Turbulence models in pulsating flows. *AIAA Journal*, 40(3):537–543, 2002.
- A. J. Simonsen and P.-Å. Krogstad. Turbulent stress invariant analysis: Clarification of existing terminology. *Physics of Fluids*, 17(8):088103, 2005.
- M. Skote and D. S. Henningson. Direct numerical simulation of a separated turbulent boundary layer. *Journal of Fluid Mechanics*, 471:107–136, 2002.
- J. Smagorinsky. General circulation experiments with the primitive equations I. the basic experiment. *Monthly Weather Review*, 91(3):99–164, 1963.
- C. Smith and S. Metzler. The characteristics of low-speed streaks in the near-wall region of a turbulent boundary layer. *Journal of Fluid Mechanics*, 129:27–54, 1983.
- A. J. Smits and D. H. Wood. The response of turbulent boundary layers to sudden perturbations. *Annual Review of Fluid Mechanics*, 17:321–328, 1985.
- P. R. Spalart and J. H. Watmuff. Experimental and numerical study of a turbulent boundary layer with pressure gradients. *Journal of Fluid Mechanics*, 249:337–373, 1993.

- K. R. Sreenivasan. Laminarescent, relaminarizing, and retransitional flows. *Acta Mechanica*, 44:1–48, 1982.
- M. Stanislas, L. Perret, and J.-M. Foucaut. Vortical structures in the turbulent boundary layer: A possible route to a universal representation. *Journal of Fluid Mechanics*, 602:327–382, 2008.
- G. D. Stefano and O. V. Vasilyev. Sharp cutoff versus smooth filtering in large eddy simulation. *Physics of Fluids*, 14(1):362–369, 2002.
- S. F. Tardu, G. Binder, and R. F. Blackwelder. Turbulent channel flow with large amplitude. *Journal of Fluid Mechanics*, 267:109–151, 1994.
- S. W. Tu and B. R. Ramaprian. Fully developed periodic turbulent pipe flow. Part 1: Main experimental results and comparison with predictions. *Journal of Fluid Mechanics*, 137:31–58, 1983.
- A. E. Vardy and J. M. B. Brown. Transient turbulent friction in smooth pipe flows. *Journal of Sound and Vibration*, 259(5):669–684, 2003.
- A. E. Vardy and J. M. B. Brown. Approximation of turbulent wall shear stresses in highly transient pipe flows. *Journal of Hydraulic Research*, 133(11):1219–1228, 2007.
- A. E. Vardy and J. M. B. Brown. Influence of time-dependent viscosity on wall shear stresses in unsteady pipe flows. *Journal of Hydraulic Research*, 48(2):225–237, 2010a.
- A. E. Vardy and J. M. B. Brown. Evaluation of unsteady wall shear stress by Zielke’s method. *Journal of Hydraulic Research*, 136(7):453–456, 2010b.
- A. W. Vreman. An eddy-viscosity subgrid-scale model for turbulent shear flow: Algebraic theory and applications. *Physics of Fluids*, 16(10):3670–3681, 2004.

BIBLIOGRAPHY

- D. Warnack and H. H. Fernholz. The effects of a favourable pressure gradient and of the Reynolds number on an incompressible axisymmetric turbulent boundary layer. Part 2: The boundary layer with relaminarization. *Journal of Fluid Mechanics*, 359:357–381, 1998.
- F. M. White. *Viscous Fluid Flow*. McGraw Hill, 2006.
- D. You and P. Moin. A dynamic global-coefficient subgrid-scale eddy-viscosity model for large-eddy simulation in complex geometries. *Physics of Fluids*, 19(6):065110, 2007.
- W. Zielke. Frequency dependent friction in transient pipe flow. *Transactions of the ASME. Series D, Journal of Basic Engineering*, 90(1):109–115, 1968.



Comparison of dynamic and WALE SGS
models.

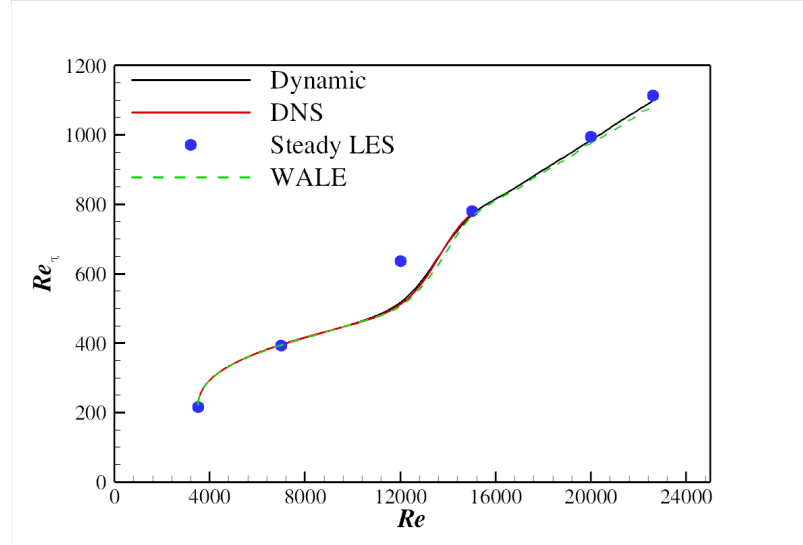


Figure A.1: Comparison of Re_τ histories for the two models with the DNS data.

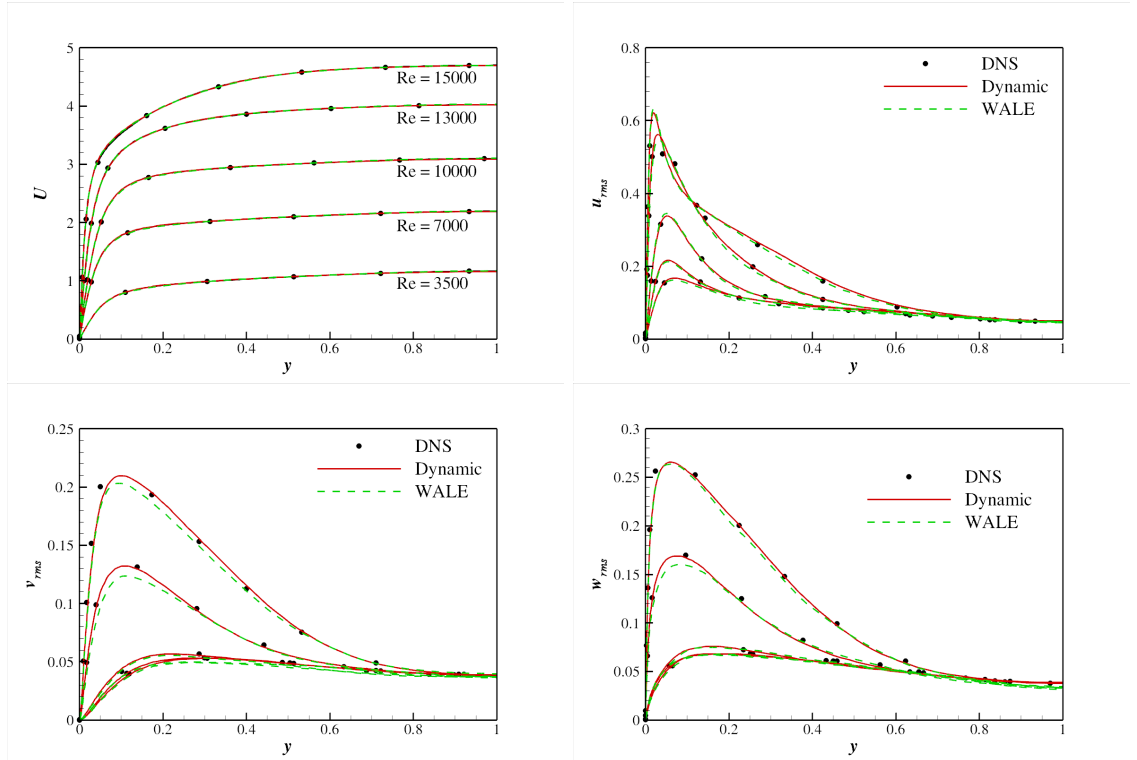


Figure A.2: Comparison of mean velocity and rms velocity fluctuations at several Reynold number for the two models with the corresponding DNS data.